Geology of the Monowai Rift Zone and Louisville Segment of the Tonga-Kermadec Arc: Regional Controls on Arc Magmatism and Hydrothermal Activity

ALEXANDRA GRAY

Thesis submitted to the University of Ottawa
in partial Fulfillment of the requirements for the
Master's degree in Earth Sciences

Department of Earth and Environmental Sciences
Faculty of Science
University of Ottawa

© Alexandra Gray, Ottawa, Canada, 2022

Abstract

The Tonga-Kermadec arc in the SW Pacific comprises a chain of more than 90 volcanic complexes. A continuous 400-km long chain of volcanic activity along the central portion of the Tonga arc has become the focus of intensive research, extending previous studies that have focused on the southern Kermadec chain. Earlier interpretations of the Tonga arc have focused on a perceived lack of volcanism between ~21°S and ~27°S, adjacent to a bend in the trench caused by the collision of the subducting Louisville Seamount Chain (LSC). During swath mapping in 2002, it was revealed that this portion of the arc, including the Louisville and Monowai segments, is in fact one of the most volcanically active parts of the Tonga-Kermadec system. At this location, a combination of oblique convergence of the Pacific Plate and southward compression due to the collision of the LSC has resulted in left-lateral strike-slip faulting and rifting of the arc crust. This has produced a series of left-stepping arc transverse graben and horst structures that localize the voluminous volcanic activity.

For this study, a new 1:250,000 scale geological map of the Louisville and Monowai segments has been constructed as a framework for a quantitative analysis of arc volcanism and the eruptive history of these segments. Two types of volcanoes dominate the arc front: deep caldera systems (collapse structures formed due to the evacuation of magma) within the arc rifts, and smaller volcanic cones between the rifts. The cone volcanoes tend to have small summit craters (<10 km^3) whereas the large caldera volcanoes have major depressions of up to 50 km^3. The cones are relatively undeformed, whereas the larger calderas are affected by multiple stages of collapse, asymmetric subsidence, and distortion caused by regional stresses. Surveys of the crater walls of the cone volcanoes show a predominance of volcaniclastic deposits, whereas the caldera volcanoes contain a high proportion of coherent lava flows. The caldera volcanoes also show a prevalence of basaltic melts compared to the more andesitic and dacitic cones. The largest caldera volcano is the Monowai volcanic complex (25°53’S) occupying a deep depression

(Monowai Rift Graben) that crosses the arc front. The volcanic complex consists of a large caldera (12 km wide, 1600 m deep) and an adjacent stratovolcano (Monowai Cone) rising nearly to sea level. We suggest that the different types of volcanoes along the Louisville and Monowai segments reflect the influence of deep structures within the arc crust that have localized strike-slip and normal faulting.

Acknowledgements

This research is a product of the Metal Earth Project funded by the Canada First Research Excellence Fund (CFREF) in partnership with the Marine Mineral Resources Group at the GEOMAR-Helmholtz Centre for Ocean Research Kiel. The Helmholtz Association, NSERC, and CFREF are acknowledged for their support through research grants and project funding. This is contribution MERC-ME-2022-10 to the modern-ancient crust project of the Metal Earth program.

I would like to thank the following people, without whom I would not have been able to complete this project.

I would first and foremost like to thank my supervisor, Dr. Mark Hannington for providing his expertise and guidance throughout this project.

I would also like to thank Alan Baxter of the Metal Oceans research group who has constantly been available to provide feedback, advice, and support throughout this project. I must also thank Mary Besaw, another masters student with the Metals Oceans group, who I have had many discussions with, troubleshooting issues we've ran into and providing advice and support to each other. Other members of the Metal Oceans group including David Diekrup, Kaitlyn Breker, Marc Fassbender, Anna Krätschell, have also been crucial in providing their own expertise at various stages of this project.

I of course would also like to thank my friends and family for all their constant support and encouragement and for keeping me sane while meeting deadlines.

Table of Contents

Abstract ii

Acknowledgements iv

Table of Contents v

List of Figures vii

List of Tables x

Chapter 1: Introduction 1

1.1 Arc Volcanism, Rifting, and Submarine Calderas 1

1.2 Thesis Objectives 3

1.3 Study Area 3

1.4 Approach and Methods 7

1.5 Published Results 8

Chapter 2: Geology of the Louisville Segment of the Tonga-Kermadec Arc: Regional Tectonic Controls on Arc Rifting and Magmatism 9

2.1 Introduction 9

2.2 Previous Work 10

2.3 Regional Geology 13

2.3.1 Arc-backarc system 13

2.3.2 Volcanoes of the arc front 15

2.3.3 Louisville Ridge and Osbourn Trough 19

2.4 Methods and Data 20

2.5 Geological Map of the Louisville and Monowai Segments 23

2.5.1 Major structures 23

2.5.2 Distribution of volcano types 26

2.5.3 Other mapped formations 27

2.6 Quantitative Analysis 28

2.7 Discussion 29

2.8 Conclusions 34

Chapter 3: Caldera Volcanoes of the Southern Tonga Arc and Related Submarine Hydrothermal Systems 67

3.1 Introduction 67

3.2 Regional Geology 69

3.3 Volcanic Front 71

3.4 Methods and Data 76

3.5 Results 77

3.5.1 Cone Volcanoes 77

3.5.2 Caldera Volcanoes 83

3.6 Evolution of the Monowai Volcanic Complex 87

3.7 Discussion 91

3.7.1 Regional tectonic controls on arc-front volcanism 91

3.7.2 Structural styles, controls on caldera collapse, and magmatic productivity 93

3.7.3 Relationship to melt sources and hydrothermal activity 96

3.8 Conclusions 99

Chapter 4: Summary and Conclusions 139

4.1 Global Database of Submarine Calderas 141

4.2 Summary Statistics of the Global Database of Submarine Calderas 143

4.3 Discussion and Conclusions 145

Conclusion 148

References 160

Appendix A: Location Maps of Relevant Research Cruises 180

Appendix B: Geological Map of the Louisville-Monowai Arc Segment 188

Appendix C: Database of Submarine Calderas 189

List of Figures

Figure 2.1 Regional bathymetric map of the Tonga-Kermadec arc-backarc system 36

Figure 2.2 Kinematic plate model and segmentation of the Tonga-Kermadec arc.....38

Figure 2.3 Geological and bathymetric map of Louisville and Monowai segments 40

Figure 2.4 Bathymetric maps of individual volcanic centers 42

Figure 2.5 Regional structure and geophysics data sets of the Louisville and Monowai Segments.....49

Figure 2.6 1:500,000 geological map of the Louisville and Monowai segments 50

Figure 2.7 Schematic illustration of the along-strike structure of the Louisville and Monowai segments 51

Figure 2.8 3D block model of the Louisville and Monowai segments 52

Figure 2.9 East-west bathymetric profiles of the Louisville and Monowai segments 53

Figure 2.10 Earthquake epicenters of the Louisville and Monowai segments 55

Figure 2.11 Fault strike length distribution at Grabens 1-3.....56

Figure 2.12 Depth of hypocenters of earthquakes in the map area.....57

Figure 2.13 Schematic illustration of plate vectors and obliquity of convergence of the Pacific plate 58

Figure 2.14 Model of principal stresses caused by the oblique subduction of the Pacific plate 59

Figure 2.15 Schematic illustration of rifting architecture in the Havre Trough and Lau Basin.....60

Figure 2.16 Gravity, magnetic, and Bouguer anomaly data over the Monowai Volcanic Complex 61

Figure 3.1 Regional bathymetric map of the Tonga-Kermadec arc-backarc system 102

Figure 3.2 Segments of the Tonga-Kermadec arc.....104

Figure 3.3 Compilation of multibeam bathymetric data of the Louisville and Monowai segments from research cruises SO-167, SO-192, SO-215, TN-309 106

Figure 3.4 Multibeam bathymetric map of the Louisville and Monowai segments from research cruise SO-192.....108

Figure 3.5 Bathymetric maps of individual volcanic centers 109

Figure 3.6 Plot of the sizes and depths of calderas of the Tonga-Kermadec arc.....117

Figure 3.7 Close-up views of V15, V16, V18, V19, V20, V21, and Monowai from research cruise SO-192 118

Figure 3.8 Stratigraphic columns of selected caldera systems surveyed during PISCES and ROPOS dives 120

Figure 3.9 Bottom photographs from Volcano 18 collected during the PISCES Dives P5-640 and P5-641 122

Figure 3.10 Bottom photographs from Volcano 19 collected during the PISCES Dives P5-635 to P5-639 124

Figure 3.11 Stitched bottom photographs of the caldera wall at Volcano 1 collected during ROPOS Dive R1052 125

Figure 3.12 Bottom photographs of Mussel Ridge and the caldera wall at Monowai collected during ROPOS R1043 and R1044 126

Figure 3.13 1:50,000 geological map of the Monowai Volcanic Complex 127

Figure 3.14 Block diagram of the Monowai Caldera showing interpreted subsurface geology 128

Figure 3.15 Bathymetric map of the Monowai Volcanic Complex from the research cruise RV *Tangaroa*, showing tectonic and magmatic features 129

Figure 3.16 Plot of eruptive volumes and duration for selected submarine volcanoes 130

Figure 3.17 Maximum predicted temperatures of hydrothermal vents for caldera settings at different water depths 131

Figure 4.1 Global distribution of submarine calderas 151

Figure 4.2 Classification of major calderas 152

Figure 4.3 Classification of "eccentricity" of calderas 152

Figure 4.4 Illustration of measurements included in the global database of submarine calderas 152

Figure 4.5 Schematic diagram of the major caldera axis and the regional structure orientation 153

Figure 4.6 Classification of submarine calderas according to crustal type (oceanic, continental, and intraoceanic arc/backarc) 154

Figure 4.7 Pie chart showing the distribution of caldera sizes within the Global Database of Submarine Calderas 155

Figure 4.8 Size distribution of submarine calderas according to geodynamic setting 155

Figure 4.9 Plots of the eccentricity of submarine calderas in relation to volcano size 156

Figure 4.10 Cumulative sizes (km^2) of the Tonga arc volcanoes and cumulative volumes (km^3) of Tonga arc calderas and summit craters 158

List of Tables

Table 2.1 Research cruises on the Louisville and Monowai Segments, Tonga Arc.....63

Table 2.2 Volcanoes of the Louisville and Monowai segments of the Arc Front, Tonga Arc……64

Table 2.3 Geological formations of the Louisville and Monowai segments, Tonga Arc ...65

Table 2.4 Interpreted eruptive volumes of volcanoes of the Louisville and Monowai segments of the Tonga Arc.....66

Table 3.1 Summary Characteristics of Volcanic Centers of the Louisville Segment, Tonga Arc.....132

Table 3.2 Calculated Volumes of Volcanic Centers of the Louisville Segment, Tonga Arc……..133

Table 3.3 Summary of Rock Types Sampled from the Volcanic Centers of the Louisville Segment, Tonga Arc.....135

Table 3.4 Comparison of Cone and Caldera Volcanoes.....137

Chapter 1

Introduction

1.1 Arc Volcanism, Rifting and Submarine Calderas

Volcanic arcs account for about 26 percent of the global magmatic budget (Perfit and Davidson, 2000), and the associated volcanic activity has an impact on the oceans, the Earth's crust and the biosphere, comparable to that of the global mid-ocean ridges. Volcanic arcs are also a major hazard for both subaerial volcanic eruptions, earthquakes, and tsunamis, which threaten many of the island archipelagos of the western Pacific and other coastal populations. At least half of the global volcanic arcs (ca. 22,000 km) are partly to completely submarine. Intraoceanic arcs of the submarine Ring of Fire have a cumulative length of ~7,000 km but are the least understood because more than 80% of the volcanoes are entirely under water.

In the western Pacific, there are as many as 45 major arc stratovolcanoes on the submarine portions of the Izu-Bonin Arc and 52 on the Mariana Arc. The 2,500-km-long Tonga-Kermadec arc is the longest, with at least 70 individual volcanoes. The spacing between the volcanoes ranges from 27 to 55 km and is typically quite regular (de Ronde et al., 2003; Hannington et al., 2005). Most of the volcanoes are giant cones, with basal diameters of ~30 km and heights of 1 to 2 km above the surrounding seafloor. Most summits of the volcanoes reach shallow water depths owing to the height of the cones; more than 90% of the volcanoes shallower than <1,600 m. Many have summit craters or calderas, the largest being 5 to 6 km in diameter, that in some cases formed as a result of massive submarine volcanic eruptions (e.g., Fiske et al., 2001).

Intraoceanic arcs occur on a basement of dominantly oceanic crust. The arcs, trenches and back-arc regions are often structurally segmented by large-scale basement structures that predate initiation of the arc and by subduction of ridges or seamount chains (e.g., Anderson et al., 2017). These features have a major impact on arc volcanism. Intraoceanic arc volcanoes are basaltic to andesitic, becoming more felsic and calc-alkaline as the arc crust thickens and the depth and extent of fractionation of the subvolcanic magmas increases. The arc magmas are mainly

products of partial melting caused by the addition of H_2O and other volatiles from subducted sediments and hydrated oceanic crust to the subarc mantle. Annual global eruption volumes from submarine volcanic arcs are thought to be on the order of ~2-5 km^3/yr (Arculus, 1999), but this estimate is poorly constrained owing to the lack of systematic mapping of submarine arc volcanoes. For example, a single arc volcano of the type on the Tonga-Kermadec arc may have an eruptive volume exceeding 10s of km^3 of magma in just a few thousand years (Graham et al., 2008). The 12 km-diameter and 1 km-deep Monowai caldera on the Tonga arc, which was first revealed by swath mapping in 2004, is now recognized as one of the largest submarine calderas anywhere in the oceans, with a total volume of 229 km^3. Such features contribute a poorly unknown but significant magmatic and volatile input to the oceans; however, there is virtually no record of such large caldera-forming eruptions in the submarine environment.

Arc volcanism is strongly influenced by changes in plate motion, rift propagation, and intrusion into thinned arc crust, which are fundamental processes in subduction zone evolution (e.g., Turner et al., 2000; Rey and Mueller, 2010; Li et al., 2018). Important mappable features of arc related to plate adjustments include: (i) reorientation of fault patterns, (ii) thickening and then thinning of the arc lithosphere, (iii) extension and eventual splitting of arc crust, (iv) melt intrusion, and (v) major eruptions and evacuation of shallow crustal magma chambers. However, little work has been done to document arc rifting and its role in arc volcanism or to identify the specific geological formations and structures that influence arc volcanism.

These questions are of particular relevance for land-based mineral exploration. Arc-backarc systems of the western Pacific margin are viewed as important modern analogues for the structure and metallogenic evolution of ancient volcanic-hosted ore deposits on land (Hannington et al., 2005; Gibson, 2005). However, a major part of the hydrothermal venting in the western Pacific today is occurring at the volcanic fronts of the arcs. This contrasts with the interpreted settings of most ancient volcanic-hosted massive sulfide deposits, which are considered to have formed mainly during arc rifting.

A majority of the world´s presently exploited volcanic-hosted massive sulfide deposits on land were originally formed by processes related to rifting of arc crust (Franklin et al., 2005). Such

rifting can be observed today along the Tonga-Kermadec Arc, but the different styles of arc volcanism, the link between regional tectonics and magmatic activity at the volcanic front, and along-strike variability in the structure of the arc as a precursor of rifting and basin opening are only partly understood. An important question is what are the conditions that lead to rifting of arc crust, and the foundering of the arc crust into deeper back-arc basins where most ancient ore deposits of this type formed.

1.2 Thesis Objectives

The aim of this thesis is to develop a more detailed picture of arc rifting in the southern part of the Tonga Arc and to examine its role in large-scale caldera formation. This is achieved by detailed geological mapping of the volcanic front of the arc, by documenting the different styles of arc volcanism (cone volcanoes versus caldera volcanoes), and by comparison with the regional geodynamic setting. The geological history of the arc front is reconstructed from mappable features at 1:250,000 scale to investigate the origin of arc rifting and to better understand how rifting of arc crust impacts local volcanism and large-scale caldera formation. Different crustal types, highly variable near-field stresses, such as local transtension, and different styles of magmatism and hydrothermal activity are examined. We suggest that regional geodynamics strongly influences the intrusion of melt into arc and the break-up of the arc into en echelon rifts and eventually back-arc spreading. The study particularly addresses the along-strike variability in the structure of the arc in response to subduction of the Louisville Ridge and opening of the nearby Lau back-arc basin. We test how melt is distributed (and eventually erupted) and how eruptive volumes are associated with different styles of volcano development and magmatic-hydrothermal activity. The research also addresses an important unsolved question of submarine arc metallogeny: at what stage in the arc rifting does the magmatic and hydrothermal activity set in and mineral deposits begin to form?

1.3 Study Area

The Tonga-Kermadec arc (Figure 2.1) is the longest continuous chain of submarine arc volcanoes in the Pacific Ring of Fire. The arc-trench system is divided at 27°S into the Tonga arc

in the north (~1300 km long) and the Kermadec arc in the south (~1200 km long). Because of its remoteness, the Tonga portion has only recently become the focus of significant research programs. It is a classic example of an intraoceanic convergent margin where Pacific Plate lithosphere is subducted beneath a volcanic island arc chain. The extensional back-arc and southward-propagating Lau Basin and Havre Trough separate the Tonga (or Tofua) and Kermadec volcanic arcs from the remnant Lau and Colville ridges. The Tonga arc includes 41 volcanoes, with summit depths ranging from 1,200 to <100 m. The Kermadec arc includes 33 submarine volcanoes, with depths ranging from 1,700 m to 200 m. The volcanoes are situated 40-70 km west of the fore-arc bulge (so-called Kermadec Ridge in the south and Tonga Ridge in the north) and 180 km west of the Horizon Deep in the Tonga Trench, the deepest point the southern hemisphere.

Although this region has the fastest plate convergence rates in the world, until 2002 the incidence of volcanic activity on the Tonga Arc was poorly known compared to the southern Kermadec Arc. Shallow submarine volcanic eruptions in Tonga were known, most notably at Metis shoal (17 °S), where eruptions were reported in 1851, 1852, 1878, 1886, 1894, 1967-68, and 1979 (a new island was created here by a volcanic eruption in 1995), and 2019 (Global Volcanism Program, 2019; Brandl et al., 2020). Submarine eruptions are also thought to have occurred repeatedly at Monowai Seamount, due to changes in the topography of the volcano which have been observed between 1998-2011 and were witnessed during SO-192 (Wright et al., 2008; Chadwick et al., 2008; Schwarz-Shampera., 2007; Watts et al., 2012; Metz et al., 2019). However, for a long time, a low incidence of volcanism was thought to prevail in the central part of the Tonga Arc, adjacent to a bend in the trench caused by the collision with the Louisville Seamount Chain. The apparent contradiction between high rates of plate convergence and the low incidence of volcanism in this area was thought to be explained by the subduction of the Louisville Seamounts. In 2002, new swath mapping was conducted during SO-167 that instead revealed this part of the arc to be one of the most volcanically active portions of the Tonga-Kermadec system. The discovery of 27 major volcanoes within a short 650 km-long segment of the arc (Figure 2.2 and 2.3) highlighted the remarkable lack of knowledge of a major portion of the western Pacific margin at the time. In this study, we examine more closely the nature of volcanism along the Louisville Segment of the arc and the origin of several large intra-arc

caldera complexes that are responsible for a large proportion of the total magmatic budget of the arc front. Most of the 41 known or suspected submarine volcanoes on the Tonga Arc were only discovered in the last two decades.

Most attention has been paid to the southern Kermadec chain, immediately north of New Zealand, which hosts 13 submarine volcanoes along a 260 km-long section of the arc (Wright and Gamble, 1999; de Ronde et al., 2003; Wright et al., 2006; Campbell et al., 2007; Graham et al., 2008). The volcanoes occur at water depths of 220 m to 1600 m, and three of the largest volcanoes have summit calderas or craters up to 3.5 km in diameter and 450 m deep. Among the largest and deepest caldera is on Brothers volcano at a water depth of 1600 m, where the first black smokers were found in this region in 1998 (Stoffers et al., 1999b). This vent site has since been extensively studied and sampled (de Ronde et al., 2005; de Ronde et al., 2011; Tontini et al., 2012; Berkenbosch et al., 2012; de Ronde et al., 2019; Martin et al., 2019; Tontini et al., 2019). Until the discovery of similar vents sites in the north in 2005 (Stoffers et al., 2006), the Tonga Arc had not been mapped or sampled.

After preliminary bathymetric mapping by the R/V *Sonne* during SO-135, a number of the other arc front volcanoes were revisited in late 2002 during the SO-167 cruise which provided the first glimpse of volcanic and hydrothermal activity on the relatively unexplored Tonga arc (Stoffers et al., 1999a; Stoffers et al., 1999b; Stoffers et al., 1999c; Wright et al., 2002; Stoffers et al., 2002). The study area was subsequently visited during the TELVE cruise in 2003 (Tonga-Eastern Lau Vents Expedition: Arculus et al., 2003; Massoth et al., 2007). However, many volcanoes and active hydrothermal sites were missed, owing to the reconnaissance nature of the expeditions. In 2007 and 2011, a number of the largest volcanoes were mapped during the SO-192, SITKAP and SO-215 (Stoffers et al., 2006b; Schwarz-Schampera et al., 2007; Peirce and Watts, 2011). These included extensive surveys of the large, active Monowai Volcanic Complex. As many as 15 other volcanoes in the north of Tonga also have been discovered and are only now being mapped in detail (Arculus et al., 2003; Rubin et al. 2012; Hannington et al., 2019; Chadwick et al., 2019; Anderson et al., 2021).

The southern Kermadec arc has been extensively surveyed for hydrothermal plume emissions during 5 surface expeditions between 1999 and 2005. NZAPLUME I, II and III covered the Kermadec arc using the New Zealand RV *Tangaroa*, and the TELVE and NoToVE cruises surveyed the Tonga arc aboard the Australian RV Southern Surveyor. Hydrothermal plumes were detected as light scattering and chemical anomalies over more than half of the volcanoes surveyed. Seventeen submersible dives were made on hydrothermally active volcanoes using the Japanese submersible SHINKAI 6500 at Brothers and the NOAA/HURL submersible PISCES V at Macauley, Giggenback, "W", Rumble V, Clark, Healy, and Brothers. At least 25 venting sites were observed at these Kermadec arc volcanoes, and most were sampled for gases and hydrothermal fluids. The southern Lau Basin along the ELSC, adjacent to our study area, also became an Integrated Study Site (ISS) of the U.S. RIDGE Program in 2002, and ongoing research in the back-arc is an excellent complement to the current work.

During the SO-167, SO-192 and SITKAP expeditions in 2002, 2005 and 2007, the first submarine hydrothermal vents and associated seafloor mineralization were discovered on the Tonga arc, greatly extending the known depth range and geographical distribution of volcanism and hydrothermal venting where no vents sites were previously known (Stoffers et al., 2002; Stoffers et al., 2006 a and b; Schwarz-Schampera et al., 2007). However, the mapping focused on only a few volcanoes at opposite ends of the Tonga arc, nearly 400 km apart; few of the 27 volcanoes discovered in between were explored. Four active hydrothermal fields were discovered along the southern Tonga Arc (Stoffers et al., 2006a and b). Two occur on Volcano 19, including a high-temperature field located at the summit of the cone (385-540 m depth) and a low-temperature field at greater depth within the summit crater (850-985 m depth). The high-temperature vents (245–265 °C) comprise clusters of large (2–10 m-high) barite, anhydrite, and sulfide chimneys. The low-temperature vents in the summit crater are surrounded by extensive deposits of Fe-oxyhydroxides. Two other hydrothermal fields were at Volcano 1 and Volcano 18s. In the large caldera at Monowai, diffuse venting, mussel beds, and oxidizing sulfides were found on the lower benches of the caldera, and a less well-defined hydrothermal plume was found near the northwest caldera wall (Schwarz-Schampera et al., 2007; Leybourne et al. 2012). These findings confirm a previously unrecognized diversity of hydrothermal venting along the arc that has not yet been fully characterized.

1.4 Approach and Methods

For this study a new 1:250,000 scale geological map of the Louisville and Monowai segments of the Tonga Arc, was constructed from a compilation of ship-based bathymetry, backscatter data, gravity and magnetics. It is the first geological map of its type along the arc front, supplemented by more detailed mapping of several of the arc volcanoes and large Monowai caldera. The detailed maps were prepared by inspection of 100 hours of archive video and sampling by the PISCES submersibles and the Canadian remotely-operated vehicle ROPOS.

A variety of different volcano types, and different depositional units were isolated to create the geological maps at 1:250,000 and 1:50,000 scale, with a focus on the volcanic stratigraphy, structure, and magmatism associated with the growth of the volcanoes and different types of caldera-forming eruptions. Crustal types with similar properties, age, and origin were gathered into distinct geological formations and then assembled into a map and legend that take into consideration the sequence of depositional events (inferred stratigraphic relationships between units), the composition of different units, tectonic fabric, and structure. The map data provide a framework for quantitative analysis of volcano growth and eruptive history, including area-age relationships and eruptive volumes related to different stages of arc rifting. Volcanic facies mapping was also conducted across several volcanic centers, and in vertical sections of their crater or caldera walls, to establish the stratigraphic sequences and eruption histories. The latter are summarized in type sections (schematic stratigraphic columns) for the different volcano types.

The study also includes a comprehensive comparison with other oceanic calderas, which are identified in a new database of more than 100 worldwide examples. This comparison identifies common near and far-field influences on caldera formation and key attributes that may contribute to anomalous magmatic and hydrothermal activity. A quantitative analysis of the magmatic productivity of a range of different types of caldera volcanoes highlights key structures and facies relationships that can also be recognized in the geological record.

1.5 Published Results

The results of this study have been presented at 3 scientific conferences:

Gray, A. (2021) Arc-front volcanic centers and hydrothermal systems along the Monowai Segment, Tonga-Kermadec Arc, SW Pacific. Presentation at the annual Ottawa-Carleton Geoscience Centre Graduate Seminar. Ottawa, ON, April 15.

Gray, A., Hannington, M.D., Stewart, M.S., Baxter, A.T., Petersen, S. (2020) Geology of the Monowai volcanic centre, Kermadec-Tonga arc: Implications for the location of caldera-hosted submarine hydrothermal systems. Poster session & abstract at the Student Minerals Conference of the Annual Prospectors & Developers Association of Canada Conference. Toronto, ON, March 1-4.

Gray, A., Hannington, M.D., Stewart, M.S., Baxter, A.T., Diekrup, D., Schwarz-Schampera, U., Gibson, H.L. (2021) Arc-front volcanic centers and hydrothermal systems along the Monowai Segment, Tonga-Kermadec Arc, SW Pacific. Poster session & abstract at the Student Minerals Conference of the Annual Prospectors & Developers Association of Canada Conference. Toronto, ON, March 8-11.

Chapters 2 and 3 of the thesis are currently being combined for submission to a peer-reviewed journal, focusing on the geology of the Tonga Arc and an investigation into arc rifting and caldera formation with implications for large-scale magmatic-hydrothermal systems. Chapter 4 contains the comparison with a newly compiled database of submarine volcanic calderas.

Chapter 2

Geology of the Louisville Segment of the Tonga-Kermadec arc: Regional Tectonic Controls on Arc Rifting and Magmatism

2.1 Introduction

Intraoceanic arcs typically have lengths of more than 1,000 km, although the active volcanic fronts may be only 50 to 70 km wide (de Ronde et al., 2003; Hannington et al., 2005). The trench, arc, and back-arc regions are often structurally segmented by large-scale basement structures that predate back-arc rifting and are strongly influenced by features of the subducting plate, such as ridges or seamount chains (e.g., Anderson et al., 2017). Back-arc basins form behind the arcs after a prolonged episode of arc rifting caused by oceanward migration and sinking of the subducting plate (i.e., slab rollback). During this time, voluminous pyroclastic volcanism can occur, shedding large amounts of pumiceous material into the nascent back-arc rift (Clift, 1995; see Brandl et al., 2020a). The earliest stages of rifting of an intraoceanic arc have been documented, for example, in several narrow depressions behind the Izu-Bonin arc (Ikeda and Yuasa, 1989; Fryer et al., 1990), at the propagating tips of the northern and southern Mariana trough (Stern et al., 1990), and in the Lau Basin (Sleeper et al., 2016). Initial rifting commonly manifests as short trough-like depressions, <100 km long and 30 to 40 km wide, in the thinned arc and back-arc (e.g., the Sumisu rift, in the northern Izu-Bonin arc: Urabe and Kusakabe, 1990). Several millions of years may elapse before a back-arc rift is wide to allow passive upwelling of mantle material, leading to true ocean-floor spreading (Martinez and Taylor, 1996).

Little is known about the structural and magmatic precursors of arc rifting and what is taking place at depth in the crust where the arc begins to rift. Questions remain concerning the nature of arc magmatism at the beginning of rifting, the optimal thickness of arc crust to rift, and the stresses that initiate splitting of the arc. Arc and back-arc magmatism are usually portrayed as products of distinctly different melt generation (or mixtures) in the subarc mantle, but the transition between the two is rarely observed (Hannington et al., 2019). Back-arc spreading, where mantle material is released to the spreading ridge, is marked by major changes in the

crustal thickness, with a narrow zone of abruptly thinned crust and a shallow Moho at the arc-to-backarc transition (Crawford et al., 2003; Dunn and Martinez, 2011). However, the controls on the location of initial arc rifting are poorly known.

This study examines initial rifting in a region of the Tonga Arc adjacent to the Lau Basin, where back-arc spreading has not yet started (Figure 2.1). The 2,500-km Tonga-Kermadec systems is one of the fastest converging subduction zones on Earth, where the effects of subduction, slab roll-back, and arc rifting and segmentation can be investigated almost in “real time” (Hannington et al., 2019). The arc front is magmatically robust, with more than 90 individual volcanoes, spaced 27 to 55 km apart along its entire length (de Ronde et al., 2003; Hannington et al., 2005). Old Pacific lithosphere is impinging on the arc-trench system at rates from 24 cm/yr at 17°S to 16.5 cm/yr at 22°S (Ruellan and Lagabrielle, 2005). Tomographic images show the Pacific Plate subducting with dips of 60-70° under the presently active volcanic arc (Zhao et al., 2007). Between 23°S and 26°S complications arise from a bend in the arc-trench system and the resulting oblique convergence with the Pacific Plate (Argus et al., 2011). Numerous researchers have speculated about the role of the subduction of the Louisville Seamount Chain (LSC) in causing the "bend" in the arc where it enters the trench (e.g., Ballance et al., 1989; Delteil et al., 2002; Ruellan et al., 2003; Contreras-Reyes et al., 2011). Here, we examine the features of the volcanic front of the arc between 23°S and 26°S and consider the style of faulting and influence of pre-existing basement structures on the rifting of the arc, including the nature of the magma plumbing system beneath the arc and when and where large-scale hydrothermal systems occur. We interpret the regular spacing of the volcanoes, the distinctive horsts and grabens that cross the arc front, and the variations in the styles of volcanism to reflect the oblique convergence of the Pacific Plate, the effects of the LSC impinging on the subduction zone and the reactivation of basement structures that localize the strain.

2.2 Previous Work

Karig (1970, 1971) first recognized that the Lau Basin formed by splitting of an island arc, although the mechanics and the consequences of rifting arc lithosphere were poorly understood.

In the 1980s and 1990s studies began to reveal the patterns of extension, volcanism, and sedimentation during arc rifting, as well as the relationship to hydrothermal circulation (Sibuet et al., 1987; Taylor et al., 1990, 1991; Wright et al., 1990). However, the link to the structure of the arcs has been difficult to establish because they are mostly buried by volcanic products, and few detailed cross sections have illuminated the early history of rifting. The manner in which magma, both intrusive and extrusive, is focused into rifting arcs also has been debated (e.g., Ribeiro et al., 2013).

Early models of back-arc basin opening in the Lau Basin proposed a simple southward propagation of rifting in advance of a single spreading ridge (Parson and Wright, 1996; Taylor et al., 1996). However, Ruellan et al. (2003) showed this could not account for the opening fabric in the back-arc region and that the current rifting must be influenced by a more complex stress regime. They concluded the stress regime in the Southern Lau Rift (SLR) is transtensional with a component of southward compression caused by the collision with the Louisville Seamount Chain (LSC) as a "buoyant indenter" (cf. Wallace, 2009). Ruellan et al. (2003) also suggested that initial opening of the Lau Basin at ~6-5 Ma coincided with the beginning of the subduction of the LSC in the north, which migrated southward until it reached its present position at ~26°. In their model, back-arc spreading in the Lau Basin was progressively "unlocked" by the passing of the seamount chain, and this is just starting in the southernmost Lau Basin at the location of the SLR (Figure 2.1).

Turner et al. (1997) and Ewart et al. (1998) suggested that the geochemical signature of the Louisville Ridge was present in lavas from the northernmost volcanic islands of Tonga (Tafahi and Niuatoputapu), which is where the ridge would have been located at 3–4 Ma at the beginning of back-arc basin opening. Since then, the collision zone between the LSC and the Tonga-Kermadec arc has migrated rapidly southward along the arc, due to its angle of approach to the trench, now at a rate of 120–180 mm yr^{-1} (Lonsdale 1988; Ballance et al. 1989). This collision resulted in significant along-strike variability in the structure of the trench, forearc, arc and back-arc (e.g., Clift et al. 1998; Clift and MacLeod 1999, Delteil et al., 2002; Ruellan et al., 2003). Significant intra-arc deformation occurs at the bend or "kink" in the trench attributed to the LSC (Pelletier and Dupont, 1990; Ruellan et al., 2003; Delteil et al., 2002; Contreras-Reyes et al.,

2011). In the last ~1 million years, the seamount chain swept southward for nearly 300 km along a segment of the arc from 23°30'S (near Volcano 14) to the Monowai Volcanic Complex in the south at 25°45'S, known as the Louisville Segment (Figure 2.2).

Early bathymetric data of the Louisville Segment suggested a lack of volcanic activity along this portion of the arc (Stoffers et al., 2002). This was interpreted as a "magmatic gap", where melt production was switched off due to subduction of the LSC (cf. Nur and Ben-Avraham, 1983). It was not until the first high-resolution multibeam surveys were conducted during SO-167 that 27 previously unrecognized volcanoes were found along the arc front of the Southern Tonga, Louisville and Monowai segments (Stoffers et al., 2002). Two distinct volcano types were noted, "cone volcanoes" and "caldera volcanoes" (Stoffers et al., 2002, 2006a; Wright et al., 2006), but the controls on the style of volcanism and arc rifting were not recognized. Previous studies suggested basement-controlled upwelling of mantle material could explain the regular spacing of the volcanoes along the arc (so-called "hot fingers": e.g., Tamura et al., 2003; Keller et al., 2008; Sleeper et al., 2016). Chains of cross-arc volcanoes were interpreted as intrusions of hydrous melt between areas with decreased melting and increased tectonism. However, others have proposed that a structurally weakened basement (e.g., due to the subduction of a seamount chain) could also account for the strong control on melt distribution along the volcanic fronts of arcs. The hypothesis was that the resulting shear stresses in the upper plate would have a strong influence on the location and amount of magma supply as the arc crust is stretched above the basement structures. Focusing of voluminous basaltic eruptions in other arc systems has been similarly attributed to segmentation of the arc crust caused by collision with buoyant features on the downgoing slab (e.g., Anderson et al., 2016, 2017; Arai et al., 2018).

Velocity models of the Tonga-Kermadec system (e.g., Nishizawa et al., 1999; Crawford et al., 2003; Contreras et al., 2011; Dunn et al., 2013) show a thickened arc crust (>10 km), dramatic thinning at the arc-to-backarc transition (to as little as ~4 km), and then thicker back-arc crust (7-8 km) formed by additions from the mantle. Back-arc spreading along the length of the Lau Basin has repeatedly stepped eastward into the thickened arc crust, as can be seen in at the propagating tip of the Southern Valu Fa Ridge today (Figure 2.3). However, it is unclear why new rifting is localized in the thick arc crust rather than at the already thinning boundary between

the arc and backarc (e.g., Fujiwara et al., 2001; Delteil et al., 2002; Ruellan et al., 2003). We suggest this is related to inherited structures in the Tonga Ridge basement.

2.3 Regional Geology

The Pacific Plate is subducting underneath the Australian Plate along the Tonga-Kermadec arc-trench system at a rate of subduction of ~240 mm/yr (Zellmer and Taylor, 2001; Smith and Price, 2006). The main elements are the Tonga-Kermadec Trench, the Tonga-Kermadec Ridge, which contains the volcanic front of the arc, and the remnant Lau-Colville Ridge which is separated from the active arc by the Lau Basin and Havre Trough (Figure 2.1).

2.3.1 Arc-backarc system

Seafloor spreading in the Lau Basin started in the north and propagated south forming the classic "V-shape" of the basin (Taylor et al., 1996). The late Miocene (~6 Ma) rifting initiated in the old forearc of the former Vitiaz Arc and stranded almost all of the original Cretaceous-Eocene arc crust on the west side of the Lau Basin, becoming part of the Lau Ridge. Arc volcanism initially continued in the west of the basin for at least several million years and then switched to the currently active Tonga (Tofua) Arc at about 3 Ma as the basin widened (Hawkins et al., 1995; Martinez and Taylor, 2006). Although the present arc magmatism on the Tonga Ridge stabilized only a few million years ago, already the arc is beginning to rift again in the north (e.g., in the NE Lau Basin and Fonualei Rift: Anderson et al., 2021; Stewart et al., 2021).

The Tonga-Kermadec chain comprises the Tonga Arc in the north (~1300 km long) and the Kermadec Arc in the south (~1200 km long). The distinction is made at ~26°S where the LSC is currently entering the trench. The deepest point in the southern hemisphere (~10850 m Horizon Deep) is located in the trench nearby. The arc-trench system is divided into eight different segments based on the arc-ridge morphology and arc-trench separation: Northern Tonga, Central Tonga, Southern Tonga (or 'Ata), Louisville, Monowai, Northern Kermadec, Central Kermadec, and Southern Kermadec (Figure 2.2: Stoffers et al., 2002, 2006a and b; Smith and Price, 2006).

In the north, the axis of the volcanic arc has a NNE orientation of ~015-020°, along the Northern Tonga, Central Tonga, and Southern Tonga ('Ata) segments, which is orthogonal to the trajectory of the Pacific Plate (Figure 2.2). The orientation of the arc changes abruptly at ~24°S to an azimuth of ~0° along the Louisville and Monowai segments and then continues south of the Monowai Volcanic Complex, once again, at ~015-020°. As a result of the bend in the arc-trench system, convergence with the Pacific Plate at this location is notably oblique between ~24°S and ~26°S. Here, well-developed extensional faults occur in the wall of the trench (Lonsdale, 1986; Ballance et al., 1989; Collot and Davy, 1998; see review in Contreras-Reyes et al., 2011), and seismic profiles ~100 km north of the collision with the LSC show pervasive fracturing and reorientation of the faults, both in the trench and on the outer rise (Contreras-Reyes et al., 2011).

Back-arc spreading in the adjacent Lau Basin occurs along the Eastern Lau Spreading Center (ELSC) and the Valu Fa Ridge (VFR). The southernmost spreading segment of the VFR approaches to within 20 km of the arc at ~24°S and has a depth of only 1,700 m. The lavas in this part of the Lau Basin are more arc-like than the MORB at the ELSC, with basalt and andesite present (Wiedicke and Collier, 1993; Watanabe et al., 2010). South of ~24°S, back-arc spreading along the VFR stops abruptly and the ridge terminates in rifted arc crust between the Southern Segment of the Tonga Arc and the Louisville Segment. South of the VFR, the back-arc region is mainly an area of stretched arc crust with abundant normal faulting but no obvious spreading (referred to as the Southern Lau Rift, SLR: Ruellan et al., 2003). This area is dominated by fault-controlled volcanoes ("ridge-and-knoll" terrain of Ruellan et al., 2003, and Fujiwara et al. 2001), with a rift fabric trending 015-030°. The ridges and knolls manifest as rugged, high-standing, and generally sediment-starved horsts and grabens. The diffuse magmatism, consisting of many isolated volcanic knolls, is interpreted as a product of intrusion into extending crust (cf. Buck, 2001). The disorganized volcanic fields in the ridge-and-knoll area may be a consequence of magmatic inflation prior to spreading, or alternatively underplating and uplift in response to the LSC entering the subduction zone at this latitude (Ruellan et al., 2003, Delteil et al., 2002; Fujiwara et al., 2001).

Scholz and Small (1997) noted that ~200 km of the Tonga-Kermadec trench at this location is characterized by very few earthquakes (the so-called "Louisville gap"), most likely reflecting the

regional compression with reduced seismicity extending south of the point of collision (Timm et al., 2013). The low seismicity of the SLR, together with the rifted volcanic basement and ridges oblique to the arc front, are consistent with a mainly transtensional stress regime (Delteil et al., 2002). Ruellan et al. (2003) further interpreted that the spreading south of the VFR is temporarily locked between 24°55'S and 27°S due to the compression exerted by subduction of the LSC.

2.3.2 Volcanoes of the arc front

More than 90 individual volcanoes occur along the volcanic fronts of the Tonga and Kermadec arcs. In Tonga, there are 41 volcanoes with summit depths ranging from 1,200 to <100 mbsl; the Kermadec arc includes 33 volcanoes, with depths ranging from 1,700 m to 200 mbsl. Eighteen volcanoes are above sea level, including the islands of the Kingdom of Tonga and the Kermadec Islands of New Zealand. However, extensive bathymetric mapping has revealed nearly continuous submarine volcanism between these island groups. The major volcanoes of the Tonga Arc are shown in Figure 2.3. They are situated 40-70 km west of the forearc bulge and 180 km west of the Tonga Trench. The arc contains an active and a remnant volcanic chain. The inactive eastern part includes the coral islands of the Tonga group and consists of uplifted carbonates and volcaniclastic sediment overlying middle Eocene to late Miocene volcanic and plutonic rocks of the arc basement (Figure 2.3a). The forearc comprises Miocene sediments that are downfaulted against flows and tuff breccias believed to have been part of the original island arc system (Hawkins, 1995). Since the Miocene, the locus of magmatism has migrated westward to the presently active volcanic chain. Some authors have suggested that subduction of the LSC, locally impeded roll-back, with flattening of the slab and tectonic erosion causing the westward migration of the arc front (Nur and Ben-Avraham, 1983; Contreras-Reyes et al., 2011).

The active part of the volcanic front is about 50-70 km wide and is dominated by basaltic volcanic cones and intervening flat areas; 27 semi-regularly spaced submarine stratovolcanoes occur on the Southern Tonga ('Ata) Segment, Louisville Segment, and Monowai Segment. The volcanic front was mapped during NZAPLUME III, NZASRoF, SO-195a (TOTAL), and SO-215 (Wright et al., 2008; Graham et al., 2008; Embley et al., 2005; Contreras-Reyes et al., 2011;

Peirce and Watts, 2011; Watts et al., 2012), and during our own research cruises: SO-135 (Haase et al., 2002), SO-167 (Stoffers et al., 2002), SITKAP and SO-192 (MANGO) (Stoffers et al., 2006b; Schwarz-Schampera et al. 2007; Chadwick et al., 2008) (Table 2.1). A number of the volcanoes were visited in 2005 using the PISCES submersibles aboard the R/V *Ka`imikai-O-Kanaloa* (SITKAP expedition) and in 2007 with the remotely-operated vehicle ROPOS (SO-192). Details contained in this paper are provided from those dives. Two distinct styles of arc-front volcanoes have been described from these cruises and by Wright et al. (2006) and Wormald et al. (2012). Most are simple "cone volcanoes", with basal diameters of 30 km and heights of 1 to 2 km above the surrounding sea floor. About 1/3 of the cones have summit craters or calderas, up to several kilometers in diameter, in some cases shoaling to <1,000 m water depth. In this study, we distinguish summit depressions on the cone volcanoes as "craters" formed during explosive eruptions, whereas larger "caldera" structures are interpreted to have formed by collapse caused by magma withdrawal. Several of the volcanoes have experienced explosive caldera-forming eruptions at depths of at least 1,500 m, similar to what has been documented in other submarine volcanic arcs (e.g., Wright and Gamble, 1999; Fiske et al., 2001) and elsewhere on the Tonga Arc (Hekinian et al., 2008; Brandl et al., 2020b). Cones with much smaller or no summit craters typically are covered by a thick carapace of volcanic ejecta. The largest structures at the arc front are the "caldera volcanoes". They occur at greater depths than the cones and have caldera-like depressions up to 15 km in diameter (e.g., Stoffers et al., 2002, 2006a; Wright et al., 2008). They range in depth from 900 to 1600 m and are among the deepest parts of the arc front. The calderas commonly contain distinctive post-caldera lava domes, indicating the presence of shallow magma.

North of ~22°S, the volcanic front of the Southern Tonga ('Ata) Segment is a broad region that includes both recent and older volcanic edifices (Figure 2.3). The oldest volcanoes feature thickly sedimented, wave-cut summits, as shallow as 150 mbsl, with much slumping, erosion and faulting of their flanks, including 'Ata Island (Stoffers et al., 2002, 2006b). Many of the volcanoes are only remnants of lava flows and volcaniclastic deposits abutting now exposed dike complexes. The characteristics of the mapped volcanoes are summarized in Table 2.2. Volcanoes 1 to 8 (Figure 2.4a-e) are described in Stoffers et al. (2002, 2006a). Volcano 1 (21°09’S) (Figure 2.4a) is a 28-km diameter complex with a shallow 7-km wide summit caldera

at about 150-250 mbsl (Hekinian et al., 2008). A large portion of the oval-shaped caldera has collapsed, leaving a 4-km long and 3-km wide flat-topped ridge at its center which is still volcanically and hydrothermally active (Stoffers et al., 2006a). Volcano 2 (21°18'S) (Figure 2.4a) is a similar size (22-km diameter) and comprises two cones, one dominated by an oval 6.5-km long summit caldera. Volcano 3 (21°39' to 21°53'S) (Figure 2.4b) also comprises two large cones of steeply dipping lavas surrounded by volcaniclastic material. The southern cone has a large 20-km diameter summit depression reaching a depth of 920 mbsl. Volcanoes 4, 5 and 6 are a cluster of submarine cones belonging to the 'Ata Volcanic Complex (21°56' to 22°27'S) (Figure 2.4c). Volcanoes 5a and 6a are among the oldest in the chain, with broad wave-cut summits and thick sediment cover. Volcano 7 (22°31' to 22°46'S) (Figure 2.4d) also consists of a complex of several stratovolcanoes, a larger 20-km diameter northern volcano and a smaller 12-km diameter stratovolcano with a small 1.2-km crater. Volcano 8 (22°51'S) (Figure 2.4e), or the Pelorus Volcano, is located at the Pelorus Reef and is a large 14-km diameter stratocone mostly buried by volcaniclastic material or caldera-derived ejecta. The lack of sector collapses on the volcanic edifice suggest that Pelorus is younger than the more eroded volcanoes to the north. Five additional volcanoes between 22°51'S and 21°31'S on the Southern Tonga Segment (Volcanoes 9 to 13) were originally identified in low-resolution bathymetry but not in subsequent surveys (Stoffers et al., 2002, 2006b).

At ~23°30'S, the line of volcanoes defining the volcanic front shifts from a NNE orientation between Volcano 1 and Volcano 14 to almost due north between Volcano 14 and Volcano 21 on the Louisville and Monowai segments (Figure 2.3b). These volcanoes are described individually in Chapter 3. Volcano 14 (23°34'S) (Figure 2.4f) consists of two cones, slightly elongated in a NE-SW direction and comprising an edifice that is 21 x 17 km and rising 1.4 km from the surrounding seafloor. The western cone has a 3.5-km diameter crater at its summit that is ~600 m deep. The smooth flanks of the cones suggest burial by ejecta from the crater-forming eruptions. Volcano 15 (23°52'S) (Figure 2.4g) is a simple, 12-km diameter volcano (rising to 1080 mbsl) with a large 4.7 x 3.9 km summit caldera. North of Volcano 15, there is also a broad 8-km diameter semicircular structure that may be a second eroded volcano or part of a larger ancestral volcano on which Volcano 15 has grown. Volcano 16 (24° 11'S) (Figure 2.4h) is an elongate complex of nested calderas, 20 x 19 km, with several peaks and depressions infilled by

younger ejecta. Volcano 18 (Figure 2.4i) consists of a pair of volcanoes: the northern (24°29'S) cone is 10 km in diameter, rises 1 km high, and occupies the center of a large SW-NE-trending fissure and exposed dike complex with >40 pyroclastic cones in a line extending 18.8 km long. The southern cone (24°35'S) is 14 km in diameter with a funnel-shaped summit crater 6.9 x 6.3 km at a depth of 1490 mbsl. Volcano 19 (24°48'S) (Figure 2.4j) is a steep-sided symmetrical cone with a diameter of 14 x 12 km and rising 950 m above the surrounding seafloor. It has an old poorly preserved summit depression, mostly filled by a younger 1.7-km diameter cone, and a younger flanking crater that is 1.8 km wide and 250 m deep. Details of this structure and associated hydrothermal venting are described in Stoffers et al., (2006a). Volcano 20 (25°12'S) (Figure 2.4k) is a 11 x 10 km caldera volcano rising 1.1 km above the surrounding seafloor. The 6.8 x 4.9-km caldera reaches a depth of 1150 mbsl. Volcano 21 (25°25'S) (Figure 2.4l) is a 13-km diameter, 1-km tall cone with a small 3-km wide summit crater.

The Monowai Segment at 26°S is marked by a shoaling of the arc front, which may be related to the immediately adjacent Osbourn Seamount impinging on the arc-trench system. The Monowai volcanic complex (25°50'S) (Figure 2.4m) comprises the 15-km diameter Monowai caldera at 1600 mbsl and the nearby 1-km high Monowai Seamount. Together, the caldera and Monowai Seamount comprise a >400 km^2 complex that is the largest volcanic feature of the Tonga-Kermadec arc. The caldera is also one of the largest known structures of its type in the oceans and is characterized by numerous ring faults, multiple parasitic cones at the rim, and a 2-km diameter resurgent dome in the center of the caldera floor. Like the other caldera volcanoes (Volcanoes 15, 16, and 20), the Monowai caldera has a distinctive elliptical shape. Although the caldera is not currently active, extensive and ongoing eruptions have been documented at the summit of the nearby cone. Monowai has been extensively studied by Davey (1980), Wright et al. (2008), Chadwick et al. (2008), Timm et al. (2011), Watts et al. (2012), Wormald et al. (2012), Paulatto et al. (2014), Metz et al. (2019) and is compared to the other volcanoes of the Tonga arc in Chapter 3.

Lavas from the Southern ('Ata) segment of the Tonga arc range from high-Mg basalt to rhyolite and belong to the low-K series (T. Worthington in Stoffers et al., 2002, 2006b). Both mafic and felsic lavas have been recovered from about half of the volcanoes in the 'Ata region, whereas all

of the volcanoes of the Louisville Segment are basaltic. The petrology of the volcanoes is discussed in greater detail in Chapter 3. Hydrothermal activity was found at Volcano 1, Volcano 14, Volcano 18, Volcano 19, and in the Monowai Volcanic complex. Hydrothermally altered and mineralized samples from the Volcanoes 1, 14, 18, and 19 show characteristics of other shallow submarine volcanic arcs, including extensive degassing and boiling of hydrothermal fluids due to the low pressures (e.g., Stoffers et al., 2006a), whereas venting at large-scale caldera faults in the Monowai volcanic complex is more typical of deeper back-arc basin volcanoes (Leybourne et al., 2012). At Monowai, the caldera low-temperature fluids are suggested to be the result of a heat source from a magma chamber with a long fluid pathway to the seafloor. This results in significant mixing, cooling, and metal sulfide precipitation (Leybourne et al., 2012).

2.3.3 Louisville Ridge and Osbourn Trough

The ~4000-km long Louisville Seamount Chain (LSC) formed at a hot spot now located near the SW Pacific-Antarctica Ridge (Lonsdale, 1986; Watts et al., 1988). Mapping and sampling show the seamounts consist of stacked weathered pillow lavas, hyaloclastite and breccia (Worthington et al. 2006). The line of large seamounts on the chain interests the Tonga-Kermadec Trench at ~26°S, where the incoming seamounts rise 4 to 5 km above the surrounding seafloor. Due to the oblique angle of the LSC, 34° to the Tonga-Kermadec Trench, the point of seamount subduction is migrating southwards at 120-180 mm/yr along the trench (Robinson et al., 2018). The collision of the trench and the LSC correlates with a large region of relative seismic quiescence, thought to be caused by subduction of the seamounts inhibiting seismicity (Peirce and Watts, 2011). Projecting the Louisville Ridge into the subduction system, its present position should be below the arc at ~22°30'S near 'Ata Island (Vallier et al., 1985). Geochemically distinct lavas near ‘Ata, with high (La/Yb)N and LREE enrichment, have been interpreted to reflect the subduction of LSC rocks with these characteristics (T. Worthington in Stoffers et al., 2002, 2006b). The westernmost seamount that is still subducting (Osbourn Seamount) has a flat surface that has been tilted down toward the trench (Ballance et al., 1989). Where the LSC has passed, subsidence of the outermost forearc led to the formation of the Horizon Deep (Contreras-Reyes et al., 2011).

At about the same location as the subducting LSC, the ~900 km Osbourn Trough is also entering the trench (Figure 2.1 and Figure 2.3). The Osbourn Trough is an E-W oriented fossil spreading ridge which became inactive prior to 87 Ma with the splitting apart of the Manihiki and Hikurangi plateaus (Beier et al., 2011). Bathymetric mapping combined with geochemical analyses of lavas across the Osbourn Trough show a 200-500 m deep axial valley with characteristics of a slow-spreading ridge (Worthington et al., 2006), however correlations with lava samples collected at IODP sites north of the Osbourn Trough indicate they were generated at a fast to super fast spreading ridge (~140 mm/yr) (Zhang et al., 2012). The presence of the slow ridge-like morphology possibly could have formed shortly prior to its cessation. Samples collected from the Osbourn Trough are mainly weathered MORB, strongly enriched in most alkali elements and light REE (Worthington et al., 2006). While active, the fast-spreading Osbourn Trough would have promoted significant volcanism at its spreading axis, however the influence of the currently subducting Osbourn Trough on the Tonga arc segments has not been previously explored.

2.4 Methods and Data

We compiled high-resolution bathymetric data from ship-based multibeam systems (MBES) as well as seafloor observations from 8 research cruises on the Louisville and Monowai segments (Table 2.1). In addition, in 1997, R/V *Yokosuka* conducted seismic surveys in the adjacent back-arc, south of the VFR (Matsumoto et al., 1997; Ruellan et al., 1998; Delteil et al., 1999), including 27 single-channel seismic reflection profiles that crossed the arc front and adjacent back-arc. Three of the profiles cross the Louisville and Monowai segments and were examined in this study.

MBES data used to map the volcanoes of the Louisville and Monowai segments were collected in 2002 during SO-167 (Stoffers et al., 2002) aboard R/V *Sonne*, in 2007 during SO-192 (Schwarz-Schampera et al., 2007) on R/V *Sonne*, and in 2014 during TN-309 of the R/V *Thomas G. Thompson* (Rolling Deck to Repository, R2R, 2014). The TN-309 data were gridded with a resolution of 30 m, the SO-167 data were gridded with a resolution of 45 m, and the data from SO-192 were gridded with a resolution of 50 m. For the Monowai volcanic complex, MBES data

originally collected and processed during SO-215 in 2011 (Peirce and Watts, 2011) were re-gridded in this study with a resolution of 30 m. The MBES data sets are used with the Global Multi-Resolution Topography data set (GMRT: Ryan et al., 2009), which has a resolution of 100 m but covers the background surrounding our areas of interest. We processed the data further by applying a calculated slope raster and hillshade raster which helps to reveal complex structure (Figure 2.3b). The slope raster is computed using ArcGIS software employing an algorithm with a 3 x 3 moving grid-cell to calculate slope at the center of 8 surrounding cells (Burrough and McDonell, 1998). The hillshade is a 3D representation of the surface with the sun's relative position taken into account for the shading of the image.

Vertical gravity gradient (VGG) derived from satellite altimetry (Sandwell et al., 2014) was used to investigate large-scale structures in the mapping region and possible buried structures. The large volcanic centers and the Louisville Seamounts are positive anomalies in the VGG, whereas features such as the arc-front grabens and Valu Fa Rift are negative anomalies (Figure 2.5). Magnetic data in Figure 2.5 are from the 2-arc minute resolution compilation, EMAG2 (Earth Magnetic Anomaly Grid: Maus et al., 2009). Although it is difficult to extract details from these data in the mapping area, due to the coarse resolution, some of the arc-front volcanoes are associated with positive magnetic anomalies, especially in the area of ridges-and-knolls adjacent to the VFR, whereas deeper structures that cross the arc are associated with magnetic lows (e.g., at Monowai: described below.

Using the combined MBES and geophysical data, and comparisons with well-mapped locations as training areas, we isolated a variety of structures, different volcano types, and 16 different geological formations to create a geological map of the Louisville and Monowai segments at 1:250,000 scale. The geological map was constructed using the approach developed for other submarine volcanic arcs (Anderson et al., 2016, 2017; Stewart et al., 2021) and at mid-ocean ridges (Klischies et al., 2019). In these studies, geological legends were created by gathering units with similar properties, age, and origin and sorting them into distinct formations, taking into consideration the crust types (and thickness, where known), sequence of depositional events, the composition of different units, tectonic fabric and structure. Contacts between formations are based on mappable boundaries in high-precision digital elevation models (DEMs) from the

compiled MBES data, supported by acoustic backscatter, other geophysical data (magnetics, gravity) and direct seafloor observations. Acoustic backscatter, used to identify sediment cover, was only available for the Monowai volcanic complex and the immediately surrounding area (Wormald et al., 2012). For volcanic terrains, the criteria for the classification of different geological elements are well-established from land-based analogues (e.g., Thouret, 1999). At the highest resolution in ship-based multibeam and backscatter it is possible to precisely identify different volcanic and sedimentary units, and stratigraphic relationships, constrained by surface texture, acoustic reflectivity, slope breaks, and relative water depth. The major structures and formations are recorded as polyline and polygon shapefiles to create a contiguous geological map. The legend was adapted from the geological legend of the Lau Basin published with Stewart et al. (2021). Complementary visual observations from submersibles and ROVs provided essential groundtruthing required for the geological mapping and important information about rock types and volcanic facies at the outcrop scale. These data were compiled in Chapter 3 from over 94 hours of bottom observations in different parts of the volcanic complexes.

The type of faulting within the Louisville and Monowai segments was investigated using the centroid moment tensors (CMTs) of shallow earthquakes recorded in the area, following Baxter et al. (2020). The earthquake epicenters and relevant data are available in the Global Centroid Moment Tensor (GCMT) open-source project (Dziewonski et al., 1981; Ekström et al., 2012). The CMTs are a graphical representation of the nine moment tensors determined for earthquake motions, which are used to calculate the strike, dip, and rake of two possible fault plane solutions. To resolve which of the two possible focal planes best represent the fault, geological data, such as the orientations of the principal structures at the location of the earthquake, are required. We used mapped lineaments from our study (Figure 2.6) to compare to a subset of the earthquake epicenters in the global database. A total of 75 CMTs, with depths of <30 km were analyzed in the study area and converted using the ArcBeachball tool (v2.2) in ArcMap following the method of Baxter et al. (2020).

All supplementary maps and data files for this study are stored on a server at the University of Ottawa, and any inquires can be directed to the author.

2.5 Geological Map of the Louisville and Monowai Segments

The mapped area of the Louisville and Monowai Segments is shown in Figure 2.6 (see Appendix B for map sheet and schematic cross section) and extends from Volcano 14 in the north (23°34'S, 176°40'W) to Volcano T in the south (26°19'S, 177°21'W), ~295 km along the arc front. Among the major features illustrated in the map is the strong structural control on the segmentation of the arc as well as the distribution of different volcano types and associated geological formations. A clear NE-SW faulting pattern, similar to that described by Campbell et al. (2007) for the central and southern Kermadec arc and by Wormald et al. (2012) at Monowai, is seen to extend the full length of the Louisville and Monowai segments adjacent to the LSC.

2.5.1 Major structures

Over 980 distinct fault segments with an average length of 3.2 km were mapped along the Louisville and Monowai segments. Lineaments were drawn on the hanging wall at the base of normal fault scarps and at the ridge line of collapse features. More than 48% of the identified faults have NE-SW orientations of between 030° and 060°, with an average of 040° closely matching the orientations of similar structures in the Havre Trough (e.g., Campbell et al., 2007). The mapped normal faults range in length from 2 km to up to 15 km, with throws reaching up to ~500 m. Ring faults, major intracaldera faults, and collapse features also were mapped among twelve large caldera structures identified in the mapping area. The caldera faults are among the largest structures mapped at the arc front, ranging in circumference from 2.5 km to 17.8 km.

A fence diagram along the length of the arc front (Figure 2.7) shows three prominent graben-like structures (G1-G3). The grabens are evenly spaced about 30 km apart and cut obliquely across the arc front, occupying en echelon positions with a left-stepping offset from south to north (Figure 2.8). The orientations of the grabens of 030-040° closely follow the general trend of mapped faults throughout the arc segment. The widths of the grabens vary from 10-40 km, with lengths of 90 km to nearly 150 km, crossing the full width of the arc front and extending into the back-arc (e.g., G1). They range in depth from 1500 to 2050 mbsl relative to the surrounding highs with absolute depths of ~1100 to 1530 mbsl.

The northernmost of the three grabens (G1), located at the north end of the Louisville Segment, is subparallel to the VFR and is continuous with back-arc structures in the ridge-and-knoll terrain described by Delteil et al. (2002) and Ruellan et al. (2003). The graben is approximately 128 km in length, ranging in width from 28 km in the south to 19 km in the north. The graben floor is relatively unfractured compared to other parts of the arc front, with only 9 faults larger than 3 km. At its deepest, the graben is 2010 mbsl and shoals to 1850 mbsl adjacent to two large caldera volcanoes (Volcano 15 and 16). The caldera volcanoes are 12 km and 20 km in diameter, respectively, with ~6 km and 9 km wide calderas. The southern end of the graben rises to 1650 mbsl where it merges with the Southern Lau Rift (SLF of Delteil et al., 2002 and Ruellan et al., 2003).

A second smaller graben (G2) in the middle of the Louisville Segment comprises two sub-basins, slightly offset from south-to-north and separated by a poorly defined sill at ~1750 and 1800 mbsl. The southern of the two sub-basins is 84 km long with a width of 12 km. It is deepest in the southwest at 1950 mbsl and shallows to 1750 mbsl in the northeast. The northern sub-basin is much shorter, at 20 km in length and 15 km wide, with a maximum depth of 1800 mbsl. Abundant faulting and volcanic features occur in this graben, in particular in the northern sub-basin, including small cones (<2 km diameter), a few larger cones and volcanic fissures (3-5 km diameter). The largest volcanic feature in the graben is the 9-km wide caldera at Volcano 20, which is located on an inflated part of the graben floor. The northern end of the graben terminates in relict arc crust.

The northern part of the Monowai segment is dominated by the Monowai Graben (G3), which contains the Monowai Volcanic Complex. The Monowai graben (G3) is the largest of the arc-transverse structures in the map area. It is wider and deeper than the other grabens and can be traced well into the back-arc, with a total length of more than 150 km. It widens to ~30 km in the SW where it is deepest (~2050 mbsl) and shoals to 1500 mbsl in the northeast where it is 13 km wide. More than 200 NE-SW normal faults have been mapped along the rift, with maximum throws of 300 m and individual strike lengths of up to 15 km. Collectively, they account for 950 m of subsidence (Figure 2.7a). The bounding faults have a strike of 25° to 30°, subparallel to the other grabens and collinear with the rifting in the adjacent back-arc ridges and knolls (N27

orientation of Delteil et al., 2002; Ruellan et al., 2003). Faulting of the floor of the graben is commonly associated with volcanic fissures, and volcanic ridges within the graben are elongated in a similar direction.

The major volcanic feature in the graben is the large 15-km diameter Monowai caldera and associated Monowai Seamount (Figure 2.4m). The caldera and cone are built on an inflated part of the broad volcanic plain of the graben, partly overlapping the graben-bounding faults. Ring faults of the caldera cut the normal faults bounding the graben faults, and prominent ridges, at least 5 km in strike length, along some of the graben-bounding faults indicate that they are probably intruded by dikes. Mass wasting of a large cone on the northwest flank of the caldera (see Chapter 3) suggests that it pre-dated the outermost ring faults and possibly formed in the earliest stages of rifting of the graben. Like the other caldera volcanoes, the Monowai caldera has an elliptical shape elongated in the extension axis, suggesting that the caldera formed while the graben was opening. Detailed maps of the complex supporting these observations have been published by Wright et al. (2008), Wormald et al. (2012), and Paulatto et al. (2014) and a larger scale map is provided in Chapter 3. Of particular interest is the evidence of large-scale hydrothermal venting along the intracaldera faults (Leybourne et al. 2012; Schwarz-Schampera et al., 2007).

Although the terminations of the grabens are difficult to identify due to the lack of high-resolution bathymetric data in those areas, a series of ridges (fault blocks) and, in some cases, branching and anastomosing structures appear to propagate into the forearc and back-arc regions. The orientations of the three main grabens are evidence of an extension axis oblique to the northerly trend of the arc segment, with $\sigma 3$ striking 120-130°. Delteil et al. (2002) and Ruellan et al. (2003) published seismic lines that crossed all of the grabens, clearly identifying their left-stepping offset from south-to-north and their westward continuation into the back-arc (Figure 2.9). However, the full extent of rifting of the arc crust was not previously known. A notable feature of all three grabens is the elliptical shape of the large central caldera volcanoes (Volcanoes 15, 16, 20, and Monowai) with clear elongation perpendicular to the long-axes of the grabens (see below).

The raised areas, or horsts, between the grabens are flat-topped areas ranging in width from 10 to 42 km. These blocks are at depths from 1530 to 1100 mbsl, similar to the surrounding arc crust, suggesting that they are intact portions of the arc separated by foundered arc crust rather than uplifted blocks. The horsts are strongly faulted and can exhibit rugged topography caused by the combination of faulting and numerous volcanic features. The most notable volcanic features on the "horsts" include Volcano 21, which sits on a 20-km wide block north of the Monowai Graben, and Volcanoes 19 and 18 which occur on the raised area between G1 and G2.

2.5.2 Distribution of volcano types

The 9 largest volcanoes of the Louisville and Monowai segments show a clear relationship to the "horst-and-graben" structures. Four are composite cones with summit craters, one is a cone lacking a summit depression and four are large caldera volcanoes. The summits of the cone volcanoes range from 900 mbsl to less than 100 mbsl, whereas the depths of the large caldera volcanoes reach 1600 mbsl, the deepest at Monowai. In general, the cone volcanoes occur on the horst-like blocks, whereas the larger caldera volcanoes are found in the graben-like depressions (Figure 2.6b and 2.7b). The sizes of the calderas clearly indicate a major withdrawal of melt, most probably linked to the graben formation (see discussion).

In addition to the larger cones and caldera volcanoes, we mapped more than 2000 smaller volcanic features >200 m in diameter. The perimeters of each volcano were drawn at the steepest inflection point nearest the base of the slope. The data are included in the 1:50,000 map layer. We further subdivide the cones and caldera volcanoes into four types shown in Figure 2.6a, which match the geological legend of the Lau Basin (Stewart et al., 2021). Cone-shaped volcanoes (Av1), which include the large stratovolcanoes on the horst blocks, are dominant. They are typically 15-20 km in diameter and 1 km high, with small summit calderas or caters, 3-7 km in diameter. Many of the cone volcanoes have radial ridges extending outward from the summits. The large caldera volcanoes occupying the graben floors are "shield-type" (Av2). They are generally larger than the cone volcanoes but have width:height ratios of >5. Smaller dome volcanoes (Av3) and fissure volcanoes (Av4) are also present throughout the map area. Fissure volcanoes are abundant, especially on the horst blocks, and typically form a prominent ridge of

pillows or volcaniclastic material abutting an exposed dike. Several of these features have strike lengths of as much as 19 km and connect multiple volcanic cones (e.g., Volcano 18).

2.5.3 Other mapped formations

The arc crust is subdivided into upper and lower formations based on the level of exposure and inferred stratigraphic position with respect to the adjacent forearc and trench (cf. Stewart et al., 2021). The areas of the different crustal types are summarized in Table 2.3. The upper arc crust (uAc1) comprises the recent volcanic, sedimentary, and intrusive rocks of the intact upper arc that has not been greatly affected by rifting and has not undergone thinning. This formation type is mainly in the undeformed parts of the arc between the arc-transverse grabens and on which the composite cones (Av1) and fissure volcanoes (Av4) have developed. The grabens expose somewhat lower rifted arc crust (uAc2) on the inner walls, which are dominated by normal faulting. The floors of the grabens are composed of upper arc crust that has been extended and lowered into the graben and include abundant volcaniclastic material shed into the graben (uAc3). Major normal faulting in uAc2 and uAc3 is partly obscured by this material and by the aprons of the large shield volcanoes and calderas.

To the east of the arc front, lower arc crust of the Tonga Ridge (lRac) is overlain by the formations of the active arc and is cut by normal faults of the three arc-transverse grabens. The relict arc crust was left behind after the opening of the Lau Basin and is no longer active (Stewart et al., 2021), consisting mostly of volcaniclastic and sedimentary material with no obvious volcanic features preserved. Upper relict arc crust (uRac) is distinguished from lRac by the level of exposure on the Tonga Ridge.

In the northernmost part of the map area, axial back-arc crust (uBac) and proximal backarc crust (mBac) occupies the southernmost tip of the VFR spreading center, which impinges on the ridge-and-knoll terrain of the SLR and is propagating into arc crust. The active spreading center is marked by an axial volcanic ridge (uBar) and proximal volcanic or tectonic ridge (mBar) bordering the neovolcanic zone but still within the rift valley. Stewart et al. (2021) identified crust on the flank of the spreading center as belonging to the transitional zone between the arc and backarc (lTc) and including volcanic or tectonic ridges (uTr) in sedimented areas. The ridge-

and-knoll terrain of the adjacent back-arc region is mapped as a single volcanic field (Bavf), although structures and volcanoes related to the cross-arc grabens extend into this area.

2.6 Quantitative Analysis

The mapped area of the Louisville and Monowai segments (59, 667 km^2) is dominated by the active arc (25.2%) and the adjacent back-arc volcanic field (42.2%). About 14.4% (8,584 km^2) of the area is relict arc crust that formed prior to the opening of the Lau Basin. Within the active arc formations (uAc1-3), 44.7% of the area is dominated by tectonic extension represented by the intensely faulted and extended upper arc crust occupying the deep grabens. These grabens account for only 11.4% of the total map area. About 1733 km^2 or 3.0% of the actively propagating SLR contains areas which are actively rifting and producing new back-arc crust. Adjacent to the SLR is also mostly extended crust rather than a product of active spreading (25,426; 42% mapped area) (see also Ruellan et al., 2003) This is consistent with the regional makeup of the SLR ridges and knolls, which is comprised of backarc rifts and arc-backarc transition formations as previously described by Ruellan et al. (2003).

The four large cone volcanoes at the active volcanic front of the arc have a total volume of 349 km^3 (Volcano 14, Volcano 18, Volcano 19, Volcano 21). The four caldera volcanoes (Volcano 15, Volcano 16, Volcano 20, and Monowai) have a total volume of 580 km^3, which suggests that the magmatic productivity of the arc is significantly greater within the extensional regions. Individual volumes for the volcanoes are shown in Table 2.4. The more than 2000 smaller volcanoes mapped in the area also account for a significant proportion of the total magmatic budget of the arc with a total volume of 387 km^3 (28% of total magmatic budget).

Nearly half (47%) of all mapped faults have an orientation of 035-045° with little variation between the grabens (G1-3) (Figure 2.10). The dominant faulting in the Monowai graben (G3) is 025-030°. The dominant faulting in G1 is 030-040° and in G2 it is 030-035°. The range of the dominant fault directions in all three grabens is between 020-045°. The dominant fault orientations rotate from 035° in G1 to 025° in G3, indicating that the rifts become more aligned

with the trench orientation (011°) to the south. This realignment, to more trench-parallel rifts, may result in less strike-slip motion occurring in the south than in the north (Yu et al., 1993; Bonnardot et al., 2007). Both extensional and strike-slip faulting occurs in the grabens, although CMT data is mainly constrained to G2 (Figure 2.10a). The faults along the graben boundaries show the greatest continuity and strike lengths up to 15 km, with the most continuous faulting in the Monowai Graben (Figure 2.11). The depths of normal faults generally scale with their length (e.g., Gudmundsson, 1992; Gudmundsson and Brenner, 2004), so the deepest faults in the map area are expected to be along the graben margins. The CMT database contains estimated depths for the locations of the hypocentres (Dziewonski et al., 1981; Ekström et al., 2012). In the map area, they range from 12.1 km to 29.4 km (depths greater than 30 km were not included in the CMT dataset analyzed) (Figure 2.12), however these should be treated with caution owing to the errors associated with locating hypocenters. Generally, earthquakes are occurring at shallower depths in the grabens (averaging 13.8 km) compared to deeper on the "horst" blocks (averaging 19.6 km) (Figure 2.12). The deeply penetrating structures are thought to control the location of the different volcanoes and possibly are linked to basement faults. It is clear that there are far more near-surface fractures and faults than there are large structures of this type, and it seems unlikely that the shallow permeability structure is a dominant control on the locations of the volcanoes.

Of the three grabens, the major seismicity has been recorded in G2 (Figure 2.10). The resolved CMTs indicate that both strike slip and normal faulting is occurring within the graben and north of the graben. The normal faults indicate that the graben is undergoing active extension, possibly propagating to the north based on the mapped faults. The strike-slip faults indicate transtension and Riedel shearing (Bonnardot et al., 2007).

2.7 Discussion

Based on the orientation of the arc segment between Monowai and Volcano 14, we calculate the convergence obliquity between the Pacific Plate motion vector and the trench as $\alpha = 71°$ consistent with previous estimates from data in the SLR (Delteil et al., 2002). The convergence

obliquity between the Pacific Plate motion and the arc front is α= 78° (Figure 2.13). In the central part of the Tonga Arc, the effect of this obliquity is greatest along the Louisville and northern Monowai segments where the arc front is rotated nearly N-S (i.e., with a shift to α= 60°). Similar geometry has been documented in the Southern Kermadec Segment (Southern Havre Trough: Campbell et al., 2007) and in Northern Tonga (Anderson et al., 2021).

At ~26°S, the southward compression caused by oblique collision of the Pacific Plate and LSC has resulted in rotation of σ1 toward the south, thereby contributing to the segmentation of the arc. It would have taken the LSC about 2.3 m.y. to traverse the 300 km of the Louisville segment (based on a southward migration of 128 mm yr^{-1}: Ruellan et al., 2003), corresponding roughly to the age of initiation of volcanism along this part of the Tonga arc (Clift and ODP Leg 135 Scientific Party, 1995). The oblique rifting also appears to have strongly influenced the distribution of melt along the presently active arc front. Basement structures developed during collision likely opened melt pathways along the arc front as the LSC passed (so-called "locking and unlocking" of Ruellan et al., 2003). The elevated topography of the arc and back-arc in the region of the LSC may also indicate structural uplift due to the seamount chain entering the subduction zone. Nur and Ben-Avraham (1983) also previously suggested that the buoyant LSC might have caused flattening of the slab and westward migration of arc magmatism in the last 3 m.y.

In our model, the strike-slip component of the obliquely converging Pacific Plate and the stresses related to the subduction of the Louisville Ridge are accommodated by the grabens and transverse ridges or horsts at the arc front (Figure 2.14). The transtension is caused by the misorientation of the arc segment relative to the converging Pacific Plate. Between ~24°S and ~26°S, the angle of convergence between the Tonga Trench and the Pacific Plate decreases from orthogonal to ~60-70°. At the bend in the arc, strike-slip faulting with a component of southward compression caused by the collision with the LSC results in the extension and segmentation at the arc front. The pattern of rifting (left-stepping grabens from G3 to G1) is in agreement with the en echelon segmentation of the SLR and also the Havre Trough, as previously documented by Caress (1991), Wright et al. (1996) and Delteil et al. (2002). The left-stepping offset from south-to-north, also identified in the seismic lines of Delteil et al. (2002)

and Ruellan et al. (2003) (Figure 2.9) could eventually localize back-arc spreading if the VFR jumps closer to the arc and continues propagating southward into these structures.

Geodetic measurements (Bevis et al., 1995) and magnetic anomalies (Zellmer and Taylor, 1999, 2001) also indicate a sharp decrease of Tonga arc motion relative to the Australian Plate at this location. Sleeper and Martinez (2016) identified the plate boundary near the southern termination of the VFR as a diffuse deformation zone where the strain is taken up not only in the back arc (ridges and knolls) but also along the arc front. The left-stepping en echelon grabens produce a local right-lateral displacement, similar to that described by Delteil et al. (2002) in the SLR (Figure 2.15). Delteil et al. (2002) estimated that internal deformation of the arc in the south could result in longitudinal displacement of the arc crust by as much as 50 km. Similar north-south displacement of the Louisville Segment, on the order of 10s of km, is easily accommodated by the horst and graben structures. This is reflected in the elliptical shapes of the large caldera volcanoes. Assuming the short axes of the elliptical calderas represent the undeformed original circular diameter, a total of 14.3 km of stretching in the direction of $\sigma 3$ has occurred between the four large calderas.

We suggest that extension in the Louisville Segment and the locations of the different types of arc volcanoes are a response to a structurally weakened basement that has been affected by the subduction of the LSC. Deep structures in the arc crust appear to have localized strike-slip faulting and normal faulting in the arc and are responsible for the horsts and grabens and the distribution of the arc magmas. They may account for the predominance of basaltic melts along the Louisville Segment versus more andesitic volcanoes on other segments of the arc.

Deformation caused by the LSC does not appear to have affected northern Tonga in the same way as in the south (Ruellan et al., 2003). If the LSC was originally continuous with the Tuvalu Seamounts north of the Lau Basin, it should have affected the northern segments of the arc-backarc system as it migrated south from ~4 Ma. That it did not may be related to the orientation of the arc-trench system at that time, which would have been almost parallel to the approaching LSC, as noted by Ruellan et al. (2003). Several relics of arc-trench extension that might have occurred as the LSC collided with the northern segments and can be seen cutting obliquely

across the arc front in the north (i.e., the Fonualei Discontinuity and Niuatoputapu Lineament (Figure 2.1): Conder and Wiens, 2011; Baxter et al., 2020). However, available bathymetric data do not reveal regular transverse faulting in the north similar to that associated with the longitudinal extension of the arc in the Louisville and Monowai segments. It is possible that such structures have been buried by arc-related volcaniclastic deposits. For example, recent data from a seismic network at the Fonualei Rift in the Northern Tonga Segment has revealed brittle faulting 14 km below the seafloor (Schmid et al. 2021).

Seismic reflection profiles across the arc basement located at ~18°-19°S (Crawford et al., 2003) and 22°30'S (Ruellan et al., 2003) reveal deeply penetrating faults, up to 1 km, that are partly concealed by arc-related sedimentary basins (see also Austin et al., 1989; Tappin et al., 1994). These faults are apparently long-lived structures in the arc basement that predate the emergence of back-arc spreading and may have controlled the segmentation of the arc during basin opening. Similar structures extending to depths of at least 5 kilometers have been observed in the arc basement at other subduction zones (e.g., Takahasi et al., 2008; Kodaira et al., 2007), but it is unclear how they interact with the overlying arc crust. A strong basement fabric oblique to the arc-trench system also has been suggested for the Havre Trough (Caress, 1991; Wright, 1993) and the Taupo Volcanic Zone (TVZ: e.g., Seebeck et al., 2014). The original Vitiaz Arc crust of the early Eocene occupied a much broader zone than the present-day arc (e.g., Bloomer et al., 1994), raising the possibility of a structurally complex basement controlling the evolution of the arc-backarc system. The dissected forearc crust of the northern Tonga Ridge, at Fonualei and Niuatoputapu, confirms that the arc basement was probably segmented from an early stage with deeply penetrating structures that were favourably oriented for reactivation (Stewart et al., 2021).

Rifting of the arc crust to accommodate the oblique convergence of the Pacific Plate (Figure 2.14) contrasts with previous models of Lau Basin deformation in which all or most of the strain caused by Pacific-Australia convergence is accommodated at the rear of the arc (Delteil et al., 2002). The locations of the grabens on the Louisville and Monowai segments are consistent with an oblique slip model that was posed to account for the left-stepping en echelon basins in the SLR. Deltiel et al. (2002) and Ruellan et al. (2003) cited examples of experimental models (e.g., Richards, 1991) that show development of such structures above reactivated basement faults.

The length and width of the grabens on the Louisville Segment may also reflect the thickness of the crust in this part of the Tonga arc (Crawford et al., 2003; Contreras et al.). Rowland et al. (2012) have shown the tendency of arc rifts to scale with the thickness of the crust; a relationship that is well documented in the segmentation of continental margin arcs (e.g., Arai et al., 2018) and has been proposed for the evolution of the Marianas and Izu-Bonin arc-backarc systems (Ikeda and Yuasa, 1989; Fryer et al., 1990; Urabe and Kusakabe, 1990; Stern et al., 1990; Stern and Amira, 1998; Anderson et al., 2017).

These findings have implications for the locations of large-scale magmatic-hydrothermal systems, as the major convective hydrothermal systems are typically rooted in the deepest faults in optimally thickened crust and the shallow permeability structure is not a major control on the location of hydrothermal upflow (Hannington et al., 2005; Cathles, 2011). The largest hydrothermal systems form when basement faults are activated and the rifts are wide enough to accommodate large intrusions. The Monowai Graben and volcanic complex are likely an example of this process. Oblique rifting and transtension, previously recognized only in the back-arc of the Louisville Segment, is shown here to extend well into the arc crust, strongly influencing the distribution of melt along the arc front. Magmatism is enhanced where the graben structures cross the arc, and high rates of extrusion occur at the intersections of the rifts with the axis of the volcanic front. The major ring complexes associated with the caldera volcanoes of the Louisville Segment confirm large magma bodies intrude the rifts. Paulatto et al. (2013) demonstrated the existence of such a large sill-like intrusion beneath the Monowai Volcanic Complex. As well, high-velocity zones (7.1 km/s at shallow depths) encountered beneath graben G1 in the north (Contreras-Reyes et al., 2011) may indicate the presence of similar mafic intrusions there.

North of the Louisville Segment, the bulk of the magmatism is associated with clusters of large volcanic cones associated with Bouguer gravity lows (Sleeper et al., 2016), whereas along the Louisville Segment, the greatest magmatic activity is in the arc-transverse rifts. The grabens are intruded by melt or at least harbour remnants of subvolcanic intrusions indicated by positive magnetic anomalies and gravity highs. Paulatto et al. (2014) presented marine gravity and magnetics data of the Monowai volcanic complex showing positive magnetic anomalies and

gravity highs under the large cone and caldera (Figure 2.16). The free-air shipbased gravity data over the Monowai volcanic complex shows a strong correlation with the topography. A broad gravity anomaly high is present throughout the complex with local gravity highs at the cone summit (134 mGal) and the caldera rim (126 mGal). The deep caldera floor produces a relative gravity low (~110 mGal) compared to the surrounding rim and Monowai cone. The magnetic anomaly data across the Monowai volcanic complex varies from approximately -800 to +1400 nT. Both the Monowai cone and caldera are characterized by localized magnetic anomaly highs, occurring at the summit of the cone and along the southern caldera rim and bench. The Bouguer gravity anomaly was calculated for the Monowai volcanic complex assuming a rock density of 2300 kg m^{-3} based on rock types from Timm et al. (2011). The Bouguer gravity anomaly map shows a lack of significant Bouguer anomaly at the Monowai cone, a Bouguer anomaly high present at the Monowai caldera, and a strong Bouguer anomaly low associated with the highly faulted area to the northwest of the caldera (Paulatto et al., 2014). This strong structural control and tectonic focusing of the basaltic melts highlights the role of the basement and arc-transverse rifts in controlling the arc magmatism. A recent eruption at Volcano F in the Northern Tonga Segment is interpreted to have occurred within a similar extensional regime (Brandl et al., 2020).

An analysis of the magmatic productivity of the Tongan volcanoes is shown in Table 2.4. The melt volumes associated with the volcanoes of the Louisville and Monowai segments (including the volumes evacuated from the calderas) total more than 860 km^3 (Table 2.4). For an estimated age of the arc front volcanoes of <1 m.y., the magmatic productivity of this portion of the arc is ~0.001 km^3/yr. This is equivalent to about 0.05% of the global annual eruption volumes from submarine volcanic arcs of ~2-5 km^3/yr (Arculus, 1999) and 0.005% of the global melt flux from mid-ocean ridges of ~18 km^3/yr (Deligne and Sigurdsson, 2015).

2.8 Conclusions

The controlling structures for rifting of arc crust vary from strike-slip to purely normal faults that may occur at different locations and different stages of arc evolution. In the early opening history of the Lau Basin, for example, rifting occurred in old forearc crust of the Tonga Ridge

rather than at the arc front or behind the arc (Hawkins, 1995). We show that rifting of the Louisville Segment is occurring at the volcanic front, coincident with arc front magmatism, where three graben structures cross the arc. Extensive strike-slip faulting accommodates lateral displacements of the crustal blocks − a common feature of extensional rifts − with stretching of the arc crust over a faulted basement as a likely control. Similar processes have been inferred for the Mariana and Okinawa Trough arc-backarc systems with oblique strike-slip faulting as a precursor of arc rifting. In both cases, a curved geometry along the subduction trench gives rise to shear stresses in the extending upper plate (Arai et al., 2018; Anderson et al., 2017). The rifting and segmentation are additionally influenced by ridge subduction (e.g., Daito Ridge and Amami Plateau east of the Okinawa Trough: Arai et al., 2018). Along the Louisville Segment of the Tonga Arc, rifting is related to the misorientation of the arc-trench system relative to the converging Pacific Plate. The shallow crust, just prior to rifting of the arc, is intruded by dike-like bodies that feed the fissure eruptions and small cones along raised portions of the arc, whereas normal faulting localized above deeper basement faults formed the grabens that host larger sill-like magma bodies and caldera volcanoes. The volcano volumes clearly show a significant amount of melt is present in the rift grabens (e.g., under the Monowai Volcanic Complex: Paulatto et al., 2013).

Structures developed along the Louisville Segment are consistent with a critical stage of rifting of the arc crust, when major faults develop, large subvolcanic intrusions are emplaced, and large hydrothermal systems may become established. En echelon grabens developed at the arc front are in agreement with the kinematic model of Ruellan et al. (2003) and Delteil et al. (2002) but record previously unrecognized early stages of arc rifting and associated volcanism as the westward subducting LSC sweeps southwards along the trench. The pattern of rifting shows many of the features observed in the transition between the Havre Trough and back-arc spreading at the VFR, such as a "ridges and knolls" volcanic and tectonic fabric. Spreading in the back-arc is interpreted to have been temporarily locked due to compression exerted by subduction of the LSC (Ruellan et al., 2003), then released when the seamount chain passed. The migrating extension is manifested at the arc front by the "horst-and-graben" architecture of the Louisville Segment. We suggest that the arc-transverse faulting is controlled by Eocene basement structures reactivated by the oblique convergence of the Pacific Plate and subduction

of the LSC. The locations of the grabens indicate a regional left-stepping segmentation of the arc with fairly homogenous extension and broadly symmetrical grabens. Eventually, spreading behind the southward propagating VFR could jump to one of the grabens, as it might have done in earlier stages of opening of the north of the Lau Basin (Sleeper et al., 2016).

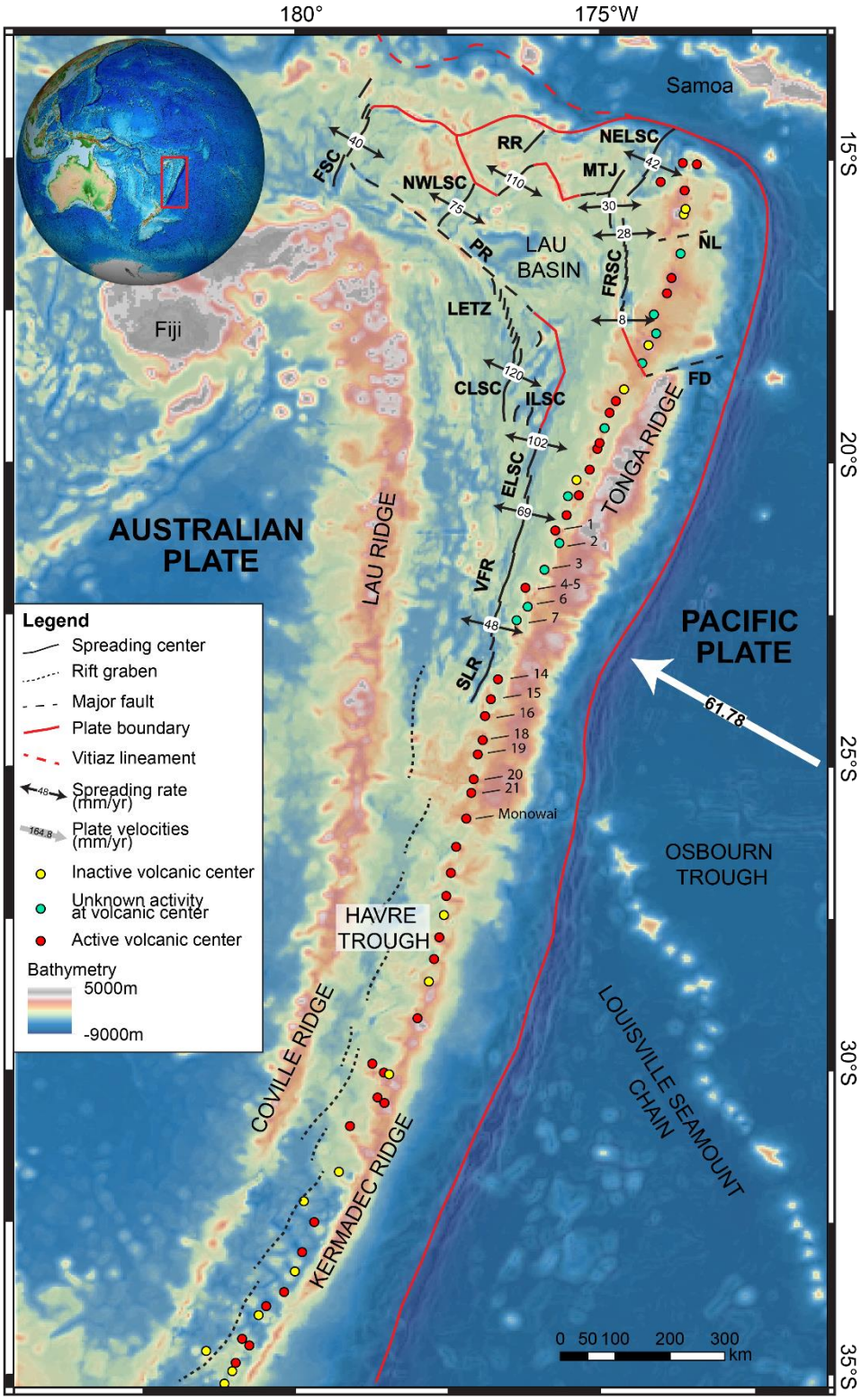

Figure 2.1 Bathymetric map of the Tonga-Kermadec system, showing the microplate boundaries and active spreading centers of Bird (2003) within the Lau Basin, modified by Baxter et al.

(2020), and the rift grabens of Campbell et al. (2007) within the Havre Trough. GPS velocities (mm/yr) and azimuths (white arrows) are shown for the Pacific Plate (Argus et al., 2011). Full-spreading rates (mm/yr) and spreading vectors (black errors) for the Rochambeau Rifts (RR) and Northwest Lau Spreading Center (NWLSC) are from Lupton et al. (2015), following Bird (2003). Spreading rates for the Central Lau Spreading (CLSC), Fonualei Rift and Spreading Center (FRSC), Eastern Lau Spreading Center (ELSC), Valu Fa Ridge (VFR), Mangatolu Triple Junction (MTJ), and the Northeast Lau Spreading Center (NELSC) are from Sleeper and Martinez (2016) and Baker et al., (2019). The spreading rate for the Futuna Spreading Center (FSC) is from Pelletier et al. (2001). Relics of arc-trench extension obliquely cross the arc front in the north (Fonualei Discontinuity (FD) and Niuatoputapu Lineament (NL). Locations of the volcanic centers (coloured circles) are shown along the arc front. Volcanic centers described in this study are indicated. Inset globe shows the position of the Tonga-Kermadec system in the SW Pacific.

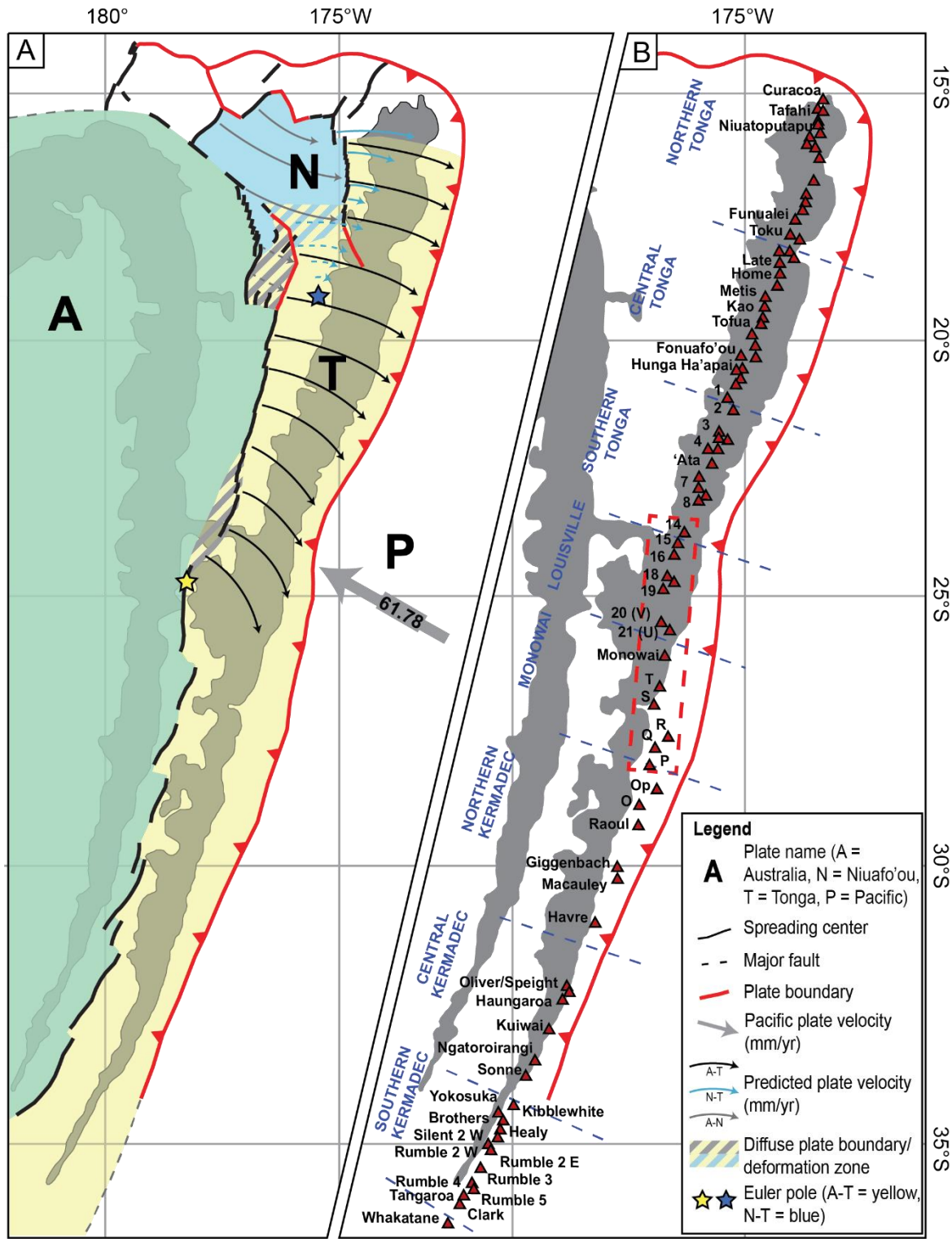

Figure 2.2 (a) Three-plate kinematic model of the Lau-Tonga-Kermadec system showing plate motion vectors and proposed poles of rotation (modified from Sleeper and Martinez, 2016). Gray shading shows regions shallower than 1500 m. (b) Segmentation of the Tonga-Kermadec arc

modified from Smith and Price (2006) showing the locations of arc volcanoes. Gray shading shows regions shallower than 1500 m. In the Louisville and Monowai segments we observe a change in orientation of the arc front (dashed red box).

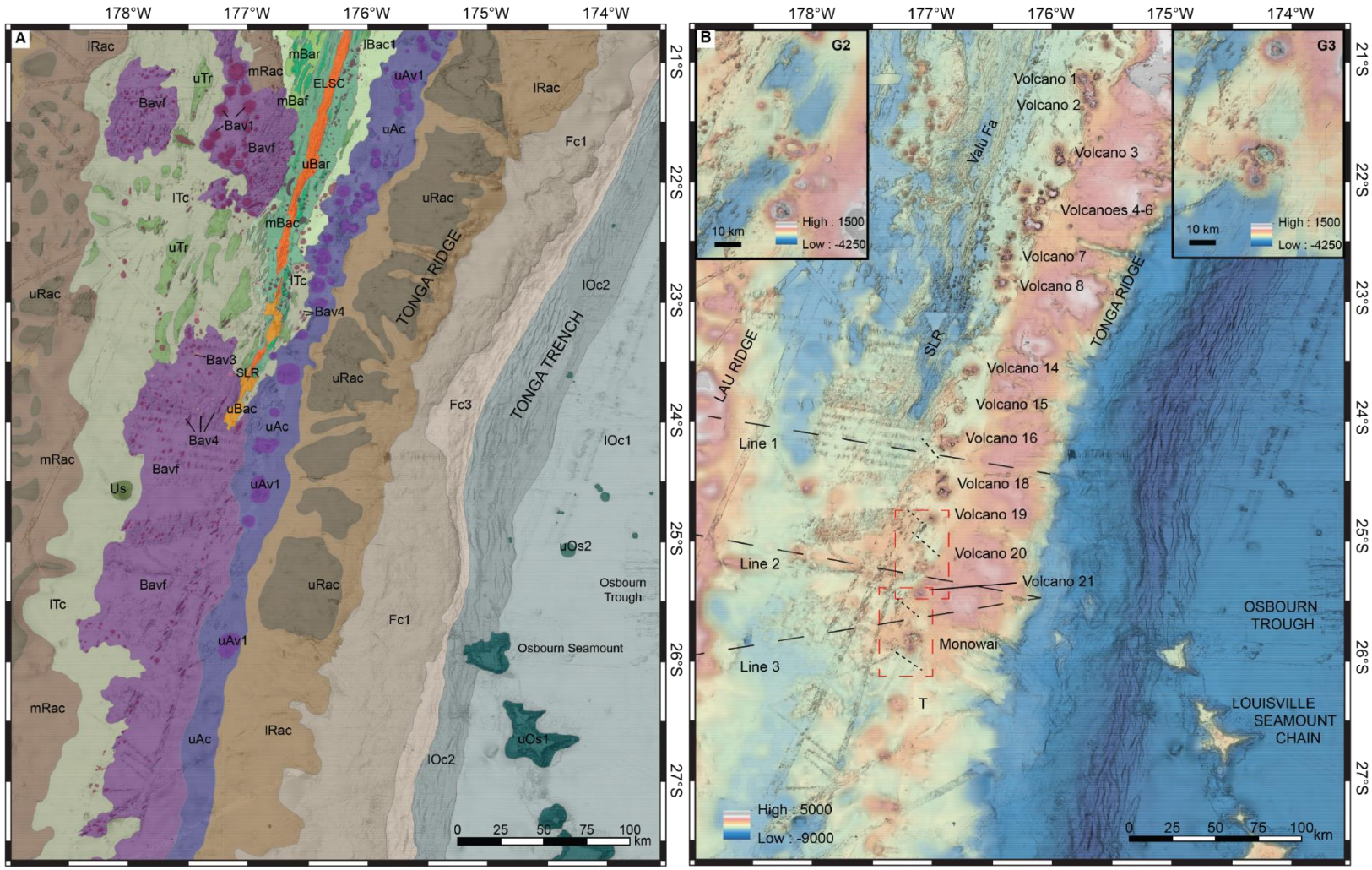

Figure 2.3 (a) Portion of the 1:1,000,000 geological map of the Lau Basin of Stewart et al. (2021), expanded southward to cover the study area. (b) Bathymetric map of the study area, covering the Louisville and Monowai arc segments. The study area contains ship tracks from ship cruises SO-167, SO-192, SO-215 (aboard R/V *Sonne*), and TN-309 (aboard R/V *Thomas G. Thompson*) combined

with GMRT datasets. The datasets are displayed with slope and hillshade functions. Volcanoes described in this study are labelled. Inset figures of the grabens G2 and G3 are also shown. NW-SE lines (short black dashed lines) show the location for the fence diagram Figure 2.7a. Lines 1-3 (black dashed line) show the locations of seismic sections from Ruellan et al. (2003) Figure 2.9.

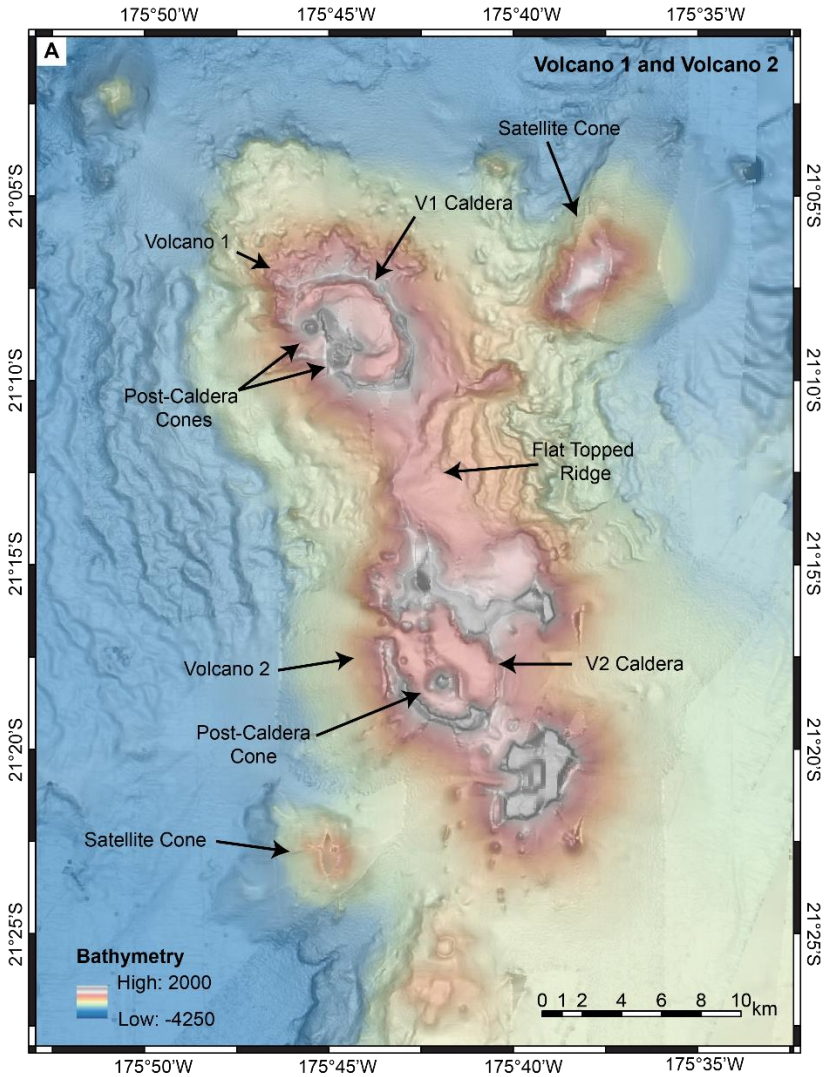
A
Volcano 1 and Volcano 2
Satellite Cone
V1 Caldera
Volcano 1
Post-Caldera Cones
Flat Topped Ridge
Volcano 2
V2 Caldera
Post-Caldera Cone
Satellite Cone
Bathymetry
High: 2000
Low: -4250
0 1 2 4 6 8 10 km
175°50'W
175°45'W
175°40'W
175°35'W
21°05'S
21°10'S
21°15'S
21°20'S
21°25'S

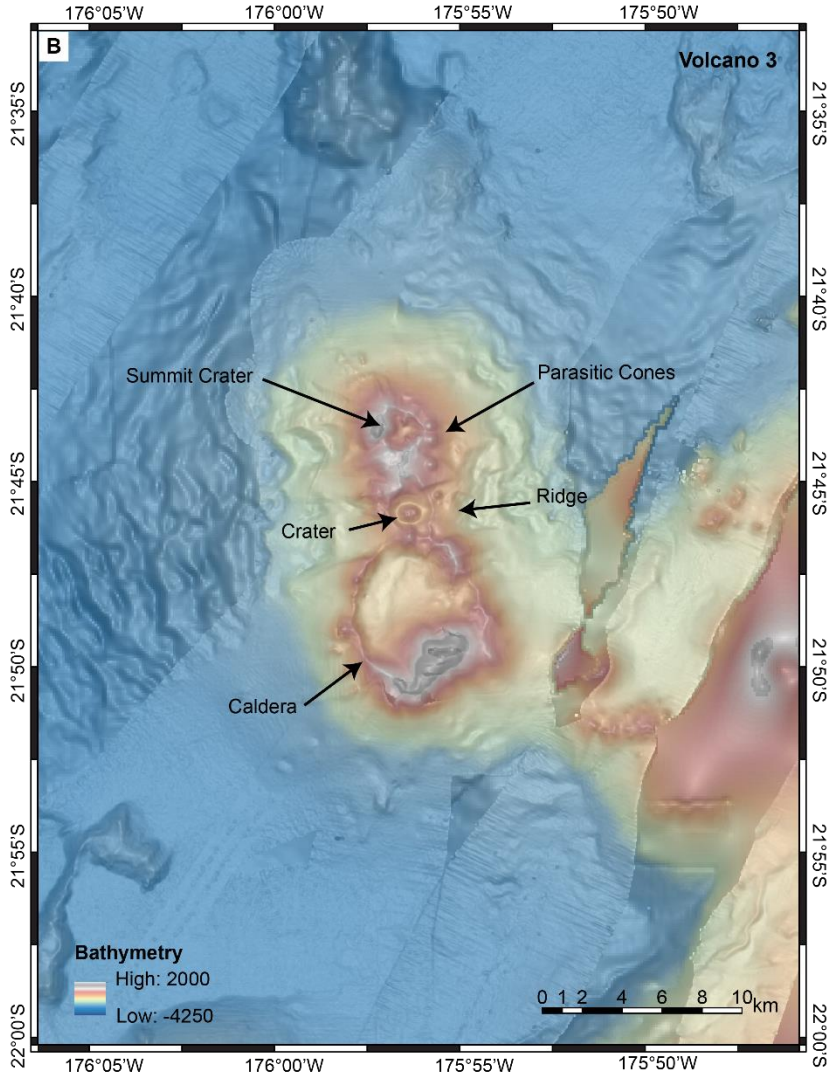
B
Volcano 3
Summit Crater
Parasitic Cones
Ridge
Crater
Caldera
Bathymetry
High: 2000
Low: -4250
0 1 2 4 6 8 10 km
176°05'W
176°00'W
175°55'W
175°50'W
21°35'S
21°40'S
21°45'S
21°50'S
21°55'S
22°00'S

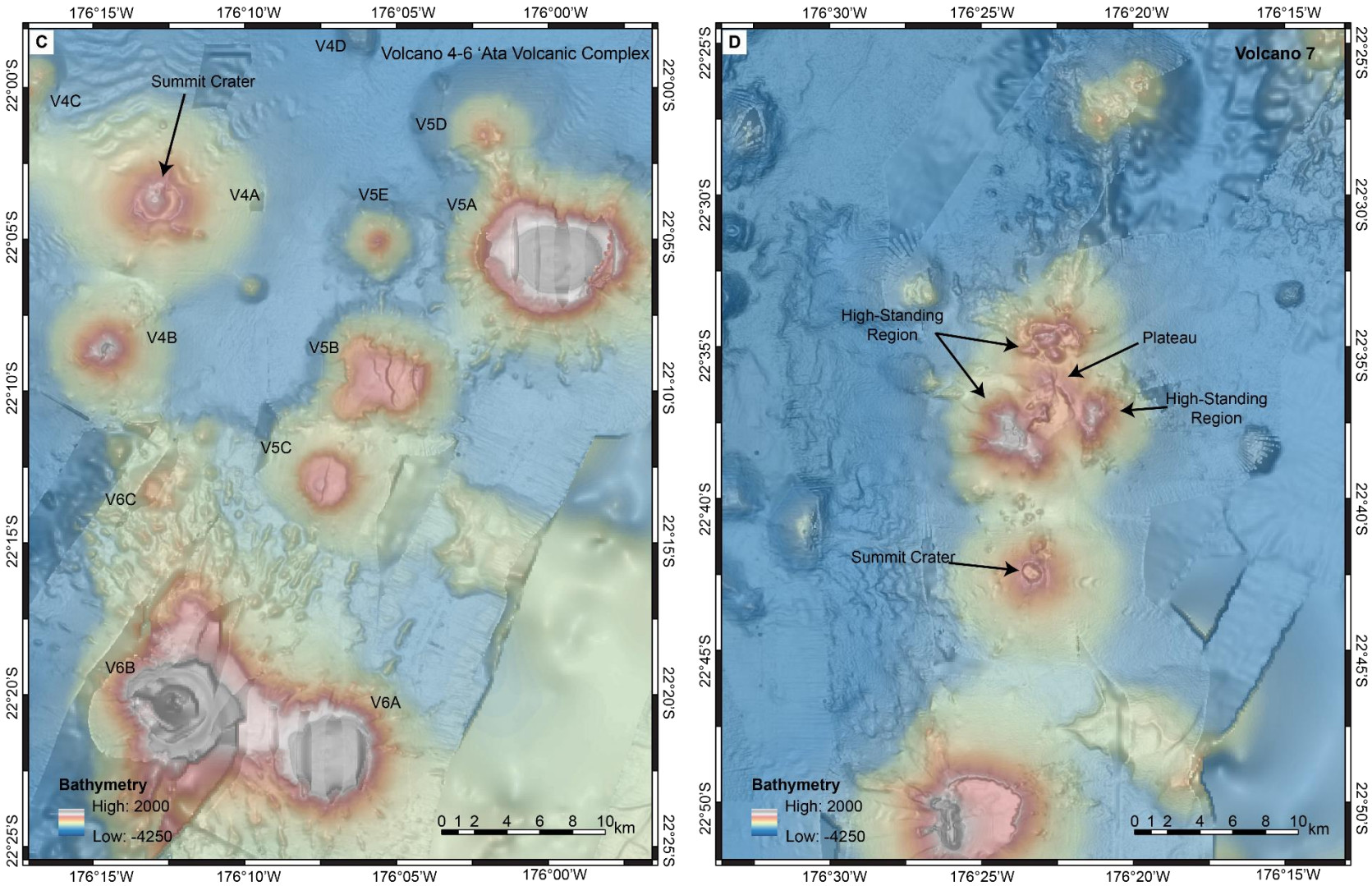
C
Volcano 4-6 'Ata Volcanic Complex
Summit Crater
V4D
V4C
V5D
V4A
V5E
V5A
V4B
V5B
V5C
V6C
V6B
V6A
Bathymetry
High: 2000
Low: -4250
0 1 2 4 6 8 10 km
176°15'W
176°10'W
176°05'W
176°00'W
22°00'S
22°05'S
22°10'S
22°15'S
22°20'S
22°25'S
D
Volcano 7
High-Standing Region
Plateau
High-Standing Region
Summit Crater
Bathymetry
High: 2000
Low: -4250
0 1 2 4 6 8 10 km
176°30'W
176°25'W
176°20'W
176°15'W
22°25'S
22°30'S
22°35'S
22°40'S
22°45'S
22°50'S

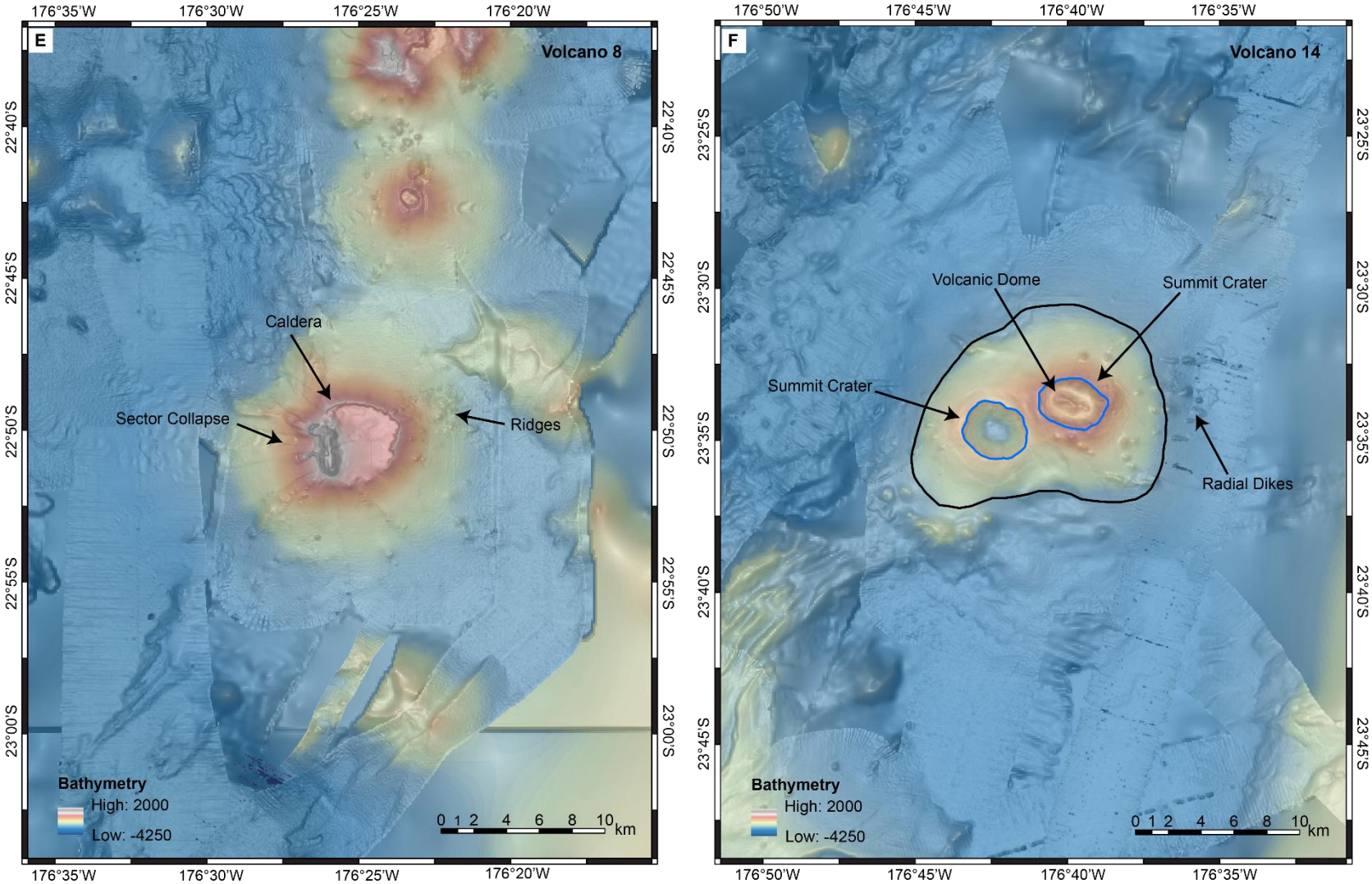
E
Volcano 8
Caldera
Sector Collapse
Ridges
Bathymetry
High: 2000
Low: -4250
0 1 2 4 6 8 10 km
176°35'W
176°30'W
176°25'W
176°20'W
22°40'S
22°45'S
22°50'S
22°55'S
23°00'S
F
Volcano 14
Volcanic Dome
Summit Crater
Summit Crater
Radial Dikes
Bathymetry
High: 2000
Low: -4250
0 1 2 4 6 8 10 km
176°50'W
176°45'W
176°40'W
176°35'W
23°25'S
23°30'S
23°35'S
23°40'S
23°45'S

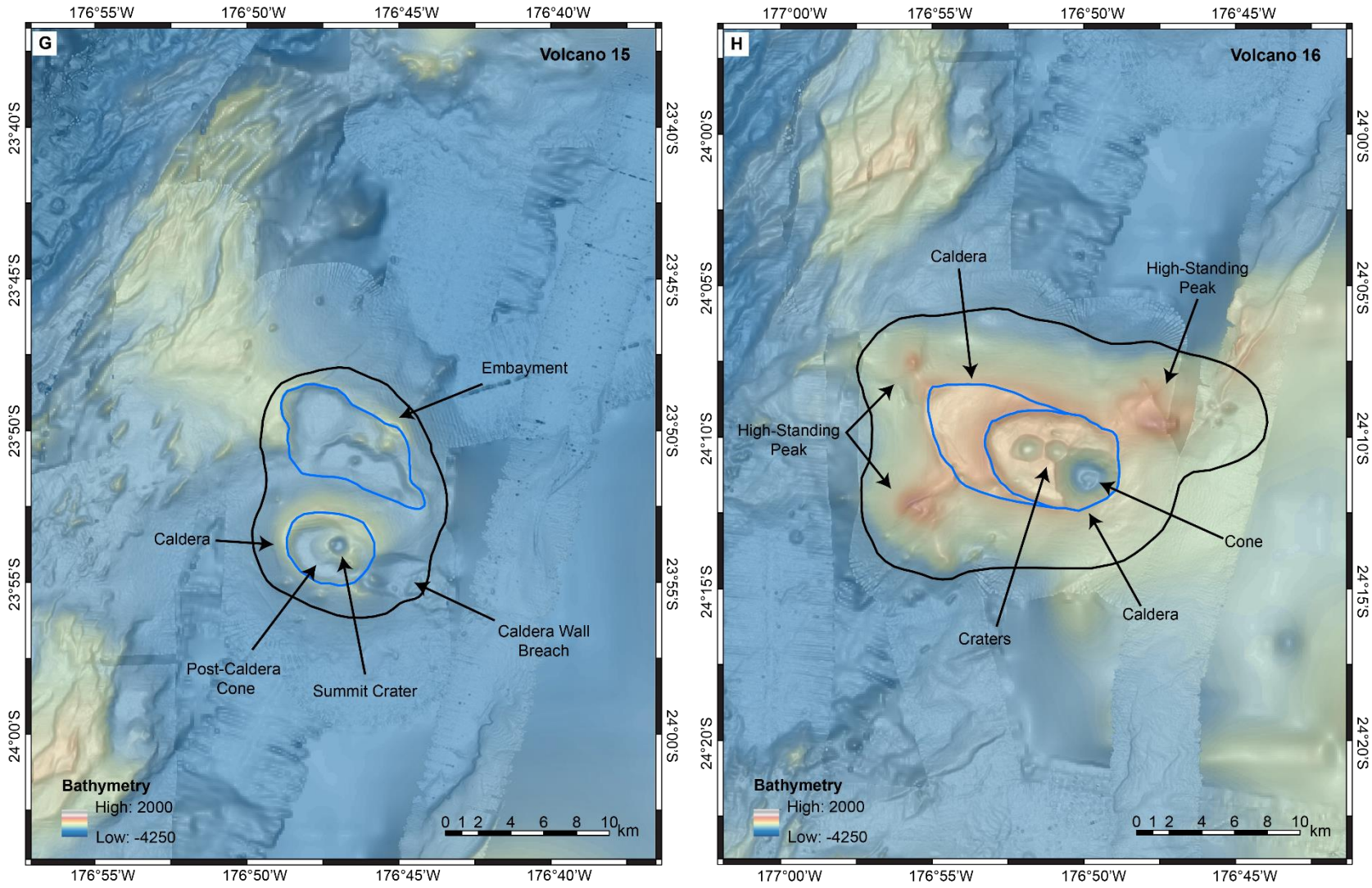
G
Volcano 15
Embayment
Caldera
Caldera Wall Breach
Post-Caldera Cone
Summit Crater
Bathymetry
High: 2000
Low: -4250
0 1 2 4 6 8 10 km
176°55'W
176°50'W
176°45'W
176°40'W
23°40'S
23°45'S
23°50'S
23°55'S
24°00'S
H
Volcano 16
Caldera
High-Standing Peak
High-Standing Peak
Cone
Caldera
Craters
Bathymetry
High: 2000
Low: -4250
0 1 2 4 6 8 10 km
177°00'W
176°55'W
176°50'W
176°45'W
24°00'S
24°05'S
24°10'S
24°15'S
24°20'S

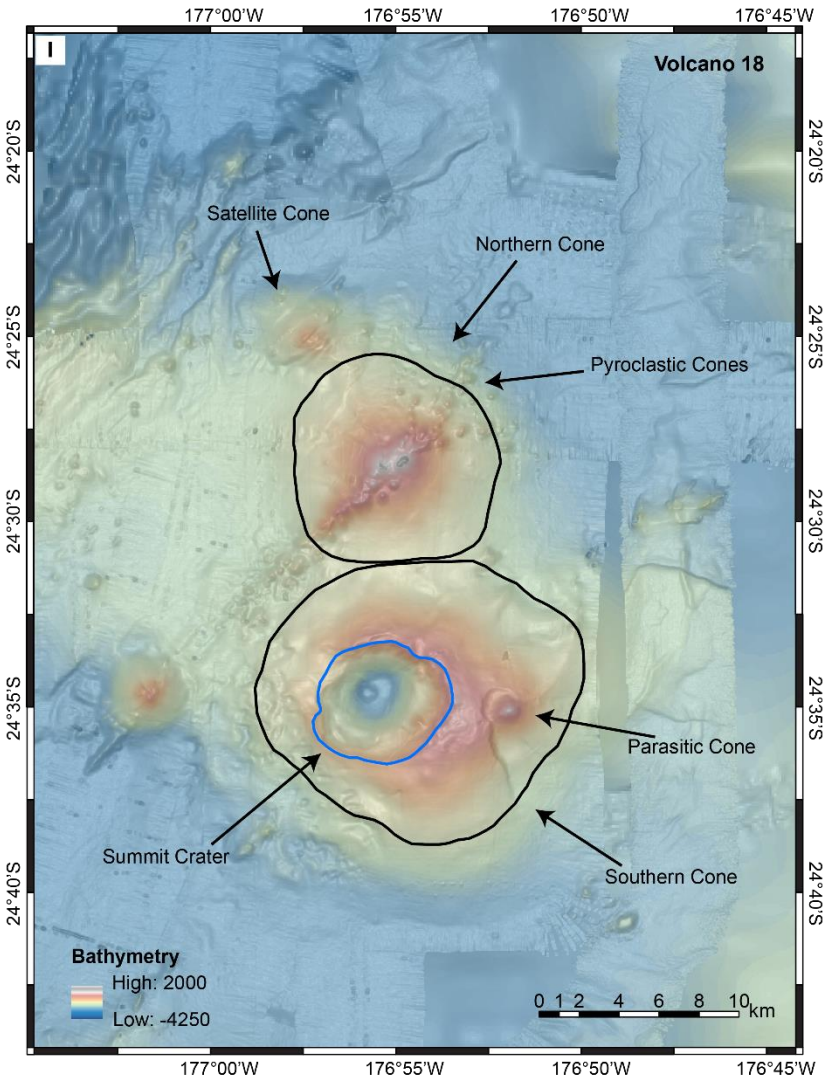
I
Volcano 18
Satellite Cone
Northern Cone
Pyroclastic Cones
Parasitic Cone
Summit Crater
Southern Cone
Bathymetry
High: 2000
Low: -4250
0 1 2 4 6 8 10 km
177°00'W
176°55'W
176°50'W
176°45'W
24°20'S
24°25'S
24°30'S
24°35'S
24°40'S

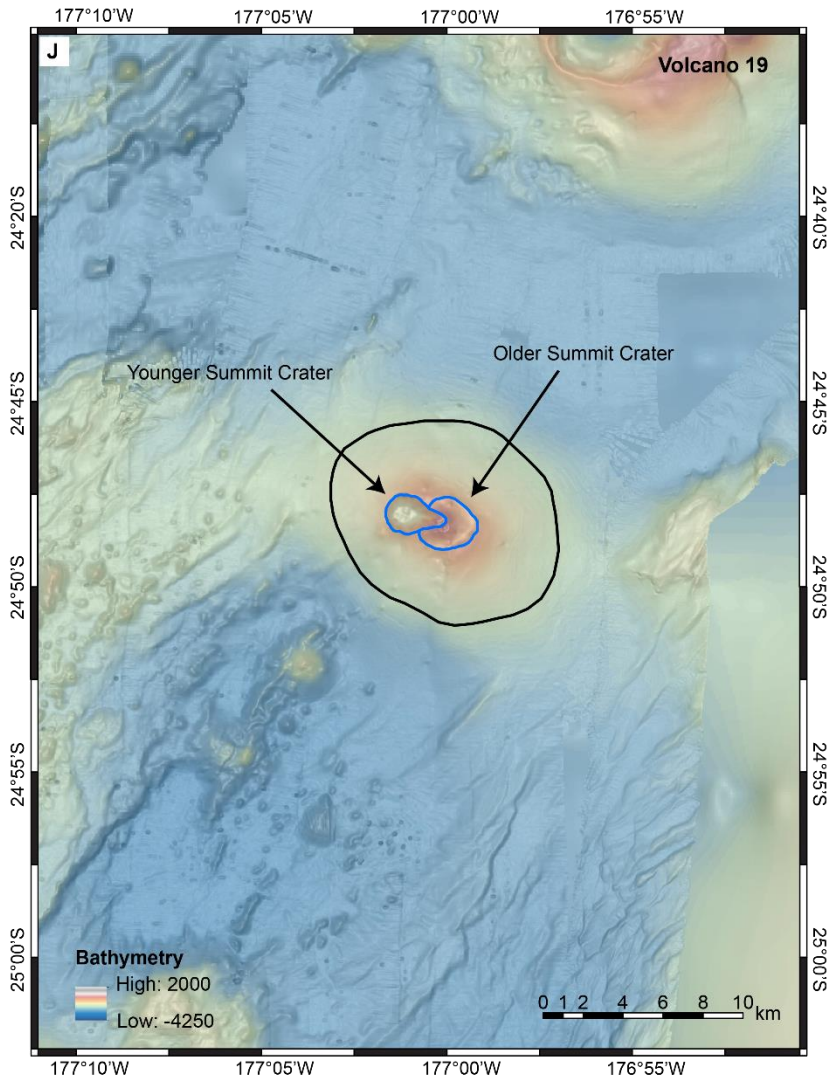
J
Volcano 19
Younger Summit Crater
Older Summit Crater
Bathymetry
High: 2000
Low: -4250
0 1 2 4 6 8 10 km
177°10'W
177°05'W
177°00'W
176°55'W
24°20'S
24°40'S
24°45'S
24°50'S
24°55'S
25°00'S

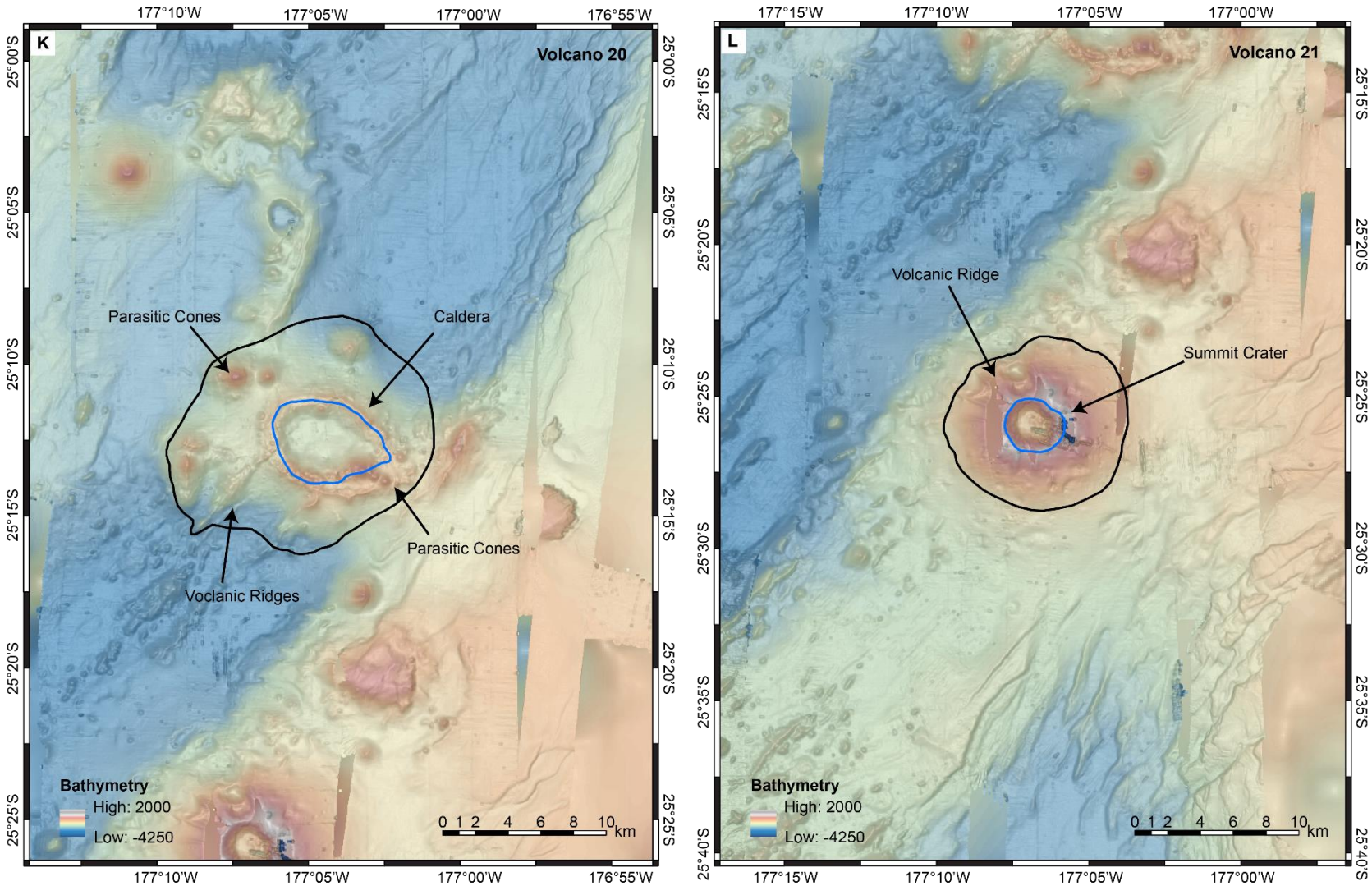
K
Volcano 20
Parasitic Cones
Caldera
Parasitic Cones
Voclanic Ridges
Bathymetry
High: 2000
Low: -4250
0 1 2 4 6 8 10 km
177°10'W
177°05'W
177°00'W
176°55'W
25°00'S
25°05'S
25°10'S
25°15'S
25°20'S
25°25'S
L
Volcano 21
Volcanic Ridge
Summit Crater
Bathymetry
High: 2000
Low: -4250
0 1 2 4 6 8 10 km
177°15'W
177°10'W
177°05'W
177°00'W
25°15'S
25°20'S
25°25'S
25°30'S
25°35'S
25°40'S

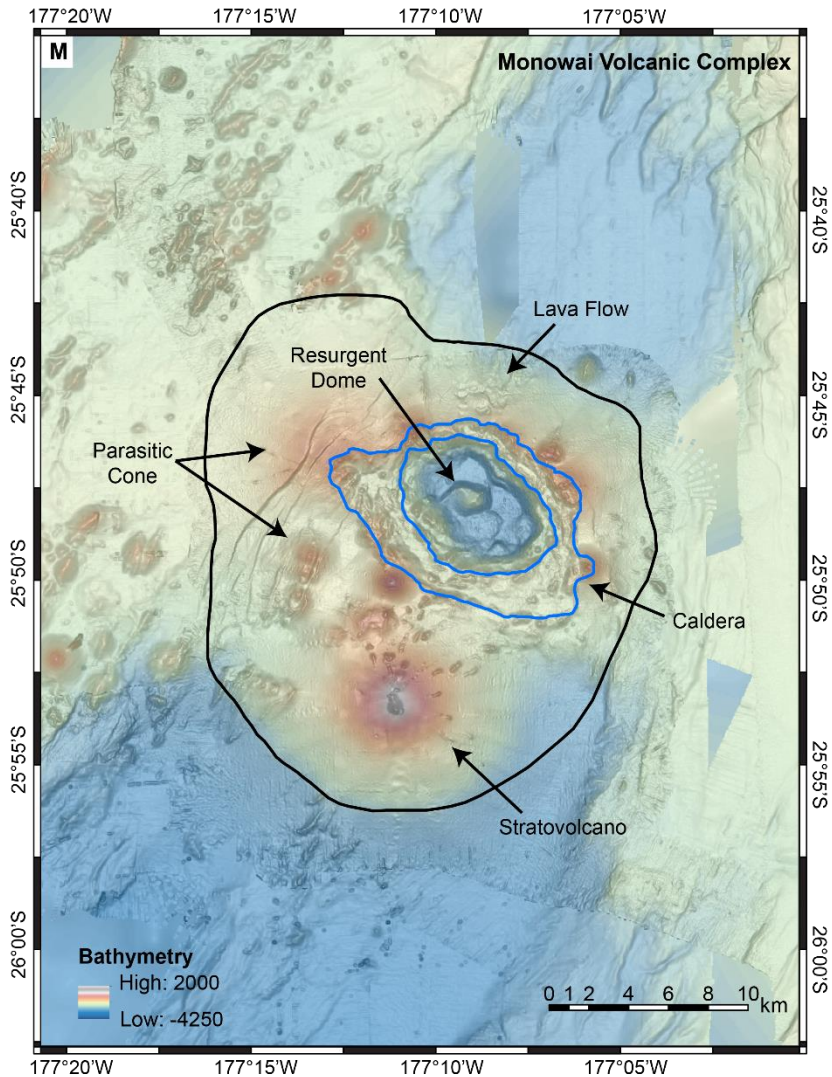

Figure 2.4 Bathymetric maps of individual volcanic centers, combining ship tracks from ship cruises SO-167, SO-192, SO-215 (aboard R/V *Sonne*), and TN-309 (aboard R/V *Thomas G. Thompson*) combined with GMRT datasets. (a) Volcano 1-2, (b) Volcano 3,

(c) Volcano 4-6, (d) Volcano 7, (e) Volcano 8, (f) Volcano 14, (g) Volcano 15, (h) Volcano 16, (i) Volcano 18, (j) Volcano 19, (k) Volcano 20, (l) Volcano 21, and (m) Monowai. Black shapes show the boundaries used for the area and volume calculations of the volcanic centers. Blue shapes show the boundaries used for the volume calculation of the calderas and craters. Area and volumes shown in Table 2.4.

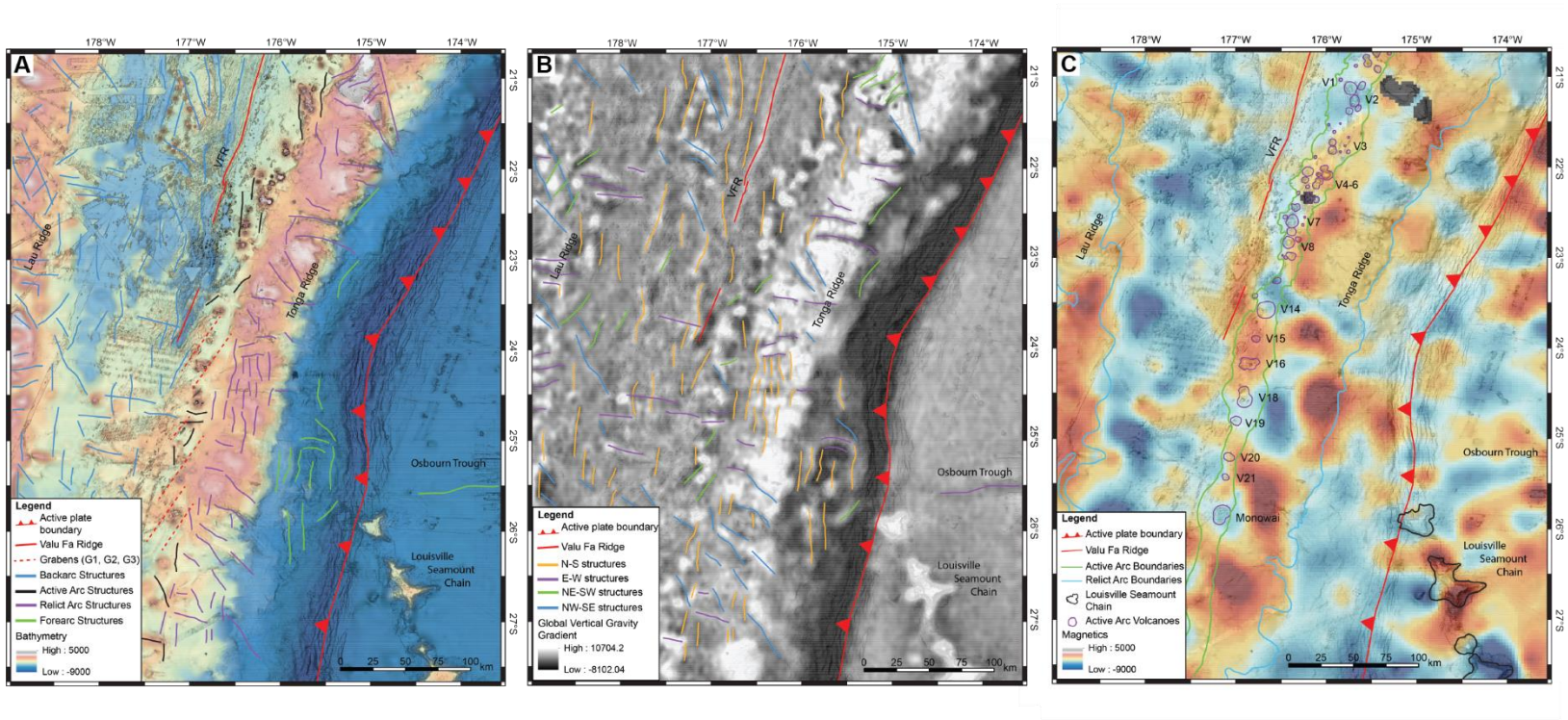

Figure 2.5 Regional map of lineaments in the central portion of the Lau Basin. (a) Lineaments classified according to orientation, interpreted from the vertical gravity gradient (VGG). (b) Classified lineament types overlain on the VGG (50% transparency) (Sandwell et al., 2014) overlain the hill-shaded bathymetry. (c) 2-arc minute resolution Earth Magnetic Anomaly Grid (50% transparency) (Maus et al., 2009) overlain hill-shaded bathymetry showing the boundaries of the arc, back-arc, and forearc crust.

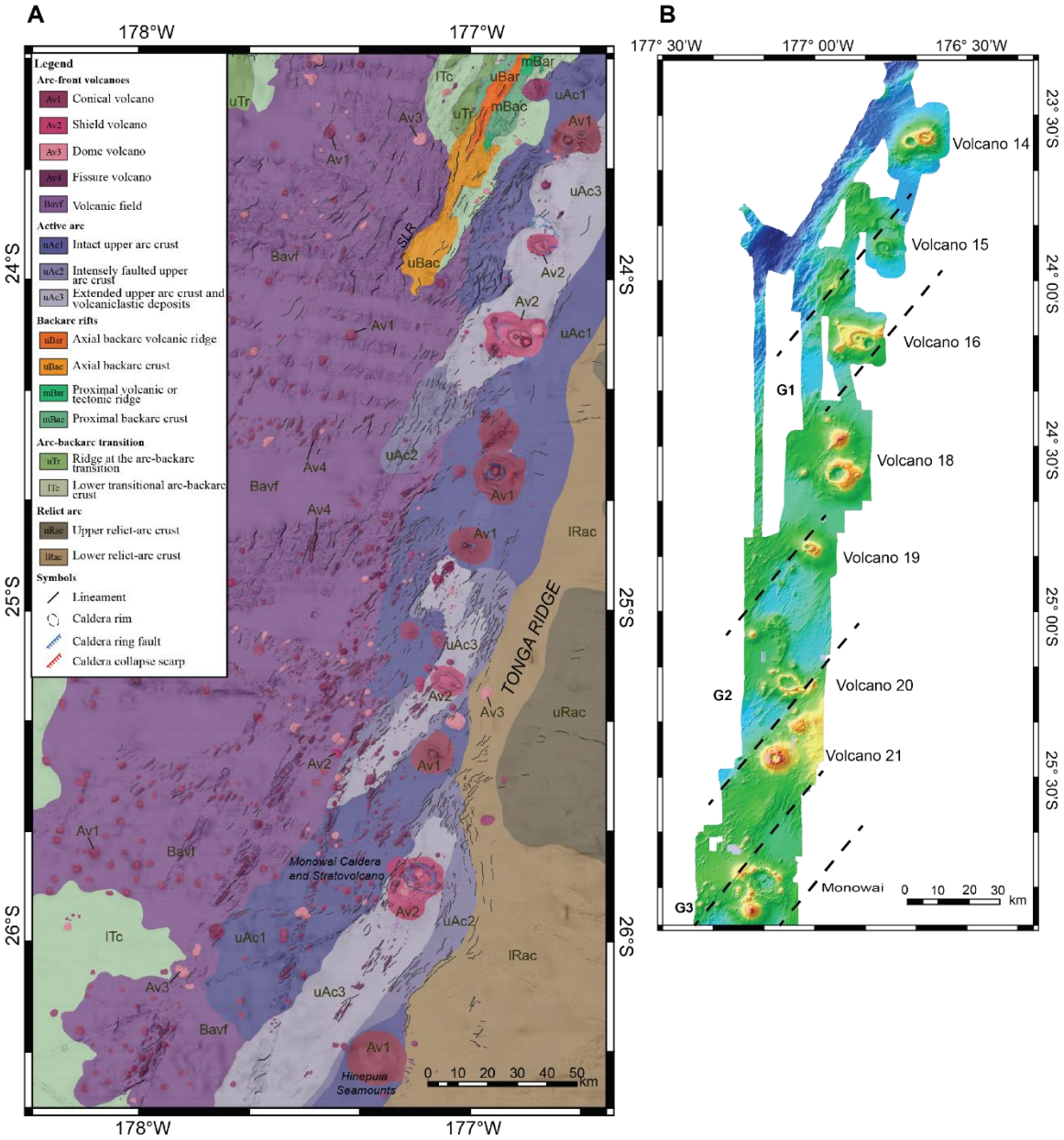

Figure 2.6 (a) Portion of the 1:250,000 geological map of the Louisville and Monowai segments (this study). (b) Bathymetric map of the Monowai and Louisville segment from SO-192 (R/V *Sonne*) research cruise (Schwarz-Schampera et al., 2007). The grabens (1-3) are labelled with their boundaries noted by dashed lines.

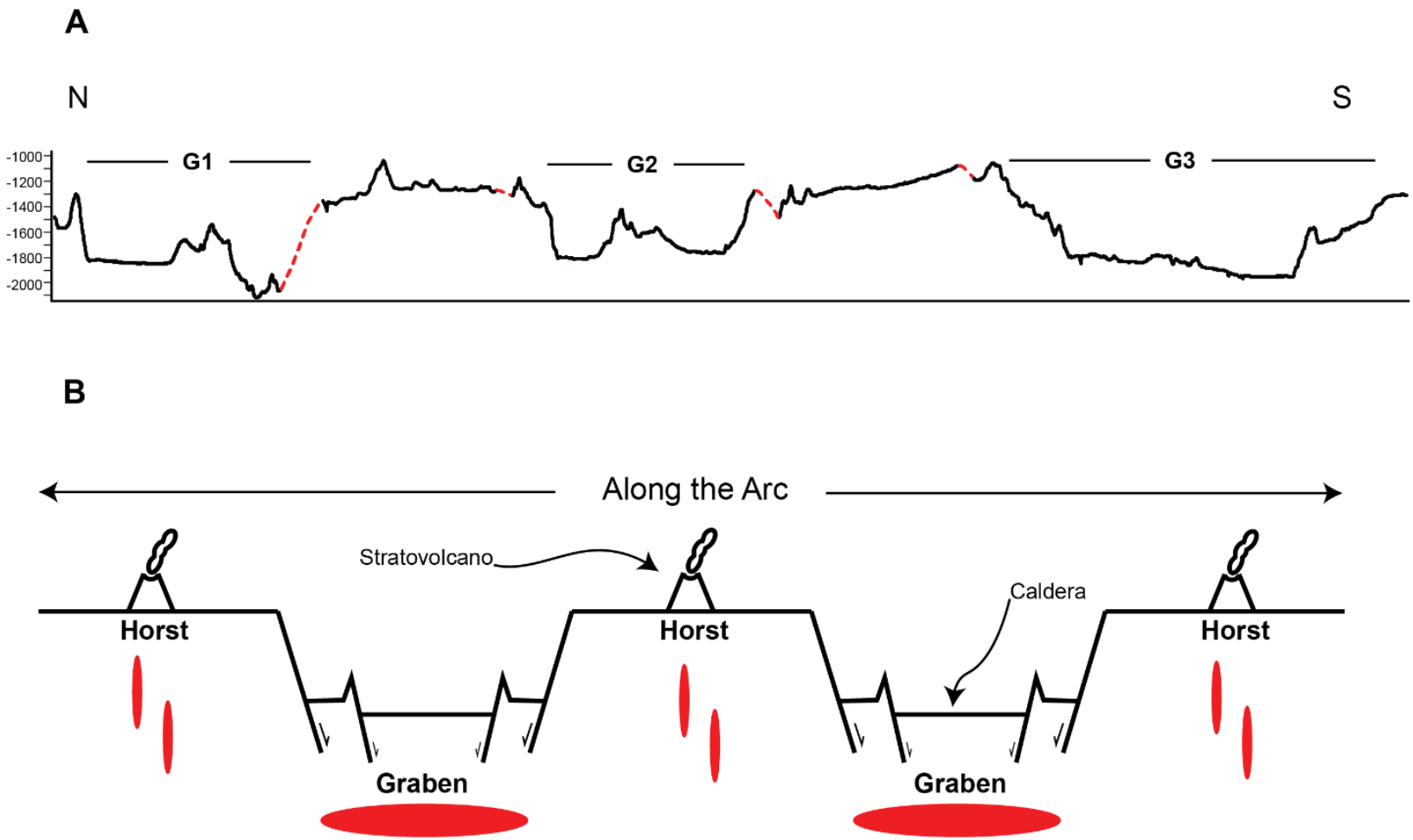

Figure 2.7 (a) Longitudinal profile through the "horst and graben" structures of the Louisville and Monowai segments of the Tonga Arc. Location of profiles are shown on Figure 2.3. Portions are inferred in order to link the profiles (red dashed lines). (b) Schematic illustration showing the cone volcanoes located on the "horst" blocks and larger caldera systems within the grabens.

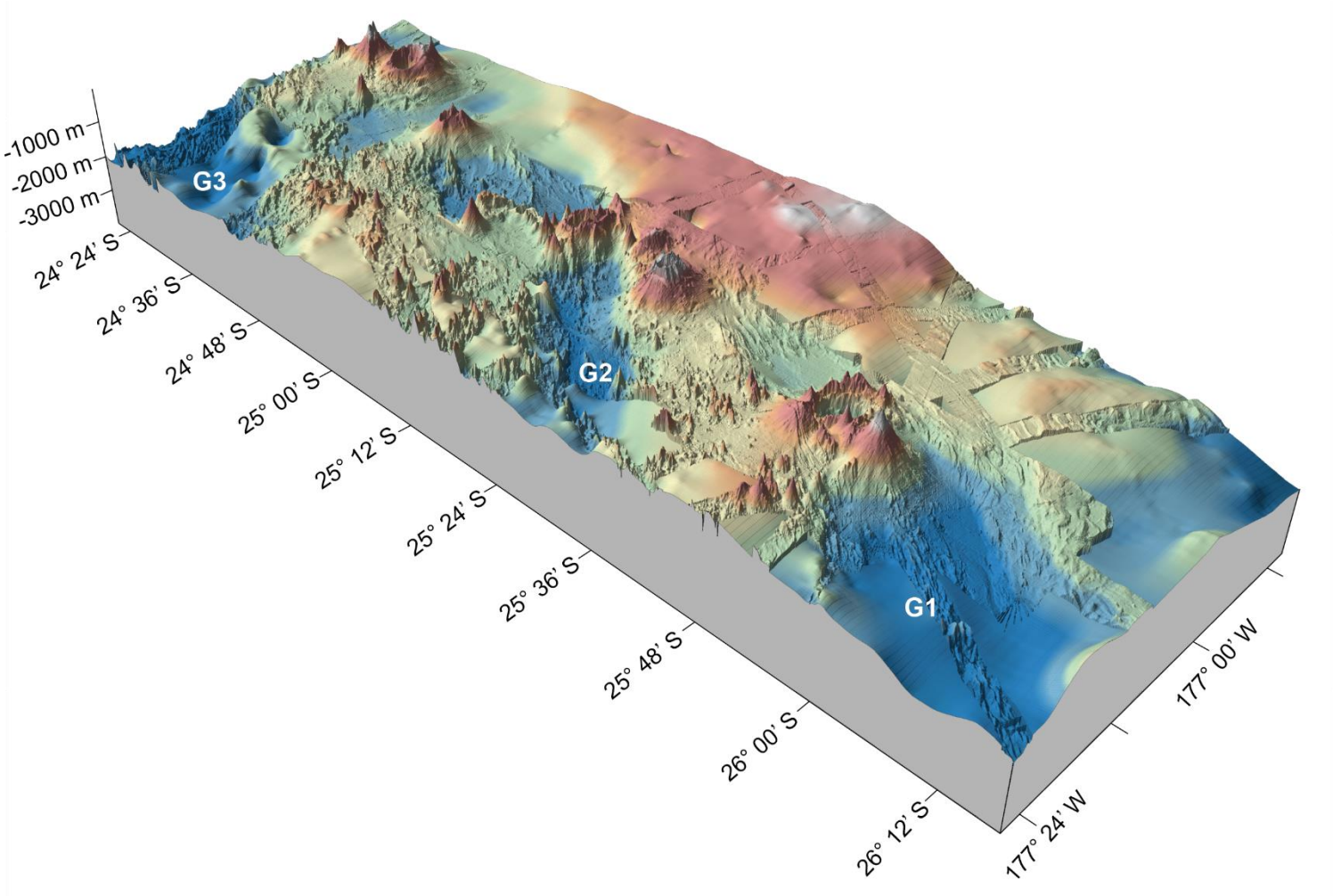

Figure 2.8 3D block model of the bathymetry covering the Louisville and Monowai Segments map area, illustrating the presence of the graben structures (G1-3). The region contains ship tracks from ship cruises SO-167, SO-192, SO-215 (aboard R/V *Sonne*), and TN-309 (aboard R/V *Thomas G. Thompson*) combined with GMRT datasets with a vertical exaggeration.

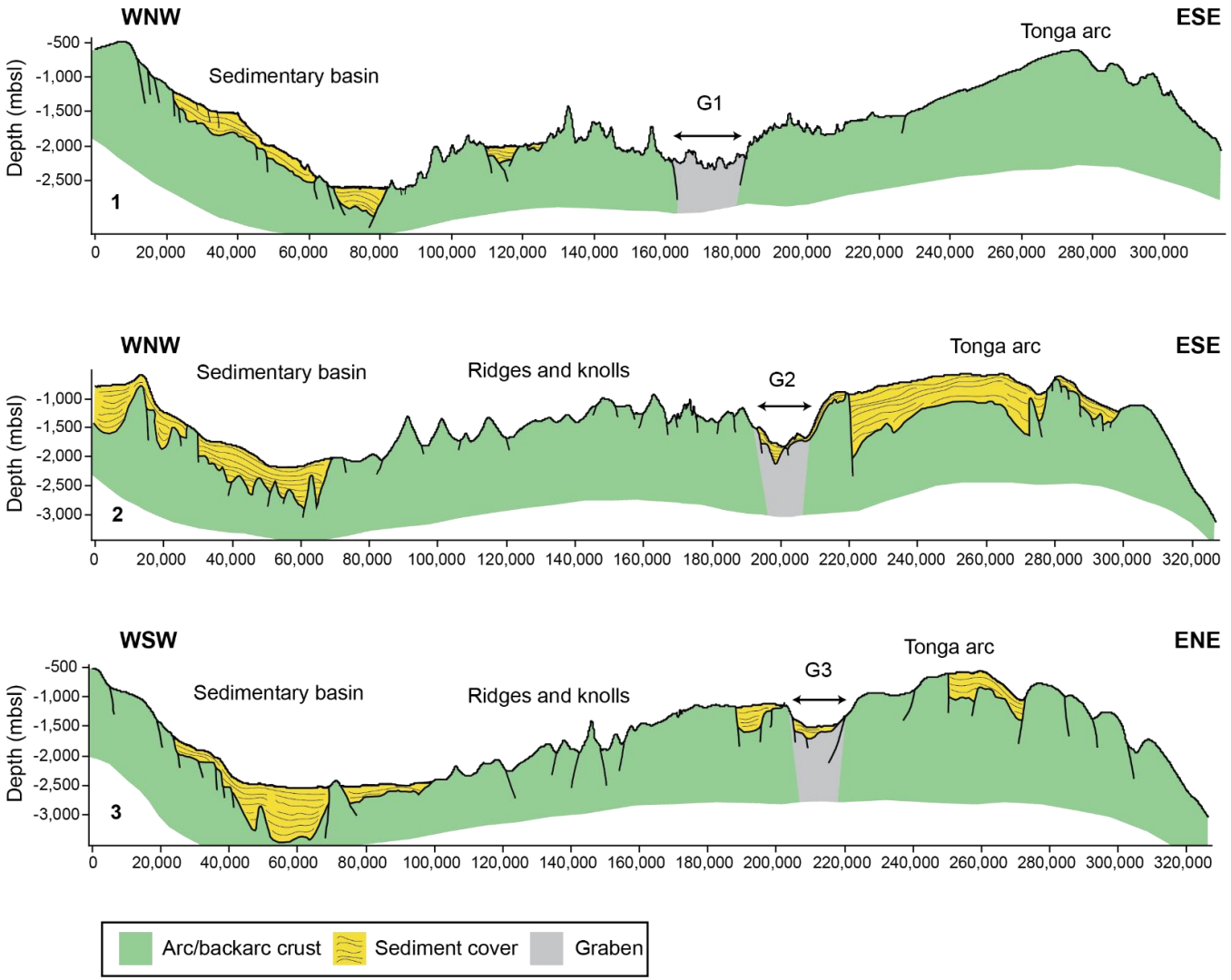

Figure 2.9 Interpretations of 2D seismic profiles crossing the Louisville and Monowai segments of the Tonga Arc (modified from Ruellan et al. 2003). The locations of the profiles are shown in Figure 2.3. Grabens G1-3 have a left-stepping offset from south to

north as seen in Figure 2.5a. Note: the sections do not include volcanoes at the arc front and cross the extensions of the grabens slightly behind the arc.

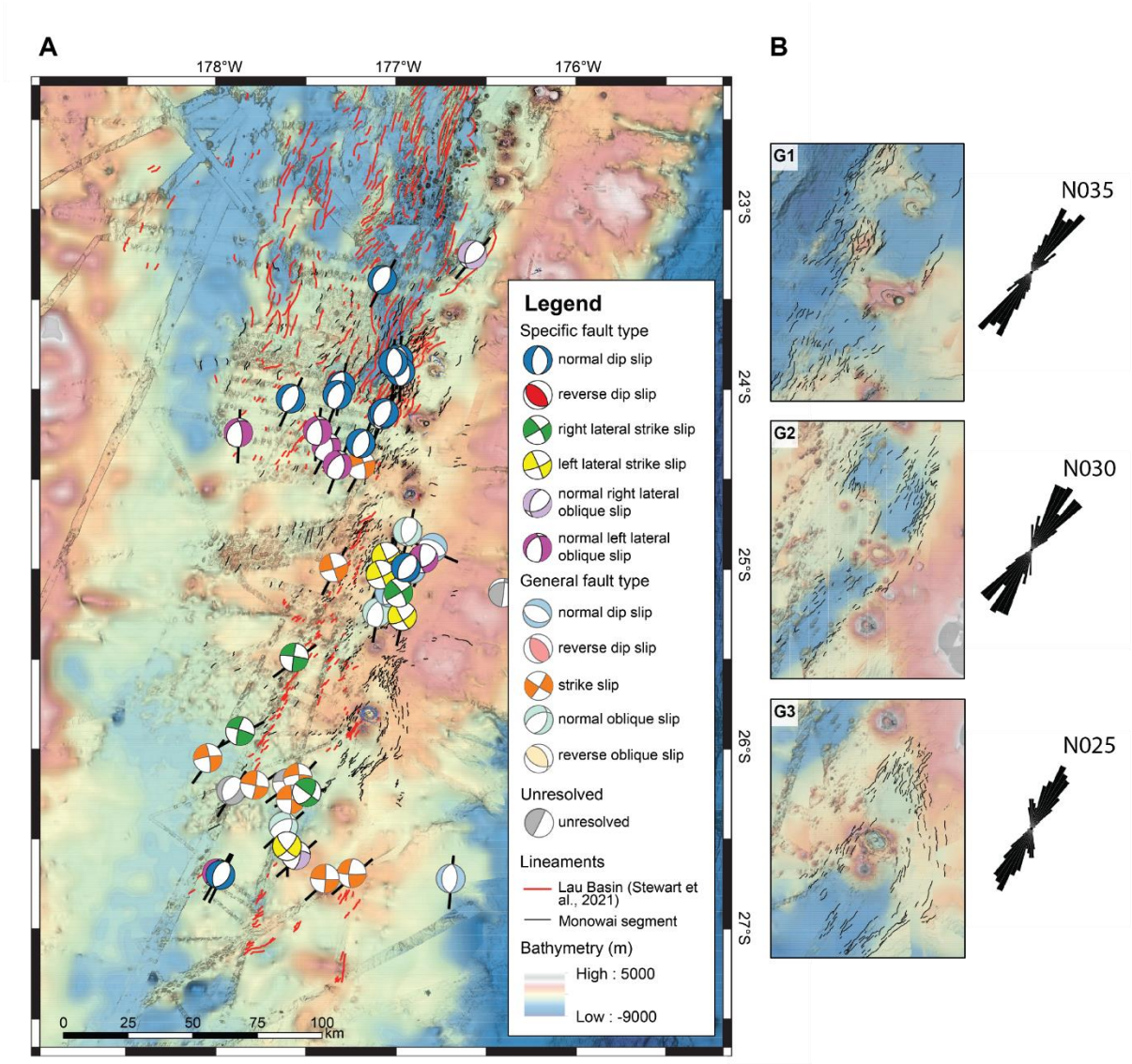

Figure 2.10 (a) Map of a portion of the Louisville and Monowai segments showing the locations of 97 earthquake epicenters and their corresponding centroid moment tensors (CMTs) from the Global Centroid Moment Tensor (GCMT) open-source project (Dziewonski et al., 1981; Ekström et al., 2012). The compression quadrants of the CMTs are colour coded according to the fault types in the key (modified from Baxter et al. 2020), using the higher resolution of mapped lineaments in this study. The CMTs and the S_{Hmax} (short black lines) were plotted using the ArcBeachball tool (v.2.2). The CMT catalogue of shallow telesiemic events shows clear evidence of strike-slip and extensional faults crossing the arc front centered on G2 south of the VFR. (b) Rose diagrams of the lineaments mapped at grabens G1-3 shown in the bathymetric map of each graben. The dominant faulting orientation (035-045°) is the same in each graben. Grabens 2 and 3 also show a secondary faulting direction of N-S.

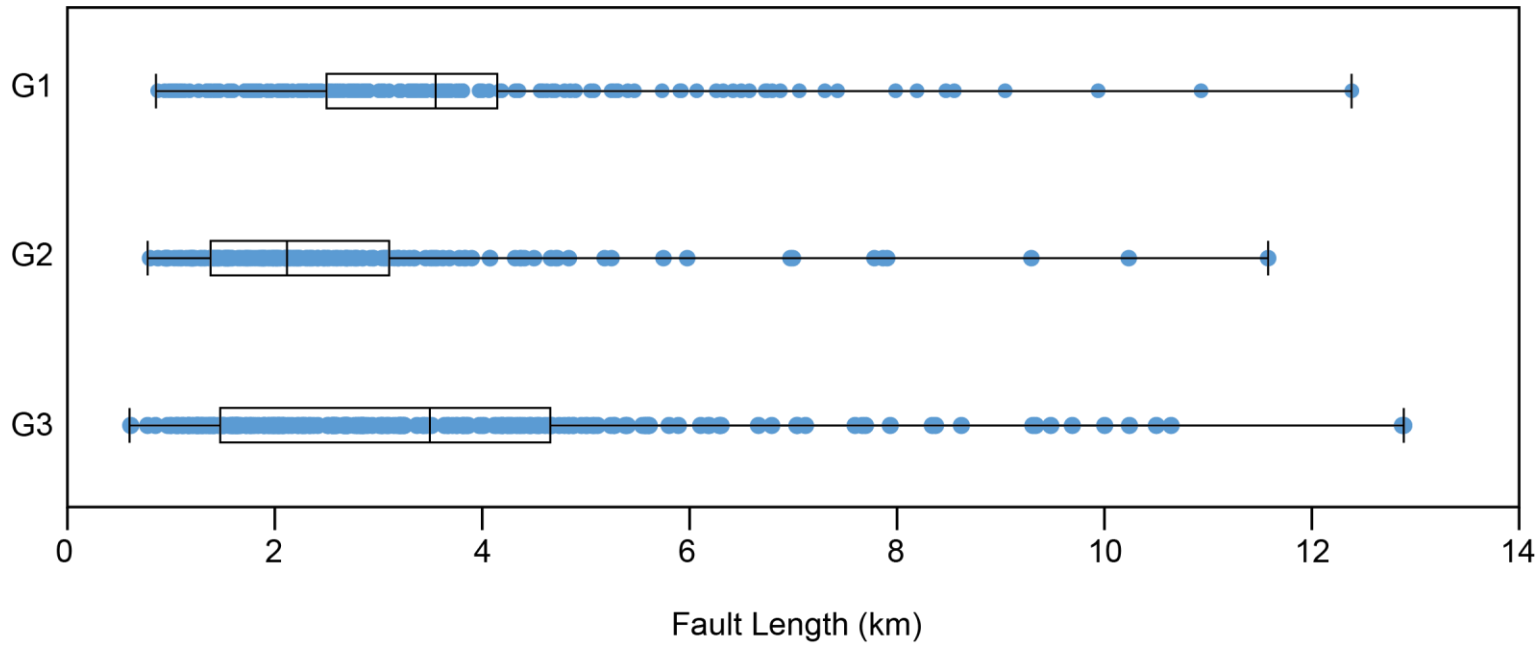

Figure 2.11 Fault strike lengths for all mapped faults in each graben (1-3). The most continuous faulting is present in the Monowai Graben (G3), with the longest fault of 13 km and a greater number of faults over 8 km in length compared to the other two grabens.

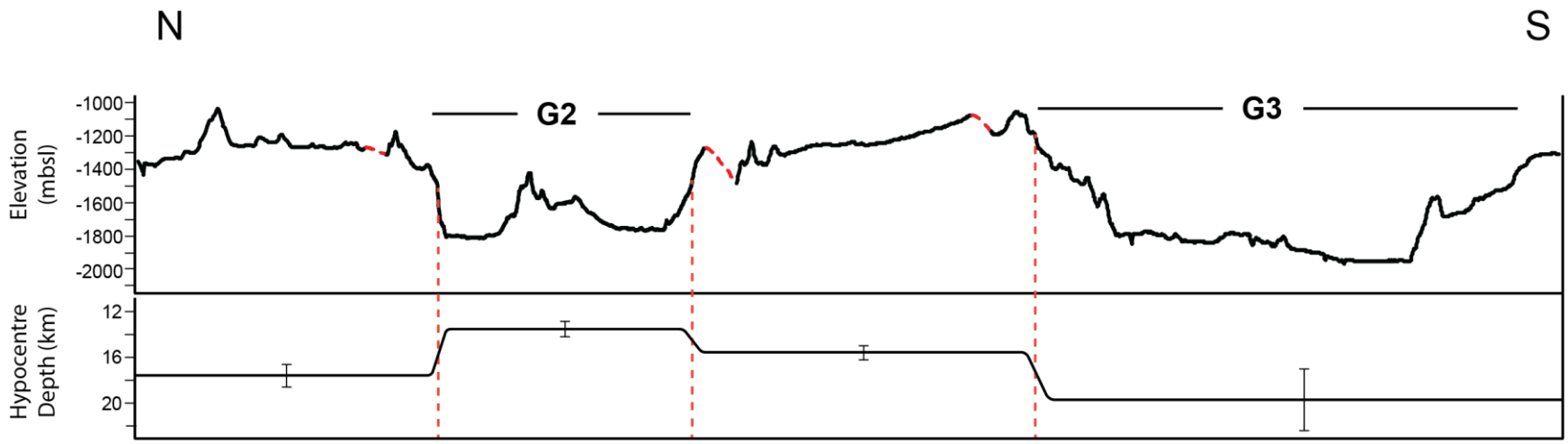

Figure 2.12 Schematic cross-section showing the average depths of hypocenters for earthquakes within the grabens 2 and 3 and the adjacent horsts in the study area. Average depth errors are shown as bars for each division. Depths are sourced from the complementary data for corresponding centroid moment tensors (CMTs) data from the Global Centroid Moment Tensor (GCMT) open-source project (Dziewonski et al., 1981; Ekström et al., 2012) (shown in Figure 2.10).

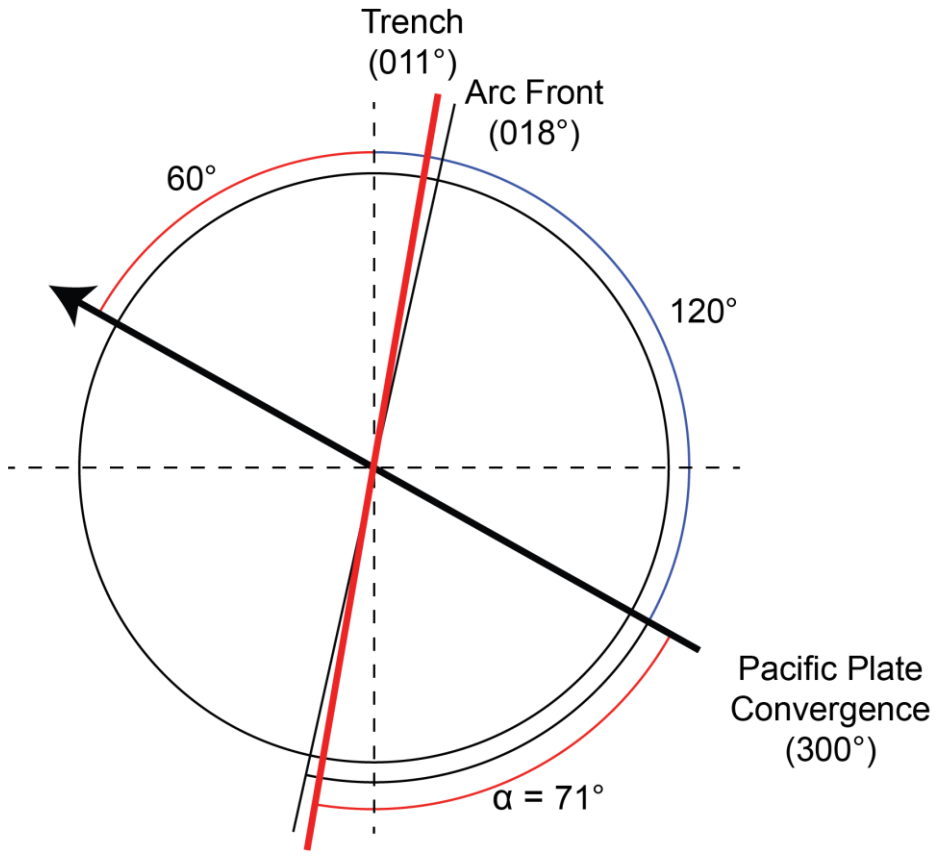

Figure 2.13 Vector diagram showing the angle of obliquity (α) between the Pacific Plate convergence (azimuth 300°) and the trench (azimuth 011°). We determine an obliquity of 71°. Similarly, between the Pacific Plate convergence and the arc front (018°) we determine an obliquity of 78°. The arc front orientation is represented by the black line and the trench orientation by the thick red line.

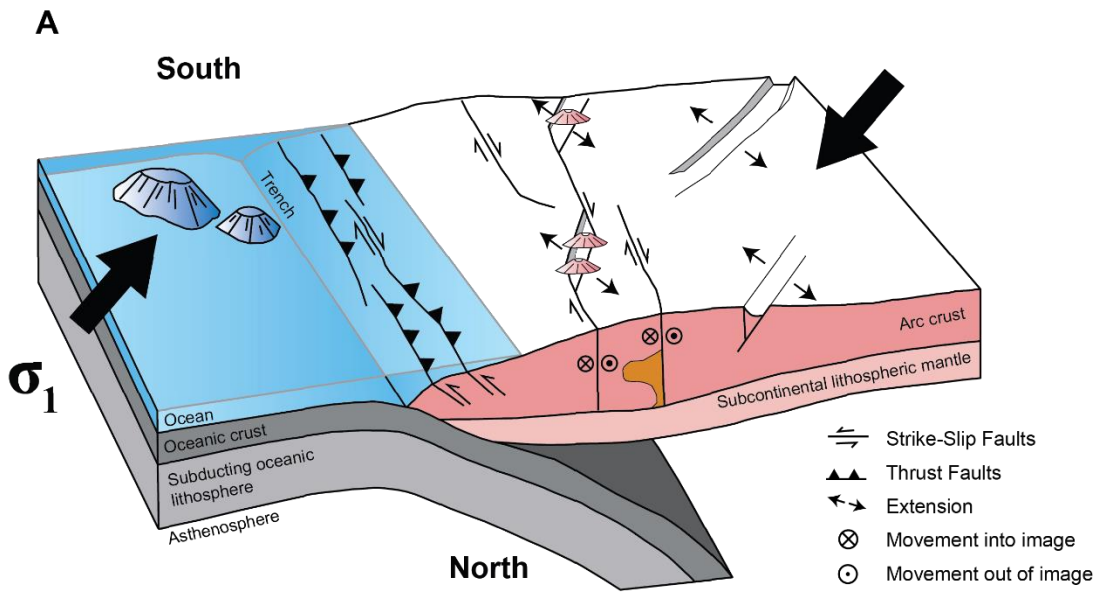

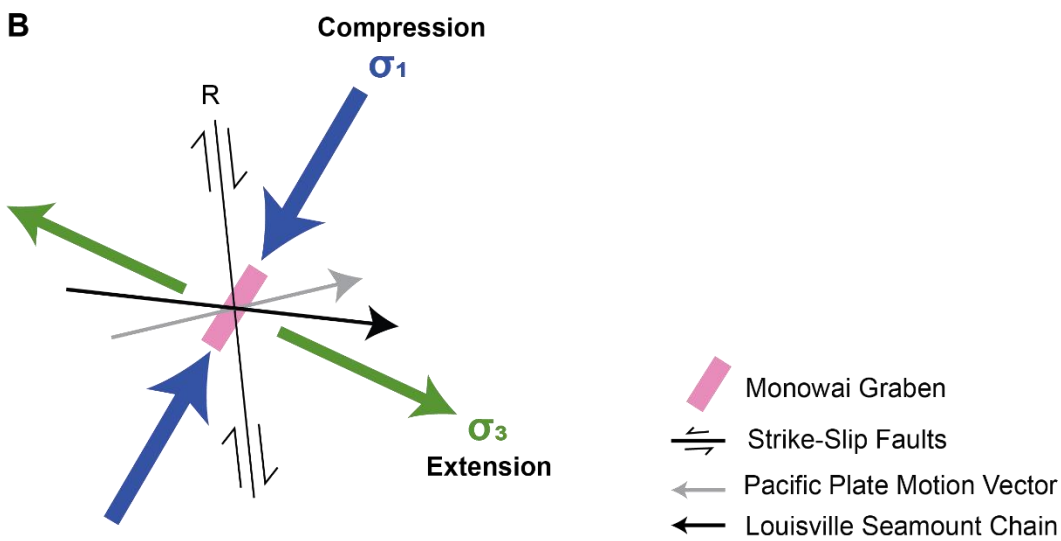

Figure 2.14 (a) Schematic illustration of the Pacific Plate subducting obliquely under the Tonga trench (looking south) (modified from Rhys et al., 2020). The subduction of the LSC is thought to have weakened the basement and influenced the extension in the Louisville segment. Extensional features (horsts and grabens) cross the arc and continue into the back-arc region, localizing arc magmas. (b) Model of the principal stresses caused by the oblique subduction and collision with the LSC, showing the opening of the Monowai Graben. Strike-slip faults present in the region are acting as Riedel shears.

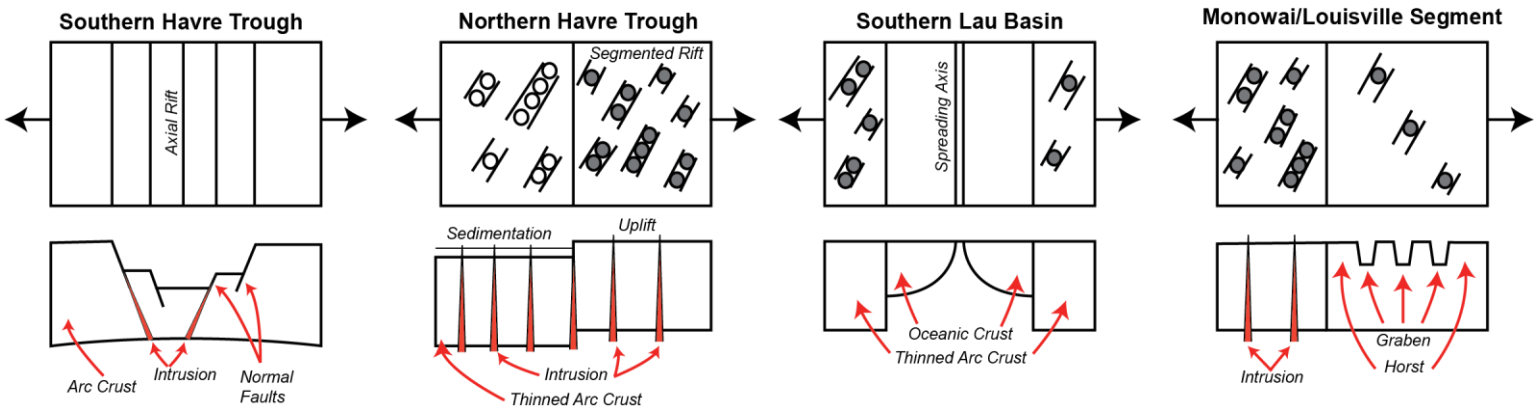

Figure 2.15 Schematic illustration of the rifting and spreading in different parts of the Havre Trough and southern Lau Basin (first three panels modified after Fujiwara et al., 2001; Monowai/Louisville from this study). The southern Havre Trough is thought to be in an early stage of rifting. The northern Havre Trough is dominated by volcanic ridges and knolls. Spreading is first established within the thinned crust of the Valu Fa Ridge in the Southern Lau Basin. At the Louisville and Monowai segments, extension results in the development of grabens and horsts in the rifting arc crust.

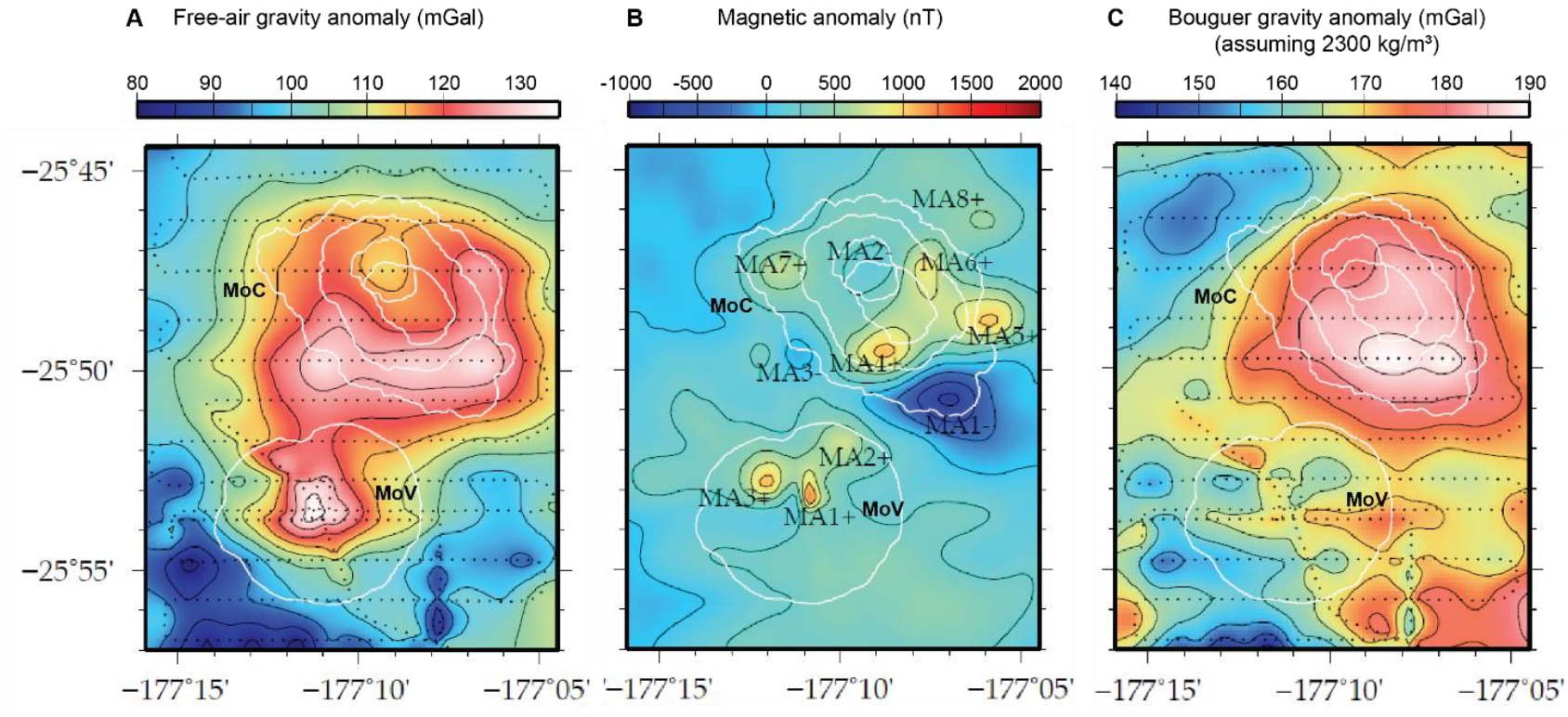

Figure 2.16 Potential field data at the Monowai volcanic center (modified from Paulatto et al., 2014). (a) Free-air gravity anomaly from the 2011 survey (SO-215; Peirce and Watts, 2011). A broad gravity anomaly high surrounds the Monowai volcanic complex, with local gravity anomaly highs at the Monowai cone and the Monowai caldera rim. A relative gravity anomaly low is present at the caldera floor. (b) Magnetic anomaly from the 2011 survey (SO-215; Peirce and Watts, 2011). The magnetic anomaly data shows a variation from -800 to +1400 nT across the complex. A strong magnetic anomaly high is present at the summit of the Monowai cone (+1432 nT) as well as multiple magnetic anomaly highs at the southeast portion of the caldera. (c) Bouguer anomaly calculated using an assumed rock density of 2300 kg m^{-3}. Over the Monowai volcanic center, a lack of significant Bouguer anomaly is present at the Monowai cone, however a Bouguer anomaly high occurs over the Monowai caldera and a Bouguer anomaly low is present to the

northwest of the caldera, where the region is highly faulted. The white lines show the location of the Monowai cone (MoV) and the Monowai caldera (MoC).

Table 2.1 Research cruises on the Louisville and Monowai Segments, Tonga Arc

Cruise ID[a]	Vessel	Year	Operations	References
SO-135	R/V *Sonne*	1998	Multibeam survey, magnetics, parasound, seismic reflection, sampling	Stoffers et al., 1999a; Wright et al., 2008; Haase et al., 2002
SO-167	R/V *Sonne*	2002	Multibeam survey, dredge sampling	Stoffers et al., 2002
NZAPLUME III	R/V *Tangaroa*	2004	PLUme mapping, dredge sampling	de Ronde et al., 2006; Graham et al., 2008
SITKAP	R/V *Ka'imikai-O-Kanaloa* (K-O-K)	2005	PISCES IV	Stoffers et al., 2006b
NZASRoF	R/V *Ka'imikai-O-Kanaloa* (K-O-K)	2005	PISCES V, sampling	Embley et al., 2005
SO-192 (MANGO)	R/V *Sonne*	2007	ROPOS, sampling	Schwarz-Schampera et al., 2007; Chadwick et al., 2008
SO-195a (TOTAL)	R/V *Sonne*	2008	Seismic refraction, swath bathymetry, gravity, magnetics	Grevemeyer and Flüh, 2008; Contreras-Reyes et al., 2011
SO-215	R/V *Sonne*	2011	Seismic, gravity, magnetics, swath bathymetry	Peirce and Watts, 2011; Watts et al., 2012

[a] See Appendix A for location maps of the listed cruises.

Table 2.2 Volcanoes of the Louisville and Monowai segments of the Arc Front, Tonga Arc

Volcano	Latitude (S)	Longitude (W)	Volcanic Edifice Type	Cruise ID[a]
Volcano 1	21°09’	175°45’	Cone with a summit caldera	SO-167 SITKAP SO-192
Volcano 2	21°18’	175°42’	Two cones, one with a summit crater	SO-167
Volcano 3	21°39’ to 21°53’	175°52’ to 176°00’	Two cones, one with a summit crater	SO-167
Volcano 4-6	21°56’ to 22°27’	175°55’ to 176°21’	Cluster of cones belonging to the 'Ata Volcanic Complex	SO-167
Volcano 7	22°31’ to 22°46’	176°18’ to 176°28’	Complex of multiple stratovolcanoes	SO-167
Volcano 8	22°51’	176°25’	Known as Pelorus Volcano, stratocone	SO-167
Volcano 14	23°34’	176°41’	Two cones, one with a summit crater	SO-167
Volcano 15 (caldera)	23°52’	176°46’	Cone with a summit caldera	SO-167
Volcano 16 (caldera)	24° 11’	176° 52’	Nested calderas	SO-167
Volcano 18	24°29’ and 24°35’	176°55’ and 76°54’	Two cones, one with a summit crater; the other a distinct line of pyroclastic cones	SO-167 SITKAP
Volcano 19	24°48’	177°01’	Cone with a summit crater	SO-167 SITKAP SO-192
Volcano 20 (caldera)	25°12’	177°05’	Caldera volcano	SO-167 NZAPLUME III
Volcano 21	25°25’	177°05'	Cone with a summit crater	SO-167 NZAPLUME III SO-192
Monowai Seamount (cone)	25°53’	177°11'	Large stratovolcano	SO-135 NZASRoF SO-192 SO-215
Monowai (caldera)	25°50’	177°10'	Caldera complex	NZAPLUME III NZASRoF SO-192 SO-215

[a] See Table 2.1 for refences to the listed cruises.

Table 2.3 Geological formations of the Louisville and Monowai segments, Tonga Arc

	Crustal Type	**Crustal Abbreviation**	**Area[a] (km^2)**	**Percentage of Total Area (%)**
Arc-Front Volcanoes	Volcanic field	Bavf	25,426.08	42.6
Active Arc	Intact upper arc crust	uAc1	8,387.41	14.1
	Intensely faulted upper arc crust	uAc2	1,862.42	3.1
	Extended upper arc crust and volcaniclastic deposits	uAc3	4,921.55	8.2
Backarc Rifts	Axial backarc volcanic ridge	uBar	138.93	0.2
	Axial backarc crust	uBac	496.28	0.8
	Proximal volcanic or tectonic ridge	mBar	48.90	0.08
	Proximal backarc crust	mBac	192.30	0.3
Arc-Backarc Transition	Ridge at the arc-backarc transition	uTr	410.49	0.7
	Lower transitional arc-backarc crust	lTc	9,198.58	15.4
Relict Arc	Upper relict-arc crust	uRac	2,045.78	3.4
	Lower relict-arc crust	lRac	6,538.53	11.0
		Total:	**59,667.24**	

[a] Areas are determined using Surface Area functions of each polygon in ArcGIS software. Boundaries used are those indicated for the formations in the Geological Map of the Louisville and Monowai Segments (Figure 2.6).

Table 2.4 Interpreted eruptive volumes of volcanoes of the Louisville and Monowai segments of the Tonga Arc

Volcanic Edifice	Volcano Type	Volcano Volume[a] (km^3)	Caldera Volume (km^3)	Total Volume (km^3)	Percentage of the Magmatic Budget (%)
Volcano 14	Cone	77	5	82	8.2
Volcano 15	Caldera	36	15.4	51.4	5.2
Volcano 16	Caldera	146	13	159	15.9
Volcano 18 N Cone	Cone	26	N/A	26	2.6
Volcano 18 S Cone	Cone	99	17	116	11.6
Volcano 19	Cone	25	2.3	27.3	2.7
Volcano 20	Caldera	83	12	95	9.5
Volcano 21[b]	Cone	27	3.5	30.5	3.1
Monowai	Caldera	229[c]	46	275	27.6
Volcano T[d]	Cone	135	N/A	135	13.5
			Total Magmatic Budget:	**997.2**	

[a] Volumes of the volcanoes are determined using the polygon volume function in ArcGIS software which calculates the volume above a minimum elevation value (Zmin), using boundaries shown in Figure 2.4.

[b] The Zmin was needed to be manually refined for Volcano 21 to remove processing artifacts from the volume calculation.

[c] The Monowai Volcanic Edifice volume is comprised of multiple parasitic cones (P1-9 = 9.9 km^3), the resurgent dome on the caldera floor (MoR = 0.5 km^3), the Monowai volcano (MoV = 13.8 km^3) and a large inflation zone (204.8 km^3). The boundaries of these structures are shown in Figure 3.13.

[d] Volcano T lacks high-resolution ship-track bathymetry, so the GMRT dataset was used to calculate volume values, resulting in possible error due to the coarseness of the GMRT dataset.

Chapter 3

Caldera Volcanoes of the Southern Tonga Arc and Related Submarine Hydrothermal Systems

3.1 Introduction

Submarine volcanoes at intraoceanic volcanic arcs vary from composite cones to large caldera volcanoes occupying areas of up to 30 km in diameter and with collapsed calderas up to 15 km wide (Wright et al., 2002; Wormald et al., 2012). Most are simple "cone volcanoes", with heights of 1 to 2 km above the surrounding sea floor. About 1/3 of the cone volcanoes have summit craters that may be several kilometers in diameter and up to ~500 m deep. Most occur at relatively shallow water depths (95% are less than 1600 m deep:) (de Ronde et al., 2003; Hannington et al., 2005). A majority of the cone volcanoes are volcanically active, with fresh lavas, well-preserved sediment-free summit calderas, and steep slump-free crater walls. Cones that lack a summit crater commonly have a thick carapace of permeable volcanic breccias and tephra. Explosive crater-forming eruptions are common, at least to depths of 1500 mbsl, evidenced by pyroclastic rocks exposed in the caldera and crater walls (including rhyolite and dacite), large tuff rings, and in the case of recent eruptions by the formation of pumice rafts at the sea surface (e.g., Fiske et al., 2001; Smith et al., 2003; Stoffers et al., 2002, 2006a and b; Brandl et al., 2020). The largest structures at the arc front are the "caldera volcanoes". The calderas are commonly the deepest points along the arc front. They often contain distinctive post-caldera lava domes, indicating the presence of shallow magma. Flow sequences are common with intervening volcaniclastic deposits exposed in the caldera walls. The two types of volcanoes contrast with volcanoes on mid-ocean ridges (MORs), which are characterized by effusive basaltic fissure eruptions and monogenetic cones, including hummocky volcanoes, pillow volcanoes, large flat-topped volcanoes, and shield volcanoes with very few pyroclastic eruptions (Devey et al.; 2010; Yeo et al., 2016).

Much of the research on submarine arc volcanoes has focused on the large stratovolcanoes at the arc front, which show significant magmatic (especially degassing) activity. The associated arc volcanism is mainly a result of partial melting caused by the addition of H_2O and other volatiles

to the sub-arc mantle from the downgoing slab. The melts are mostly basaltic and tholeiitic (Stern and Bloomer, 1992; Pearce and Peate, 1995), becoming more andesitic and calc-alkaline as the arc crust thickens and the depth and extent of fractionation of the magmas increases (Pearce and Stern, 2006). The larger and deeper caldera volcanoes are associated with melting caused by extension and rifting of the arc basement, in some cases thought to be associated with mantle upwelling beneath the arc (e.g., Taylor et al., 1991; Contreras-Reyes et al., 2011).

The Tonga-Kermadec arc (Figure 3.1) is host to more than 90 volcanoes along its 2,500 km length from New Zealand to northern Tonga (de Ronde et al., 2003; Hannington et al., 2005). They include the typical cone volcanoes of the volcanic front as well as larger caldera complexes (Wright et al., 2002; Wormald et al., 2012). More than 70% of the volcanic centers along the arc front are hydrothermally active or passively degassing, with numerous hydrothermal systems located in the summit craters and larger calderas (Leybourne et al., 2012; de Ronde et al., 2019). Hydrothermal vent fields in the summit craters of the cone volcanoes are small or ephemeral (e.g., Stoffers et al., 2006a). However, significant hydrothermal systems are known in the much larger caldera volcanoes, where the hydrothermal vents are almost always localized along the caldera walls or on post-caldera domes (Leybourne et al., 2012). The highest-temperature hydrothermal venting is mainly restricted to the largest and deepest calderas, which provide the necessary structural control for focusing hydrothermal fluids and the high pressures to prevent boiling (Hannington et al., 2005).

In this paper, we examine 8 different volcanoes at the active volcanic front of the Tonga Arc between 24°S and 26°S (Figure 3.2): five cone volcanoes (Volcanoes 14, 17, 18, 19, and 21), three of the larger caldera volcanoes (Volcanoes 15, 16, and 20), and the Monowai Volcanic Complex near 26°S. The latter includes one of the largest and deepest submarine calderas in the oceans. Prior to the 2002, a volcanic gap was thought to be present along the arc between the subaerial Hunga volcano (20°34’S) and Monowai. Subsequent bathymetric mapping revealed 27 volcanic centers in the gap, confirming that volcanism is continuous along the arc (Figure 3.3). However, relatively little work has been published on the volcanoes. Volcano 18, Volcano 19, and Volcano 21 have been studied during several cruises (SO-167, SITKAP, and SO-192: Stoffers et al., 2002; Stoffers et al., 2006b; Schwarz-Schampera et al., 2007). During the

SITKAP cruise in 2005, a number of the volcanoes were visited using the PISCES submersibles aboard the R/V *Ka`imikai-O-Kanaloa*. During SO-192/2 in 2007 three of the volcanoes between 21°S (Volcano 1) and 25°S (Volcano 19), as well as the large Monowai Volcanic Complex, were visited with the Canadian remotely-operated vehicle ROPOS. Comprehensive mapping also has been carried out at the Monowai Volcano (Brothers et al., 1980; Davey et al., 1980; Chadwick et al., 2008; Wright et al., 2008; Timm et al., 2011; Leybourne et al., 2012; Watts et al., 2012; Wormald et al., 2012; Paulatto et al., 2014; Metz et al., 2019). This study extends the mapping of Monowai and compares its morphology, surficial deposits, lava flows, and general structure to the other volcanoes at the arc front. Using high-resolution multibeam and the bottom surveys with PISCES IV and V and with ROPOS, we document the main caldera and crater sequences among the different volcano types. We show that the large 400 km^2 Monowai caldera formed mainly in response to NW-SE-directed extension in the Monowai Graben and that the dominant volcanic facies record mainly effusive eruptions related to the rifting and subsidence and a large 2-km diameter resurgent dome. Similar large calderas in graben-like depressions are mapped at Volcanoes 15, 16 and 20. The rift grabens are interpreted to have focused significant volumes of magma into the base of the crust as mainly sill-like intrusions. By contrast, the much smaller cone volcanoes are dominated by fissure eruptions, thick sequences of volcaniclastic deposits and mainly dike-like intrusions. These differences are thought to have important implications for hosting large-scale hydrothermal systems among the caldera volcanoes, similar to hydrothermal systems associated with large basaltic calderas in the geological record on land.

3.2 Regional Geology

The Tonga-Kermadec arc-trench system (Figure 3.1) is an intraoceanic convergent plate margin which extends from northern Tonga to New Zealand and formed as a result of the westward subduction of the Pacific Plate underneath the Australian Plate (Smith and Price, 2006; Taylor et al., 1996). Current subduction of the Pacific Plate is at a rate of 240 mm/yr (Bevis et al., 1995; Zellmer and Taylor, 2001). The system consists of the Tonga-Kermadec Trench, the Tonga-Kermadec Ridge, which contains the active volcanic front of the arc, and the remnant Lau-Coville Ridge which is separated from the Tonga-Kermadec Ridge by the actively extending Lau Basin and Havre Trough. The active arc comprises a chain of more than 70 stratovolcanoes

(Smith and Price, 2006). The arc is divided into eight different segments based on changes in the arc-ridge-trench separation: Northern Tonga, Central Tonga, Southern Tonga, Louisville, Monowai, Northern Kermadec, Central Kermadec, and Southern Kermadec (Figure 3.2: Smith and Price, 2006). The major stratovolcanoes are spaced about 50 km apart. Eighteen of the volcanoes, including the islands of the Kingdom of Tonga and Kermadec Islands of New Zealand, rise above sea level; however extensive bathymetric mapping has revealed nearly continuous submarine volcanism between these island groups. North of 23°S, the summits of the volcanoes reach <200 mbsl, whereas further south the volcanoes are somewhat deeper (summits mostly >400 mbsl).

In the north, the axis of the active volcanic arc has a NNE orientation of ~015-020° along the Southern Tonga, Central Tonga, and Northern Tonga segments (Figure 3.2), which is orthogonal to the trajectory of the Pacific Plate. However, at ~24°S, the orientation of the arc switches abruptly to azimuth ~0° along the Louisville Segment and then continues south of the Monowai Volcanic Complex at ~015-020° at the approximate location of the obliquely subducting Louisville Seamount Chain. Back-arc spreading in the north occurs along the ELSC and the Valu Fa Ridge, which is propagating southward and intersects the arc at ~24°S. The Havre Trough, in the south, is not actively spreading but is opening in a series of strike-slip basins that accommodate a small component of oblique convergence with the Pacific Plate (Delteil et al., 2002; Campbell et al., 2007).

Collision with the LSC is thought to have played an important role in the segmentation of the Tonga-Kermadec arc system. Adjacent to the LSC both the arc and the near back-arc regions exhibit along-strike variation in their structure and magmatism resulting from the abrupt change in the orientation of the arc (see Chapter 2). Oblique convergence of the Pacific Plate at this location is at least partly accommodated by rifting of the arc crust along the Louisville Segment (Delteil et al., 2002; Ruellan et al., 2003; Argus et al., 2011; Chapter 2). Oblique extension was previously recognized in the back-arc in the Southern Lau Rift, but significant intra-arc deformation has now been documented in the adjacent arc crust in a number of graben-like structures crossing the full width of the arc. In Chapter 2 it was shown that large caldera-like seafloor depressions floored by andesite and basalt have developed where the thickened are crust

is actively rifting. However, the origins of these large structures are not well understood. Some may be mainly structural features, rather than products of caldera-forming eruptions, whereas others are underlain by large subvolcanic intrusions, as at Monowai (Paulatto et al., 2014).

3.3 Volcanic Front

The Tonga arc includes 41 submarine volcanoes with summit depths ranging from 1,200 to <100 m; the Kermadec arc includes 33 submarine volcanoes, with depths from 1,700 m to 200 m. In Tonga, the arc includes a western active portion and an eastern remnant volcanic chain. The inactive part consists of uplifted carbonates and volcaniclastic sediment overlying middle Eocene to late Miocene volcanic and plutonic rocks of the arc basement and includes the coral islands of the Tonga group. Since the Miocene, the locus of magmatism has migrated westward to the presently active volcanic chain (Hawkins, 1995). Some authors have suggested that subduction of the Louisville Seamount Chain, locally impeded roll-back, with flattening of the slab and tectonic erosion causing the westward migration of the arc front (Nur and Ben-Avraham, 1983; Contreras-Reyes et al., 2011).

The major volcanoes of the Tonga Arc are shown in Figure 3.3 and 3.4. Most are situated 40-70 km west of the forearc bulge and 180 km west of the Tonga Trench. The active part of the volcanic front is about 50-70 km wide and is dominated by discrete volcanic cones or clusters and intervening flat areas. The Southern Tonga or 'Ata Segment, Louisville Segment, and Monowai Segment include 21 semi-regularly spaced submarine volcanic centers. Many of these were mapped during NZAPLUME III, NZASRoF, SO-195a (TOTAL), and SO-215 (Wright et al., 2008; Graham et al., 2008; Embley et al., 2005; Contreras-Reyes et al., 2011; Peirce and Watts, 2011; Watts et al., 2012), and during our own research cruises: SO-135 (Haase et al., 2002), SO-167 (Stoffers et al., 2002), SITKAP and SO-192 (MANGO) (Stoffers et al., 2006b; Schwarz-Schampera et al. 2007; Chadwick et al., 2008). Table 2.2 summarizes which cruises visited each of the volcanoes described below.

North of ~22°S, the volcanic front of the Southern Tonga ('Ata) Segment widens noticeably and includes both recent and older volcanic edifices (Figure 3.3). The oldest volcanoes feature

thickly sedimented, wave-cut summits as shallow as 150 mbsl with slumping, erosion and faulting of their flanks, including 'Ata Island. Many of the volcanoes are only remnants of lava flows and volcaniclastics abutting now exposed dike complexes. Fresh lavas cover the more youthful stratocones. Most of the large volcanoes have summit calderas or craters, but some are distinct cones lacking any summit depression. Many are associated with smaller satellite cones and radial fissures (i.e., dike swarms). Other large volcanoes are dominated by broad circular collapse features which are either the remnants of stratovolcanoes or represent large-scale subsidence structures. The following descriptions are from T. Worthington reported in Stoffers et al. (2002, 2006b). Volcano 1 of the Southern Tonga ('Ata) Segment (21°09'S) (Figure 3.5a) rises from a depth of 1800 mbsl to 65 mbsl, with a basal diameter of 28 km, elongated to the NW-SE. The summit hosts a large 7 km by 4.5 km wide caldera, also elongated to the NW-SE. The summit caldera rim is at depths of 150 to 250 mbsl, and the caldera floor is at 450 mbsl. Post-caldera volcanism has occurred at this complex indicated by the presence of post-caldera cones within and along the rim of the summit caldera.

Volcano 2 (21°18'S) (Figure 3.5a) is connected to Volcano 1 by a 4 km by 3 km flat-topped ridge with a hummocky terrain on its flanks suggesting a complex history of multiple sector collapses. Volcano 2 is comprised of two intergrown cones surrounded by two relict ridges (trending NNW and ENE) and two valleys (trending E, SW). The NW cone is larger, with a height of 1.2 km high and a diameter of 22 km, shoaling to 150 mbsl and elongated NW-SE. The summit is dominated by a large 6.5 km by 4.5 km caldera trending NW-SE. The flat-lying caldera floor is at 550 mbsl, with the well persevered caldera rims in the SW and NE rising to 150 and 200 mbsl, respectively. Post-caldera cones delineate a NW-SE trending volcanic lineament that subdivides the caldera floor in two halves.

Volcano 3 (21°39' to 21°53'S) (Figure 3.5b) is comprises two large stratovolcanoes. The northern cone is a relatively simple but morphologically old cone, rising from ~1700 mbsl to 150 mbsl, with a basal diameter of 15 km. The summit includes a poorly preserved 2.5-km diameter, 500-m deep caldera. The caldera rim reaches 250-300 mbsl along portions in the west and south, whereas some valleys cut the rim to 450 mbsl in the N-NE and to 350 mbsl in the SW. The southern volcano is larger (16 km in diameter and 1.6 km high) and more complex than the

northern cone. It contains a circular 6.2 km by 5.9 km summit caldera-subdivided into three segments: a NW rim ranging from 550-750 mbsl, a NE rim which is more irregular and ranges from 350-650 mbsl, and a southern rim which rises to 50 mbsl. The caldera floor reaches a maximum depth of 920 mbsl and is mostly buried by young volcaniclastic sediments from volcanism along the SE caldera rim.

Volcanoes 4-6 belonging to the 'Ata Volcanic Complex (21°56' to 22°27'S) (Figure 3.5c), a cluster of 14 submarine cones. The eastern volcanoes are flat-topped and heavily sedimented, suggesting no recent summit eruptions have occurred there. The western volcanoes, in contrast, are steep stratocones with fresh lavas (Stoffers et al., 2002), indicating a westward migration of the volcanism. Volcanoes 5a and 6a are among the oldest in the chain, with broad wave-cut summits and thick sediment cover.

Volcano 7 (22°31' to 22°46'S) (Figure 3.5d) is also a complex of two stratovolcanoes. The northern volcano is the larger of the two, with a basal diameter of 20 km. It rises from 1950 mbsl with an irregular morphology of three elevated ramparts; in the north with a summit at 400 mbsl, in the east with a summit at 350 mbsl, and in the SW with a summit at 250 mbsl. These regions are connected by a sunken plateau at depths of 450-700 mbsl. The ramparts possibly represent an old eroded caldera, originally at least 6.3 km in diameter, which has undergone collapse. The southern volcano is a simple stratocone with a basal diameter of 12 km. The cone also rises from 1950 mbsl to a summit at 480 mbsl. The summit hosts a 1.2-km diameter, 200-m deep caldera.

Volcano 8 or the Pelorus Volcano (22°51'S) (Figure 3.5e) is located at the Pelorus Reef. It is a large 14-km diameter simple stratocone, rising 1.4 km from 1450 mbsl to 50 mbsl. Pelorus Volcano hosts a 5- km diameter circular caldera, with the floor reaching 500 mbsl. The caldera rim reaches 50 mbsl everywhere but in the west it is buried by post-caldera volcanism. Post-caldera volcanism along the western rim has formed two cones, 1 km and 1.5 km in diameter and rising to 50 mbsl and 35 mbsl, respectively.

Five additional volcanoes between 22°51’S and 21°31’ S (Volcanoes 9 to 13) were originally identified in low-resolution bathymetry but have not been mapped in subsequent surveys (Stoffers et al., 2002, 2006b).

At ~23°30'S, the line of volcanoes defining the volcanic front shifts from a NNE (between Volcano 1 and Volcano 14) to almost due north between Volcano 14 and Volcano 21 (Figure 3.2). The volcanoes along the arc front in this segment include four large calderas that are not associated with composite cones, three that are stratovolcanoes with summit calderas, and two that are cones lacking summit depressions. These volcanoes were briefly described in Chapter 2 and are described in more detail in this paper from cruise report data for SO-167, SO-192 and SITKAP.

The summits of the major cones range from 900 mbsl to less than 100 mbsl, whereas the depths of the large caldera volcanoes reach 1600 mbsl (the deepest at Monowai) (Figure 3.6). The spacing of the volcanoes is at least partly controlled by structural segmentation of the arc with a clear NE-SW faulting pattern (see Chapter 2), similar to that described by Campbell et al. (2007) for the central and southern Kermadec arc and by Wormald et al. (2012) at Monowai. In general, the cone volcanoes occur on horst-like segments of the arc front, whereas the deeper calderas are mostly found in graben-like depressions. The depths of the horsts are similar to the surrounding arc crust, suggesting that they are not uplifted blocks, but rather intact portions of the arc separated by foundered arc crust.

Volcano 14 (23°34’S) (Figure 5f) comprises two intergrown cones, 17.8 x 13 km and rising 1.4 km from the surrounding seafloor. The eastern cone hosts a 4.2 x 3.2 km, ~300-m deep summit; the caldera on the western cone is 3.9 x 3.6 km and 640 m deep summit crater. Volcano 15 (23°52’S) (Figure 5g) is a 12-km diameter, 300-m high cone with a 4.7 x 3.9 km caldera. Directly north of the cone is an 8-km semicircular embayment interpreted to be a highly eroded second caldera or the northern portion of a larger ancestral Volcano 15. Volcano 16 (24° 11’S) (Figure 5h) is a 19-km diameter, 1.2-km high edifice with an irregular form. It contains three high standing peaks, joined by a 12 x 6.3 km summit plateau. Volcano 18 (Figure 5i) consists of a pair of volcanoes; a northern cone (24°29’S) and southern cone (24°35’S). The northern cone

is 10 km in diameter and 1.1 km high with a striking alignment of >40 pyroclastic cones on a fissure cutting the volcano. The southern cone is a larger 14-km diameter, 1.1-km high cone with a funnel-shaped 6.9 x 6.3 km summit crater. Volcano 19 (24°48'S) (Figure 5j) is a 14-km diameter, 0.9-km high cone with an old summit crater, infilling cone, and a younger western crater. Volcano 20 (25°12'S) (Figure 5k) is a 11 x 10 km diameter caldera volcano rising 1.1 km from the surrounding seafloor. The caldera floor reaches a depth of 1150 mbsl and the caldera rim is at 700-800 mbsl. Volcano 21 (25°25'S) (Figure 5l) is a 13-km diameter, 1-km high symmetrical cone with a small 3 km summit crater.

The Monowai Volcanic Complex at 26°N (Figure 5m) comprises the 15-km diameter Monowai caldera and the nearby 1-km high Monowai Seamount. Together, the caldera and large cone occupy 420 km^2 and form the largest submarine volcanic feature of the Tonga-Kermadec arc. Although the large seamount was mapped repeatedly, the caldera was completely unknown until 2004 (Wright et al., 2008; Graham et al., 2008). The Monowai Seamount has a dramatic conical shape and smooth flanks resulting from frequent pyroclastic eruptions (Chadwick et al., 2008; Wright et al., 2008, Watts et al., 2012; Metz et al., 2019). It was first surveyed with modern single-beam bathymetry throughout 1977-1979 after observations of volcanic activity in 1977 (Davey, 1980). The summit is highly unstable, with periodic flank collapses. Repeat bathymetric surveys over the Monowai cone revealed dramatic changes in the topography since 1998 caused by multiple collapses of the summit and regrowth of the cone (Schwarz-Schampera et al., 2007; Chadwick et al., 2008; Wright et al., 2008; Watts et al., 2012). The nearby caldera was not found until 25 years after the first mapping of Monowai Seamount when the survey area was expanded during the NZAPLUME III expedition. It has since been extensively studied by Wright et al. (2008), Chadwick et al. (2008), Timm et al. (2011), Watts et al. (2012), Wormald et al. (2012), Paulatto et al. (2014), and Metz et al. (2019). However, the relationship between the giant caldera and the large Monowai cone is unclear. It is still uncertain whether the ongoing eruptions at the cone are fed laterally by a pluton under the caldera complex or by a smaller magma chamber located beneath the cone. The latter is supported by differences in the basalt compositions (Graham et al., 2008; Timm et al., 2011) and also the presence of radial ridges present on the flanks of the stratovolcano which may represent radial cracks due to inflation of an underlying magma chamber. However, a large magma body is still considered to be present

under the caldera complex based on modelling of gravity (Paulatto et al., 2014). The entire complex lies within the 2000 m deep Monowai graben that crosses the active arc. The 75-km long graben is a NE-SW-trending rift bound by 300-m high extensional faults that can be traced across the arc front into the backarc. It crosses the arc at an oblique angle, subparallel to the regional tectonic fabric and related to a component of dextral convergence between the Pacific and Australian plates at this location (e.g., Campbell et al., 2007; see also Chapter 2).

Volcanic rocks from the Central and Southern ('Ata) segments of the Tonga arc range from high-Mg basalt to rhyolite and belong to the low-K series (T. Worthington in Stoffers et al., 2002, 2006b); Smith and Price, 2006). Rocks from the Tongan islands are commonly silicic, whereas the volcanoes of the Louisville Segment are generally basaltic (Table 3.1) (e.g., T. Worthington in Stoffers et al., 2002); Wright et al., 2003; Smith et al., 2010; Timm et al., 2013). Details of the sampled volcanic rocks from Volcano 14 to Monowai are described below. Hydrothermal activity was found at Volcano 18, 19, and Monowai (Stoffers et al., 1999a, b, c; Schwarz-Schampera et al., 2007; Wright et al., 2002; Stoffers et al., 2002; Stoffers et al., 2006a and b; Leybourne et al. 2012) and is also described below.

3.4 Methods and Data

In Chapter 2 we presented the first large-scale geological map of the Louisville and Monowai segments at 1:500,000, identifying two distinct types of volcanoes at the arc front: cone volcanoes on the intact blocks of arc crust (e.g., Volcanoes, 18, 19, and 21) and large caldera volcanoes in graben-like structures between the blocks (e.g., Volcanoes 15, 16, 20, and the giant Monowai caldera). Here we present details of the Monowai rift and volcanic complex at 1:50,000 and compare it to the other volcanoes.

Multibeam bathymetric surveys, bottom observations, and sampling of the arc volcanoes were conducted during research cruises NZAPLUME III, NZASRoF, SO-195a (TOTAL), and SO-215 (Wright et al., 2008; Graham et al., 2008; Embley et al., 2005; Contreras-Reyes et al., 2011; Watts et al., 2012), and during our own research on SO-135 (Haase et al., 2002), SO-167 (Stoffers et al., 2002), SITKAP and SO-192 (MANGO) (Stoffers et al., 2006a and b; Schwarz-

Schampera et al. 2007; Chadwick et al., 2008). For the Monowai volcanic complex we used MBES data collected during the 2011 research cruise SO-215 aboard R/V *Sonne* and gridded with a resolution of 30 m (Peirce and Watts, 2011). For other volcanoes of the Louisville segment, we used MBES data collected in 2002 during SO-167 (Stoffers et al., 2002), in 2007 during SO-192 (Schwarz-Schampera et al., 2007), and in 2014 during TN-309 on the R/V *Thomas G. Thompson* (Rolling Deck to Repository, R2R). The TN-309 data were gridded with a resolution of 30 m, SO-167 data were gridded with a resolution of 45 m, and the SO-192 data were gridded with a resolution of 50 m. These data sets were further processed in this study by applying a calculated slope raster and hillshade raster to aid in revealing complex structures. The slope raster is computed using ArcGIS software employing an algorithm with a 3 x 3 moving grid-cell to calculate slope at the centre of 8 eight surrounding cells (Burrough and McDonell, 1998). The hillshade is a 3D representation of the surface with the sun's relative position taken into account for the shading of the image.

Details of the geological mapping at Monowai are provided in Chapter 2. Extensive sampling and bottom photography provided essential groundtruthing for all of the volcanic complexes. We used data compiled from close to 95 hours of bottom surveys using the Canadian ROV ROPOS deployed during SO-192 in 2007 and the manned submersible PISCES IV and V during SITKAP in 2005 (Stoffers et al., 2006b; Schwarz-Schampera et al., 2007). Complementary visual observations from submersibles and ROVs provided important information about rock types, volcanic facies and structure at the outcrop scale and are the basis of composite stratigraphic sections of the different volcanoes presented here.

3.5 Results

3.5.1 Cone Volcanoes

Volcano 14

The two cones that comprise Volcano 14 (Figure 7a) include a small summit crater on the eastern cone and a deeper summit crater on the western cone. The eastern cone is symmetrical with smooth flanks a steep-walled summit crater with a floor at more than 800 mbsl. Multiple small

volcanic domes are built upon the crater floor, with the largest 700 m in diameter and rising 100 m. The smooth flanks suggest the cones are buried by crater-forming eruption ejecta. Small volcanic domes on the smooth flanks appear to be remnants of radial dikes, but due to the subdued relief they likely pre-date the crater-forming eruptions and have been partly buried. The incised nature of the crater on the eastern cone suggests that it is older than the western cone.

The summit crater on the slightly smaller western cone is 640 m deep. Due to the steep walls of the crater and the lack of slump deposits, it appears to be very young. The flanks of the entire cone include five small volcanic domes up to 400 m in diameter and 50 m high.

Dredging of the eastern cone recovered samples from the western flank, inner wall of the eastern crater, and the inner wall of the western crater. Samples from the flank of the volcano included weakly weathered pumice with devitrification banding and pyroxene microphenocrysts. Samples from the inner wall of the eastern crater were pumice and weathered aphyric andesite and plagioclase-phyric andesite. Samples from the elongate volcanic dome on the floor of the crater were also pyroxene microphenocryst-bearing pumice. A wide range of volcanic rocks were sampled from the inner wall of the western crater, including pyroxene microphenocyrst-bearing pumice, weakly weathered basalt, aphyric basalt, aphyric andesite, aphyric dacite, and highly weathered plagioclase and olivine gabbro. The wide range of lithologies suggest that eruptions from the western cone might have sampled nearly the full crustal thickness of the arc.

Volcano 18

A pair of volcanoes are grouped in the Volcano 18 cluster (Figure 3.7d). Both have smooth flanks, covered by volcaniclastic material, possibly ejected from the crater on the southern cone.

The northern cone is smaller and crossed by a striking line of >40 small pyroclastic cones that define an 18-km long NE-SW fissure cutting the volcano. The largest of the pyroclastic cones is 800 m in diameter and 150 m high, occurring in the middle of the fissure. Small sector collapses occur on the NE flank of the largest cone, which likely occurred as a result of the cone-forming eruptions. Several satellite cones are present that are cut by NE-SW trending faults.

The larger southern cone hosts a large funnel-shaped summit crater with a rim between 390 and 950 mbsl and a crater floor at 1520 mbsl. The steep walls of the crater (45-50° slopes) suggest that it formed recently, similar to the western crater on Volcano 14. A bench on the eastern wall of the crater marks different pyroclastic flow units (see below) overlain by a thick ejecta blanket up to 500 m thick. The northern flank and rim of the crater are crossed by minor NE-SW lineaments, parallel to the much larger fissure in the north, and they are likely exposed dikes. The crater-forming eruption is interpreted to have been a single event due to the thick ejecta blanket in the east and the simple funnel-shaped morphology of the crater.

The summit crater of the southern cone was surveyed during PISCES dives P5-640 and P5-641 in 2005. The dives collected stratigraphically controlled samples from: 1) the upper part of the northern crater wall, 2) the lower part of the eastern crater wall, and 3) a small cone on the eastern flank of the volcano (Figure 3.7d). These locations were chosen to sample lavas associated with the crater-forming eruption, possible "pre-crater" lavas at the bottom of the crater, and "post-crater" resurgent volcanism on the flank, respectively. The stratigraphic relationships observed in the crater wall are summarized in a schematic stratigraphic column in Figure 3.8. Three pyroclastic units were mapped from 1250 mbsl to 500 mbsl along the northern crater wall. The lowermost sequence from 1250 to ~900 mbsl was poorly exposed but included sections of sub-welded fine-grained massive pumice, typically weakly altered, and locally cut by veins of white clay. From 900 to 580 mbsl, a middle pyroclastic sequence, which was better exposed, consists of alternating beds of poorly sorted pumice clasts (≤ 50 cm) and massive fine-grained pyroclastic flow material with sub-welding textures (Figure 3.9a-d). Above 770 mbsl, dark grey ash beds of andesitic-basaltic clasts and darker more mafic enclaves are more common (Figure 3.9e). The middle and upper pyroclastic flows are separated from each other at 580 mbsl by a 3-5 m thick series of well-bedded debris flows. The upper pyroclastic flow is otherwise identical to the middle sequence.

In the eastern wall of the crater, the middle and upper pyroclastic flow sequences were at depths of 777 to 637 mbsl. Here, columnar jointing is locally well developed in the thicker pyroclastic flows, indicating welding. Basaltic ash beds and mafic enclaves are more common higher in the

sequence, and the more coherent units display cooling joints with varying orientations over a few meters (Figure 3.9f).

The lowermost pyroclastic units in the crater showed evidence of locally intense chlorite and clay alteration in samples collected during SO-167 (Stoffers et al., 2002). During the PISCES dive P5-641 alteration and veining was observed at the same location within the lowermost of the pyroclastic flow sequences, but outcrops of the chlorite-clay rock recovered during SO-167 were not located. Evidence of water-column anomalies, with high values of ^{3}He isotopic abundance, ΔpH, Fe values, and dissolvable Fe/Mn (Massoth et al., 2007) also were found in the crater, but focused hydrothermal venting was not observed. Diffuse hydrothermal venting and cloudy water was observed on the small basaltic cone at the eastern flank of the Volcano 18 during SO-192. An area of very low-temperature discharge (up to 2 °C above ambient) with iron-silica chimneys and bacterial mats was found on the upper part of the cone (440-270 mbsl) (Stoffers et al., 2006b). The cone consists of massive flows of basaltic andesite (aa-textured), generally 5-10 m thick, with coherent inner parts and breccia units between the flows. The flows clearly overlie the pyroclastic sequences from the earlier crater-forming event(s).

Dredging of the NE upper flank of the northern cone retrieved fresh scoriaceous aphyric basalt, weakly weathered plagioclase-phyric basalts, and weathered quartz-hornblende pumice. The basalt samples were dominant on the young cones along the 18-km fissure, whereas pumice (identical to that from Volcano 16) was dominant at the large central cone along the fissure.

Two dredges in the summit crater of the southern cone recovered samples from mid-depth up the crater wall and at the crater rim. Samples from mid-depth in the crater included variably weathered aphyric andesite, plagioclase-phyric andesite, aphyric dacite, plagioclase-phyric dacite, aphyric pumice with devitrification textures, and strongly chloritized and sheared fault-gouge material. All except the pumice is interpreted to represent lavas emplaced prior to the crater forming eruption. Samples from the rim of the crater were dominated by weathered aphyric pumice with devitrification textures. Minor fragments of weathered olivine- and plagioclase-phyric basalt and aphyric basalt, and weathered conglomerate were also recovered. The pumice samples are interpreted to represent the crater-forming event.

Volcano 19

The symmetrical steep-sided cone at Volcano 19 is dominated by an old, poorly preserved summit crater on the east side, an infilling cone, and a younger western crater (Figure 3.7e). In the older crater, only the eastern walls and parts of the northern walls are preserved, and it has been mostly infilled by a younger cone, 1.7 km diameter and rising to the volcano's maximum height of 450 mbsl. The western wall of the old crater has been greatly affected by the formation of the younger crater, 1.8 km in diameter and 250 m deep (1025 mbsl floor). The younger infilling cone in the eroded summit crater has partly collapsed into the younger crater and down the southern flank of the volcano. On the floor of the younger crater are two small slump blocks or post-eruptive volcanic features, 250 m in diameter and less than 100 m high, partially infilling the crater.

Volcano 19 was explored during both the SITKAP and SO-192 cruises. The young, steep-sided crater on the west side of the summit was surveyed during PISCES dives P5-636 and P5-367 and along the southern and eastern walls of the crater; a third dive (P5-635) examined the base of the wall (Figure 3.8). The young crater and complex summit area of the volcano were surveyed during PISCES dives P5-368 and P5-639 and also visited during ROPOS dives R1046b, R1047 and R1048 in 2007. The lower parts of the crater walls were covered by sediment and volcanic talus (Figure 3.10a-b), but the steep sides exposed massive columnar-jointed flows throughout. The crater floor and lower 50 m, from 1030 to 970 mbsl, was covered by sediment (Figure 3.10c) and 20 m of volcanic talus adjacent to the crater walls. From 950 to 750 mbsl, the nearly vertical walls of the crater comprise ~200 m of the massive basalt (Figure 9b). In this section, abundant dikes are exposed in the crater wall from 1020 to 790 mbsl (Figure 3.10d-e). Massive columnar-jointed flows outcrop from 800 to 730 mbsl (Figure 3.10f) and probably represent the exposed lower part of the infilling cone at the top of the volcano.

Two hydrothermal fields were identified at Volcano 19: a high-temperature field (up to 265 ^{o}C) with active chimneys at the top of the infilling cone, and low-temperature Fe-oxide deposits among a swarm of dikes at the bottom of the steep-sided crater (described in detail in Stoffers et al., 2006a). The hydrothermal field at the summit of the volcano on the infilling cone is one of

the highest-temperature vent fields known along the Tonga-Kermadec arc. Focused venting is observed along a narrow NE-SW trending ridge at the top of the cone complex, where clusters of barite and anhydrite chimneys occur. At water depths of ~540 m in a small pit crater on the central cone, groups of small chimneys and low-relief mounds of barite and anhydride are present. From these chimneys, clear two-phase venting was observed. In the younger steep-sided crater, along its southern wall, extensive Fe-oxyhydroxide crusts occur along a 900-m portion of the base of the crater at depths of 985 to 850 mbsl. Near the center of this field, clusters of Fe-oxyhydroxide and silica chimneys cover an area of 200 x 300 m. Diffuse venting is present throughout the field.

Volcano 21

Volcano 21 is the shallowest cone on the segment, with a summit crater that shoals to a water depth of only 160 m (Figure 3.7g). The volcanic is almost perfectly symmetrical, with a simple funnel-shaped crater that reaches a depth of 800-850 mbsl. Volcanic ridges radiate outward from the upper parts of the volcano to the base of the cone. Although the volcano does not show signs of recent eruptions or hydrothermal activity, small pits are evident on its flank.

The summit crater was surveyed during a single ROPOS dive (R1045) from a depth of 670 to 200 mbsl (Figure 3.8). The bottom of the crater from 670 to 660 mbsl is dominated by course talus of aphyric and plagioclase-phyric basalt and andesite (Schwarz-Schampera et al., 2007). From 660 to 550 mbsl, the crater wall exposes basalt dikes with columnar jointing that intrude screens of volcaniclastic material. The volcaniclastic units contain abundant dark grey angular clasts (≥15 cm) in a finer-grained matrix with no clear bedding. The intruded volcaniclastic units are notably Fe-stained (due to weathering). From 550 mbsl and upwards, the intensity of the Fe-staining and dikes decreases, and from 535 mbsl, bedding in the volcaniclastics becomes apparent and is increasingly common at shallower depths. The bench separating the lower dike section from the volcaniclastic deposits is clearly visible in the bathymetry. Two sills were observed at depths of 540 mbsl and 475 mbsl (Figure 3.8). At 420 mbsl, the volcaniclastic material is locally altered. Unconsolidated ash and lapilli are identified at ~340 mbsl and

dominate the upper portion of the section. Recovered volcanic rocks from the crater wall consisted of dense plagioclase- and clinopyroxene-phyric, vesicular basalt and andesite.

3.5.2 Caldera Volcanoes

The large shallow caldera at Volcano 1 is located within the Southern Tonga segment and has been previously described by Stoffers et al. (2006a). Its large 7 km by 4.5 km wide caldera reaches depths of 400 mbsl, possibly due to a partial collapse or breach of a large post-caldera cone thought to have formed in the centre of the caldera before the collapse and resulting in an eastward sloping plateau. The SW flank of Volcano 1 is cut by major faults, trending E-W and NE-SW with throws of up to 200 m. ROPOS dives (R1052 and R1054) revealed coherent basalt flows at the base of the caldera wall, overlain by a bedded volcaniclastic unit and capped by a thin unit of finely bedded tuff. The upper walls are dominated by weakly bedded volcaniclastic units with abundant, densely packed lithic blocks (Figure 3.11). Stoffers et al. (2006a) described extensive areas of low-temperature (30-70° C) gas-rich venting on young scoria cones at the crater rim.

The main caldera volcanoes of the Tonga Arc (Volcano 15, 16, 20, and Monowai) are located farther the south, along the deeper Louisville and Monowai segments.

Volcano 15

Volcano 15 is a complex group of nested calderas (Figure 3.7b). The largest and most intact is 4.7 x 3.9 km and elongated in a NW-SE direction. The caldera rim is at 1080 mbsl to 1500 mbsl in the southeast, where the caldera wall is breached. The caldera floor at 1420 mbsl is flat but disrupted by a 2-km diameter and 120-m high cone with its own summit crater (1.3 km in diameter and up to 150 m deep) and a smaller 900-m diameter and 200-m high close to the breach in the SW wall of the caldera. North of the large intact caldera, there are two broad 8- to 10-km diameter semicircular embayments that are older calderas or part of a larger ancestral volcano on which Volcano 15 has grown. Both relict calderas have flat, heavily sedimented

caldera floors. A number of small, isolated cones up to 600 m in diameter and 150 m high are located within and around the nested calderas.

Dredging at Volcano 15 recovered samples from the area of the breach in the caldera wall, at the intra-caldera dome, the northern caldera wall, and at the inner scarp of the first embayment in the north of the complex. Samples from the breached wall of the intact caldera included weathered aphyric pumice with devitrification banding and hard quartz-bearing pumice. Dredging of the intra-caldera dome containing the small crater at the caldera floor also recovered pumiceous material containing xenoliths of olivine-plagioclase basalt, and andesite within the quartz-bearing pumice. The predominance of aphyric pumice and the hard quartz-bearing pumice suggests that the post-caldera dome and the crater were not formed by the same eruption. The weathering of the samples suggests this part of the volcano has been inactive for at least 10s of ka (T. Worthington in Stoffers et al. 2002). Highly weathered aphyric pumice and small fragments of less weathered pumice were sampled from the caldera-like embayment to the north consistent with it being and older feature of the complex. The origins of this embayment have not been confirmed, however samples determined that it pre-dates the post-caldera activity.

Volcano 16

Volcano 16 is a similarly large complex of nested calderas and craters (Figure 3.7c), elongated ESE-WNW. The outer summit plateau at 800 mbsl has been interpreted as a large caldera, 12 km by 6.3 km that has been infilled by younger ejecta. The caldera rim is still partly preserved in the west and may have originally linked the three high standing peaks of the volcanic complex. Within the older caldera is a younger, 8 km by 5.6 km structure with a slightly deeper floor at 900 mbsl, also elongated ESE-WNW. This younger caldera still has a well-defined rim; however it has been mostly infilled by later eruptions, including three small craters, from as little as 1.2 km in diameter up to 3.6 km in diameter and 450 m deep (1500 mbsl). The largest and deepest of these young craters hosts a small 900-m diameter and 50-m high late-stage cone. The flanks of the Volcano 16 complex are smooth and gently sloping, indicating a thick blanket of volcaniclastic material from multiple caldera-forming eruptions. Some NE-SW trending faults

are present on the NE and SW peaks, which may control the caldera bounds in part and control the location of small.

Dredging of the deepest caldera recovered weakly weathered hornblende- and quartz-bearing pumice as well as hornblende-quartz dacite, quartz-plagioclase dacite, and diorite blocks. The dacite blocks are thought to be remnants of post-caldera volcanic domes, whereas the pumice is likely a product of recent eruptions that infilled the smaller caldera. Samples from the outermost caldera rim (peak at the SW corner), included hornblende- and quartz-bearing pumice with devitrification textures and inclusions of weathered mafic lavas and a block of weathered andesite.

Volcano 20

Volcano 20 is a broad, shallow caldera that rises 1.1 km above the surrounding seafloor (Figure 3.7f). The flat floor of the caldera is at 1150 mbsl, and the caldera rim is at 700 to 800 mbsl. Along the SE of the caldera wall, small cones up to 100 m tall and 1.4 km in diameter have been built, disrupting the otherwise outer caldera rim. The SW flank of the caldera volcano is crossed by several volcanic ridges (up to 100 m tall) that extend 6.7 km in the direction of the regional NE-SW tectonic fabric.

Dredging on the peak of a cone along the southeast rim recovered dark grey, vesicular, microphyric basaltic lava and small amounts of grey-brown altered rock containing native sulfur and pyrite. Dredging on the north rim recovered fresh, dark grey-brown, vesicular microphyric andesitic gravel and minor microphyric dacite. A parasitic cone to the north of the caldera was also sampled, retrieving vesicular basaltic lava with minor rhyolitic pumice pebbles.

Monowai

The Monowai volcanic complex contains the largest caldera in on the arc, measuring 14.2 x 8.8 (Figure 3.7h) km and up to ~1 km deep. The caldera has a volume of 46 km^3, which is about 4.5 times the average size of the summit craters on the cone volcanoes (~10 km^3) (Table 3.2). The

center of the caldera is 1145 m above the surrounding seafloor, which is dominated by a 30-km wide and 150-km long graben. The caldera has an elliptical shape that is elongated in a NW-SE direction, generally orthogonal to the graben-bounding faults. Early studies suggested that the elliptical shape of the caldera is related to trench-parallel faulting. However, Wormald et al. (2012) and this study show that the long axis of the caldera is oblique to the trench and therefore must reflect some degree of transtension. Abundant ring faults occur around the perimeter of the caldera and include both inward and outward dipping faults. The faults defining the outer margins of the caldera are thought to be mostly inward dipping, whereas the innermost rings faults have been interpreted as later outward-dipping faults (Timm et al., 2011; Paulatto et al., 2014). Graham et al. (2008) suggested that the ring faults represent the outer rims of two nested calderas resulting from two separate caldera-forming events. We suggest that they are intracaldera bench-faults within a single large subsiding structure (see below).

At least 6 parasitic cones occur around the outermost ring faults. They range in size from 1.3 to 6.5 km in diameter, with heights from 200 to 550 m. The cones vary from circular to subcircular in shape, and many are elongated and misshapen. The parasitic cones occur most abundantly on the eastern and western sides of the caldera and are spaced 500 m to 2.5 km apart. There is no preferred orientation; rather, they appear to be elongated parallel to the adjacent caldera rim and therefore likely represent eruptions along the ring faults. Other cones appear to have been affected by the caldera ring faults and have experienced scarp collapses. Three cones located adjacent to the western caldera rim are highly faulted and deformed by the NE-SW graben boundary faults. Several cones show unexpectedly high backscatter, indicating recent eruptions, and several extracaldera flows extending up to 4 km have been observed associated with parasitic cones on the north rim (Wormald et al., 2012). A number of fissure ridges are also evident throughout the intracaldera region, following the general trend of the caldera rim. At the center of the caldera, a 2-km diameter and 300 m high resurgent dome sits on the lowermost caldera floor.

Dredged samples from the caldera range from basalt in the outermost parasitic cones to basaltic andesite in the intracaldera lavas (see Discussion). Samples from the Monowai cone are tholeiitic basalt. Although there are no recent volcanic flows related to the resurgent dome,

extensive low-temperature hydrothermal venting has been observed along the innermost caldera faults at Mussel Ridge, suggesting that it has been recently volcanically active (Leybourne et al. 2012; Schwarz-Schampera et al., 2007). Mussel Ridge was visited in 2005 during one PISCES dive (P5-612) and subsequent ROPOS dives (R1043 and R1044) found a large area of diffuse venting, mussel beds, and oxidizing sulfides. Along the flank and summit of Mussel Ridge a dense colony of mussels and tube worm clusters was found covering the seafloor. Multiple sulfur chimneys were found with diffuse venting at temperatures ranging from 15 to 39°C. The substrate consists of massive coherent basalt, but clear evidence of weathered massive sulfide could be seen beneath the mussels (Figure 3.12a-b). Mineralized samples were collected from the vent sites (ROPOS Dive R1043 and R1044, samples 26TVG A-G: Schwarz-Schampera et al., 2007). They consist of barite-pyrite and sulphur-rich crusts and altered vesicular basalt with fractures lined by pyrite, realgar, and barite. The low recorded venting temperatures and weathered sulfides indicate this may be a mature hydrothermal system, with its maximum activity having already occurred after the latest eruptions. A less well-defined hydrothermal plume was found near the northwest caldera wall, but there are no signs of significant hydrothermal activity at this location (Leybourne et al., 2012; Embley et al., 2005). However, only a small part of the caldera has been explored for hydrothermal activity.

3.6 Evolution of the Monowai Volcanic Complex

Figure 3.13a shows the distribution of the main geological formations mapped in the vicinity of the Monowai volcanic complex at 1:50,000 scale. The map shows the large caldera complex and nearby cone, occupying ~420 km^2, built on a raised portion of the graben floor. The caldera shape is typical of fault control, associated with early-stage of rifting of the arc (e.g., Wormald et al., 2012; this study). The raised graben floor is considered to be a manifestation of early inflation of the rift preceding caldera collapse. However, there is no clear evidence of lava flows that might have ponded on the floor of the rift during or after the formation of the caldera (Figure 3.13b). Instead, we infer a mainly structural collapse and subsidence due to withdrawal of magma.

The detailed map of the caldera shows the outermost ring faults which are inward-dipping normal faults with throws of up to 500 m. The innermost faults are interpreted to be outward dipping and define an inner caldera floor with an area of 8.3 km x 5.5 km (Figure 3.14). Several of the inward-dipping faults are observed at surface as intracaldera volcanic ridges. The traces of the outward-dipping faults at the caldera floor are more difficult to define. Their locations have previously been interpreted by Paulatto et al. (2014) and are consistent with analytical models of caldera faulting of Acocella (2007). The series of intracaldera volcanic ridges leading down to the caldera floor (including Mussel Ridge), are interpreted here to be the seafloor expressions of the outward-dipping reverse faults, also suggested by Paulatto et al. (2014).

Wormald et al. (2012) suggested that the long axis of the inner part of the caldera is slightly different from that defined by the outermost ring faults (with an orientation of 135° compared to 125°), and therefore the stress field controlling caldera formation has shifted through time, with several stages of collapse resulting in the formation of nested calderas. However, the reprocessing of the multibeam and slope shading in this study show clear benches along the intracaldera faults and no evidence that the outermost faults of the caldera have been cut by later intracaldera faults (i.e., as would be expected if they were nested calderas). We interpret the development of the benches to reflect a continuous evolution of the caldera rather than different stages of subsidence with continuous asymmetric collapse of the caldera. Paulatto et al. (2014) similarly interpreted the caldera as the result of long-lived collapse of a single structure, with late-stage resurgence following the deformation of the caldera floor during collapse. Observations during PISCES and ROPOS dives indicate that post-collapse sediment cover is greater on the upper benches than on the lower benches and caldera floor, which confirms a progressive lowering of the caldera, with accumulation of volcanic talus and breccia at the base of the lowermost bench.

The benches within the caldera are relatively flat and appear to have formed by uplift on the outward-dipping reverse faults. Several of the sharp ridges on the lowermost bench could be seafloor expressions of dike-like intrusions (e.g., at Mussel Ridge), which would account for the local hydrothermal activity. Seafloor observations also indicate the presence of partly exposed dikes overlain by pillow lavas. The pillow lavas of Mussel Ridge are less sediment covered than

the lavas of the resurgent cone and therefore represent a younger basalt eruption. The ridge is bordered by the caldera wall faults and the NE-SW trending faults. Along the crest of Mussel Ridge, linear outcrops of massive coherent basalt were observed, possibly indicating a dike-like intrusion. Numerous small round volcanic features on the lower bench faults are mostly pillow mounds (Figure 3.15), confirmed by observations made during ROPOS dives. Mussel Ridge and the other post-collapse magmatic features on the benches (pillow mounds and dikes) all have less sediment cover than the caldera floor or resurgent dome, indicating that they post-date the latest caldera subsidence and are possibly the source of a prominent lava flow at the bottom of the caldera partly surrounding the resurgent dome (Figure 3.15). The resurgent dome at the center of the caldera is a multi-vent complex that rises 275 m from the caldera floor. High-resolution multibeam shows that it is a partially collapsed dome or pillow mound with a smaller feature on its southern flank and a collapse scar at its summit.

The parasitic cones at the margin of the caldera are dissected by the caldera ring faults and partially collapsed. The heavily incised cones indicate that the caldera has grown in size since their formation. The largest cone on the west side of the caldera is also cut by graben-bounding faults that do not appear to be part of the Monowai caldera. These larger cones may represent the pre-rift volcanism prior to caldera formation, consistent with the heavily sedimented pyroclastic material on their flanks. The northern flank of the caldera complex is covered by a series of lava flows. The southern flank is buried by the volcaniclastic apron of the large Monowai stratovolcano.

Although the caldera margin is prone to intrusions and topographic instability, resulting in significant mass wasting, the steepness of the caldera wall exposes an intact caldera sequence. A ROPOS dive on the NE caldera wall (R1042 location in Figure 3.7h) showed the depositional sequence from the caldera floor up to the outer rim of the caldera (Figure 3.8). The caldera succession consists of 850 m of volcanic breccia, pillow lava and coherent flows, flow breccia, and finally bedded volcaniclastics at the base. The lowermost 250 m of breccia (Lower Basalt Breccia) consists of large blocks of massive basalt typical of megabreccia sequences formed by rapid mass wasting into a subsiding caldera. This unit is overlain by 120 m of massive basalt and pillow lavas with few outcrops, 40 m of flow top breccia, and 200 m of bedded volcaniclastic

material with abundant scoria and black sand. The Lower Basalt Breccia is separated from 160 m of Middle Basalt Breccia by a thin pillowed flow. The breccia facies is comprised of variably to poorly sorted massive basalt clasts (flow and pillow fragments up to bomb size). The near-vertical caldera wall in the lower 410 m confirms that the breccia sequences are in place and not simply accumulated talus at the bottom of the caldera. The middle of the section, from 1200 mbsl to 1000 mbsl, is dominated by 160 m of massive coherent to pillowed basaltic flows (Upper Massive Flow unit) and 40 m of broken massive lava (possible flow top). From 1000 mbsl to 810 mbsl the sequence comprises 190 m of bedded volcaniclastic material ranging from fine sand to lapilli and some larger blocks and bombs. Ash layers are locally interbedded with coarser, thicker units. In this section of the caldera wall, the large range in clast sizes (from fine tuff to lapilli, and occasionally blocks and bombs) could be interpreted as mass flow deposits. However, the pyroclasts range from rounded scoria clasts to much denser, less vesiculated clasts; this material may have formed from hot magmatic to phreatomagmatic eruptions.

The large Monowai cone to the southeast of the caldera is the most active submarine volcano currently known in the area. It rises from >2 km depth to within 100 m of sea level, and since it was first discovered during an eruption in 1977, the volcano has been continuously monitored and has experienced many large T-phase earthquake swarms (i.e., magma movement). Owing to its large size and frequent eruptions, Monowai is a volcanic hazard in the region. Particle plumes have been documented on the flank of the volcanically active cone (Leybourne et al., 2012), but their origin is uncertain and may be related to ongoing pyroclastic eruptions. The cone is basaltic, with the most recent eruptions comprised of plagioclase-phyric basalts (Haase et al., 2002; Graham et al., 2007). It has a distinctly symmetrical shape, with the only notable morphology being a series of radial ridges, interpreted as exposures of radial dikes on its flanks. The ridges have a relief of ~50 m but can range up to 100 m. They are mostly present on the mid-lower slopes and appear to be mostly buried by volcaniclastic material shed from the volcano. Of note is that the volcano is not affected by the NE-SW trending faults, indicating that it is younger than the most recent NW-SE extension in the Monowai graben.

There have been numerous studies of the changes in morphology of the Monowai cone due to summit eruptions (e.g. Chadwick et al., 2005; Wright et al., 2008; Chadwick et al., 2012; Watts

et al., 2012; Metz et al., 2019). Between 1998 and 2004, the Monowai stratovolcano experienced a change in the summit depth from 42 mbsl to 132 mbsl as well as the addition of a collapse feature on the southeast side (Wright et al., 2008). Mapping of the volcano during SO-192 in 2007 showed summit eruptions had infilled a sector collapse scar and the summit had risen to 98 mbsl. The flank of the cone was surveyed during an active eruption in 2007 (ROPOS dive R1041). The dive was abandoned part way through due to zero visibility approaching the summit of the cone. At the dive site, visible discolouration and upwelling was observed at the surface in multiple locations, likely related to a small cone building on the southern side of the summit and along the length of the collapse scar. The ROPOS operation began at a depth of 3350 mbsl and moved upwards to the active cone where it encountered pulsed debris flows and turbidity currents from the building cone. A significant area of the collapse scar was also unapproachable due to steam eruptions and turbidity currents. Bombs were observed in the debris from the building cone. The dive was abandoned after reaching a height of approximately 500 mbsl.

Table 3.3 summaries the rock types sampled at each volcano described above.

3.7 Discussion

3.7.1 Regional tectonic controls on arc-front volcanism

The origin and evolution of large caldera complexes of intraoceanic volcanic arcs is closely related to the regional stress regime. A general model for island-arc rifting, which controls many of the largest volcanic complexes of the Tonga-Kermadec system, has been proposed by Fujiwara et al. (2001). In this model, the southern Havre Trough represents an early stage of arc rifting, dominated by normal faulting. Volcanism associated with rifting is confined to linear zones along the normal fault scarps. In the northern Havre Trough, the axial rift zone becomes segmented and is overprinted by MORB-like "ridge and knoll" terrain caused by intrusion into the back-arc crust. Regularly spaced segmentation of the arc (e.g., Wright et al., 2006) is caused by a right-lateral component of convergence between the Pacific and Australian plates, with increasing obliquity from south to north (Campbell et al., 2007; Delteil et al., 2002; Ruellan et al.; this study: Chapter 2). Thus, extension which normally occurs orthogonal to the advancing

Pacific Plate, is oblique to the arc front and trench as observed at the Valu Fa Ridge, an active spreading axis directly north of the study area.

Chapter 2 showed that the regional structure along the length of the arc at the Louisville and Monowai segments is dominated by the NE-SW trending grabens (and horsts) with arc stratovolcanoes mainly developed on the highs and large collapse calderas in the graben-like rifts. In addition to thinning of the arc crust, the rifting allows larger volumes of mafic magma to rise higher in the crust and therefore the formation of larger mafic calderas. In the prevailing stress fields, calderas become elongated parallel to the least compressive stress direction, which has been well documented at Monowai (e.g., Wormald et al., 2012) and elsewhere (this study). In their model, the long axis of the caldera corresponds to the minimum principal stress direction (ShMin), and the fissure ridges with cone volcanoes correspond to the maximum horizontal principal stress (ShMax). Other large calderas on the Louisville segment (e.g., Volcano 20, Volcano 16, and Volcano 15) are similarly elongated in the direction ~110-135°, oblique to the arc front. In contrast, the summit calderas of cone volcanoes (Volcano 18, Volcano 19, and Volcano 21) do not show a preferred shape or orientation, although they are cut by major dike swarms with a consistent NE-SW direction reflecting the maximum horizontal compressive stress direction. Whereas the large graben-bounding faults accommodate magma intrusion as sills, the fractures on the intervening horst blocks are mainly occupied by dike-like volcanoes (Chapter 2). The different styles of volcanism reflect the structural imprint of the oblique convergence and collision with the LSC. Faults crossing the horst blocks, including dike-like fissure volcanoes, represent ongoing breakup of the arc crust, as observed in the Havre Trough (Campbell et al., 2007). The Monowai volcanic complex, which is the largest of the arc-front volcanoes (>400 km^2, including the caldera and the cone), occurs at a location on the arc that coincides with the thickest crust in the region (Martinez et al., 2006) as well as the collision zone of the Louisville Ridge (Figure 3.1). The arc and adjacent backarc are strongly influenced by local magmatic inflation (ridges and knolls) and the subduction of the Louisville Ridge and Osbourne Trough (Delteil et al., 2002; Ruellan et al., 2003; this study: Chapter 2).

This strong structural control on magmatic productivity, with rifting dominated by effusive eruptions and shield volcanoes, has been documented previously in other early arc rifts (e.g.,

Anderson et al., 2016). Fissure eruptions on horst blocks are precursors of larger-scale rifting and graben formation. Eruptions associated with early rifting and eventual graben are thought to be related to favourably oriented basement structures reactivated by the component of convergence of the Pacific Plate and the LSC impinging on the subduction trench (Chapter 2).

3.7.2 Structural styles, controls on caldera collapse, and magmatic productivity

All calderas go through a series of changes beginning with regional tumescence, eruption, collapse, and resurgence (Smith and Bailey, 1968; Lipman, 2000). The most common form of caldera collapse is by voluminous eruption of melt (>10 km^3 of magma) that evacuates the underlying magma chamber and leads to collapse of the overlying, now unsupported, volcanic cone (Acocella, 2007). The erupted material is deposited as thick sequences of pyroclastic material and pumice, which are well exposed in the caldera walls. However, this model is mostly inferred from land-based calderas. There is virtually no record of the history of large submarine caldera-forming eruptions. The dominant volcanic facies exposed in the walls of the calderas of the Tonga Arc are volcanic breccia, pillow lava and coherent flows, columnar-jointed flows, flow breccia, and bedded volcaniclastics, including welded units in the more silicic volcanoes. Among the major differences between the different caldera types are the abundance of pyroclastic material, with the total thickness of coherent flow units much greater in the large basaltic calderas. In the volcanoes of the Tonga arc, the eruptive sequence is dominated by early megabreccia formation and effusive eruptions (i.e., massive flows), followed by hundreds of meters of bedded volcaniclastic materials, as observed in ROPOS and PISCES dives on the volcanoes of the Louisville and Monowai segments. Post-caldera activity includes the extrusion of late volcanic domes and/or a change in style to more effusive eruptions. At many of the volcanoes, it appears that this sequence was repetitive, with caldera-forming eruptions followed by reconstruction of the basaltic stratovolcanoes, followed by additional caldera-deepening eruptions.

The summit craters of the cone volcanoes are typically <10 km^3 (Table 3.2). The sequence of eruptions of the cone volcanoes is represented by Volcanoes 18, 19 and 21. The summit craters are all much smaller and shallower than the large caldera volcanoes and are generally

symmetrical in shape. They show a range of evacuated volumes from 0.9-3.5 km^3, except for Volcano 18 which hosts a larger and deeper, 17 km^3, summit caldera (Table 3.2). At Volcano 18, the summit crater exposes >700 m of pyroclastic material with increasing mafic clasts towards the top (lithic-rich volcaniclastics in Figure 3.8), suggesting that the crater formation may have been triggered by a basaltic intrusion into the underlying magma chamber, which was then mostly erupted (Schwarz-Schampera et al., 2007). Post-caldera resurgence occurred which built the flanking cone, composed of similar basaltic andesite flows in the upper part of the pyroclastic flow sequence. At Volcano 19, the summit crater is more complex with a younger 2-km wide, 1000-m deep crater superimposed on an earlier structure, highlighting the frequency of eruptions. At Volcano 21, the symmetrical shape of the volcano and the summit crater is typical of a single volcanic vent with the entire cone constructed by pyroclastic eruptions from the central depression. The many basaltic to andesitic dikes observed in the crater wall suggest that this vent is fissure-controlled.

The caldera volcanoes reflect a greater amount of evacuated material >10 km^3. Volcano 1 was the first large caldera complex mapped on the Tonga Arc (Stoffers et al., 2006a and b). It is a large 28 km diameter caldera volcano hosting a 7 x 4.5 km elongated caldera. Dives along the caldera determined this center formed as the result of numerous repeated small eruptions and a major sector collapse rather than single large eruptions (Stoffers et al., 2006b). Volcanoes 15 and 16 are a similar size overall but formed as large composite calderas with nested craters suggesting multi-stage evolution. Volcano 15 consists of at least two nested calderas that have undergone some collapses to the east. However, to the north of the main edifice is a series of apparently older, eroded calderas, together at least 10 km in length. Volcano 16 consists of a single large caldera with as many as 5 nested and partially infilled calderas and. The large 9-km wide caldera at Volcano 20 is approximately the same width as the Monowai caldera but is shallower and has a more uniform depth (~1750 -1925 mbsl). A large ring of parasitic cones outside the inner caldera suggests that the full width of the complex may be as much as 14 km.

The Monowai caldera complex formed along a continuous series of inward-dipping intracaldera normal faults and outward-dipping faults (Figure 3.14) that are now mostly buried by post-caldera mass wasting and basalt. The fault pattern is likely a result of a deflating magma

chamber (e.g., Lipman, 1997; Roche et al., 2000; Timm et al., 2013), with the lowermost benches and caldera floor formed by reverse movement on the outward-dipping faults when the magma chamber reinflated, as in the emplacement of the resurgent dome. Analogue experiments confirm the development of such faults as a result of differential uplift as a result of overpressure conditions in the underlying magma chamber (Walter and Troll, 2001; Acocella, 2007). This could explain features such as Mussel Ridge, in the lower part of the caldera. Paulatto et al. (2014) suggest that outward-dipping reverse faults at Monowai may be related to the edge of a large shallow magma chamber modelled by gravity and magnetic data. However, these faults are often difficult to identify due to reactivation or overprinting.

The large volume of inflated crust surrounding the Monowai caldera could represent the initial stage of regional tumescence and doming of the rocks overlying the magma chamber. Pillow lavas exposed on the lower walls of the Monowai caldera may represent material of a pre-Monowai lava shield. Caldera formation was likely coincident with voluminous eruption of basaltic-andesitic pyroclastic rocks exposed along the middle to upper caldera walls (Figure 3.8). The episodic nature of the eruptions is indicated by the presence of thin-bedded to laminated tuffaceous units that separate coarser, thick-bedded, and massive deposits of scoria and blocks, most likely emplaced by eruption density currents. The extracaldera region surrounding Monowai is covered by ejecta that may be from caldera-forming eruptions or from the numerous parasitic cones. However, a large volume of effusive magmatic products (e.g., breakout lava flows and flank eruptions) has not been identified outside the caldera that could account for its large size.

The volume of the Monowai caldera is nearly 4 times larger than that of the summit craters of the typical arc-front volcanoes such as Volcano 18, Volcano 19, and Volcano 21, which had erupted volumes of <10 km^3, assuming total evacuation of the magma chamber during summit collapse. By comparison, the eruptive volume of the Monowai caldera is 46.2 km^3, comprising the upper caldera (29.2 km^3) and deeper portions (17.6 km^3) (calculated using the boundaries in Figure 3.13b). We assume that there was no stratocone previously built on top of the caldera. The resurgent dome (0.5 km^3), all parasitic cones (9.9 km^3), and the nearby stratovolcano (13.8 km^3) total 24.2 km^3. The difference between the volume of eruptive products and the collapse volume

(a difference of 22 km^3), suggests that a significant amount of magma is missing. This may be explained by i) non-eruptive collapse of the caldera as result of regional extension, ii) low preservation of the erupted material, or iii) eruptions of pyroclastic material that was dispersed from the source (White et al., 2015). The volume of extracaldera melt in the form of parasitic cones and, possibly, the large Monowai cone is about 55% of the total volume of the caldera. If the Monowai cone and parasitic cones were sourced from magma below the caldera, then least 45% of the caldera volume is due to subsidence without eruption directly from the caldera. This could be accommodated by draining of subvolcanic magma into newly created space caused by rifting. Some of this drained magma also may be accounted by the expansion of the Monowai pluton southwest of the caldera complex, as suggested by the gravity model of Paulatto et al. (2014). They modelled the shape of the magma reservoir (so-called Monowai pluton) underlying the caldera based on gravity and magnetics and predicted a SW-directed arm beyond the caldera that ultimately reaches the active Monowai stratovolcano and could account for some of the missing melt. Such large magma reservoirs require only a small percentage of the chamber volume to be evacuated in order to trigger caldera formation (10-30% by volume according to Geyer et al., 2006). Moreover, the low rates of volcanic output compared to cone volcanoes (see below) conserves heat that can sustain large-scale magmatic-hydrothermal systems.

The maximum age of the Monowai caldera is less than 1 million years, assuming a nominal opening rate of the Monowai graben of several cm/yr and a width of 30 km. An age of less than 0.78 Ma for the complex also was suggested by Paulatto et al. (2014) magnetic chrons, although these are poorly recorded, if at all, at the volcanic front of the arc. Thus, the volcanic output is estimated to have been at least 3.5×10^{-4} km^3/yr. This is lower, on average than the eruption rates estimated for the Monowai cone and other cone volcanoes of the Louisville segment, which erupted smaller volumes but over much shorter time scales (Figure 3.16).

3.7.3 Relationship to melt sources and hydrothermal activity

Unlike many of the cone volcanoes along the Tonga-Kermadec arc, which are commonly silicic (e.g., T. Worthington in Stoffers et al., 2002, 2006b; Wright et al., 2003; Smith et al., 2010; Timm et al., 2013), Monowai is one of the few large basaltic calderas. Volcano 1 and Volcano

19, and also Haungaroa and Rumble II West farther to the south, are also large basaltic caldera volcanoes (Wright et al., 2006; Stoffers et al., 2006). The basaltic lavas from the Monowai caldera are thought to be primitive melts injected into the arc crust, as opposed to the more evolved, volatile-rich magmas in the cone volcanoes. Samples from the caldera range from basalt in the outermost parasitic cones to basaltic andesite in the intracaldera lavas (50-63 wt.% SiO_2: Graham et al., 2008; Timm et al., 2011). The basaltic andesite is thought to have formed by fractional crystallization of the more primitive (MgO-rich) basalt (Timm et al., 2013). Samples from the Monowai cone are tholeiitic basalt (49-51 wt.% SiO_2). Although the differences between the caldera lavas and the nearby cone are minor, variations in Al_2O_3, for example, are consistent with different eruptive events (Timm et al., 2013). Following the caldera collapse, more mafic melt from a shallower magma chamber erupted to form the resurgent dome (Kemner et al., 2015). This is consistent with the suggestions of Paulatto et al. (2014) of a shallow dense body of gabbroic and mafic rock underlying the Monowai caldera and representing the solidified or partially solidified magma chamber. Timm et al. (2013) concluded that low volatile contents and low glass content (<7 vol%) of the oldest Monowai basalts are consistent with mainly effusive, rather than explosive eruptions. However, volcaniclastic material was erupted with the younger basaltic andesite, as observed in the caldera wall. The latest caldera volcanism was previously thought to be represented by the resurgent dome; however, our study identifies the youngest lavas at Mussel Ridge. Lava from Mussel Ridge, which approaches andesite in composition (Timm et al., 2013), indicates a probable heat source beneath this part of the caldera, which is driving the current hydrothermal activity. This may be related to the remnants of the magma reservoir lying under the southern half of the complex (Paulatto et al., 2014).

More than 70% of the volcanic centers along the Tonga-Kermadec arc are thought to be hydrothermally active, with a majority of the hydrothermal systems hosted by summit craters of the cone volcanoes or in the larger calderas (Leybourne et al., 2012; de Ronde et al., 2019). Many are also centers of volcanic degassing, with persistent magmatic or hydrothermal plumes in the overlying water column (Massoth et al., 2003; Massoth et al., 2004; Massoth et al., 2005; de Ronde et al., 2015). However, significant hydrothermal systems capable of forming large SMS deposits are known only in the largest and deepest caldera volcanoes (e.g., Volcano 1 and Monowai on the Tonga Arc and the Brothers Volcano along the Kermadec Arc: de Ronde et al.,

2001, 2005; Stoffers et al., 2006; Leybourne et al., 2012). By comparison, most of the vent fields in the summit calderas of the cone volcanoes are small or ephemeral (Stoffers et al., 2006a; de Ronde et al., 2019). The larger and deeper calderas provide the necessary structural control for focusing hydrothermal fluids and the high pressures to prevent boiling (Hannington et al., 2005; see below).

The caldera walls and postcaldera faulting also provide deeply-penetrating pathways for hydrothermal circulation. The largest calderas have continuously evolving permeability for large-scale hydrothermal systems. The most favourable configuration is the combination of outward-dipping reverse faults and inward-dipping normal faults like those identified at Monowai. In this situation, at different stages of caldera evolution, cold seawater is drawn down through one set of faults while the heat of the underlying magma chamber drives fluids up along the other (Stix et al., 2003; Mueller et al., 2009). During initial collapse, inward-dipping faults will tend to close as the caldera floor subsides, potentially trapping hydrothermal fluids, whereas outward-dipping faults will open during subsidence, releasing them. During caldera resurgence the opposite occurs, with the inward-dipping faults typically opening while outward-dipping faults tend to close (Stix et al., 2003). This repeated opening of new pathways for the ascent of melt and fluids is favourable for the most productive hydrothermal systems. In contrast, the smaller summit calderas of the cone volcanoes form in a piston-like fashion through pyroclastic eruption, resulting in poorly developed fluid pathways. The shallow permeability structure cannot be a primary control on the location of large-scale hydrothermal systems (Hannington et al., 2005). The most probable upflow zones are the particular faults that tap the deepest hydrothermal reservoirs that may reside below the volcano. Thus, the largest faults in the Monowai caldera located along the outmost caldera wall are the most likely master faults, with continuous lengths of over 10 km and throws of 900 m. The inner benches similarly have lengths of 5 km and throws up to 500 m.

The greater water depths of the largest calderas are also important to prevent boiling of the hydrothermal fluids and maintain the high fluid temperatures. At Monowai, water depths of 1630 m are more than 1000 m greater than in the average water depth of the summit craters of the cone volcanoes. Boiling temperatures at the bottom of the Monowai caldera are inferred to reach

up to >360 °C (Figure 3.17), compared to the highest recorded temperature of 265 °C at the active vents on Volcano 19. The water depths in the summit calderas of the cone volcanoes at Volcano 19 and Volcano 18 are 1025 and 1520 mbsl, respectively, where boiling limits vent fluid temperatures to <265 °C. The only significant high-temperature venting on the Kermadec arc is also in the largest and deepest caldera at Brothers Volcano. Active black smoker vents and massive sulfide deposits occur on the wall of the caldera at a water depth of 1600-1670 m, with lower temperature venting and apparent magmatic degassing at a 350 m high dacitic volcanic cone on the caldera floor (de Ronde et al., 2001, 2005).

3.8 Conclusions

The different styles of volcanism between cone volcanoes and larger caldera complexes on the Tonga Arc reflect the emplacement of smaller magma chambers (dikes) at higher levels beneath the horsts and larger, sill-like magma chambers beneath the extensional grabens (see Chapter 2). The elliptical shape of the largest calderas may be the result of 1) an elongated underlying magma chamber (Acocella, et al., 2002), 2) superposition and overlap of multiple collapse structures (Marti et al., 1994), 3) asymmetric subsidence (Kennedy et al., 2004), or 4) distortion due to regional stress fields. Chapter 2 suggests the distribution of different types of volcanoes is related to reactivated basement structures, and their shape in part related to the obliquity of convergence of the Pacific Plate and the LSC impinging on the subduction trench. By comparison with the caldera volcanoes, which are influenced by the regional NW-SE extensional direction, the small summit calderas of the cone volcanoes are undeformed and mostly circular.

The cone volcanoes are dominated by explosive pyroclastic eruptions and lack the massive effusive eruptive products of the larger calderas. Observations at the base of the caldera sequence at Monowai show that the pre-caldera constructional edifice was dominated by massive flows and pillow lavas. The eruption of these lavas occurred in an area of inflation of the rift valley floor that formed in response to NW-SE-directed extension. Caldera subsidence resulted in part from voluminous eruption of basaltic to andesitic lava and partial evacuation of the magma chamber and was facilitated by the regional extension. The caldera collapse was long-lived and episodic, as indicated by the step-like intracaldera benches and the presence of thin-

bedded to laminated tuff units interrupting the lavas flows in the caldera wall. Following the caldera-forming event, younger volcanic eruptions and hydrothermal activity has become focused along the innermost caldera-forming faults at Mussel Ridge.

Major arc-related rifts and calderas like Monowai are almost always intruded by large sill-like bodies, 2-3 km deep and up to 10s of km wide (e.g., Cathles 2013). This contrasts with the mid-crustal sheeted dikes that dominate the earlier phases of arc rifting (e.g., in the Lau Basin: Turner et al., 1999). We suggest that the large graben-like structures of the Louisville Segment accommodate large sill-like bodies, indicated by the sizes of the calderas, whereas the intervening parts of the arc, which are not yet fully extended, are mainly intruded by dikes that feed much smaller fissure volcanoes and cones. The eruptive volumes are compared in Figure 3.16 (modified after Watts et al., 2012). At Monowai, a rate of melt production and migration corresponding the volume of the caldera would be comparable to some of the largest volcanic shield volumes of other large oceanic islands and seamounts. By contrast the eruptive volumes of the cone volcanoes are as much as an order of magnitude smaller.

These observations have important implications for understanding ancient analogues. Large submarine caldera complexes are important geological locations for ore deposits and can host a variety of deposit types including VMS, epithermal, polymetallic vein, and some porphyry Cu systems (Gibson, 2005; Stix et al., 2003). Processes such as caldera-collapse and post-collapse resurgence may provide sufficient heat, structural pathways for fluids, and host-rock permeability for mineral deposits to form (e.g., Steven and Eaton, 1975; McKee, 1976; Slack and Lipman, 1979; Stix et al., 2003). Many volcanogenic massive sulfide (VMS) deposits have been shown to have a spatial and temporal association with large submarine calderas (Galley et al., 1998; Franklin et al., 2005; Gibson et al., 2007). The complex fault systems combined with large-scale subvolcanic heat sources provide excellent opportunities for the development of hydrothermal cells needed for the formation of VMS deposits. However, we suggest that only the largest and deepest caldera complexes produce the largest deposits. In general, smaller volcanic centers are associated with much smaller deposits; the result of smaller magma reservoirs, shallower depths and lower temperatures, and repeated explosive eruptions. The large size of the Monowai pluton is comparable to some of the largest subvolcanic intrusions in the

geological record, such as the large sill-like Flavrian pluton of the Noranda volcanic complex (Gibson et al., 2007). The Monowai volcanic complex and Noranda cauldron are nearly identical in size, dominated by 15-km wide subsidence structures with multiple parasitic volcanoes, and deeply penetrating marginal faults. Both large volcanic complexes are completely contained within a 30-40 km wide rift graben.

Details of different arc volcanoes presented in this study provide a useful comparison to other modern systems. Table 3.4 lists some of the key distinguishing features of volcanoes that formed under different conditions. Many of these features can also be directly compared to the volcanic centers of ancient greenstone belts, including, for example, the Archean megacauldrons of the Blake River Group (e.g., Mueller et al., 2009; Pearson and Daigneault, 2009). Key features of these megacauldrons include 1) regionally extensive mafic dike swarm, 2) overall domal geometry, 3) cross-cutting radial and concentric fault patterns, and 4) mappable volcanic facies variations (and alteration assemblages) that reflect the volcano evolution.

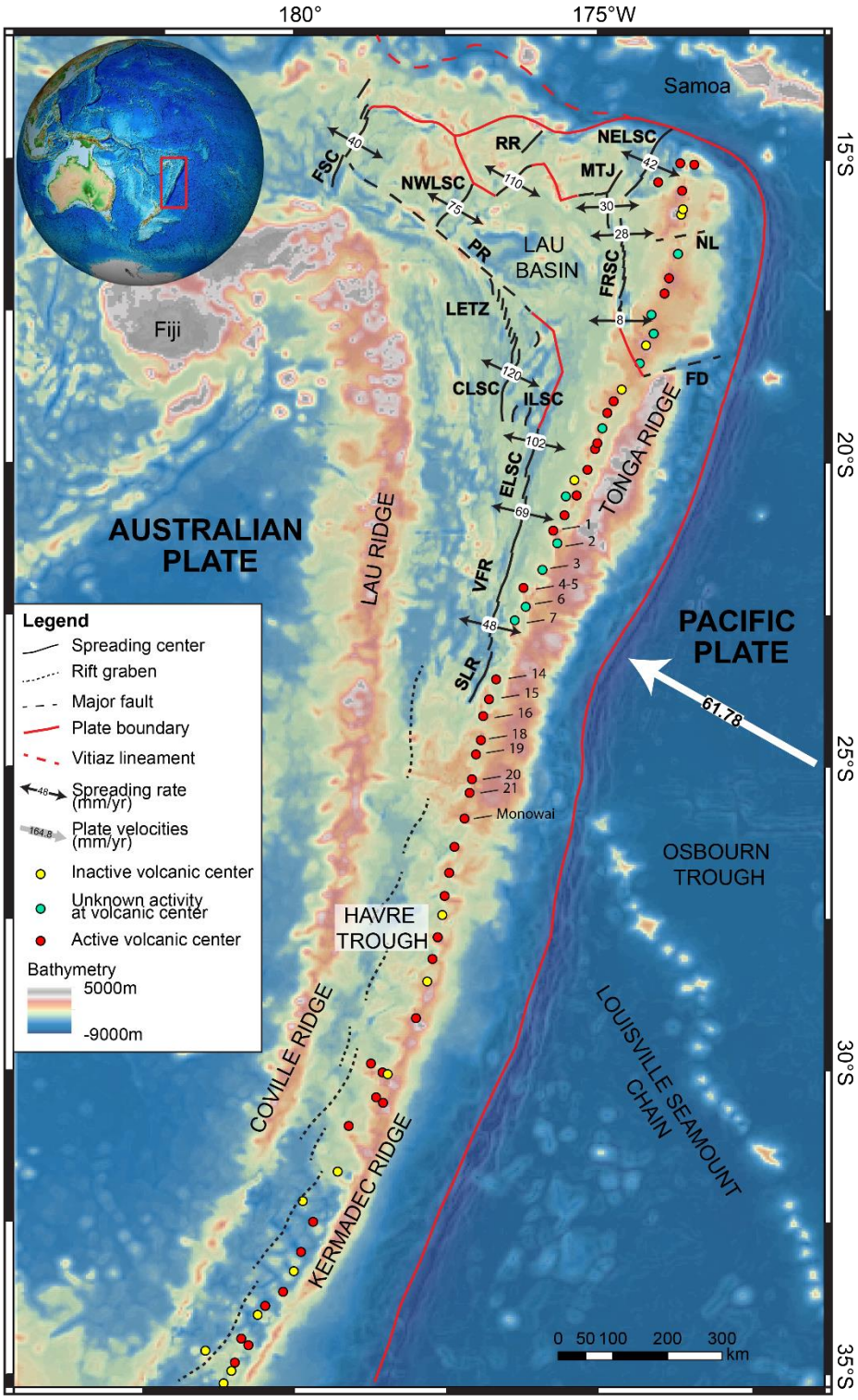

Figure 3.1 Bathymetric map of the Tonga-Kermadec system, showing the microplate boundaries and active spreading centers of Bird (2003) within the Lau Basin, modified by Baxter et al. (2020), and the rift grabens of Campbell et al. (2007) within the Havre Trough. GPS velocities

(mm/yr) and azimuths (white arrows) are shown for the Pacific Plate (Argus et al., 2011). Full-spreading rates (mm/yr) and spreading vectors (black errors) for the Rochambeau Rifts (RR) and Northwest Lau Spreading Center (NWLSC) are from Lupton et al. (2015), following Bird (2003). Spreading rates for the Central Lau Spreading (CLSC), Fonualei Rift and Spreading Center (FRSC), Eastern Lau Spreading Center (ELSC), Valu Fa Ridge (VFR), Mangatolu Triple Junction (MTJ), and the Northeast Lau Spreading Center (NELSC) are from Sleeper and Martinez (2016) and Baker et al., (2019). The spreading rate for the Futuna Spreading Center (FSC) is from Pelletier et al. (2001). Relics of arc-trench extension obliquely cross the arc front in the north (Fonualei Discontinuity (FD) and Niuatoputapu Lineament (NL). Locations of the volcanic centers (coloured circles) are shown along the arc front. Volcanic centers described in this study are indicated. Inset globe shows the position of the Tonga-Kermadec system in the SW Pacific.

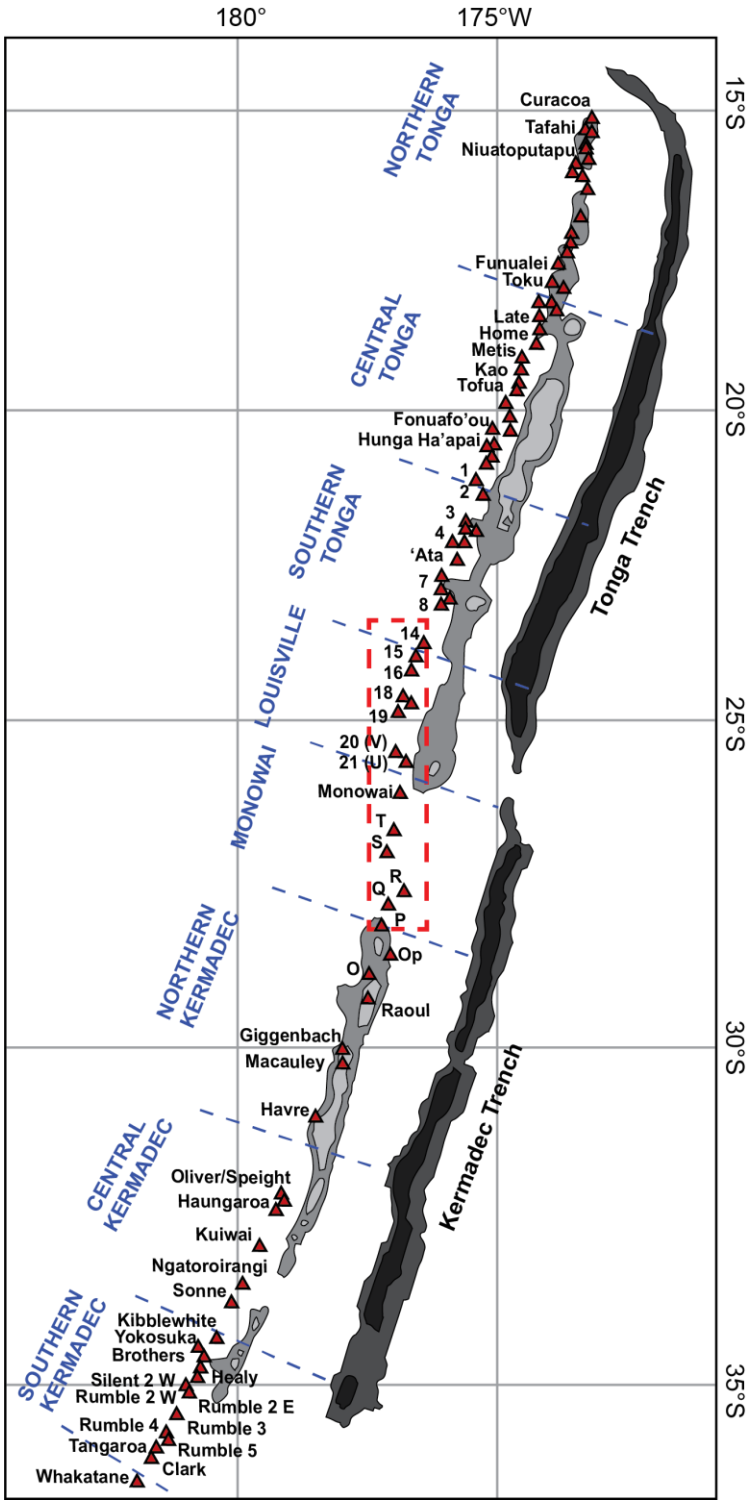

Figure 3.2 Segmentation of the Tonga-Kermadec arc modified from Smith and Price (2006) showing the locations of arc volcanoes. The ridge is defined by 1500 and 1000m contours (light

greys), the trench axis is defined by 8000 and 7000m contours (dark greys). In the Louisville and Monowai segments we observe a change in orientation of the arc front (dashed red box).

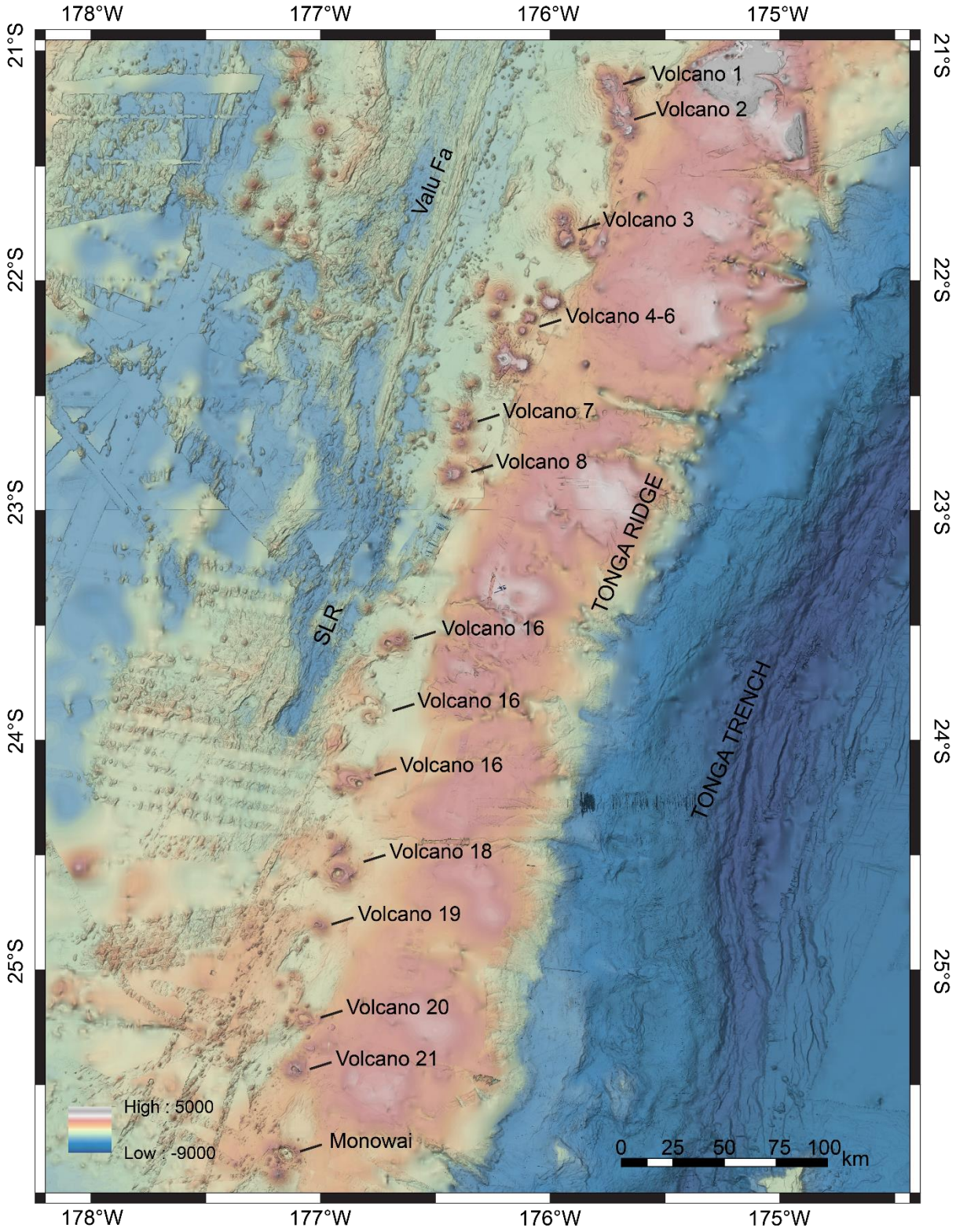

Figure 3.3 Bathymetric map of the study area, covering the Louisville and Monowai arc segments, showing the locations of the individual volcanoes and their relationship to ethe

adjacent back-arc and trench. The bathymetric data include the ship tracks from research cruises SO-167, SO-192, SO-215 (aboard R/V *Sonne*), and TN-309 (aboard R/V *Thomas G. Thompson*) combined with GMRT datasets. The datasets are displayed with slope and hillshade functions.

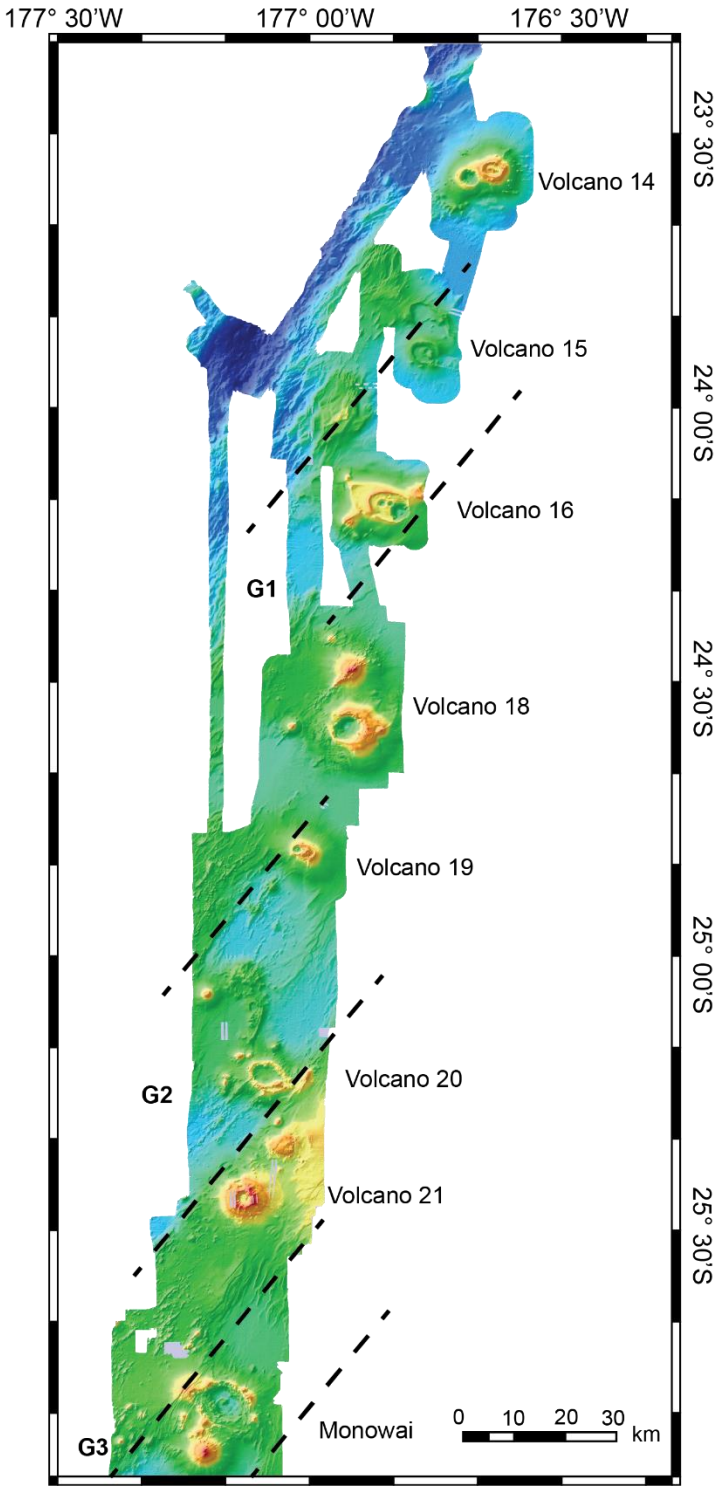

Figure 3.4 Bathymetric map of the Louisville and Monowai segment from SO-192 (R/V *Sonne*) research cruise (Schwarz-Schampera et al., 2007). The grabens (1-3) are labelled with their boundaries noted by dashed lines. Major volcanic centers are also labelled.

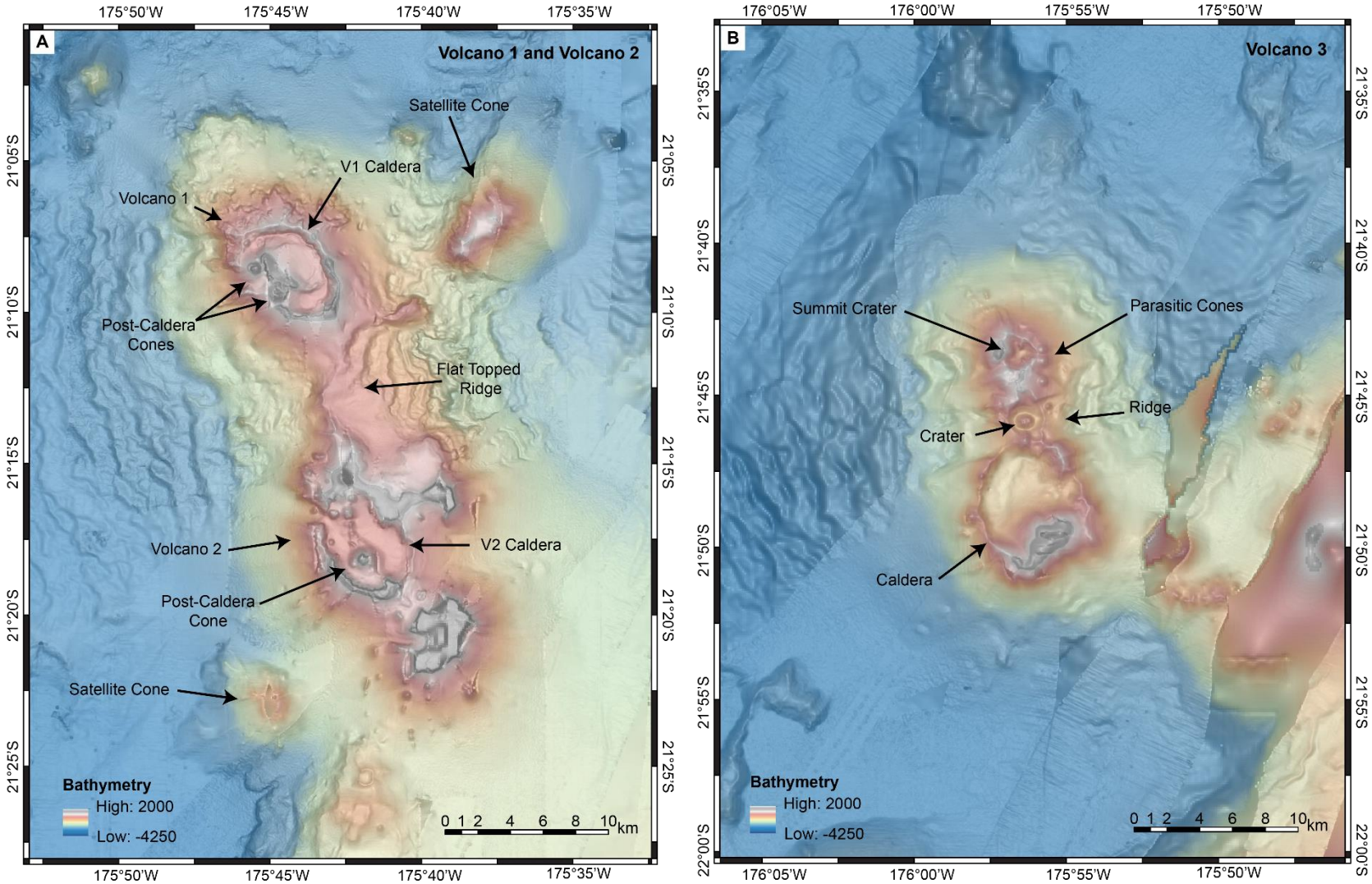
A
Volcano 1 and Volcano 2
Satellite Cone
V1 Caldera
Volcano 1
Post-Caldera Cones
Flat Topped Ridge
Volcano 2
V2 Caldera
Post-Caldera Cone
Satellite Cone
Bathymetry
High: 2000
Low: -4250
0 1 2 4 6 8 10 km
175°50'W
175°45'W
175°40'W
175°35'W
21°05'S
21°10'S
21°15'S
21°20'S
21°25'S
B
Volcano 3
Summit Crater
Parasitic Cones
Ridge
Crater
Caldera
Bathymetry
High: 2000
Low: -4250
0 1 2 4 6 8 10 km
176°05'W
176°00'W
175°55'W
175°50'W
21°35'S
21°40'S
21°45'S
21°50'S
21°55'S
22°00'S

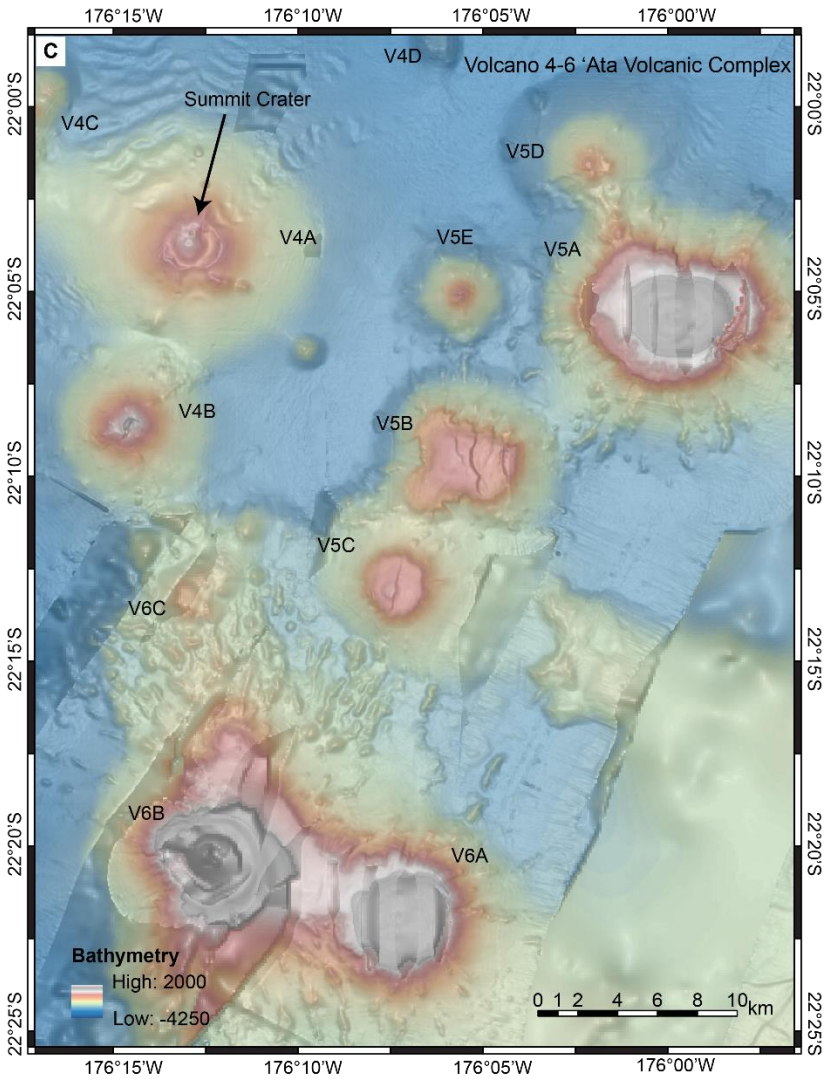
C
Volcano 4-6 'Ata Volcanic Complex
Summit Crater
V4D
V4C
V5D
V4A
V5E
V5A
V4B
V5B
V5C
V6C
V6B
V6A
Bathymetry
High: 2000
Low: -4250
0 1 2 4 6 8 10 km
176°15'W
176°10'W
176°05'W
176°00'W
22°00'S
22°05'S
22°10'S
22°15'S
22°20'S
22°25'S

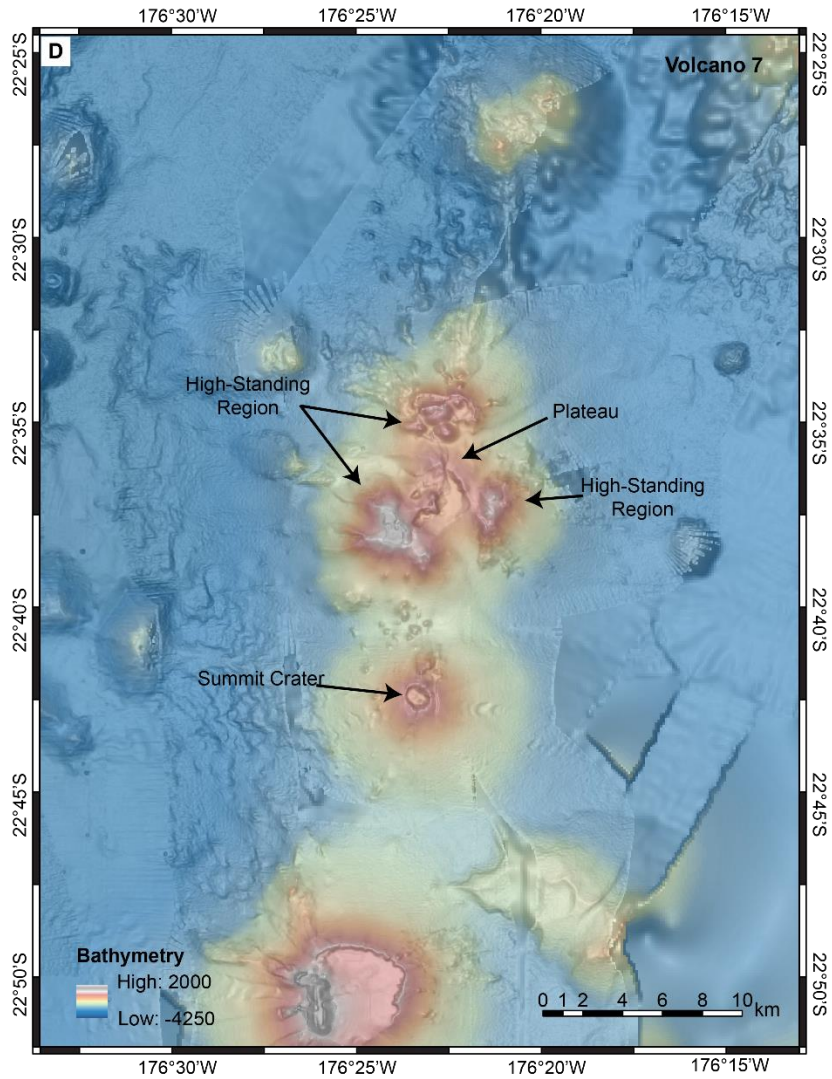
D
Volcano 7
High-Standing Region
Plateau
High-Standing Region
Summit Crater
Bathymetry
High: 2000
Low: -4250
0 1 2 4 6 8 10 km
176°30'W
176°25'W
176°20'W
176°15'W
22°25'S
22°30'S
22°35'S
22°40'S
22°45'S
22°50'S

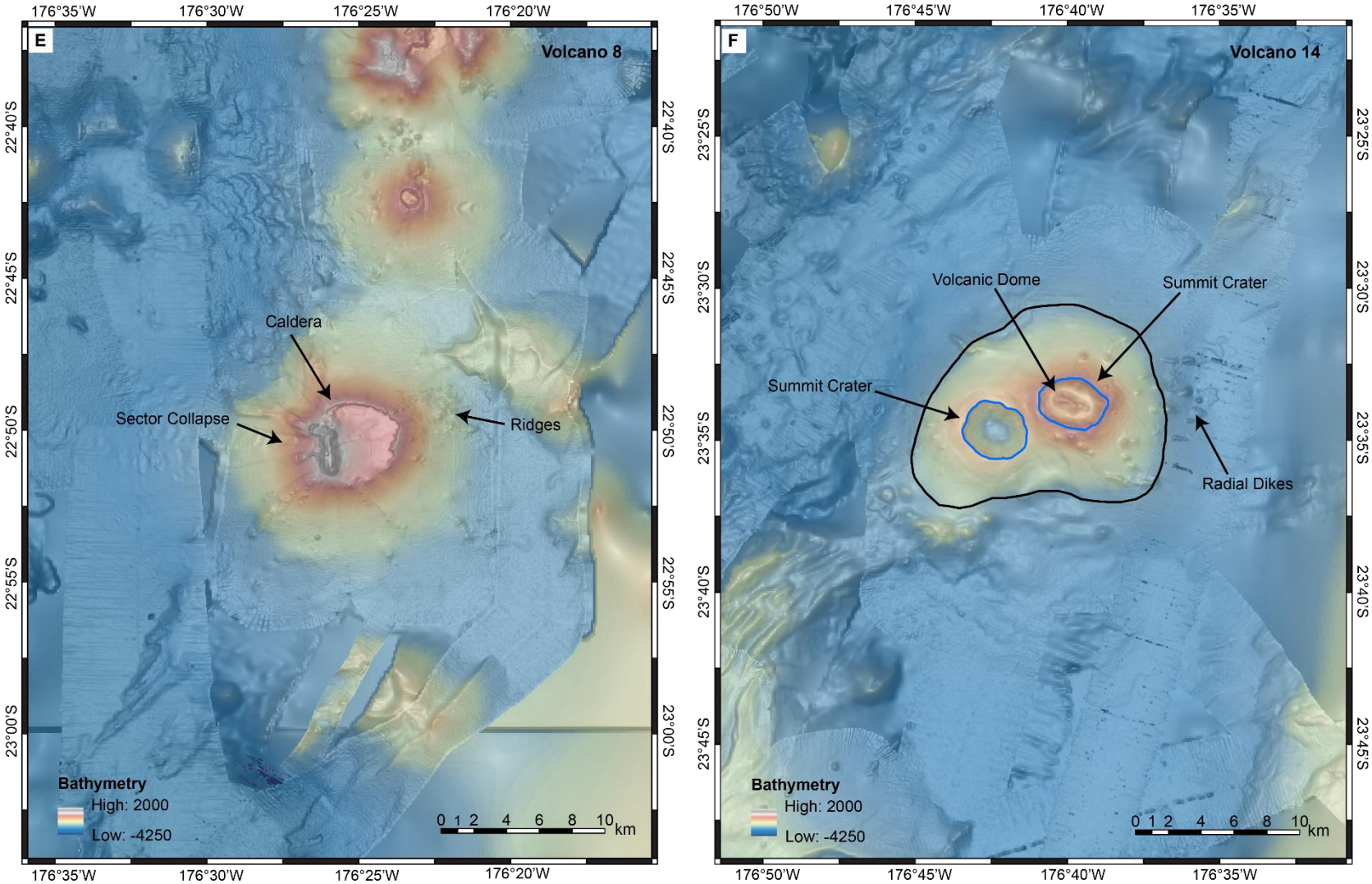
E
Volcano 8
Caldera
Sector Collapse
Ridges
Bathymetry
High: 2000
Low: -4250
0 1 2 4 6 8 10 km
176°35'W
176°30'W
176°25'W
176°20'W
22°40'S
22°45'S
22°50'S
22°55'S
23°00'S
F
Volcano 14
Volcanic Dome
Summit Crater
Summit Crater
Radial Dikes
Bathymetry
High: 2000
Low: -4250
0 1 2 4 6 8 10 km
176°50'W
176°45'W
176°40'W
176°35'W
23°25'S
23°30'S
23°35'S
23°40'S
23°45'S

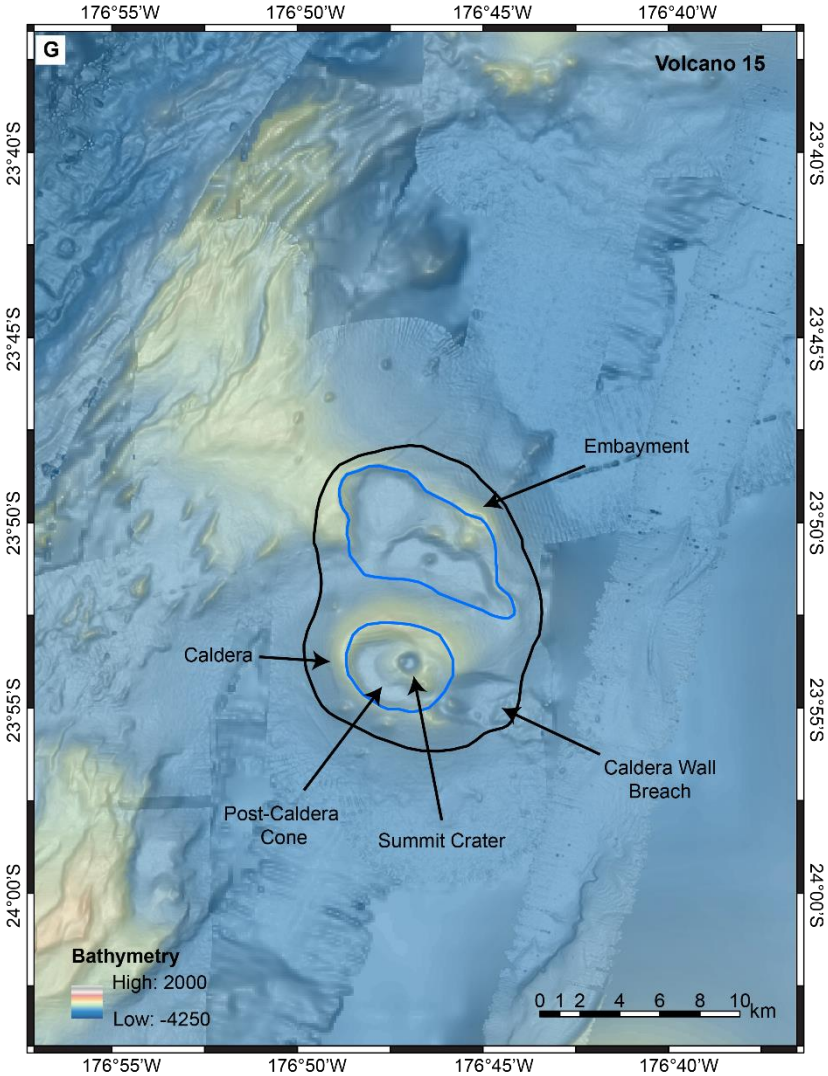
G
Volcano 15
176°55'W
176°50'W
176°45'W
176°40'W
23°40'S
23°45'S
23°50'S
23°55'S
24°00'S
Embayment
Caldera
Post-Caldera Cone
Summit Crater
Caldera Wall Breach
Bathymetry
High: 2000
Low: -4250
0 1 2 4 6 8 10 km

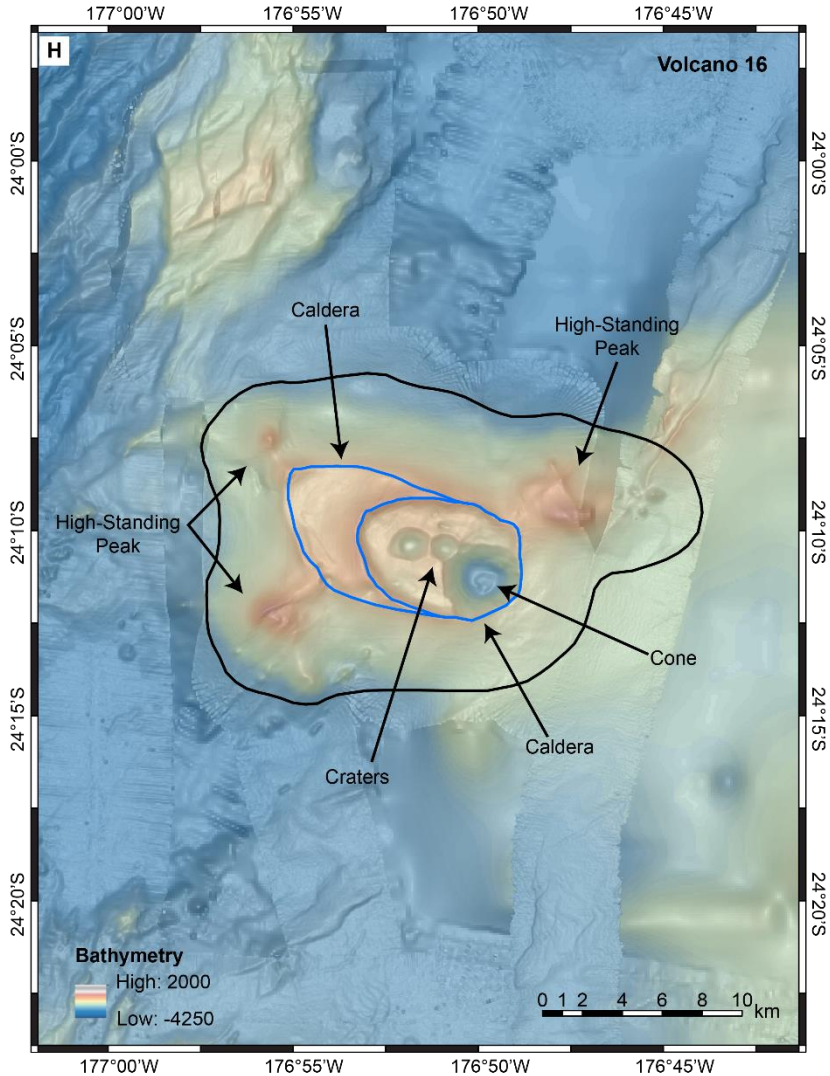
H
Volcano 16
177°00'W
176°55'W
176°50'W
176°45'W
24°00'S
24°05'S
24°10'S
24°15'S
24°20'S
Caldera
High-Standing Peak
High-Standing Peak
Cone
Caldera
Craters
Bathymetry
High: 2000
Low: -4250
0 1 2 4 6 8 10 km

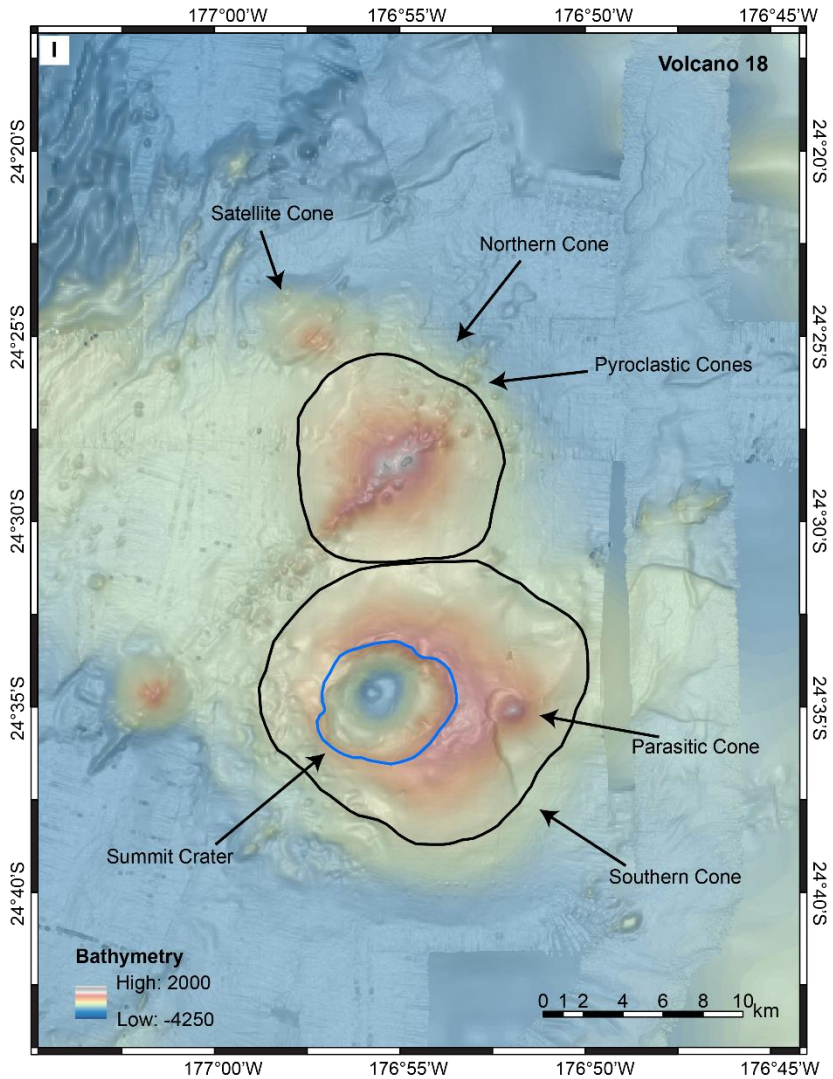
I
Volcano 18
Satellite Cone
Northern Cone
Pyroclastic Cones
Parasitic Cone
Summit Crater
Southern Cone
Bathymetry
High: 2000
Low: -4250
0 1 2 4 6 8 10 km
177°00'W
176°55'W
176°50'W
176°45'W
24°20'S
24°25'S
24°30'S
24°35'S
24°40'S

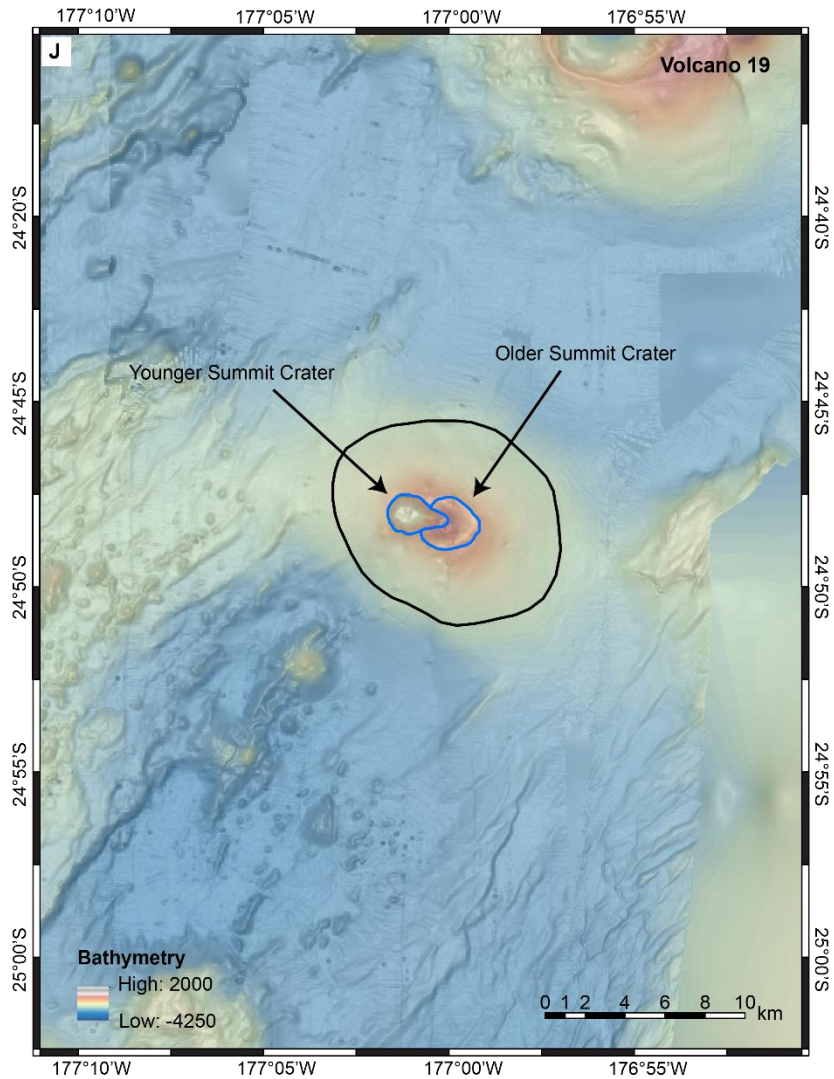
J
Volcano 19
Younger Summit Crater
Older Summit Crater
Bathymetry
High: 2000
Low: -4250
0 1 2 4 6 8 10 km
177°10'W
177°05'W
177°00'W
176°55'W
24°20'S
24°40'S
24°45'S
24°50'S
24°55'S
25°00'S

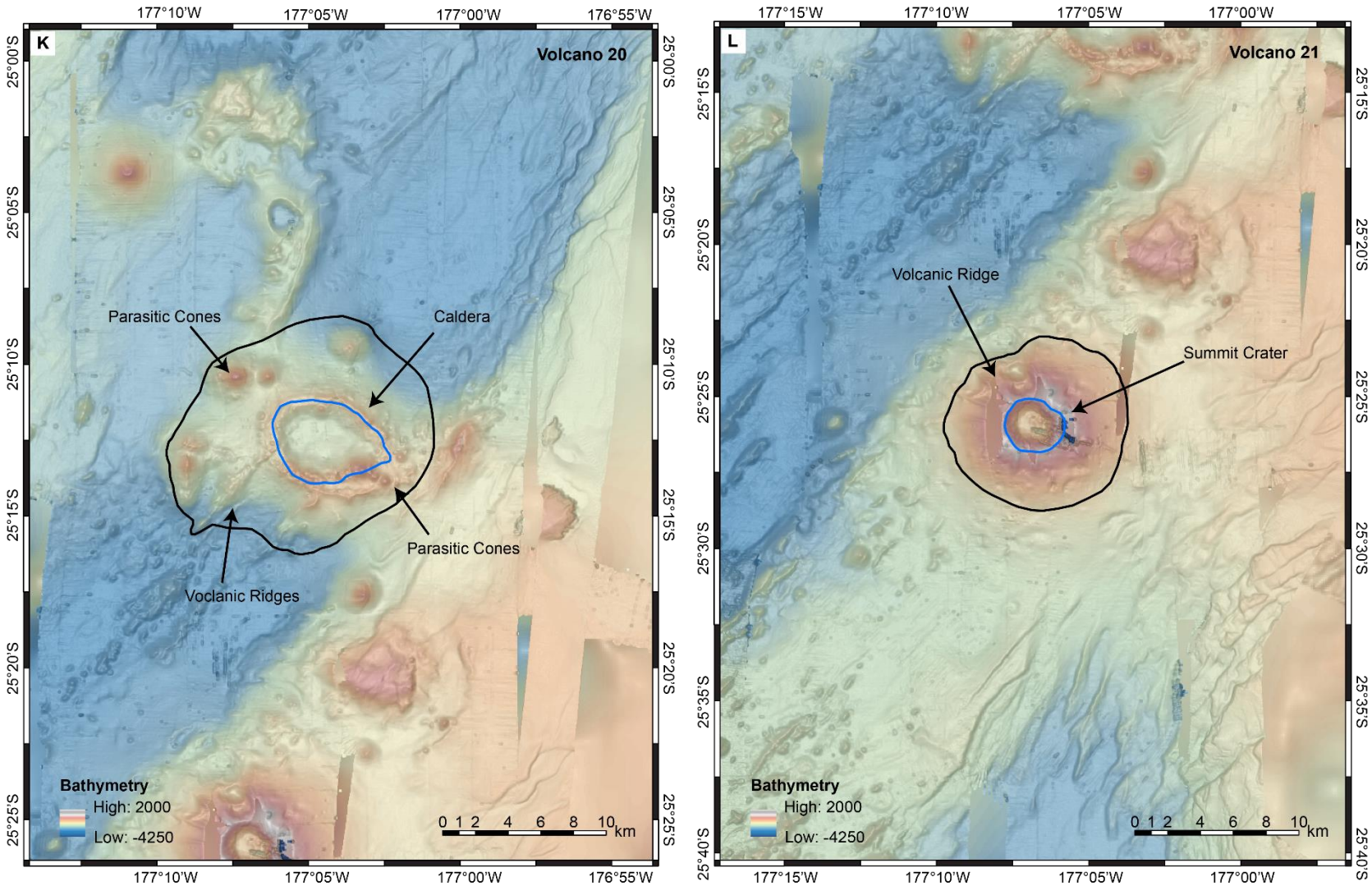
K
Volcano 20
Parasitic Cones
Caldera
Parasitic Cones
Voclanic Ridges
Bathymetry
High: 2000
Low: -4250
0 1 2 4 6 8 10 km
177°10'W
177°05'W
177°00'W
176°55'W
25°00'S
25°05'S
25°10'S
25°15'S
25°20'S
25°25'S
L
Volcano 21
Volcanic Ridge
Summit Crater
Bathymetry
High: 2000
Low: -4250
0 1 2 4 6 8 10 km
177°15'W
177°10'W
177°05'W
177°00'W
25°15'S
25°20'S
25°25'S
25°30'S
25°35'S
25°40'S

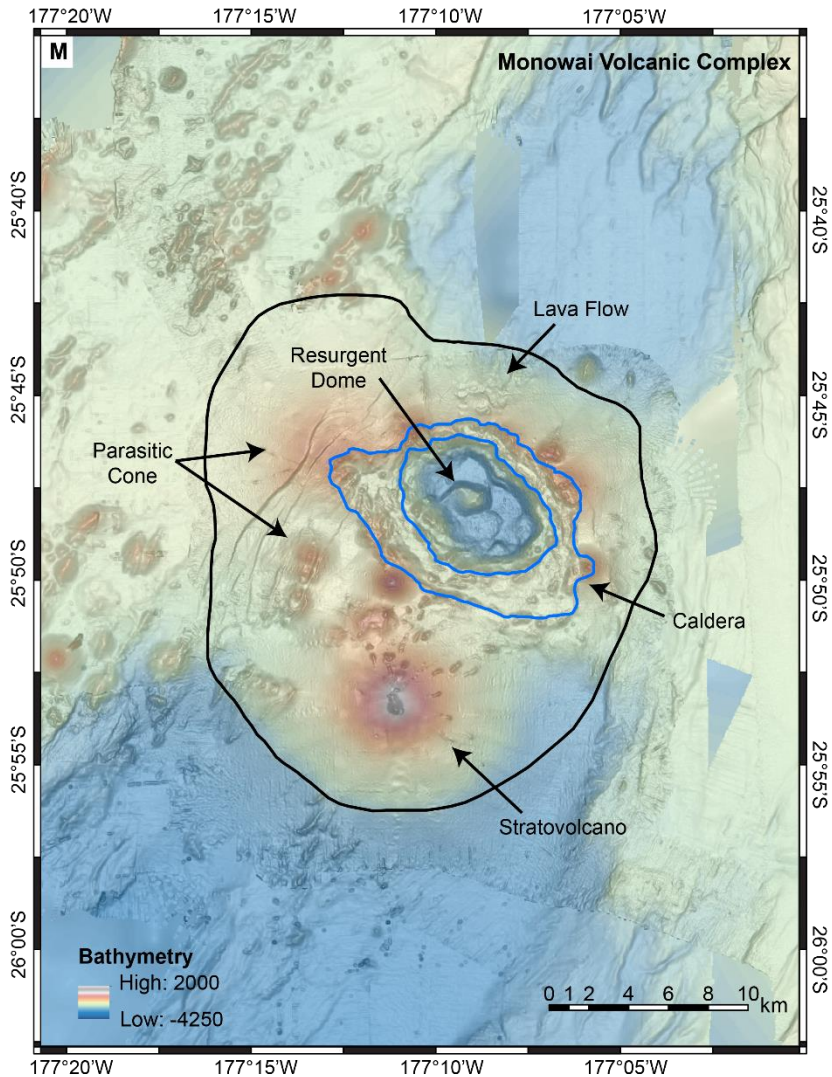

Figure 3.5 Bathymetric maps of individual volcanic centers, combining ship tracks from ship cruises SO-167, SO-192, SO-215 (aboard R/V *Sonne*), and TN-309 (aboard R/V *Thomas G. Thompson*) combined with GMRT datasets. (a) Volcano 1-2, (b) Volcano 3,

(c) Volcano 4-6, (d) Volcano 7, (e) Volcano 8, (f) Volcano 14, (g) Volcano 15, (h) Volcano 16, (i) Volcano 18, (j) Volcano 19, (k) Volcano 20, (l) Volcano 21, and (m) Monowai. Black shapes show the boundaries used for the area and volume calculations of the volcanic centers. Blue shapes show the boundaries used for the volume calculation of the calderas and craters. Area and volumes shown in Table 2.4.

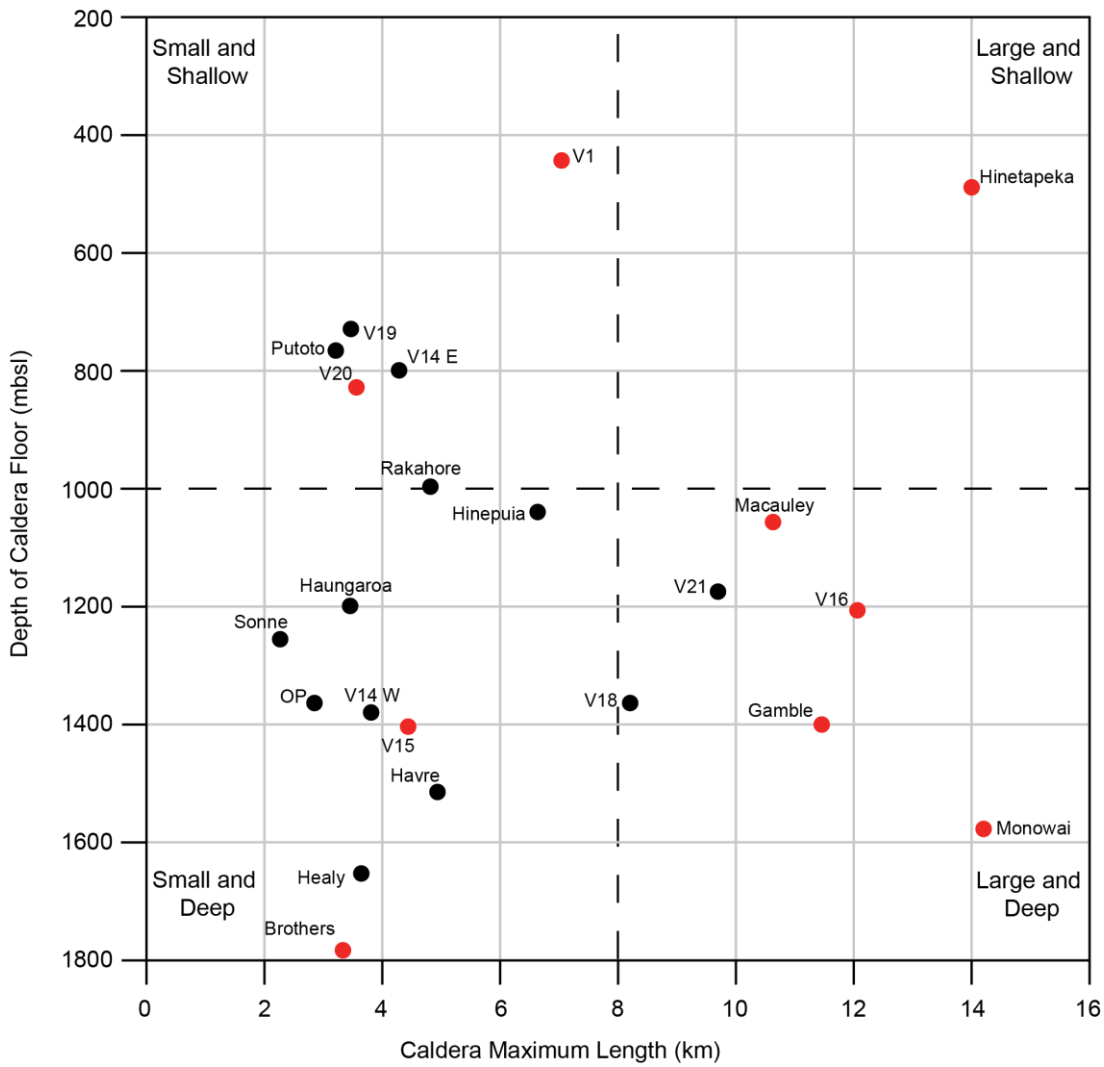

Figure 3.6 Plot of caldera size (maximum length) versus the water depth of caldera floor for major Tonga-Kermadec calderas, including the summit craters of volcanic cones (black circles) and larger caldera volcanoes (red circles). The plot has been divided into four quadrants: small and shallow calderas, large and shallow calderas, small and deep calderas, and large and deep calderas. Within the small and shallow quadrant (<8 km length and <1000 mbsl) we observe smaller caldera volcanoes (V1 and V20), which are still either deeper or larger than the summit craters of the cone volcanoes in this quadrant. The large and shallow quadrant (>8 km length and <1000 mbsl depth), only the caldera volcano Hinetapeka is present, which is a shallow caldera relative to its size. The small and deep (<8 km length and >1000 mbsl depth) is dominated by summit craters of cone volcanoes, which are small in size but exhibit a range of crater floor depths. The large and deep quadrant (>8 km length and >1000 mbsl depth) is dominated by the large caldera volcanoes. Most notably is Monowai which is the largest and one of the deepest caldera volcanoes along the Tonga-Kermadec arc.

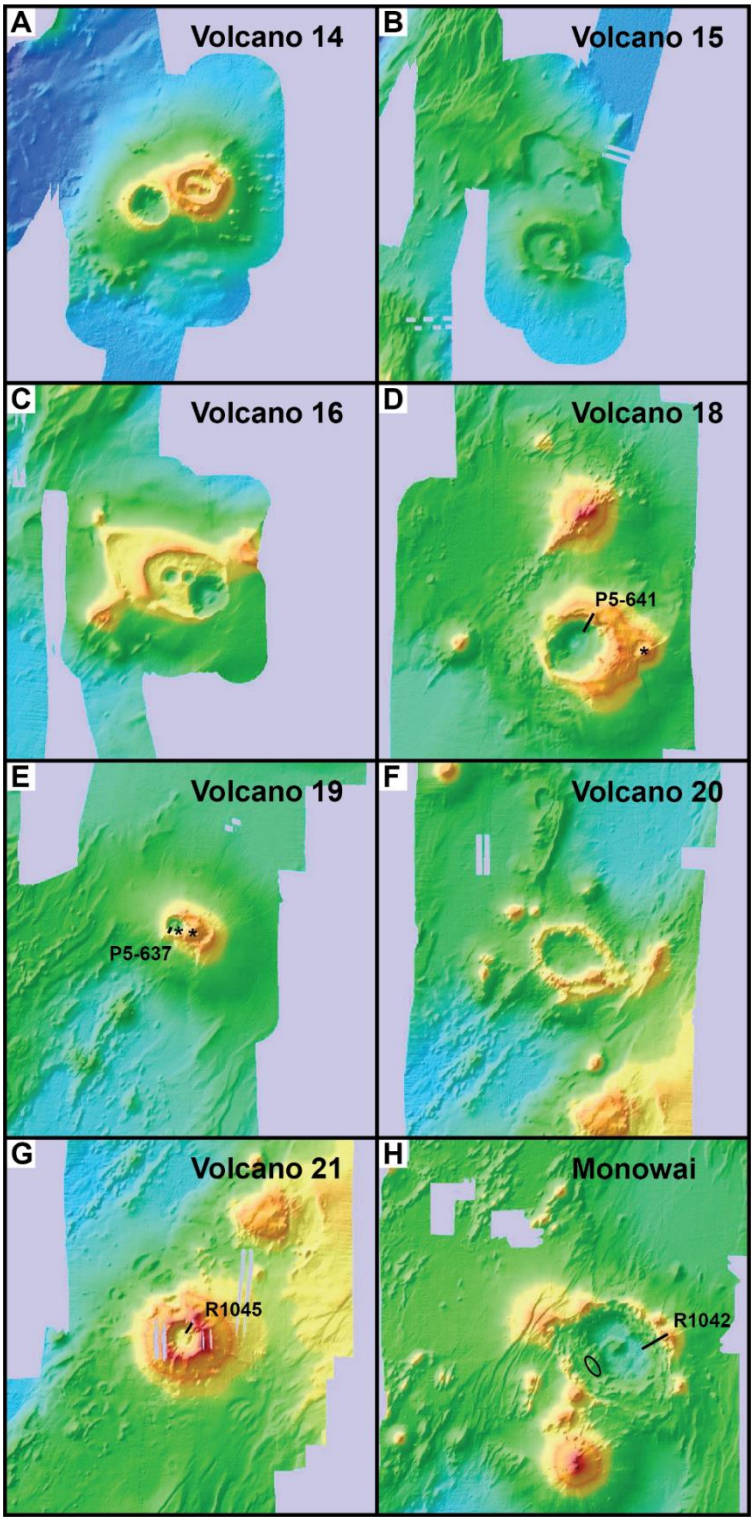

Figure 3.7 Close view of the bathymetric maps of individual volcanic centers from the research cruise SO-192 (aboard R/V *Sonne*). (a) Volcano 14, (b) Volcano 15, (c) Volcano 16, (d) Volcano 18, (e) Volcano 19, (f) Volcano 20, (g) Volcano 21, and (h) Monowai. PISCES and ROPOS dive

paths are denoted with black lines. Locations of active hydrothermal active is denoted with black stars and ellipses. At Monowai, the hydrothermal activity is located at Mussel Ridge (black ellipse).

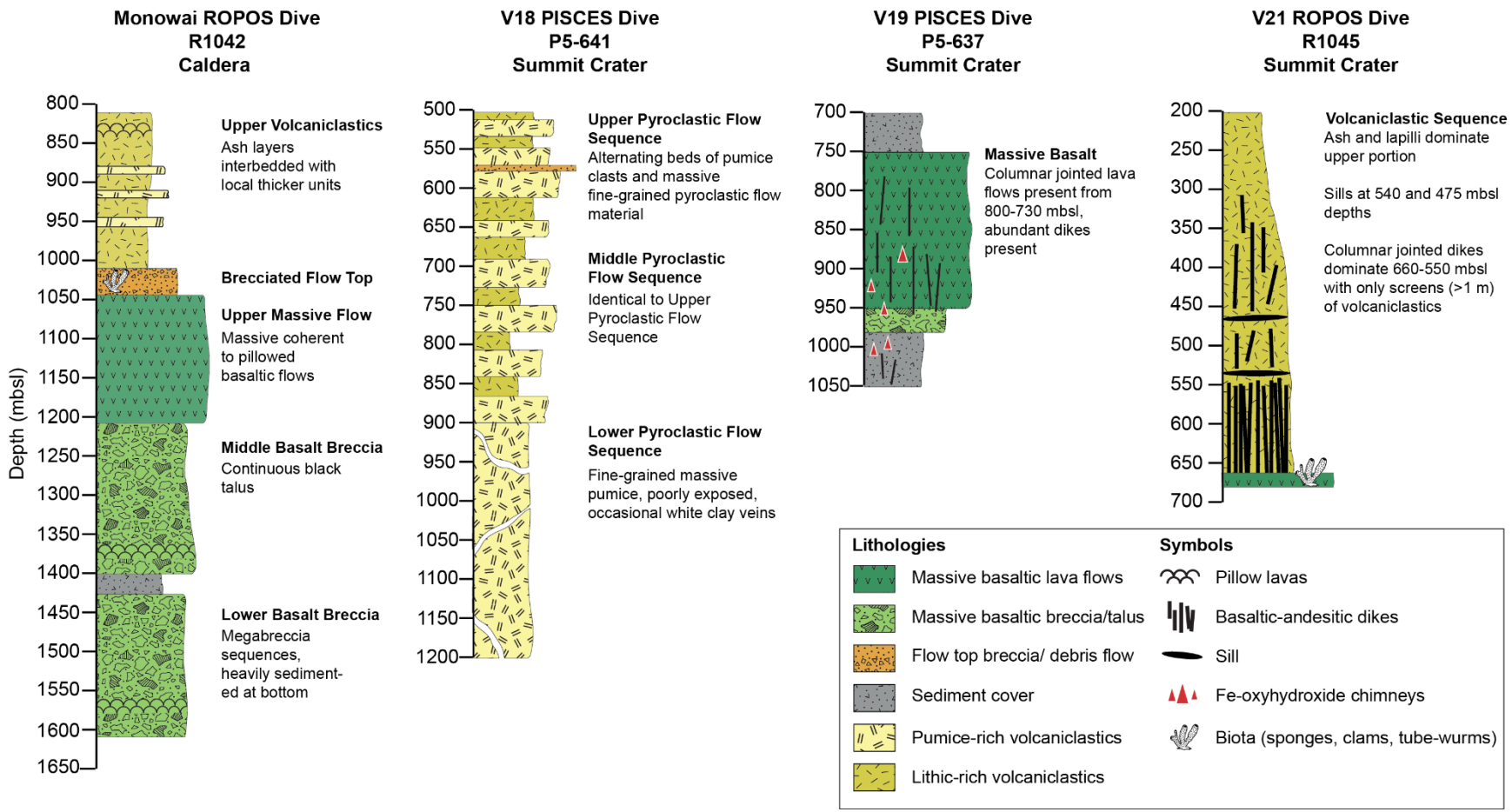

Figure 3.8 Stratigraphic columns of the Monowai caldera and cone volcanoes compiled from results of PISCES and ROPOS surveys. The Monowai caldera wall was surveyed during the R1042 dive (Schwarz-Schampera et al., 2007) (location in Figure 3.7h). The lower caldera wall is dominated by megabreccia sequences and talus blocks whereas the upper wall is dominated by massive flows and volcaniclastics (see text for details).The summit crater at Volcano 18 cone was surveyed during PISCES dive P5-641 (Stoffers et

al., 2006b) (location in Figure 3.7d). The entire crater wall is dominated by pyroclastic flow sequences (see text for details). The western crater of Volcano 19 was surveyed during the PISCES dive P5-637 (Stoffers et al., 2006b) (location in Figure 3.7e). The base of the section is concealed by sediment and volcanic talus; the middle and upper crater wall are dominated by massive columnar-jointed basalt flows and abundant dikes. The crater of Volcano 21, surveyed during ROPOS dive R1045 (Schwarz-Schampera et al., 2007) (location in Figure 3.7g), is similarly dominated by mafic dikes in the lower part and volcaniclastic material in the upper part.

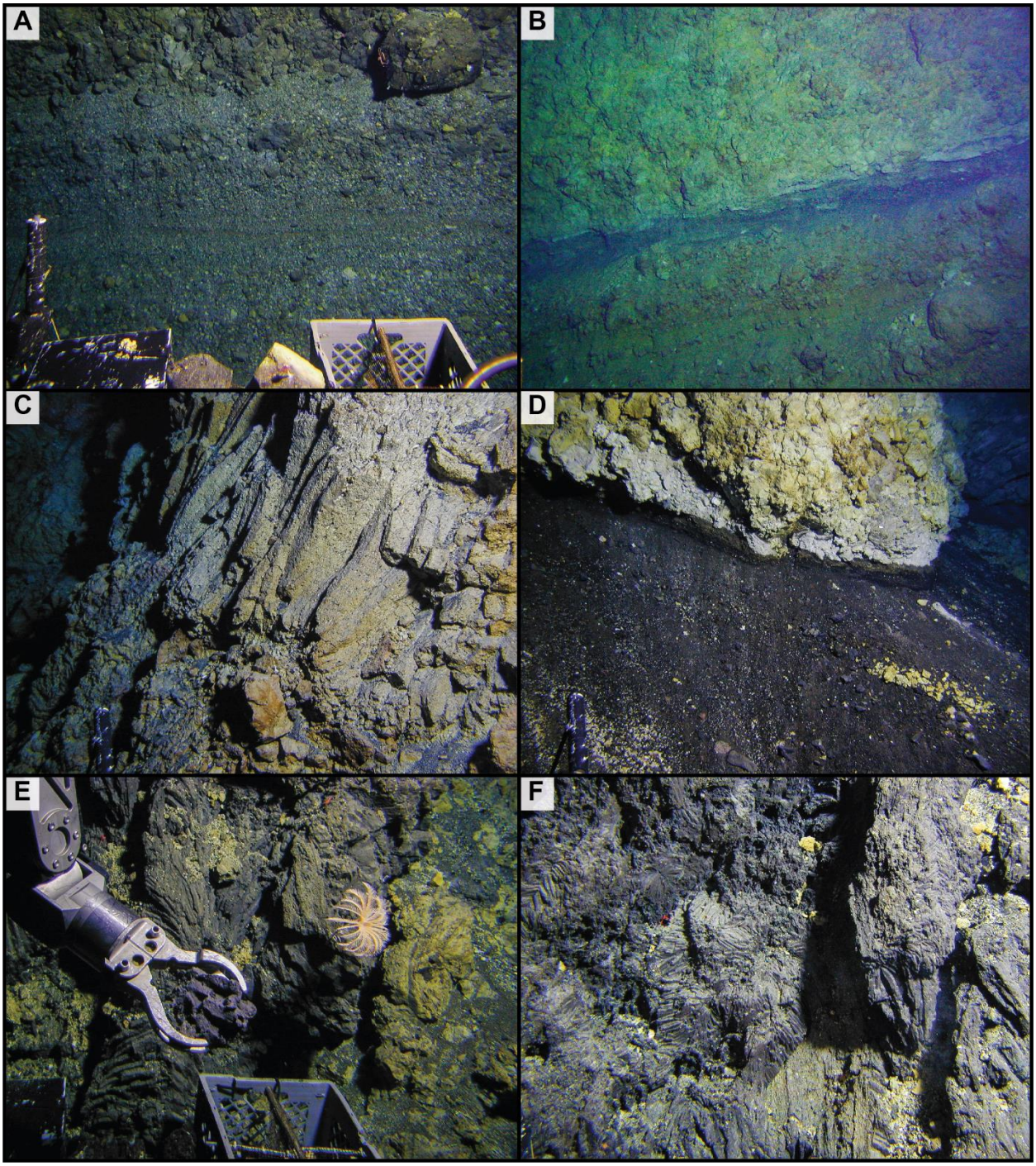

Figure 3.9 Bottom photos of Volcano 18 collected during the PISCES dives in 2005 (Stoffers et al., 2006b). A) The lower unit consists of fine and coarse ash beds, overlain by a massive pumice bed at a depth of 584 mbsl (P5-641). B) Bedded fine and coarse ash beds divided from the overlying massive pumice bed by a dark basaltic ash layer at a depth of 747 mbsl (P5-640,). C)

Columnar jointing in a sub-welded massive dacitic pumice, indicating slow cooling, at a depth of 668 mbsl (P5-640). D) A massive dacitic pumice bed overlying a coarse, black basaltic ash bed, at a depth of 640 mbsl (P5-640). E) Sub-vertical contact (adjacent to the coral) between an enclave of dark andesitic pumice and a lighter dacitic pumice bed, depth of 637 mbsl (P5-640). F) Dark grey to black andesitic pumice within a lighter dacitic pumice bed, depth of 637 mbsl (P5-640). Irregular cooling joints suggest the andesitic enclave was injected into the cooler dacitic magma. (Supervising scientist during P5-640 and P5-641: Worthington).

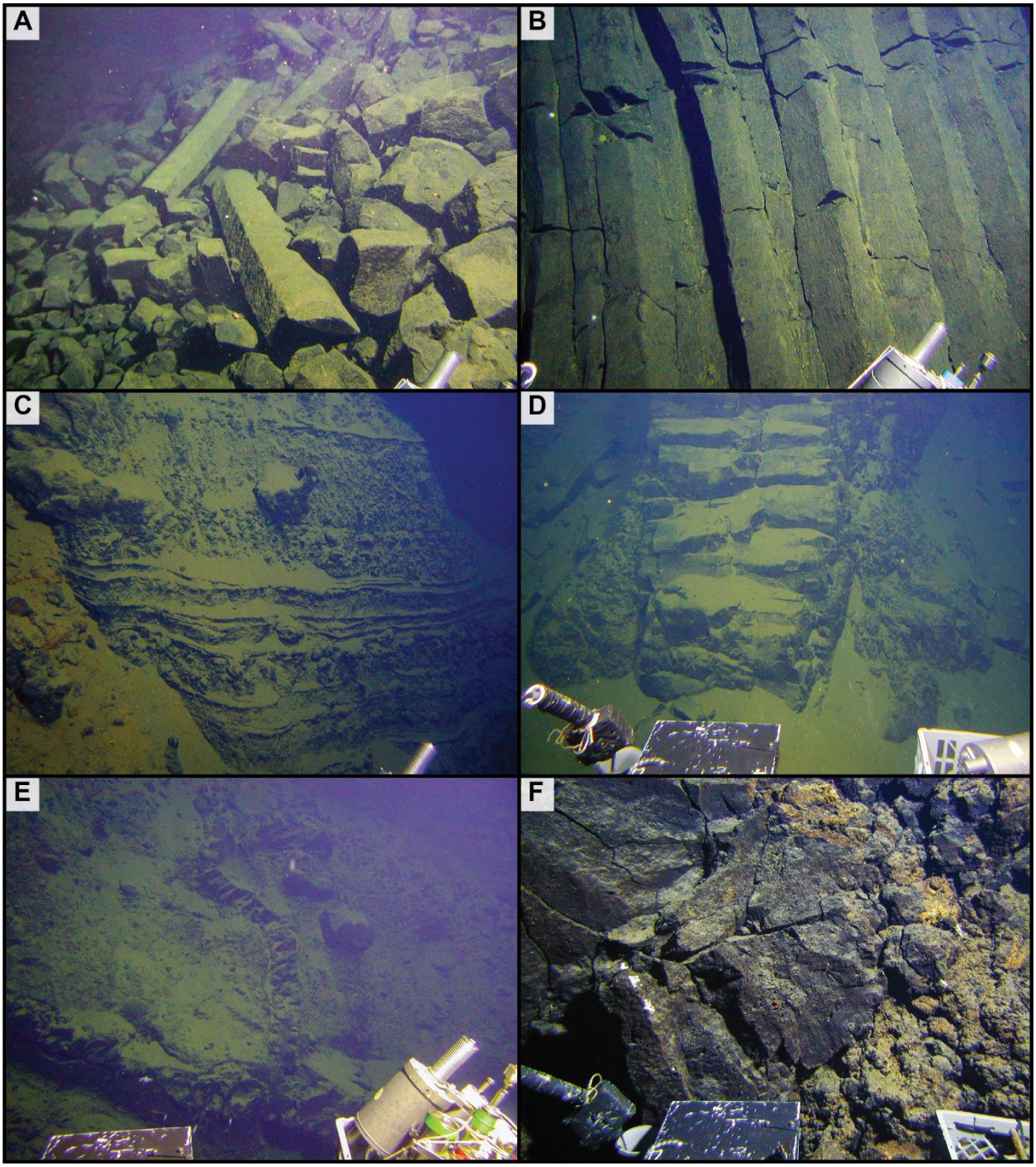

Figure 3.10 Bottom photos of Volcano 19 collected during the PISCES dives in 2005 (Stoffers et al., 2006b). A) Massive talus at the base of the caldera wall, comprised of massive lavas and large fragments of lavas displaying columnar jointing which have broken off from the caldera wall, depth of 902 mbsl (P5-635, supervising scientist: Massoth). B) Massive basalt-to-basaltic-andesite lavas, displaying columnar jointing along the caldera wall at a depth of 888 mbsl (P5-635, supervising scientist: Massoth). C) Some layers of lithic-rich volcaniclastic material and

massive lavas exposed under sediment cover, depth of 971 mbsl (P5-636, supervising scientist: Hannington). D) Massive dyke of basaltic composition at a depth of 896 (P5-637, supervising scientist: Schwarz-Schampera). E) Basaltic dyke at a depth of 901 (P5-638, supervising scientist: Massoth). F) Massive basalt-to-basaltic-andesite lavas at a depth of 477 (P5-639, supervising scientist: Hekinian).

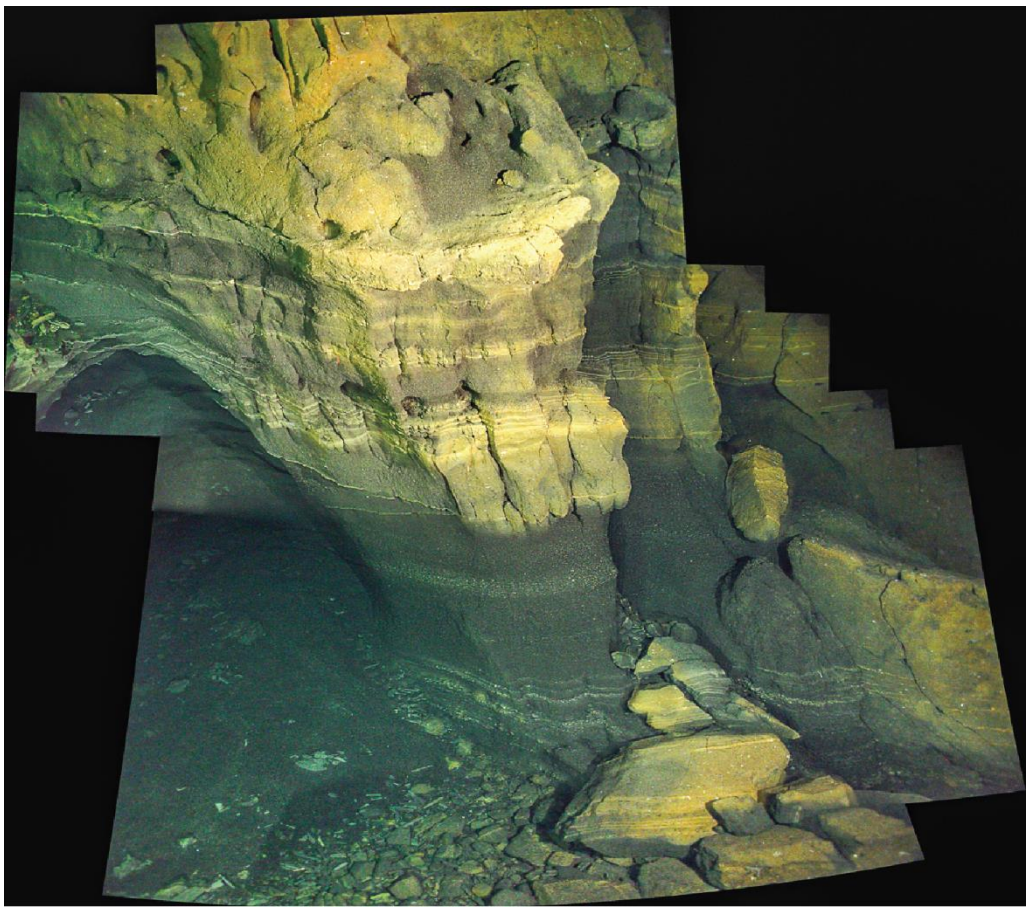

Figure 3.11 Composite of bottom photos showing a portion of the near vertical caldera walls with layered volcaniclastic deposits. The bottom darker section shows volcaniclastic sediments separated by fine ash beds. Some units in this section are comprised of angular lithics of various lithologies and ash with some reverse grading. Overlying these units are layers of well-bedded fine ash layers. Photos were collected during the ROPOS R1052 Dive during the SO-192 research cruise (Schwarz-Schampera., 2007).

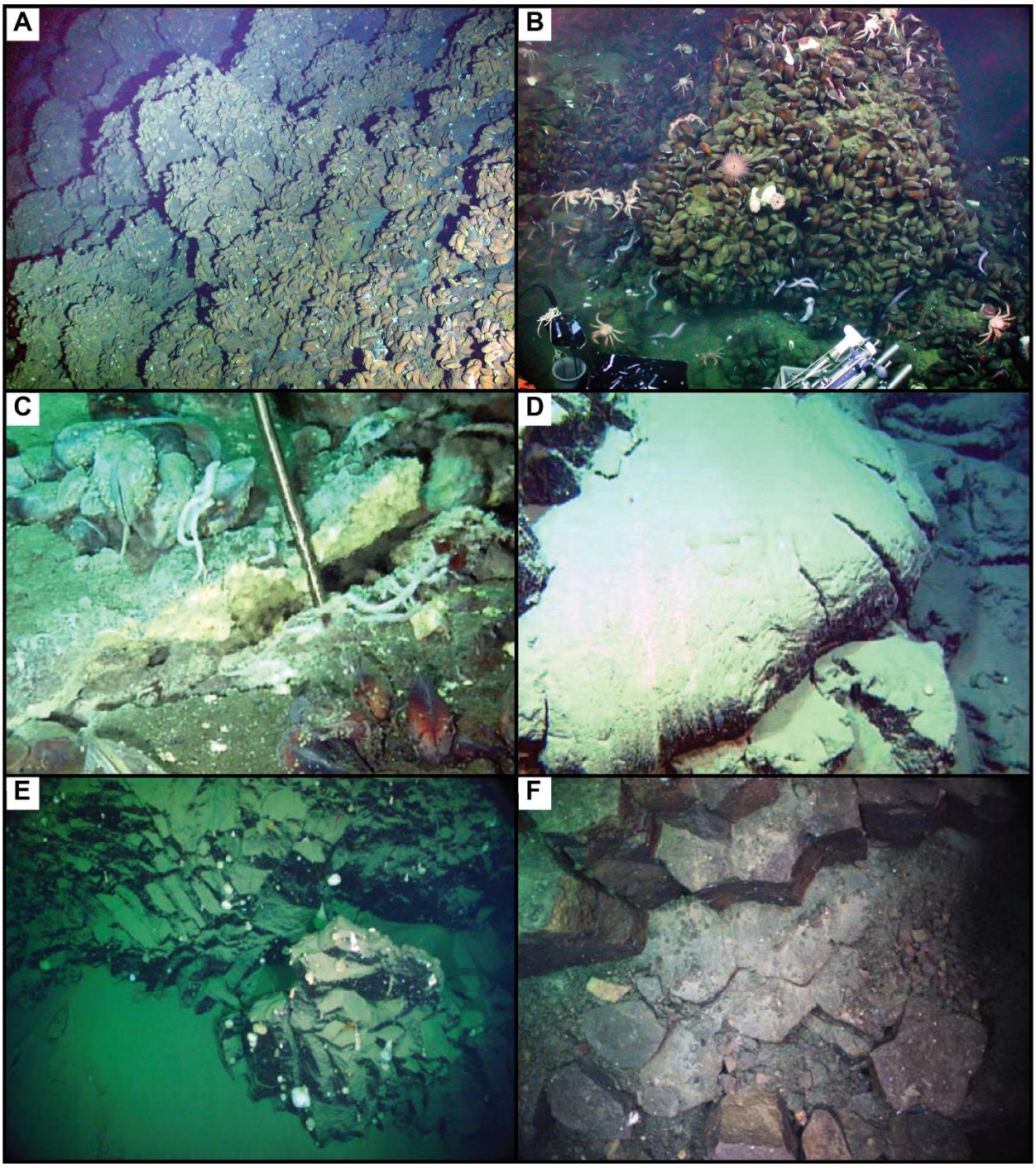

Figure 3.12 Bottom photos of the Monowai Volcanic Complex collected during the ROPOS dives in 2007 (Schwarz-Schampera et al., 2007). (a) Cluster of mussels along the flank and summit of Mussel Ridge. The substrate is comprised of massive coherent basalt and some visible weathered massive sulfides. Samples collected from the vent sites consist of barite-pyrite, sulphur-rich crusts, and altered vesicular basalt (ROPOS Dive R1043 and R1044). (b) Vent fauna and clusters of mussels along Mussel Ridge, covering altered massive basalt (PISCES dives). (c) Fluid sampling at a low-temperature discharge vent at Mussel Ridge collected during

the ROPOS dive R1043. (d) Lobate basaltic flow adjacent to a massive intrusive dike close to Mussel Ridge (photographed during R1043). (e) Highly sedimented caldera floor, sedimented covered basaltic lavas displaying columnar jointing. (f) Columnar jointed basalts associated with the intrusion of massive vertical dikes, observed during ROPOS dives.

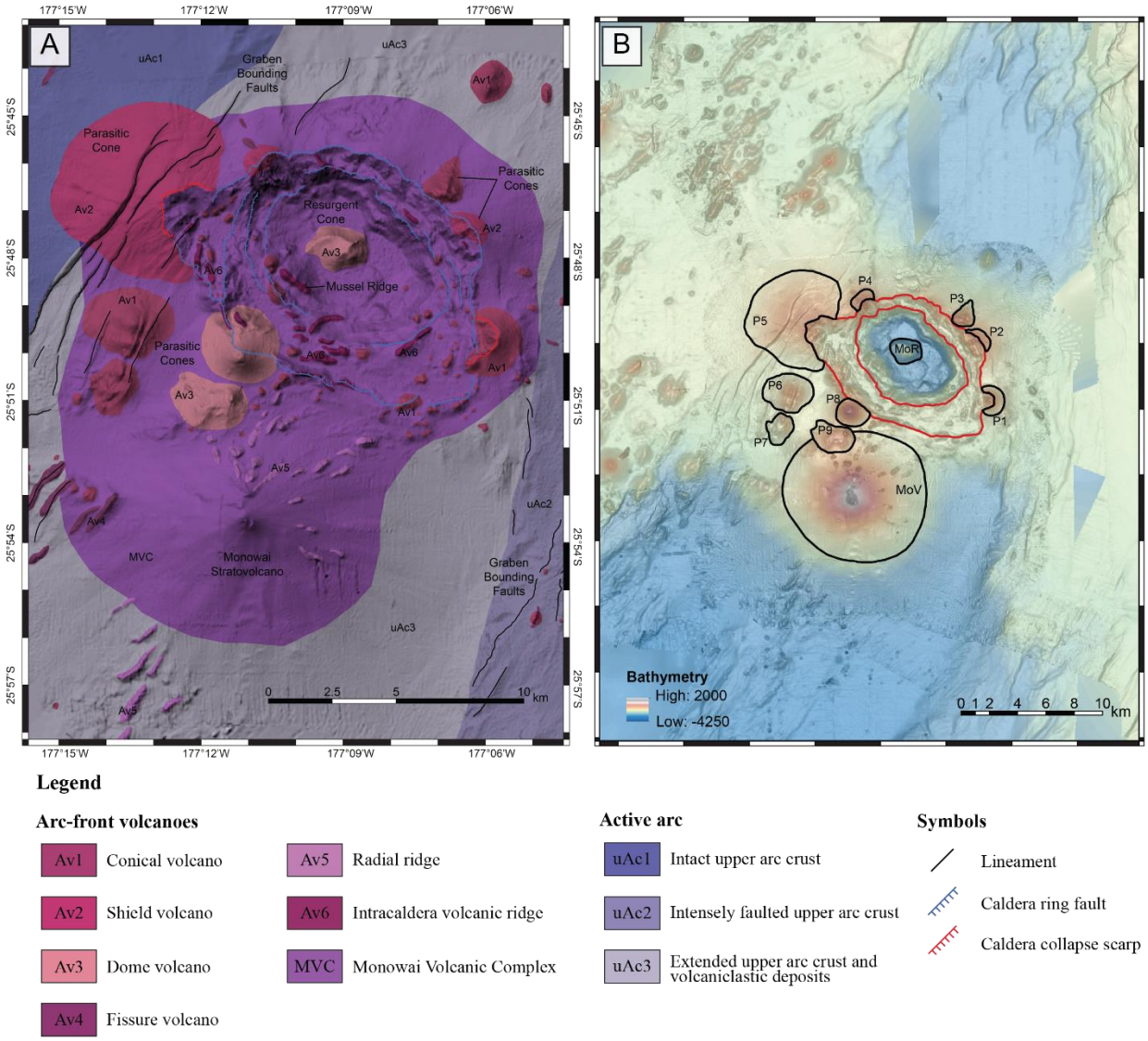

Figure 3.13 (a) Geological map of the Monowai Volcanic Complex at 1:50,000 scale. (b) Bathymetric map of the Monowai Volcanic Complex outlining the boundaries of the Monowai Stratovolcano (MoV), resurgent dome (MoR), and parasitic cones (P1-9) in black and the inner and outer Monowai caldera upper rims in red.

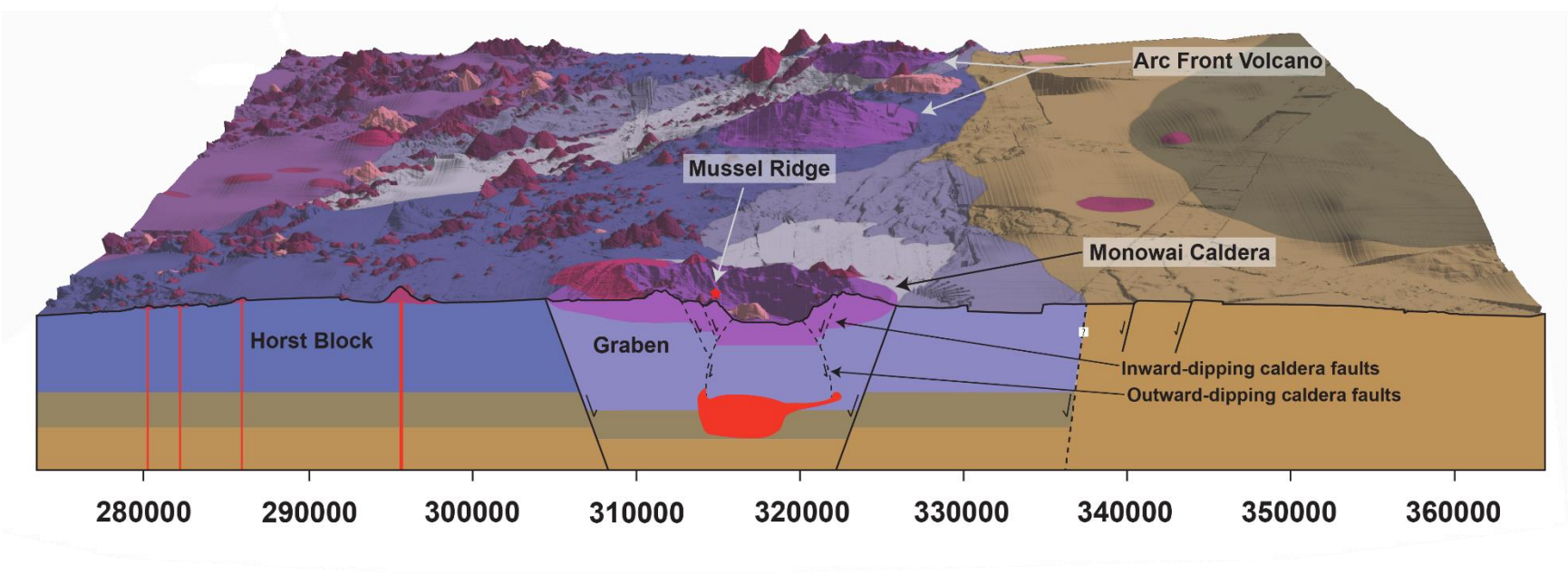

Figure 3.14 Block diagram of the Monowai graben showing the interpreted subsurface geology of the Monowai Caldera (Mussel Ridge: red star). The Monowai caldera is interpreted to contain the configuration of inner outward-dipping faults and outer inward-dipping faults. The inward-dipping faults are observed at surface as intracaldera ridges. The outward-dipping faults are interpreted to be the innermost structures intersecting the caldera floor.

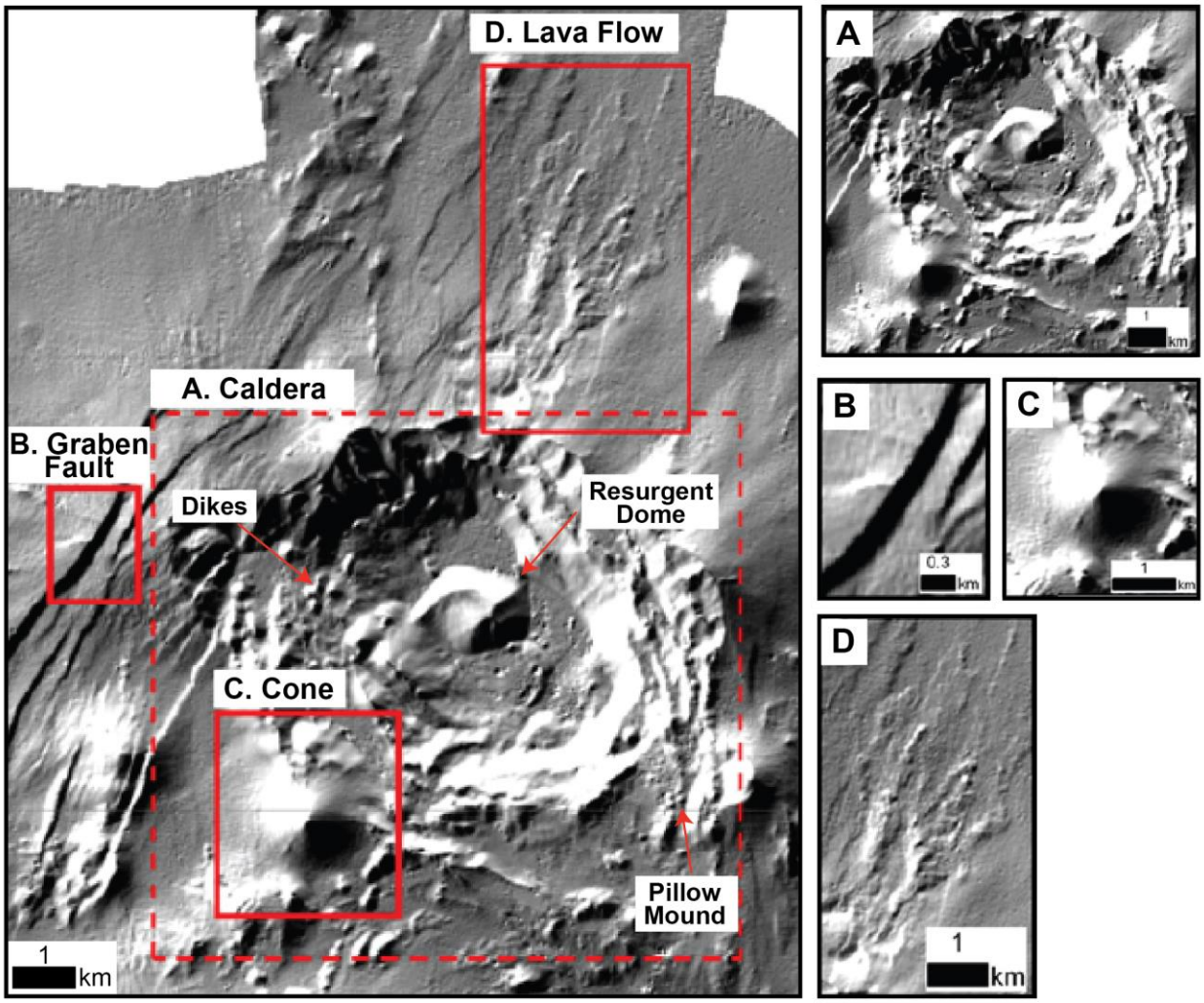

Figure 3.15 Bathymetric data from the RV Tangaroa (Wright et al., 2008) with the ArcGIS hillshade function applied, showing tectonic and magmatic features at the Monowai volcanic complex (modified from Wormald et al., 2012). Close up of (a) Monowai caldera and caldera bounding ring faults, (b) graben bounding fault, (c) parasitic cone on the SW caldera rim, and (d) lava flow to the NE of the Monowai caldera.

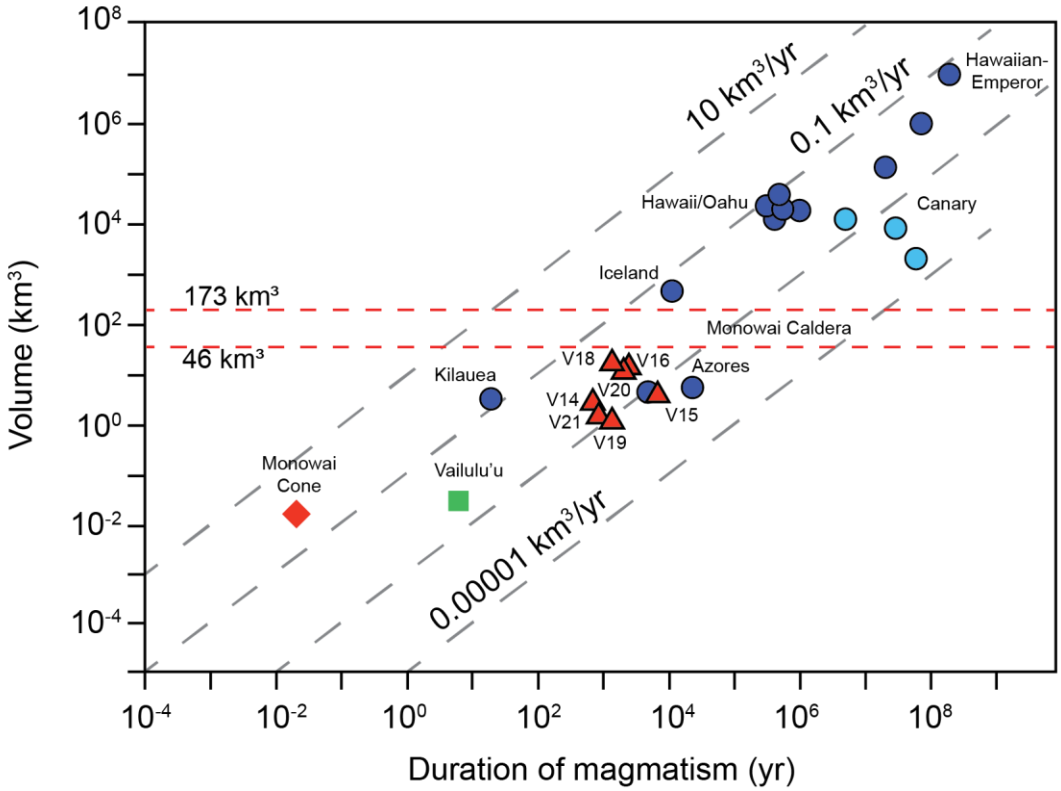

Figure 3.16 Plot of eruptive volume versus estimated duration of magmatism for selected submarine volcanoes (modified from Watts et al., 2012). Symbols: red diamond = Monowai cone (2011 eruption; Watts et al., 2012); red triangles = calderas from this study when possible; blue circles = selected seamounts and ocean islands (Crisp, 1984); green square = Vailulu'u, light blue circles = data from >9,000 seamounts which formed during 0-30 Myr, 95-125 Myr, and 105-110 Myr (Watts et al., 2006). We estimate the volcanic output of the Monowai volcanic complex to have been at least 3.5 x 10^{-4} km^3/yr, assuming it is no older than the 0.78 Ma age suggested by Paulatto et al. (2014). This is a minimum rate, because if the volcano was younger, there would have been less time to erupt the same volume of melt.

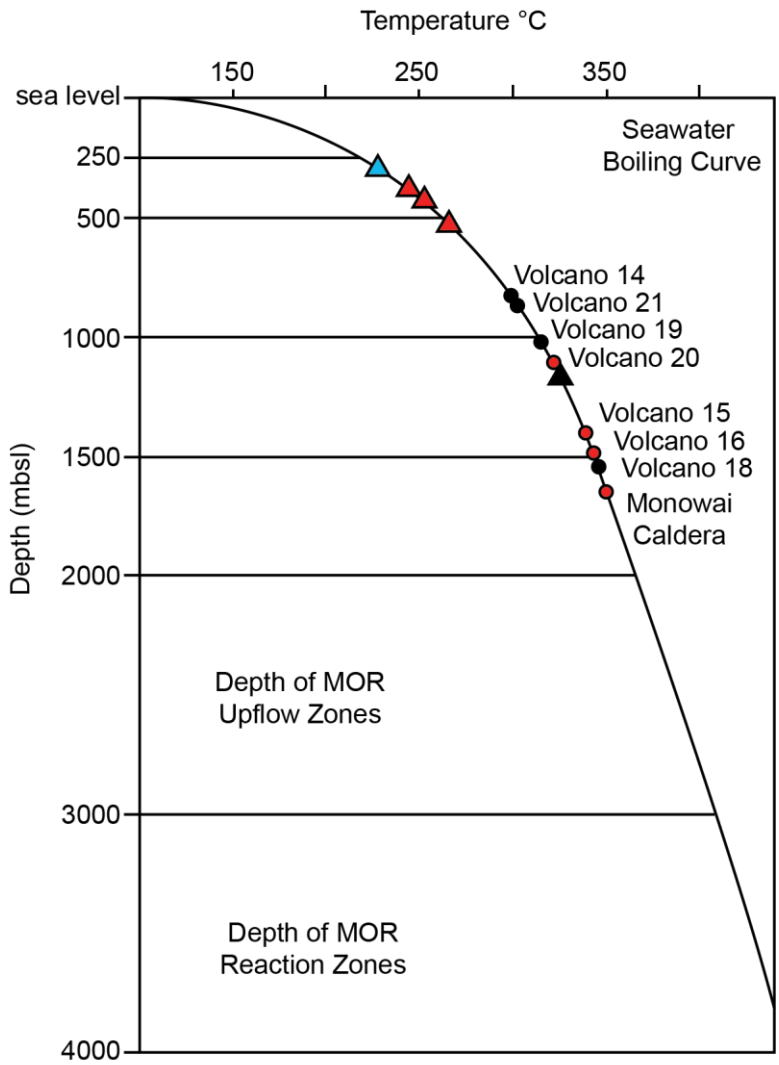

Figure 3.17 Boiling curve for seawater showing the maximum temperatures of submarine hydrothermal vents that are possible at the different volcanoes (red circles = caldera volcanoes, black circles = cone volcanoes) (modified from Stoffers et al., 2006a). Boiling vents were observed at Volcano 19 (red triangles) at depths of 540 mbsl (265 °C), 433 mbsl (253 °C), and 385 mbsl (245 °C). Low-temperature venting has also been observed at Mussel Ridge at Monowai (<60 °C; depth represented by black triangle) and at Volcano 18 (<10 °C, depth represented by blue triangle). The maximum possible temperatures of hydrothermal vents in the Monowai caldera would be ~350 °C.

Table 3.1 Summary Characteristics of Volcanic Centers of the Louisville Segment, Tonga Arc

Volcano	Feature (if multiple cones)	Latitude (S)	Longitude (W)	Volcano Type	Diameter (km)	Height (km)	Summit Depth (mbsl)	Caldera/Crater Dimensions (km)	Caldera/Crater rim depth (mbsl)	Caldera/Crater floor depth (mbsl)	Composition[a]	Description
Volcano 14	Eastern Cone Western Cone	23°34’	176°41’	Cone	13 11	1.5 1.2	480 780	4.2 x 3.2 3.9 x 3.6	480 780-920	780-820 1420	Basaltic-Andesite	Two cones, one contains a summit crater
Volcano 15		23°52’	176°46’	Caldera	12	0.7	1080	4.7 x 3.9 (summit), 8 (old, eroded caldera)	1080	1420	Basaltic-Andesite	Nested calderas, large old caldera to the NE
Volcano 16		24° 11’	176° 52’	Caldera	19	1.3	550	8 x 5.6	800	900	Dacite	Nested calderas
Volcano 18	Northern Cone Southern Cone	24°29’ 24°35’	176°55’ 176°54’	Cone	10 14	1.1 1.1	190 150	N/A 6.9 x 6.3	N/A 390-950	N/A 1520	Basalt Andesitic-Dacite	Two cones; one contains a summit crater distinct line of pyroclastic cones
Volcano 19		24°48’	177°01’	Cone	14	0.9	450	1.8	850	1025	Basalt	Cone with a summit crater
Volcano 20		25°12’	177°05’	Caldera	11	1.1	700	6.8 x 4.9		1150	Basaltic-Andesite	Caldera volcano
Volcano 21		25°25’	177°05'	Cone	13	1	160	3	160-400	800-850	Basaltic-Andesite	Cone with a summit crater
Monowai Volcanic Complex	Volcano Caldera	25°50’	177°10'	Caldera	15	0.9	98	N/A 14.2 x 8.8	N/A 600-850	N/A 1630	Basaltic-Andesite Basaltic-Andesite, Dacite	Large stratovolcano and caldera complex

[a] Compositions for each volcano are indicated based on completed research dives and samples collected. Volcano 14-16 are determined from samples collected during the SO-167 research cruise (Stoffers et al., 2002). Volcano 18 was sampled during the research cruise SO-167 (Stoffers

et al., 2002) and SITKAP (PISCES) (Stoffers et 2006b). Volcano 19 was sampled during the research cruise SO-167 (Stoffers et al., 2002), SITKAP (PISCES) (Stoffers et 2006b), and SO-192 (ROPOS) (Schwarz-Schampera et al., 2007). Volcano 20 was sampled during the research cruise SO-167 (Stoffers et al., 2002) and NZAPLUME III (Graham et al., 2008). Volcano 21 was sampled during the research cruise SO-167 (Stoffers et al., 2002), NZAPLUME III (Graham et al., 2008), and SO-192 (ROPOS) (Schwarz-Schampera et al., 2007). The Monowai Volcanic Complex was sampled during the research cruises NZAPLUME III (Graham et al., 2008), NZASRoF (Embley et al., 2005), and SO-192 (ROPOS) (Schwarz-Schampera et al., 2007).

Table 3.2 Calculated Volumes of Volcanic Centers of the Louisville Segment, Tonga Arc

Volcanic Center	Area (km^2)	Constructional Volume[a] (km^3)	Caldera Volume[b] (km^3)	Caldera/Crater
Volcano 14	165	77	3.2 1.8	Western summit crater Eastern summit crater
Volcano 15	131	36	10.8 4.6	Northern nested calderas Southern nested calderas
Volcano 16	286	146	13	Caldera
Volcano 18	243	26 (Northern cone) 99 (Southern cone)	17	Southern summit crater
Volcano 19	84	25	1.4 0.9	Young summit crater Old, infilled crater
Volcano 20	161	83	12	Caldera
Volcano 21[c]	80	27	3.5	Summit crater
Monowai	421	229[d]	29 17	Outer caldera Inner caldera

[a] Volumes are calculated using the ArcGIS polygon volume function, where volumes are determined above a minimum elevation value (Zmin). The volumes are determined using boundaries for each volcanic center where the flank slopes shallow to approximately horizontal shown in Figure 3.5.

[b] Caldera volumes are calculated using ArcGIS polygon volume function, where volumes are determined below a maximum elevation value (Zmax). The boundaries of the volume calculation are denoted by the caldera rims (shown in Figure 3.5).

[c] The Zmin was needed to be manually refined for Volcano 21 to remove processing artifacts from the volume calculation.

[d] The Monowai Volcanic Edifice volume is comprised of multiple parasitic cones (P1-9 = 9.9 km^3), the resurgent dome on the caldera floor (MoR = 0.5 km^3), the Monowai volcano (MoV = 13.8 km^3) and a large inflation zone (204.8 km^3). The boundaries of these structures are shown in Figure 3.13b.

Table 3.3 Summary of Rock Types Sampled from the Volcanic Centers of the Louisville Segment, Tonga Arc

Volcano	Composition	Sampled Rock Types[a]	Location	Cruise ID[b]
Volcano 14	Basaltic-Andesite	Pumice with devitrification banding and Px microphenocrysts Pumice, aphyric andesite, Px-phyric andesite Px pumice, aphyric basalt, aphyric andesite, minor aphyric dacite, Pl/Ol gabbro	Western flank Eastern crater Western crater	SO-167
Volcano 15	Basaltic-Andesite	Aphyric pumice, Qtz-pumice Pumiceous material with Ol/Pl basalt, Qtz-pumice with andesite fragments Aphyric pumice	Breached caldera wall Intra-caldera dome Northern embayment	SO-167
Volcano 16	Dacite	Hbl/Qtz pumice, Hbl/Qtz dacite, Qtz/Pl dacite, diorite Hbl/Qtz pumice with devitrification textures, andesite	Deepest nested caldera SW outer peak	SO-167
Volcano 18	Basalt, Andesitic-Dacite	Aphyric basalt, Pl-phyric basalt, Qtz/Hbl pumice Aphyric andesite, Pl-phyric andesite/dacite, aphyric pumice with devitrification textures	Northern cone flank Southern crater	SO-167 SITKAP (PISCES)
Volcano 19	Basalt	Ol/Pl basalt (displaying columnar jointing)	Young crater	SO-167 SITKAP (PISCES)
Volcano 20	Basaltic-Andesite	Basaltic lava, grey-brown altered rock with native sulfur and Py Microphyric andesite and dacite	Cone along southeast rim North caldera rim	NZAPLUME III
Volcano 21	Basaltic-Andesite	Pl/Cpx-phyric basalt and andesite, unconsolidated ash and lapilli	Summit crater	SO-192 (ROPOS)
Monowai	Basaltic-Andesite Basaltic-Andesite, Dacite	Basaltic andesite lavas, basaltic volcaniclastics Brt/Py and sulfur-rich crusts, basaltic lavas, aphanitic rocks with Py/Brt/realgar mineralization Pl-aphanitic to porphyritic basalt, scoria ash	Caldera Caldera vent sites Stratovolcano	SO-192 (ROPOS)

[a] Mineral abbreviation in the table are as follows; quartz (Qtz), olivine (Ol), plagioclase (Pl), pyroxene (Px), hornblende (Hbl), clinopyroxene (Cpx), pyrite (Py), and barite (Brt).

[b] See Table 2.1 for relevant research cruise references.

Table 3.4 Comparison of Cone and Caldera Volcanoes

	Volcano	Ring Faults	Bench Faults	Cross Cutting Faults	Resurgent Domes
Caldera Volcanoes	Volcano 1	yes	no	yes: E-W and NE-SW faults cutting SW flank	yes: formed in center of caldera before collapsing; also, smaller cones along the caldera rim
	Volcano 15	yes: additional caldera faults throughout the nested calderas	no	no	yes: a cone and dome on the floor of the youngest caldera
	Volcano 16	yes: minor faults on SE flank in addition to those within the complex	yes: caused by the formation of the younger calderas within the older, eroded structure	yes: NE-SW faults cutting the NE and SW peaks	yes: small cone built within the largest of three craters in the youngest caldera
	Volcano 20	yes (remnant)	no	yes NE-SW	yes: cones present on the SE caldera wall
	Monowai	yes: multiple ring faults throughout caldera	yes: multiple inner benches	yes: NE-SW faults cutting the parasitic cones in the NW	yes: resurgent dome present in the center of the caldera floor
Cone Volcanoes	Volcano 14	no	no	no	yes: small cones/ridge formed on the eastern crater floor
	Volcano 18	no	yes: bench present on eastern crater wall	yes: NW flank of northern cone cut by NE-SW faulting	no
	Volcano 19	yes: on older crater	no	no	yes: old crater has been infilled by a younger cone
	Volcano 21	no	no	no	no

Table 3.3 Continued

Volcano	Parasitic Cones	Radial Dike Swarms	Fissure Eruptions	Sector Collapses	Elongated	Hydrothermal Activity
Volcano 1	yes: 1 km diameter to the E of volcano	yes	possibly control location of small cones	yes: along SE rim	yes: NW-SE	yes: sulphur gases, nontronite
Volcano 15	yes: small cones present on the flanks	no	no	yes: in the SW of the caldera wall	yes: NW-SE	no
Volcano 16	no	possible	no	no	yes: ESE-WNW	no
Volcano 20	yes: multiple cones surrounding the caldera volcano	no	yes: volcanic ridges trending NE on the SW flank	no	yes: NW-SE	no
Monowai	yes: multiple parasitic cones around the rim of the caldera	yes: on the flanks of the stratovolcano	yes: possibly resulting in Mussel Ridge	yes: inward along the NW and SE caldera rim	yes: NW-SE	yes: low-temperature vents, mussel beds, oxidizing sulfides
Volcano 14	yes: small volcanic domes on flanks	yes: eastern cone and crater	no	minor on eastern crater	no	no
Volcano 18	yes: northern cone cones forming a NE-SW lineament	no	yes: northern cone (18-km long)	no	no	yes: chlorite and clay-altered ash, diffuse venting on small parasitic cone
Volcano 19	yes: minor on SW and NE flanks of volcano	possible	no	yes: infilling cone has undergone partial collapse	no (nested craters)	yes: high temperature vents, barite-sulfide chimneys, Fe-oxide deposits
Volcano 21	no	yes: northern flanks contain radial dikes	no	yes: small sector collapse on northern flank	no	no

Chapter 4

Summary and Conclusions

Caldera volcanoes are among the largest volcanoes on Earth. Calderas are volcanic depressions formed by the eruption or evacuation of magma from a subsurface reservoir. The sizes of the calderas can vary greatly, from <1 km in diameter to over 70 km for some large continental calderas (Lipman, 2000; Cole et al., 2005; Branney and Acocella, 2015). Often calderas are sites of intense geothermal activity and mineralization, such as the Valles Caldera in New Mexico (Cole et al., 2005). The sizes and shapes reflect the underlying magma chamber as well as the regional stress regime which exert important tectonic control on fluid pathways and the thermal and hydrologic state of the calderas (Holohan et al., 2005).

More than 640 caldera volcanoes are known on the continents (Geyer and Martí, 2008), but the numbers in the oceans are less clear. There are estimated to be >24,000 discrete volcanoes in the oceans with heights of at least 100 m, including 8,500 that are more than 1 km high (Kim and Wessel, 2011; Sigurdsson, 2015). Most occur on the global mid-ocean ridges, which account for 75% of global volcanism, but many thousands are intraplate volcanoes (Harris et al., 2014). Hundreds of volcanoes are also known on the submarine portions of island arcs along the Pacific Ring of Fire, with at least 150 large stratovolcanoes now mapped on the Izu-Bonin, Mariana, and Tonga-Kermadec systems.

Many of the largest submarine volcanoes have summit calderas that range from a few hundred meters to 10s of kilometers in diameter, as on land. Calderas and smaller summit craters are particularly common on arc stratovolcanoes that dominate magmatic productivity at convergent margins (Embley et al., 2012). The largest submarine calderas (>10 km in diameter) occur at continental margin arcs (e.g., Santorini in the South Aegean Volcanic Arc; Tavui and Rabaul in easternmost PNG; Campi Flegrei in Italy; Palinuro Seamount in the Tyrrheninan Sea; Deception Island on the Western Antarctic Peninsula). Many are associated with rifting of thickened arc crust as in the Desmos Cauldron in the Manus Basin, or continental crust as in the Izena Cauldron in the Okinawa Trough (Martinez and Taylor, 1996; Kimura, 1985). The large Hakurei caldera in the Sumisu Rift (Taylor et al., 1991; Glasby et al., 2000) and the Monowai caldera in

the Tonga Arc (this study) are thought to have formed in arc crust that is actively rifting along pre-existing basement structures. Other large calderas occur in intraoceanic backarc settings, such as Niuatahi in the NE Lau Basin, the Kuwae caldera between Epi and Efate islands in Vanuatu, and the Nifonea caldera in the Vate Trough (Monzier et al., 1994; Embley and Rubin, 2018; Anderson et al., 2016). Smaller craters are common at the summits of cone volcanoes of intraoceanic arcs, such as Sumisu and Myojin in the Izu-Bonin Arc, East Diamante and West Rota in the Mariana Arc, Macauley and Gamble Seamounts on the Kermadec Arc (Tamura et al., 2005; references; Wright et al., 2006; Stern et al., 2007; Graham et al., 2008; Stern et al., 2014). Many intraplate and MOR volcanoes also have large summit calderas (e.g., Axial Volcano on the Juan de Fuca Ridge; Foundation Seamounts; Taney Seamounts: Hooft and Detrick, 1995; Clague et al., 2000; Coumans et al., 2015). The latter have similarities to large hot spot volcanic centers such as Kilauea on Hawaii, the Galapagos Islands, and Krafla on Iceland. The largest calderas are, however, found on the continents (e.g., >400 km^2 Valles Caldera; >2000 km^2 Yellowstone Caldera), reflecting the important control of crustal thickness in caldera formation.

Large calderas, both subaerial and submarine host a range of ore deposit types such as volcanogenic massive sulfide (VMS) deposits, epithermal Au-Ag veins systems, polymetallic veins, and some porphyry Cu systems (Sillitoe and Bonham, 1984; Rytuba, 1994; Gibson, 2005; John et al., 2008). Some of the largest island arc calderas are very similar in size and shape to large VMS-hosting calderas in the geological record, such as the Hokuroku Basin of Japan and possibly the Noranda “cauldron” in the Abitibi Greenstone Belt of Quebec (Cathles, 1993; Kerr and Gibson, 1993).

This chapter presents a comparison of the volcanic cones and caldera complexes of the southern Tonga Arc with other submarine calderas worldwide, compiled in a new Database of Submarine Calderas (Figure 4.1 Global map of database) (Appendix C). A quantitative analysis of the magmatic productivity of submarine calderas in different settings identifies a number of common features, including near and far-field geodynamic influences on their formation and particular configurations that are most closely associated with large-scale melting and magmatic-hydrothermal systems. For example, an association with thickened crust is evident and thought to be because this type of crust retains heat and melt and allows for emplacement of large magma

chambers. Magmatically robust oceanic caldera complexes have long been associated with mantle plumes (White et al., 1993; Geldmacher et al., 2005; Fallloon et al., 2007; Pietruszka et al., 2013). However, it is uncertain whether anomalous melting above a plume is the trigger of caldera formation or if thinning of the crust at calderas serves to tap the mantle more effectively than at other locations. These questions are addressed in the following discussion.

4.1 Global Database of Submarine Calderas

In this study, the physical attributes of more than 100 submarine calderas in five main settings have been compiled in a new database. The entries include calderas in mid-ocean ridge settings, intraplate settings, rifted continental margins, volcanic arcs at ocean-continent collisions, and subduction related arc-backarc basins. The distribution of the calderas is shown in Figure 4.1 and their key attributes are listed in below and in Appendix C. The database was compiled from the literature and from existing volcano databases, such as the Smithsonian Global Volcanism Program (Global Volcanism Program, 2013). Attributes of the calderas were assigned from data and descriptions in the cited references. Caldera shapes and dimensions were also determined independently from inspection of General Bathymetric Chart of the Oceans (GEBCO Compilation Group, 2021), Global Multiresolution Topography (GRMT) (Ryan et al., 2009), and the global gravity data sets (Sandwell et al., 2014). For the subaerial portions of some volcanoes, Google Earth Pro v. 7.3.4 was used for structural measurements.

The attributes table includes entries for location, crustal type/thickness, stress regime, geodynamic setting, composition, rock types, volcanic facies (e.g., predominance of coherent or volcaniclastic deposits), caldera type, activity, presence of resurgence cone or dome (height and diameter if possible), structural measurements (lengths, eccentricity, orientation of axis, elongation direction, area, volume, regional structure orientation, β value, depths of the caldera floor and rim, subsidence), age, presence of faults (amount and throw if possible), mineralization if present, temperature of active venting, alteration cruise ID and research vessel, samples collected, and references. Names of the calderas were included where accepted names have been published (e.g., from the GEBCO Undersea Feature Names database). The latitude and longitude of the approximate center of each caldera is recorded in decimal degrees, together with a general

location name. The crustal type and setting are defined as either continental arc/back-arc, continental rift, continental arc, intraoceanic arc, intraoceanic back-arc, and oceanic. When possible, estimates of crustal thickness are recorded, generally as a range. The geodynamic settings include the arc front, back-arc basin, mid-ocean ridge, rift zone, intraplate hot spot, and continental hot spot, and are classified according to the stress regime (generally extensional or transtensional). The type of caldera is also defined as (1) a single caldera independent of other structures; (2) nested calderas; (3) a caldera complex with overlapping caldera structures and volcanic edifices of different ages; (4) a summit crater, which is generally a smaller depression located at the summit of a volcanic cone (illustrated in Figure 4.2).

The recorded dimensions of the calderas are assigned based on their long and short axis (Lmax and Lmin, respectively) measured from the edges of the rims. The orientations of these measurements are also recorded. These measurements are then used to determine the eccentricity (E) of the caldera, which is a measure of the deviation from a purely circular shape. The value of E is the ratio of the semi minor and semi major axis ($E = \sqrt{1 - \frac{b^2}{a^2}}$; "b" represents $\frac{1}{2}$ Lmin and "a" represents $\frac{1}{2}$ Lmax) with values ranging from 0 to 1 (a value of 0 corresponding to a perfect circle: illustrated in Figure 4.3). The direction of elongation is recorded, for example, by "elongated NW-SE. The depths below sea level of the caldera floor and the caldera rim are recorded as maximum, minimum, and average values, as most calderas are not uniformly flat. The average is the mid-point between the maximum and minimum values. Positive values are assigned to the portions of volcanoes above sea level; negative values are below sea level. The amount of collapse the caldera or the depth of the depression of a summit crater is indicated as "subsidence", although some depressions may have formed by explosive deformations rather than structural collapse. This value is determined from the absolute difference between the average floor and rim depth illustrated in Figure 4.4. Where possible, the area (km^2) and the volume (km^3) of the depression is recorded from the literature sources (black text) or calculated using ArcGIS analytical tools (red text). Where continuous bathymetric data or literature sources were not available, the areas and volumes were calculated assuming a simple ellipse and simple cylindrical or conical shapes (blue text).

Geological features, including seabed geomorphology and composition, fabric, major structures, and lithology are also recorded, where they have been established. The orientations of the caldera shapes, generally related to regional structures, are recorded as the acute angle between the regional structure and Lmax (β) (illustrated in Figure 4.5). Major regional structures that may host the calderas are identified (e.g., larger basin or rift-bounding faults). Where possible, the attributes table includes entries for the age of the caldera, if samples have been collected, if it is currently active, or if it has been determined in other ways (e.g., subsidence rate or basin opening). The explosivity index (VEI) is given, categorized using the caldera volumes and reference tables (Newhall and Self, 1982).

4.2 Summary Statistics of the Global Database of Submarine Calderas

Of the 121 calderas in the current database, 20 are oceanic, 17 are in continental crust (7 in submerged continental crust and 10 notable continental calderas), and 84 involve both oceanic and continental crust (Figure 4.6). At least 16 coincide with the global LIP occurrences (Bryan and Ernst, 2008; Ernst et al., 2008; Hoernle et al., 2010; Ernst, 2014), confirming a close link to mantle plumes in some cases. Of the calderas, 16 % are between 50 - 100 km^2 and only 15 % are larger than 100 km^2 in area. Of the calderas with areas greater than 100 km^2, 22 % are in continental crust, 33% are intraoceanic arc calderas, and 44% are island arc calderas (Figure 4.7). The largest intraoceanic calderas are Toba caldera (Barison Mountains; >2500 km^2), Taupo (Taupo Volcanic Zone; 876 km^2), Kussharo (Shiretoko-Akan Volcanic Chain; 408 km^2), Kikai (Ryukyu Island; 300 km^2), and Taal Lake (Luzon Island, Philippines; 267 km^2). By comparison, the largest continental calderas are Ngorogoro (Ngorongoro Volcanic Highlands; 285 km^2), Long Valley (Sierra Nevada; 450 km^2), Valles (Rio Grande Rift; 465 km^2), and Yellowstone which is greater than 2500 km^2.

The most common submarine calderas are found on intraoceanic arcs (n = 71), followed by mid-ocean ridges (n = 15) and back-arc basins (n = 13). Fewer examples are found in continental crust (n= 4), continental margin arcs (n = 5), intraplate oceanic environments (n = 4), and rift zones (n = 9). Figure 4.8 shows the variation in caldera sizes in different geodynamic settings. The calderas in continental margin settings average 77 km^2 with four over 50 km^2 in size (Tavui,

Rabual, Campi Flegrei, and Santorini). Of the intraoceanic arc calderas, 18 are over 50 km^2 (including Monowai, Volcano 16, Sumisu, Macauley, etc.), with an average size for these large calderas of 43 km^2 (excluding the megacaldera Toba). The back-arc basin calderas average 46 km^2 in size; mid-ocean ridge calderas are 13 km^2 on average, intraplate oceanic calderas are 38 km^2, and rift zone calderas are 214 km^2, generally reflecting the thickness of the underlying crust. Only 4 back-arc basin calderas (Deception, Palinuro, Epi, and Niuatahi), one mid-ocean ridge caldera (Taney Seamount), 2 intraplate oceanic calderas (Askja and Krafla), and 5 rift zone calderas (Reporoa, Ngorogoro, Taupo, Valles, Suswa) calderas are larger than 50 km^2. By comparison, all of the land-based calderas in continental settings (Yellowstone, Long Valley, Sturgeon Lake, and Crater Lake) are over 50 km^2, averaging 213 km^2 in size not including the megacaldera Yellowstone.

The majority of submarine calderas are elliptical to a degree, with only 12 calderas having an eccentricity of 0 (e.g., including Kolumbo, Esmeralda, Kick ‘em Jenny, Suiyo, etc.). Over 65 % of the calderas instead are slightly elliptical with eccentricities between 0 and 0.7, and relatively few have eccentricities between 0.7 and 1. The more elliptical calderas, with greater *E* values, are generally larger, while the smaller calderas tend to be more circular (Figure 4.9). One possible reason is that oblique rifting may facilitate collapse and play an important role in forming large caldera systems.

Caldera-forming eruptions can be a devastating volcanic event (e.g., Krakatau, Toba, Yellowstone, Rabaul, Taal, etc.). This is indicated in the database by the VEI magnitude. Based on eruptive volume and VEI (8), the Toba caldera formed from the largest and most explosive eruptions among the submarine calderas, with a volume of >1000 km^3 and plume height of >20 km (Newhall and Self, 1982; Mason et al., 2004). Many of the calderas (n = 89) have VEI magnitudes ranging from 4-6, with eruptive volumes ranging from >0.1 - >10 km^3. These caldera-forming eruptions can be major volcanic hazards to surrounding populations.

4.3 Discussion and Conclusions

Among the mapped volcanoes on the Tonga Arc, 5 are cone volcanoes with summit craters totalling 75 km^2. There are fewer caldera volcanoes, but the total area occupied by the calderas is more than 200 km^2. The average volume of the large calderas (16 km^3) is over 230% larger than the average summit craters (4.8 km^3) (see Table 3.2). The average size of the cone volcanoes is 51 km^3, whereas the average caldera volcano is 124 km^3. The average caldera volcano is 143 % larger than the cone volcanoes.

The largest submarine caldera of the Tonga Arc is at Monowai (46 km^3), over 30 km^3 larger than the following largest caldera, Volcano 16 (13 km^3). The deep summit crater at the Volcano 18 southern cone (17 km^3) slightly larger than the Volcano 16 caldera however still approximately 30 km^3 smaller than the large Monowai caldera (Figure 4.10). Major submarine calderas of a size similar to Monowai occur along other intraoceanic arcs or back-arc basins (e.g., Sumisu, Izu-Bonin Arc (39 km^3); W Roto, Mariana Arc (56 km^3); Niuatachi, Lau Basin (69 km^3). The largest intraoceanic arc caldera of similar size to Monowai is Niuatahi in the Lau Basin. A major difference between Monowai and Niuatahi and the other large submarine calderas, such as Desmos Cauldron and Izena Cauldron, is that the current rifting is occurring in arc crust close to the arc front rather than in the back-arc. Whereas Desmos and Izena are forming as a result of slab rollback and orthogonal extension, the formation of the Monowai graben and caldera is related to plate rotation and transtension (e.g., Baxter et al., 2020; see Chapter 2). This confirms that microplate dynamics as well as melt anomalies play an important role in the formation of the largest calderas.

Similar-sized caldera complexes are known on the Kermadec and Mariana arcs at the Macauley and West Rota volcanoes. The Macauley caldera is at least 35 km in and elongated 055°. The caldera rim has an average depth of 625 mbsl and the floor reaches 1125 mbsl, shallower than Monowai. Like Monowai, Macauley has numerous small cones along its western and southern rim in addition to a 700-m diameter, 300-m high post-caldera cone-on the inner eastern wall (Wright et al., 2006). In contrast to Monowai, which is basaltic, dacitic lavas and tephra have been recovered from Macauley, and the tephra ages are very young (~6.3 ka: Smith et al., 2003).

The silicic composition of the caldera is consistent with the shallow emplacement, thickened arc crust and more evolved arc lavas of the Kermadec arc. The mode of formation of the caldera is also interpreted to have been a mass expulsion of melt and pyroclastic material, compared to the more effusive eruptions at Monowai. The shallower water depths at Macauley promoted magma vesiculation and fragmentation (Llyod et al., 1996; Wright et al., 2003; Wright et al., 2006).

The West Rota Volcano is a large, 28-km diameter cone with a 10 x 6 km summit caldera located in the southern Mariana Arc. The caldera is elongated to the NNW-SSE with the caldera rims reaching 300 mbsl and a uniform caldera floor at 1500 mbsl (Basu, 2016). The levelling of the caldera floor is thought to be a result of infilling by intracaldera tuff and (Stern et al., 2007). ROV dives along the inner caldera walls revealed 900 m of the volcanic stratigraphy dominated by andesites at the lower wall and rhyolite and basalt in upper sections. The caldera formation is thought to have been associated with a major felsic eruption, possibly up to 40 km^3 in volume. The felsic magma is considered to be from a mid-crustal melt (Takahashi et al., 2007). The proximity of the volcano to the major West Rota Fault may explain the large felsic eruptions at this location that are not observed elsewhere along the Mariana Arc (Stern et al., 2007).

Compared to Macauley and West Rota, Monowai has had a complex geological history, dominated by the continuous opening of the Monowai Graben (Chapter 2). The deep subsidence of the caldera and progressive opening of the graben since 0.78 Ma have contributed to the voluminous basaltic.

Similar large basaltic calderas can be expected in thickened crust which is now undergoing rifting, promoted by oblique subduction, transtensional stress regimes, high heat flow, and mantle anomalies (e.g., plumes, LIPs). This contrasts with many large silicic continental caldera systems which on land, which include clusters of cones and domes produced by small scale pre-caldera eruptions as well as major collapses from the explosive evacuation of large magma chambers (Lipman, 2000). The pre-caldera volcanism commonly includes clusters of vents, generally in linear or arcuate patterns controlled by early ring faults or regional tectonic structures, or a combination of both. These characteristics have some similarity to the origin of

large deep marine caldera structures such as the Monowai volcanic complex, including the important role of basement structures in the localization of rifting and eventual caldera collapse.

Conclusion

The Lau-Tonga-Kermadec system is the fastest converging subduction zone on Earth, where old Pacific lithosphere is subducting beneath the Indo-Australian Plate. Extension in the back-arc region has separated the Tonga and Kermadec volcanic arcs from the remnant Lau and Colville ridges, with the current opening of the Lau Basin propagating southward towards the Havre Trough. Numerous researchers have speculated about the consequences of oblique subduction of the Pacific Plate and collision with the Louisville Seamount Chain (LSC), and in particular the bend in the arc where the LSC enters the trench. Prevailing stresses have segmented the Tonga-Kermadec system into 8 different sectors with varying arc-ridge morphology and arc-trench separation. The Louisville and Monowai segments occur immediately adjacent to the LSC. Here, both the arc and the near back-arc regions exhibit along-strike variation in their structure and magmatism resulting from the abrupt change in the orientation of the arc-trench system. The oblique convergence causes left-lateral strike-slip faulting along the Louisville Segment and rifting of the arc crust. Oblique extension, previously, is shown here to have caused significant intra-arc deformation, including graben-like structures crossing the full width of the arc. This deformation has strongly influenced the distribution of melt and the style of magmatism along the arc front. A previously inferred "seismic gap" at this location is now recognized as an area of intense faulting and magmatic activity.

This study presents a new compilation of marine geophysical data from 8 research cruises that investigated the area between 2002 and 2011. The first geological map of the Louisville and Monowai segments is presented at 1:500,000 scale, derived from high-resolution ship-based multibeam, satellite altimetry, magnetics, and direct seafloor observations and sampling. The mapping shows that evenly spaced arc-transverse faults, related to Pacific Plate convergence and southward compression due to the collision with the LSC, are the main controls on arc magmatism. The study shows that rifting of the thickened arc crust initiates in the arc-transverse strike-slip faults followed by normal faulting due to transtension in a series of en echelon rift grabens. These structures manifest at the arc front as "horst and graben structures" that are the precursors of arc rifting. The shallow crust, just prior to splitting of the arc, is intruded by dike-like bodies that feed fissure volcanoes and small cones along the horsts, whereas normal faulting

localized above deeper basement faults accommodates larger sill-like magma chambers and caldera volcanoes in the grabens. The locations of the grabens indicate a regional left-stepping segmentation of the arc. This pattern of rifting in the thickest part of the arc crust, caused by oblique convergence and ridge subduction, contrasts with conventional models of breakup in which all or most of the extension occurs in thinned crust at the rear of the arc.

The largest structure at the arc front is the Monowai graben, a 30-km wide rift bound by 300-m high extensional faults and traceable for at least 150 km across the arc front. This major feature of the arc contains the Monowai volcanic complex, which is the largest volcano of the Tonga-Kermadec arc. Three significant active hydrothermal systems have been found at arc-front volcanoes along the Louisville and Monowai segments. Most occur in summit calderas of still active volcanic cones, and exhibit different characteristics (e.g., high- vs low-temperature venting, boiling, magmatic contributions to the hydrothermal system) depending on the settings. A major control on venting along the arc front is water depth (900 m at Volcano 19 to over 1600 m at Monowai caldera), with the highest temperatures inferred for the deep vents and significant volcanic degassing at the shallow vents.

A comparison with caldera volcanoes elsewhere in the oceans and on the continents indicates that the presence of microplate dynamics, regional stress regimes, presence of basement structures, and melt anomalies are important factors in the formation of large caldera systems. Large calderas similar in size to Monowai occur in other intraoceanic arcs and back-arc basins where formation may be promoted by rifting in the back-arc or within the arc front, either resulting from slab rollback or plate rotation. The largest submarine and continental calderas show an elliptical nature, with the largest calderas generally showing an increasing eccentricity trend. This indicates a possible important control on forming these large caldera systems is oblique rifting, which can facilitate further collapse. The Monowai complex shows similarities with the large silicic calderas on land which host many pre-caldera features (e.g., cones and domes) and major collapse structures resulting from the evacuation of a large magma chamber. The pre-volcanism is generally controlled by either or a combination of early ring faults or regional tectonic structures. At Monowai and these large continental calderas, the importance of

basement structures in localizing the location of rifting and the subsequent caldera collapse is highlighted.

Large submarine calderas like Monowai are potentially important ore-forming environments, hosting a range of ore deposit types. The processes that form calderas also provide the heat, structural pathways for fluids, and sufficient host-rock permeability, required for the formation of the mineral deposits. Many ancient ore-hosting submarine calderas are only partially preserved or highly deformed, which makes it difficult to study these processes. Therefore, modern submarine calderas, and especially large back-arc megacalderas where the key features can be mapped in their entirety are important analogues. Understanding how these processes evolve over the life cycle of a submarine caldera complex can provide important guides for mineral exploration.

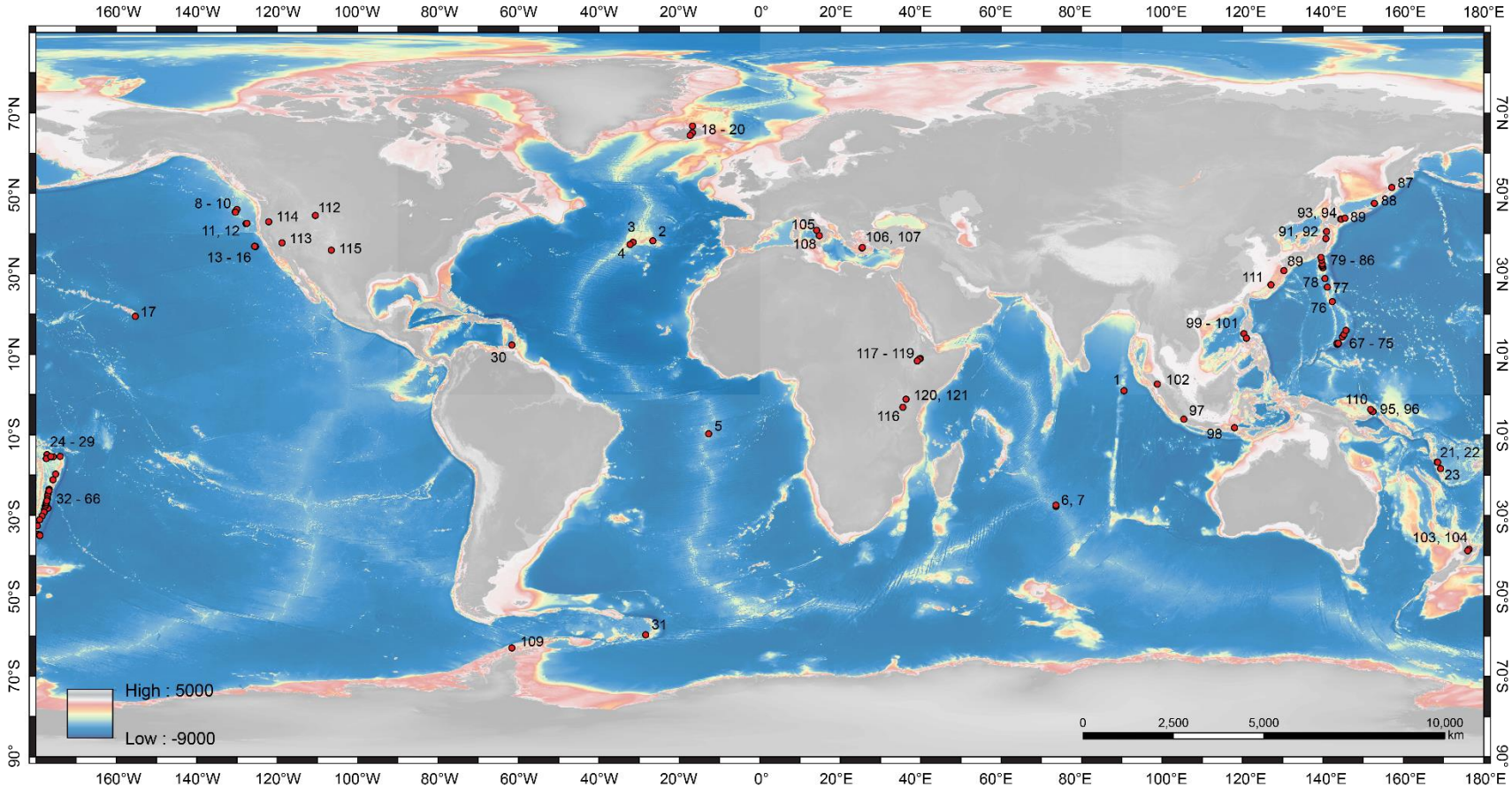

Figure 4.1 Global distribution of the 124 calderas included in the Database of Submarine Calderas. See Database of Submarine Calderas (Appendix C) for names of calderas.

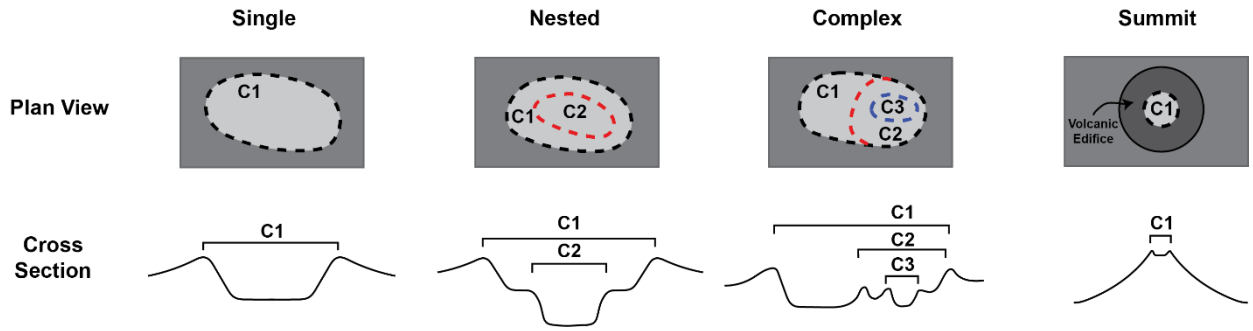

Figure 4.2 Schematic illustration of different major caldera types in plan view and cross section: (1) single caldera, (2) nested calderas, (3) caldera complex, and (4) summit crater.

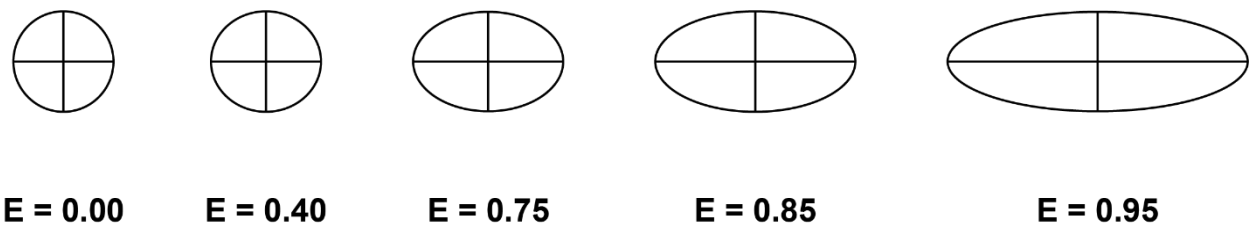

Figure 4.3 Schematic illustration of eccentricity values. E = 0 represents a perfect circle, with the caldera becoming more elongated as E approaches 1.

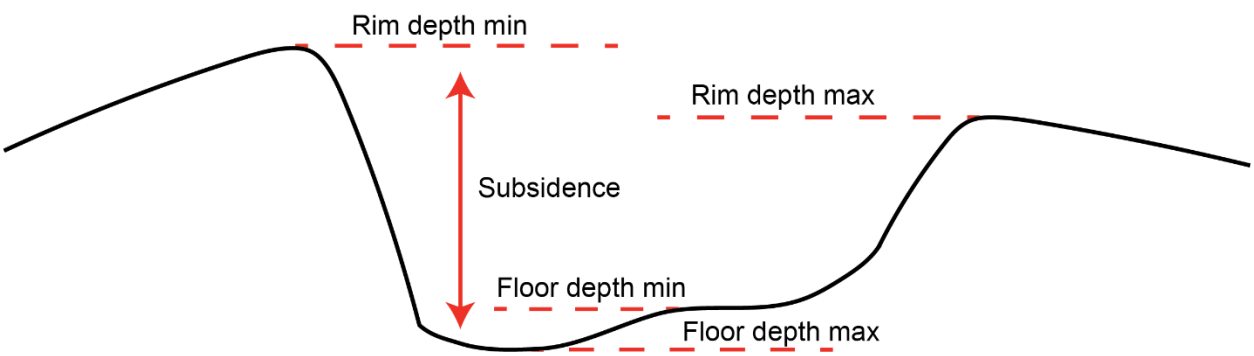

Figure 4.4 Schematic illustration of the measurements included in the global database of submarine calderas. The subsidence is the difference between the average rim and floor depths.

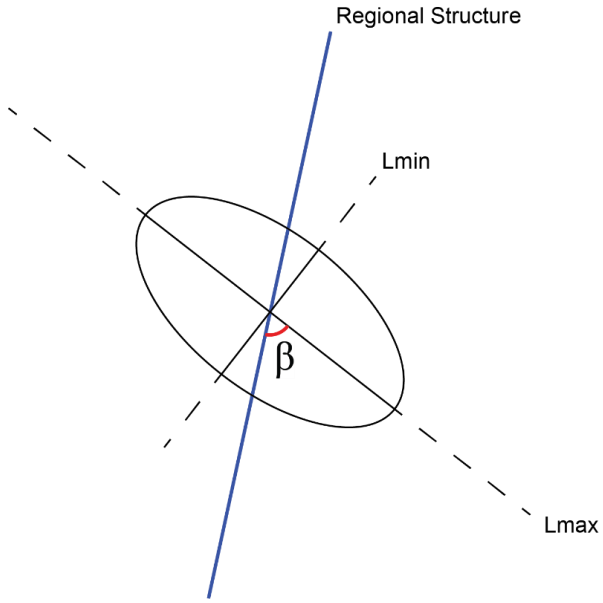

Figure 4.5 Schematic illustration of the orientation of the caldera axis. The recorded β value is the acute angle between the orientation of the Lmax (long axis) of the caldera and the orientation of the regional structure fabric.

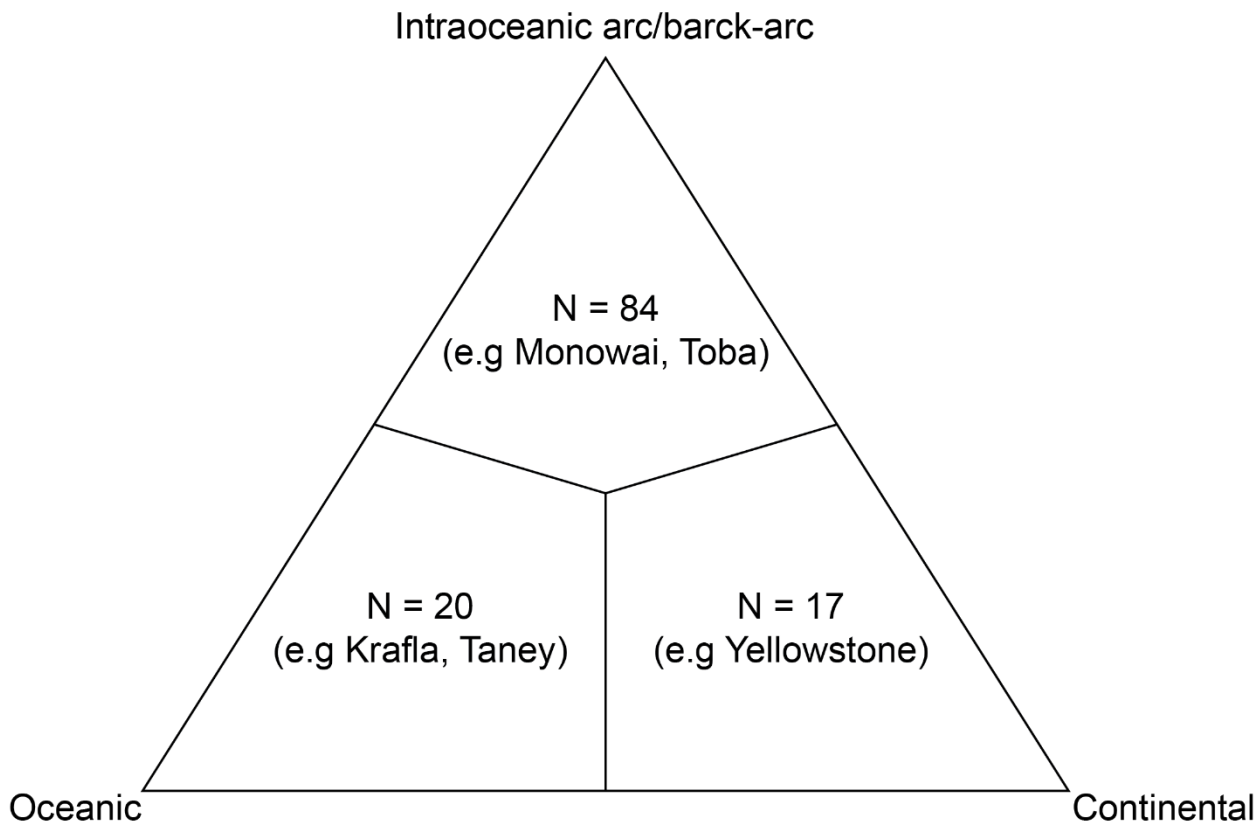

Figure 4.6 Ternary diagram illustrating the numbers of different types of caldera volcanoes in oceanic, continental, and intraoceanic arc/back-arc crust from the Database of Submarine Calderas. Some notable calderas in each group are indicated.

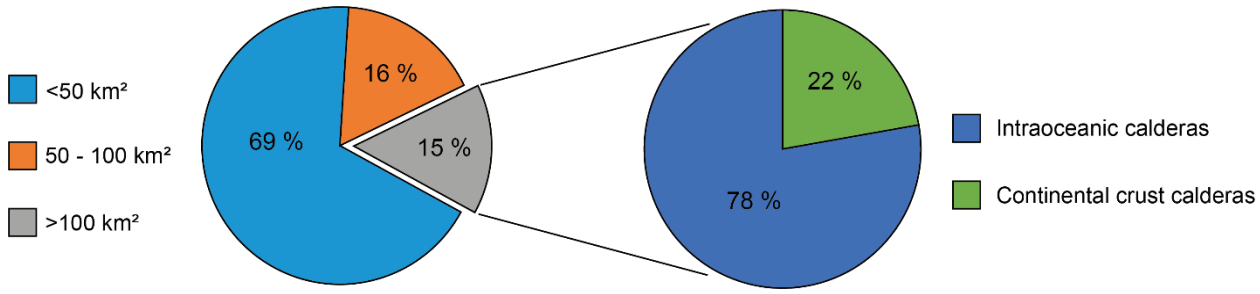

Figure 4.7 Pie chart showing the sizes (km^2) of calderas from the Database of Submarine Calderas. Of the calderas greater than 100 km^2, the majority (78 %) are intraoceanic calderas while only a small percent (22%) are on continental crust.

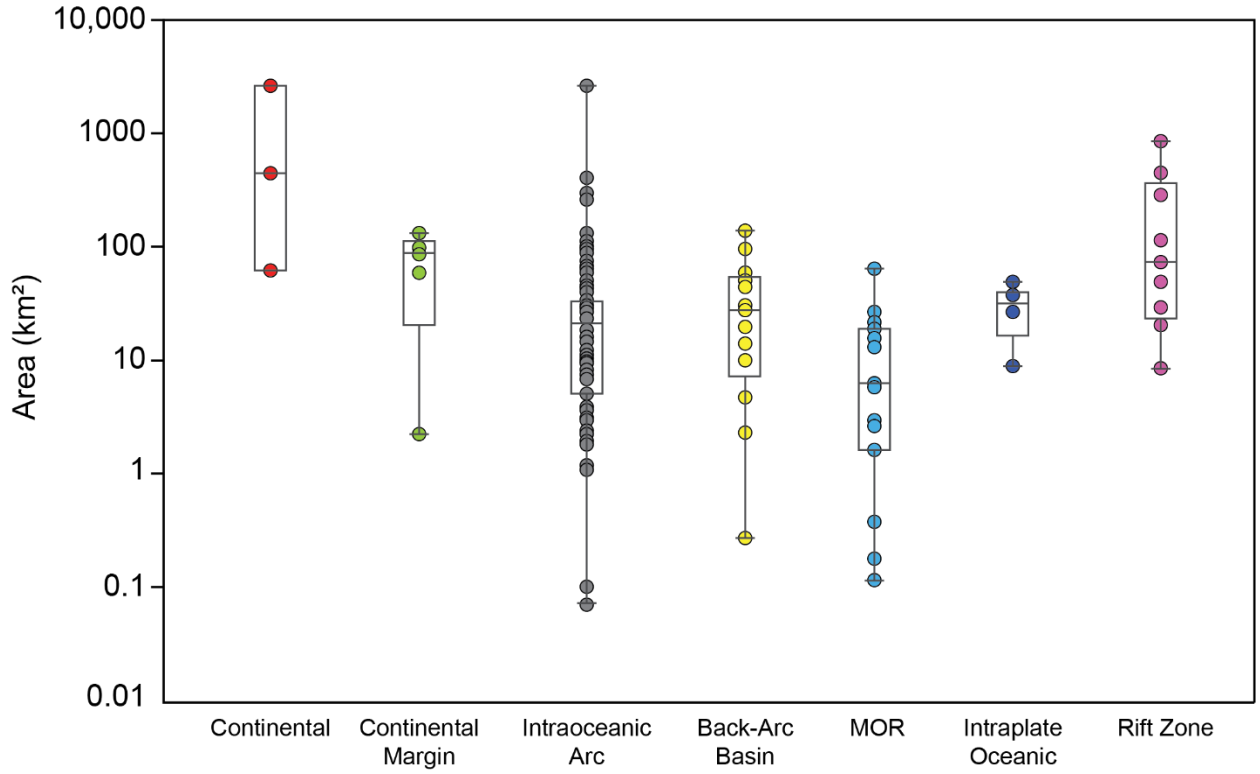

Figure 4.8 Plot showing the sizes (km^2) of calderas in different crustal settings from the Database of Submarine Calderas. Geodynamic settings include continental (red, n = 4), continental margin (green, n= 5), intraoceanic arc (grey, n = 71), back-arc basin (yellow, n = 13),

mid-ocean ridge (light blue, n = 15), intraplate oceanic (dark blue, n = 4), and rift zone (pink, n = 9).

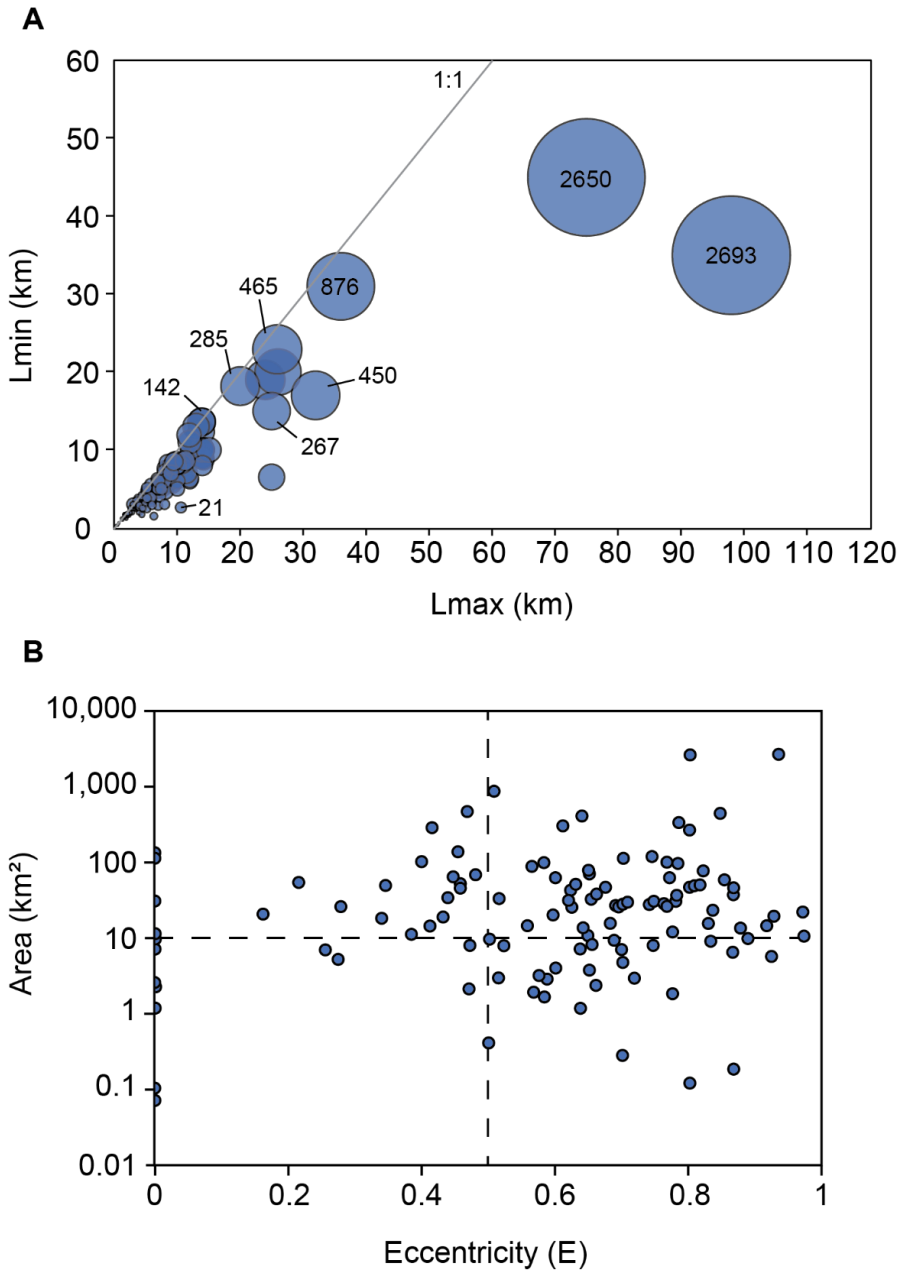

Figure 4.9 (a) Plot of Lmax versus Lmin, with symbol sizes representing the sizes of the calderas (area in km^2 from the Database of Submarine Calderas). A 1:1 line shows a perfect circular caldera, with larger calderas diverging significantly off the line. (b) Plot of caldera sizes

(km^2) versus eccentricity (*E*). An eccentricity of 0 indicates a perfectly circular caldera, while increasing to 1 indicates increasing elongation. The plot area is divided into four quadrants with bounds at 10 km^2 size and E = 0.5. The left quadrants contain the calderas which are less eccentric; with the top left quadrant containing larger calderas (>10 km^2) and the bottom left quadrant containing smaller calderas (<10 km^2). Some of the smallest calderas (~0.1 km^2) are perfectly circular. The right quadrants contain the calderas with greater eccentricity; the top right quadrant containing the larger calderas (>10 km^2) and the bottom right quadrant containing smaller calderas (<10 km^2). Generally the larger calderas are more eccentric, with their size and elongation likely in part controlled by regional stress fields.

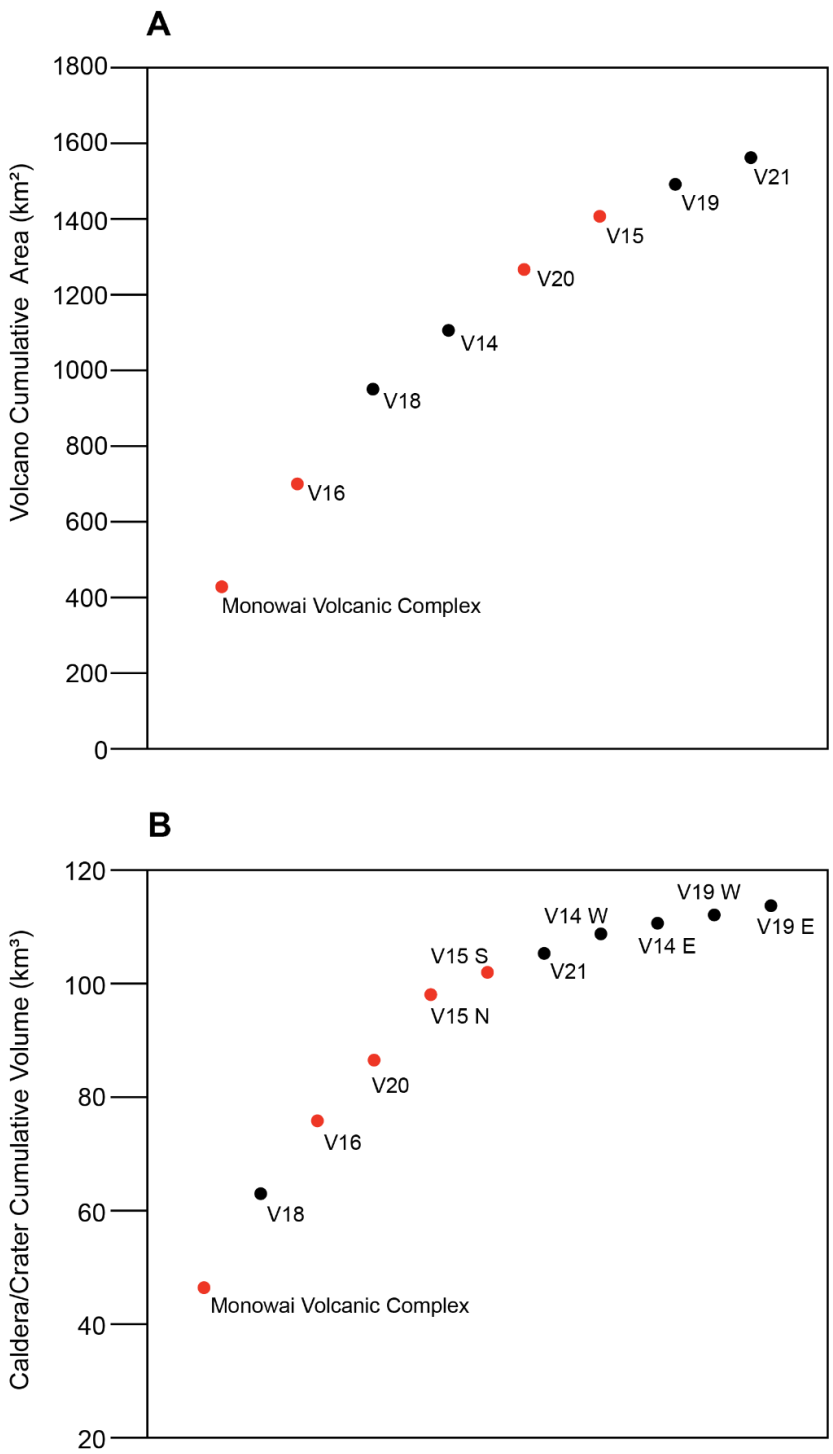

Figure 4.10 (a) Plot of the cumulative sizes (km^2) for the Tonga Arc caldera and cone volcanoes of this study from largest to smallest (caldera volcanoes = red circles, cone volcanoes = black circles). Individual areas are shown in Table 3.2. (b) Plot of the cumulative volumes (km^3) for

the Tonga Arc calderas and summit craters of this study from largest to smallest (calderas = red circles, summit craters = black circles). Individual volumes are shown in Table 3.2.

References

Anderson, M. O., Hannington, M. D., Haase, K., Schwarz-Schampera, U., Augustin, N., McConachy, T. F., and Allen, K., 2016, Tectonic focusing of voluminous basaltic eruptions in magma-deficient backarc rifts. Earth and Planetary Science Letters, **v. 440**, p. 43–55

Anderson, M. O., Chadwick Jr., W. W., Hannington, M. D., Merle, S. G., Resing, J. A., Baker, E. T., Butterfield, D. A., Walker, S. L., Augustin, N., 2017, Geological interpretation of volcanism and segmentation of the Mariana back-arc spreading center between 12.7°N and 18.3°N. Geochemistry, Geophysics, Geosystems, **v. 18**, p. 2240-2274, doi:10.1002/2017GC006813

Anderson, M. O., Norris-Julseth, C., Rubin, K. H., Haase, K., Hannington, M. D., Baxter, A. T., Stewart, M. S., 2021, Geologic and Structural Evolution of the NE Lau Basin, Tonga: Morphotectonic Analysis and Classification of Structures Using Shallow Seismicity. Frontiers in Earth Science, v. 9, doi:10.3389/feart.2021.665185

Arai, R., Kodaira, S., Takahashi, T., Miura, S., Kaneda, Y., 2018, Seismic evidence for arc segmentation, active magmatic intrusions and syn-rift fault system in the northern Ryukyu volcanic arc. Earth, Planets and Space, **v. 70**, p. 61

Arculus, R. J., 1999, Origins of the continental crust. Journal and Proceeding of the Royal Society of New South Wales, **v. 132**, p. 83-110

Arculus, R., and Shipboard Participants, 2003, The TELVE expedition to the Tofua arc and adjacent Valu Fa Ridge of the southern Lau Basin, Cruise SS02/03, March 14-April 3: http://www.marine.csiro.au/nationalfacility/voyagedocs/2003/0203s.htm

Argus, D. F., Gordon, R. G., DeMets, C., 2011, Geologically current motion of the 56 plates relative to the no-net-rotation reference frame. Geochemistry, Geophysics, Geosystems, **v. 12**, no. 11, 13 p., doi:10.1029/2011GC003751

Austin, J. A., Taylor, F. W. Jr., Cagle, C. D., 1989, Seismic stratigraphy of the central Tonga Ridge. Marine and Petroleum Geology, **v.6**, p. 71-92

Baker, E. T., Walker, S. L., Massoth, G. J., Resing, J. A., 2019, The NE Lau Basin: Widespread and abundant hydrothermal venting in the back-arc region behind a superfast subduction zone. Frontiers in Marine Science, **vol. 6**, doi:10.3389/fmars.2019.00382

Ballance, P. F., Scholl, D. W., Vallier, T. L., Stevenson, A. J., Ryan, H., and Herzer, R. H., 1989, Subduction of a Late Cretaceous Seamount of the Louisville Ridge at the Tonga Trench: A model of normal and accelerated tectonic erosion. Tectonics, **v. 8**, p. 953–962

Basu, N. K., 2006, Geology and geochemistry of West Rota, a large submarine caldera in the Southern Mariana Arc. MS Thesis, University of Texas at Dallas, Richardson, 99 p.

Baxter, A. T., Hannington, M. D., Stewart, M. S., Embley, J. M., Breker, K., Krätschell, A., Petersen, S., Brandl, P. A., Klischies, M., Mensing, R., Anderson, M. O., 2020, Shallow Seismicity and the Classification of Structures in the Lau Back-Arc Basin. Geochemistry, Geophysics, Geosystems, **v. 21**, doi:10.1029/2020GC008924

Beier, C., Vanderkluysen, L., Regelous, M., Mahoney, J. J., Garbe, D., 2011, Lithospheric control on geochemical composition along the Louisville Seamount Chain. Geochemistry, Geophysics, Geosystems, **v. 12**, doi:10.1029/2011GC003690

Berkenbosch, H. A., de Ronde, C. E. J., Gemmell, J. B., McNeill, A. W., Goemann, K., 2012, Mineralogy and formation of black smoker chimneys from Brothers Submarine Volcano, Kermadec Arc. Economic Geology, **v. 107**, p. 1613-1633

Bevis, M., Taylor, F. W., Schutz, B. E., Recy, J., Isacks, B. L., Helu, S., Singh, R., Kendrick, E., Stowell, J., Taylor, B., Calmantli, S., 1995, Geodetic observations of very rapid convergence and back-arc extension at the Tonga arc. Nature, **v. 374**, p. 249–251

Bird, P., 2003, An updated model of plate boundaries. Geochemistry, Geophysics, Geosystems, **v. 4(3)**, doi:10.1029/2001GC000252

Bloomer, S. H., Ewart, A., Hergt, J. M., Bryan, W. B., 1994, Geochemistry and origin of igneous rocks from the outer Tonga Forearc (Site 841) *In* Hawkins, J., Parson, L., Allan, J (*Eds*) Proceedings of the Ocean Drilling Program, Scientific Results, **v. 135**, p. 625-646

Bonnardot, M.-A., Régnier, M., Ruellan, E., Christova, C., Tric, E., 2007, Seismicity and state of stress within the overriding plate of the Tonga-Kermadec subduction zone: Stress regime in the Tonga-Kermadec Area. Tectonics, **v. 26**, doi:10.1029/2006TC002044

Buck, W. R., 2001, Accretional curvature of lithosphere at magmatic spreading pro-duces an elastically supported axial high. Journal of Geophysical Research, **v. 106**, p. 3953–3960

Brandl, P. A., Hannington, M. D., Geersen, J., Petersen, S., Gennerich, H.-H., 2020a, The submarine tectono-magmatic framework of Cu-Au endowment in the Tabar-to-Feni island chain, PNG. Ore Geology Reviews, **v. 121**, doi:10.1016/j.oregeorev.2020.103491

Brandl, P. A., Schmid, F., Augustin, N., Grevemeyer, I., Arculus, R. J., Devey, C. W., Petersen, S., Stewart, M., Kopp, H., Hannington, M. D., 2020b, The 6-8 Aug 2019 eruption of 'Volcano F' in the Tofua Arc, Tonga. Journal of Volcanology and Geothermal Research, **v. 390**, 9 p., doi:10.1016/j.jvolgeores.2019.106695

Branney, M. and Acocella, V., 2015, Calderas *In* Sigurdsson, H., Houghton, B., Rymer, H., Stix, J., McNutt, S. (*Eds.*) Encyclopedia of Volcanoes, Academic Press, p. 299 - 315

Brothers, R. N., Heming, R. F., Hawke, M. M., Davey, F. J., 1980, Tholeiitic basalt from the Monowai seamount, Tonga-Kermadec ridge (Note). New Zealand Journal of Geology and Geophysics, **v. 23**, p. 537–539

Bryan, S. E., and Ernst, R. E., 2008, Revised definition of Large Igneous Provinces (LIPs). Earth-Science Reviews, **v. 86**, p. 175–202

Campbell, M. E., Rowland, J. V., Wright, I. C., Smith, I. E. M., 2007, Oblique rifting along the central and southern Kermadec Arc front (30°-36°S), SW Pacific: Kermadec Arc Front Rifting. Geochemistry, Geophysics, Geosystems, v. 8, doi:10.1029/2006GC001504

Caress, D. W., 1991, Structural trends and back-arc extension in the Havre Trough. Geophysical Research Letters, **v. 18**, p. 853–856

Cathles, L. M., 1993, Oxygen isotope alteration in the Noranda mining district, Abitibi greenstone belt, Quebec. Economic Geology, **v. 88**, p. 1483-1511

Cathles, L. M., 2011, What processes at mid-ocean ridges tell us about volcanogenic massive sulfide deposits. Mineralium Deposita, **v. 46**, p. 639–657

Chadwick, W. W., Wright, I. C., Schwarz-Schampera, U., Hyvernaud, O., Reymond, D., and de Ronde, C. E. J., 2008, Cyclic eruptions and sector collapses at Monowai submarine volcano, Kermadec arc: 1998-2007. Geochemistry, Geophysics, Geosystems, **v. 9**, 17 p., doi:10.1029/2008GC002113

Chadwick, W. W., Rubin, K. H., Merle, S. G., Bobbitt, A. M., Kwasnitschka, T., Embley, R. W., 2019, Recent Eruptions Between 2012 and 2018 Discovered at West Mata Submarine Volcano (NE Lau Basin, SW Pacific) and Characterized by New Ship, AUV, and ROV Data. Frontiers in Marine Science, **v. 6**, doi:10.3389/fmars.2019.00495

Clague, D. A., Reynolds, J. R., Davis, A. S., 2000, Near-ridge seamount chains in the northeastern Pacific Ocean. Journal of Geophysical Research: Solid Earth, **v. 105**, p. 16541–16561

Clift, P. D., 1995, Volcaniclastic sedimentation and volcanism during the rifting of Western Pacific backarc basins. *In:* Taylor, B. and Natland, J., (*Eds.*) Active Margins and Marginal Basin of the Western Pacific, American Geophysical Union, doi:10.1029/GM088

Clift, P. D. and ODP Leg 135 Scientific Party, 1994, Volcanism and sedimentation in a rifting island-arc terrain: an example from Tonga, SW Pacific. Geological Society, London, Special Publications, **v. 81**, p. 29–51

Clift, P. D., MacLeod, C. J., Tappin, D. R., Wright, D. J., Bloomer, S. H., 1998, Tectonic controls on sedimentation and diagenesis in the Tonga Trench and forearc, southwest Pacific. Geological Society of America Bulletin, **v. 110**, p. 483-496

Clift, P. D., and MacLeod, C. J., 1999, Slow rates of subduction erosion estimated from subsidence and tilting of the Tonga forearc. Geology, **v. 27**, p. 411-414

Cole, J., Milner, D., Spinks, K., 2005, Calderas and caldera structures: a review. Earth-Science Reviews, **v. 69**, 26 p.

Collot, J.-Y., and Davy, B., 1998, Forearc structures and tectonic regimes at the oblique subduction zone between the Hikurangi Plateau and the southern Kermadec margin. Journal of Geophysical Research: Solid Earth, **v. 103**, p. 623–650

Conder, J. A., and Wiens, D. A., 2011, Shallow seismicity and tectonics of the central and northern Lau Basin. Earth and Planetary Science Letters, **v. 304**, p. 538–546

Contreras-Reyes, E., Grevemeyer, I., Watts, A. B., Flueh, E. R., Peirce, C., Moeller, S., and Papenberg, C., 2011, Deep seismic structure of the Tonga subduction zone: Implications for mantle hydration, tectonic erosion, and arc magmatism. Journal of Geophysical Research, **v. 116**, 18 p.

Coumans, J. P., Stix, J., Clague, D. A., Minarik, W. G., 2015, The Magmatic Architecture of Taney Seamount-A, NE Pacific Ocean. Journal of Petrology, **v. 56**, p. 1037–1067.

Crawford, W. C., Hildebrand, J. A., Dorman, L. M., Webb, S. C., Wiens, D. A., 2003, Tonga Ridge and Lau Basin crustal structure from seismic refraction data: Tonga ridge and Lau basin crustal structure. Journal of Geophysical Research. Solid Earth, **v. 108**, 19 p.

Crisp, J. A., 1984, Rates of magma emplacement and volcanic output. Journal of Volcanology and Geothermal Research, **v. 20**, p. 177-211

Davey, F. J., 1980, The Monowai seamount: an active submarine volcanic centre on the Tonga-Kermadec ridge (Note). New Zealand Journal of Geology and Geophysics, **v. 23**, p. 533–536

Deligne, N. I., and Sigurdsson, H., 2015, Global Rates of Volcanism and Volcanic Episodes. *In* Sigurdsson, H., Houghton, B., Rymer, H., Stix, J., McNutt, S. (*Eds.*) Encyclopedia of Volcanoes, Academic Press, p. 265-272

Delteil, J., Ruellan, E., Matsumoto, T., Kobayashi, K., Wright, I. C., 1999, Deformation distribution in the Havre Basin (SW Pacific), EOS Transactions American Geophysics Union, Fall Meeting Supplement, F1137

Delteil, J., Ruellan, E., Wright, I., Matsumoto, T., 2002, Structure and structural development of the Havre Trough (SW Pacific): Development of Havre Trough. Journal of Geophysical Research. Solid Earth, **v. 107**, 17 p.

de Ronde, C. E., Faure, K., Bray, C. J., Chappell, D. A., Wright, I. C., 2003, Hydrothermal fluids associated with seafloor mineralization at two southern Kermadec arc volcanoes, offshore New Zealand. Mineralium Deposita, **v. 38**, p. 217–233

de Ronde, C. E. J., Hannington, M. D., Stoffers, P., Wright, I. C., Ditchburn, R. G., Reyes, A. G., Baker, E. T., Massoth, G. J., Lupton, J. E., Walker, S. L., Greene, R. R., Soong, W. R., Ishibashi, J., Lebon, G. T., Bray, C. J., Resing, J. A., 2005, Evolution of a submarine magmatic-

hydrothermal system: Brothers Volcano, Southern Kermadec Arc, New Zealand. Economic Geology, **v. 100**, p. 1097-1133

de Ronde, C. E. J., Daughney, C., Wright, I., Embley, B., Arculus, R., Faure, K., Baker, E., Graham, I., Christenson, B., Law, C., Massoth, G., Garlick, R., Safi, K., George, S., Wilson, C., Gerring, P., Britten, K., Greene, R., Dunkin, M., Stanley, R., Walker, S., McDonall, S., Baier, A., Vailea, 'A., Houia, S., Graaf, J., 2006, NZAPLUME III New Zealand American PLUme Mapping Expedition, 23 September – 17 October, 2004

de Ronde, C. E. J., Stucker, V. K., 2015, Seafloor Hydrothermal Venting at Volcanic Arcs and Backarcs. *In* Sigurdsson, H., Houghton, B., Rymer, H., Stix, J., McNutt, S. (*Eds.*) Encyclopedia of Volcanoes, Academic Press, p. 823-849

de Ronde, C. E. J., Massoth, G. J., Butterfield, D. A., Christenson, B. W., Ishibashi, J., Ditchburn, R. G., Hannington, M. D., Brathwaite, R. L., Lupton, J. E., Kamenetsky, V. S., Graham, I. J., Zellmer, G. F., Dzaik, R. P., Embley, R. W., Dekov, V. M., Munnik, F., Lahr, J., Evans, L. J., Takai, K., 2011, Submarine hydrothermal activity and gold-rich mineralization at Brothers Volcano, Kermadec Arc, New Zealand. Mineralium Deposita, **v. 46**, p. 541-584

de Ronde, C. E. J., Humphris, S. E., Höfig, T. W., Reyes, A. G., IODP Expedition 376 Scientists, 2019, Critical role of caldera collapse in the formation of seafloor mineralization: The case of Brothers volcano. Geology, **v. 47**, p.762-766

Devey, C.W., German, C.R., Haase, K.M., Lackschewitz, K.S., Melchert, B., Connelly, D.P., 2010, The relationships between volcanism, tectonism, and hydrothermal activity on the southern equatorial Mid-Atlantic Ridge. *In* Rona, P.A., Devey, C.W., Dyment, J., Murton, B.J. (*Eds*), Diversity of Hydrothermal Systems on Slow Spreading Ocean Ridges. American Geophysical Union, Washington, D. C, p. 133–152, doi:10.1029/2008GM000756

Dunn, R. A., and Martinez, F., 2011, Contrasting crustal production and rapid mantle transitions beneath back-arc ridges. Nature, **v. 469**, p. 198–202

Dunn, R. A., Martinez, F., Conder, J. A., 2013, Crustal construction and magma chamber properties along the Eastern Lau Spreading Center. Earth and Planetary Science Letters, **v. 371–372**, p. 112–124

Dziewonski, A. M., Chou, T.-A., Woodhouse, J. H., 1981, Determination of earthquake source parameters from waveform data for studies of global and regional seismicity. Journal of Geophysical Research, **v. 86 (B4)**, p. 2825–2852, doi:10.1029/JB086iB04p02825

Embley, R. W., de Ronde, C. E., Massoth, G. J., Wright, I. C., Butterfield, D. A., Clark, M. R., Chadwick, W. W., Lupton, J. E., Malahoff, A., Rowden, A. A., Stott, M., Evans, L. J., Greene, R. R., Opatkiewicz, A., Roe, K., 2005, Hydrothermal systems on Kermadec arc volcanoes revealed by PISCES V submersible dives, AGU, Fall Meeting, Abstracts, **v. 44 (**A04E)

Embley, R. W., de Ronde, C. E. J., Merle, S. G., Davy, B., Tontini, F. C., 2012, Detailed Morphology and Structure of an Active Submarine Arc Caldera: Brothers Volcano, Kermadec Arc. Economic Geology, **v. 107**, p. 1557–1570

Embley, R. W., and Rubin, K. H., 2018, Extensive young silicic volcanism produces large deep submarine lava flows in the NE Lau Basin. Bulletin of Volcanology, **v. 80**, 36 p.

Ekström, G., Nettles, M., Dziewoński, A. M., 2012, The global CMT project 2004–2010: Centroid-moment tensors for 13,017 earthquakes. Physics of the Earth and Planetary Interiors, **v. 200–201**, doi:10.1016/j.pepi.2012.04.002

Ernst, R. E., 2014, Large Igneous Provinces. Cambridge University Press, 653 p.

Ernst, R. E., Wingate, M. T. D., Buchan, K. L., Li, Z. X., 2008, Global record of 1600–700Ma Large Igneous Provinces (LIPs): Implications for the reconstruction of the proposed Nuna (Columbia) and Rodinia supercontinents. Precambrian Research, **v. 160**, p. 159–178

Ewart, A., Collerson, K. D., Regelous, M., Wendt, J. I., Niu, Y., 1998, Geochemical Evolution within the Tonga–Kermadec–Lau Arc–Back-arc Systems: The Role of Varying Mantle Wedge Composition in Space and Time. Journal of Petrology, **v. 39**, p. 331-388

Falloon, T. J., Danyushevsky, L. V., Crawford, T. J., Maas, R., Woodhead, J. D., Eggins, S. M., Bloomer, S. H., Wright, D. J., Zlobin, S. K., Stacey, A. R., 2007, Multiple mantle plume components involved in the petrogenesis of subduction-related lavas from the northern termination of the Tonga Arc and northern Lau Basin: Evidence from the geochemistry of arc and backarc submarine volcanics: Tonga Arc and Lou Basin Lavas. Geochemistry, Geophysics, Geosystems, **v. 8**, 45 p.

Fiske, R. S., Naka, J., Iizasa, K., Yuasa, M., Klaus, A., 2001, Submarine silicic caldera at the front of the Izu-Bonin arc, Japan: Voluminous seafloor eruptions of rhyolite pumice. Geological Society of America Bulletin, 12 p.

Franklin, J. M., Gibson, H. L., Jonasson, I. R., Galley, A. G., 2005, Volcanogenic Massive Sulfide Deposits. *In* Hedenquist, J. W., Thompson, J. F. H., Goldfarb, R. J., Richards, J. P. (*Eds*) One Hundredth Anniversary Volume, Economic Geology, p. 523-560, doi:10.5382/AV100

Fryer, P., Saboda, K. L., Johnson, L. E., Mackay, M. E., Moore, G. F., Stoffers, P., 1990, Conical Seamount: SeaMARC II, ALVIN Submersible, and Seismic-Reflections studies *In* Fryer, P., Pearce, J. A., Stokking, L. B., (*Eds*) Proceedings of the Ocean Drilling Program, Initial Reports, **v. 125**, p. 3-11

Fujiwara, T., Yamazaki, T., Joshima, M., 2001, Bathymetry and magnetic anomalies in the Havre Trough and southern Lau Basin: from rifting to spreading in back-arc basins. Earth and Planetary Science Letters, **v. 185**, p. 253–264

GEBCO Compilation Group, 2021, GEBCO 2021 Grid, doi:10.5285/c6612cbe-50b3-0cff-e053-6c86abc09f8f

Geldmacher, J., Hoernle, K., Bogaard, P., Duggen, S., Werner, R., 2005, New $^{40}Ar/^{39}Ar$ age and geochemical data from seamounts in the Canary and Madeira volcanic provinces: Support for the mantle plume hypothesis. Earth and Planetary Science Letters, **v. 237**, p. 85–101

Geyer, A., and Martí, J., 2008, The new worldwide collapse caldera database (CCDB): A tool for studying and understanding caldera processes. Journal of Volcanology and Geothermal Research, **v. 175**, p. 334–354

Gibson, H. L., 2005, Volcano-hosted ore deposits. *In* Marti, J. and Ernst, G. (*Eds*) Volcanoes and the Environment. Cambridge University Press, doi:10.1017/CB09780511614767

Glasby, G. P., Iizasa, K., Yuasa, M., Usui, A., 2000, Submarine Hydrothermal Mineralization on the Izu–Bonin Arc, South of Japan: An Overview. Marine Georesources & Geotechnology, **v. 18**, p. 141–176

Global Volcanism Program, 2013, Volcanoes of the World, v 4.10.3 (15 Oct 2021), *In* Venzke, E. (*Eds*) Smithsonian Institution, doi:10.5479/si.GVP.VOTW4-2013

Global Volcanism Program, 2019, Report on Lateiki (Tonga) *In* Sennert, S. K. (*Eds*) Weekly Volcanic Activity Report, 13 November-19 November 2019. Smithsonian Institution and US Geological Survey, doi:10.5479/si.GVP.VOTW4-2013

Gudmundsson, A., 1992, Formation and growth of normal faults at the divergent plate boundary in Iceland. Terra Nova, **v. 4**, p. 464–471

Gudmundsson, A., and Brenner, L. S., 2009, Local stresses, dyke arrest and surface deformation in volcanic edifices and rift zones. Annals of Geophysics, **v. 47**, p. 1433-1454

Graham, I. J., Reyes, A. G., Wright, I. C., Peckett, K. M., Smith, I. E. M., and Arculus, R. J., 2008, Structure and petrology of newly discovered volcanic centers in the northern Kermadec-southern Tofua arc, South Pacific Ocean: Northern Kermadec Arc Volcanoes. Journal of Geophysical Research: Solid Earth, **v. 113**, 24 p.

Grevemeyer, I. and Flüh, E. R., 2008, FS Sonne Cruise Report SO195 TOTAL, Tonga Thrust earthquake Asperity at Louisville Ridge. Leibniz-Institut für Meereswissenschaften an der Christian-ALbrechts-Universität zu Kiel, 106 p.

Haase, K. M., Worthington, T. J., Stoffers, P., Garbe-Schönberg, D., and Wright, I., 2002, Mantle dynamics, element recycling, and magma genesis beneath the Kermadec Arc-Havre Trough: Kermadec Arc-Havre Trough. Geochemistry, Geophysics, Geosystems, **v. 3**, p. 1–22

Hannington, M.D., de Ronde, C.D.J., Petersen, S., 2005, Sea-floor tectonics and submarine hydrothermal systems. Economic Geology 100th Anniversary Volume, Society of Economic Geologists, p. 111-141

Hannington, M. D., Kopp, H., Schnabel, M., 2019, RV SONNE Fahrbericht/Cruise Report SO267: ARCHIMEDES I: Arc rifting, metallogeny and microplate evolution—An integrated geodynamic, magmatic and hydrothermal study of the Fonualei Rift System, NE Lau Basin. GEOMAR, 275 p.

Harris, P. T., Macmillan-Lawler, M., Baker, E. K., 2014, Geomorphology of the oceans. Marine Geology, **v. 352**, p.4-24

Hawkins, J. W. Jr., 1995, The Geology of the Lau Basin. *In* Taylor, B. (*Eds*) Backarc Basins. Springer, Boston, MA, doi:10.1007/978-1-4615-1843-3_3

Hejrani, B., Tkalčić, H., Fichtner, A., 2017, Centroid moment tensor catalogue using a 3-D continental scale Earth model: Application to earthquakes in Papua New Guinea and the Solomon Islands. Journal of Geophysical Research, **v. 122**, p. 5517-5543

Hekinian, R., Mühe, R., Worthington, T. J., Stoffers, P., 2008, Geology of a submarine volcanic caldera in the Tonga Arc: Dive results. Journal of Volcanology and Geothermal Research, **v. 176**, p. 571–582

Hjörleifsdóttir, V. and Ekström, G., 2010, Effects of three-dimensional Earth structure on CMT earthquake parameters. Physics of the Earth and Planetary Interiors, **v. 179**, p. 178-190.

Hoernle, K., Hauff, F., van den Bogaard, P., Werner, R., Mortimer, N., Geldmacher, J., Garbe-Schönberg, D., Davy, B., 2010, Age and geochemistry of volcanic rocks from the Hikurangi and Manihiki oceanic Plateaus. Geochimica et Cosmochimica Acta, **v. 74**, p. 7196–7219

Holohan, E. P., Troll, V. R., Walter, T. R., Münn, S., McDonnell, S., Shipton, Z. K., 2005, Elliptical calderas in active tectonic settings: an experimental approach. Journal of Volcanology and Geothermal Research, **v. 144**, p. 119-136

Hooft, E. E. E., and Detrick, R. S., 1995, Relationship between axial morphology, crustal thickness, and mantle temperature along the Juan de Fuca and Gorda Ridges. Journal of Geophysical Research: Solid Earth, **v. 100**, p. 22499–22508.

Ikeda, Y., and Yuasa, M., 1989, Volcanism in nascent back-arc basins behind the Shichito Ridge and adjacent areas in the Izu-Ogasawara arc, northwest Pacific: evidence for mixing between E-type MORB and island arc magmas at the initiation of back-arc rifting. Contributions to Mineralogy and Petrology, **v. 101**, p. 377–393

John, D. A., Henry, C. D., Colgan, J. P., 2008, Magmatic and tectonic evolution of the Caetano caldera, north-central Nevada: A tilted, mid-Tertiary eruptive center and source of the Caetano Tuff. Geosphere, **v. 4**, p. 75-106

Karig, D. E., 1970, Ridges and basins of the Tonga-Kermadec Island Arc System. Journal of Geophysical Research, **v. 75**, p. 239–254

Karig, D. E., 1971, Origin and development of marginal basins in the western Pacific. Journal of Geophysical Research, **v. 76**, p. 2542–2561

Keller, N. S., Arculus, R. J., Hermann, J., Richards, S., 2008, Submarine back-arc lava with arc signature: Fonualei Spreading Center, northeast Lau Basin, Tonga: Geochemistry of the Fonualei Spreading Center. Journal of Geophysical Research: Solid Earth, **v. 113**, 28 p.

Kerr, D. J., and Gibson, H. L., 1993, A comparison of the Horne volcanogenic massive sulfide deposit and intracauldron deposits of the Mine Sequence, Noranda, Quebec. Economic Geology, **v. 88**, p. 1419–1442

Kim, S.-S., and Wessel, P., 2011, New global seamount census from altimetry-derived gravity data: New global seamount census. Geophysical Journal International, **v. 186**, p. 615–631

Kimura, M., 1985, Back-arc rifting in the Okinawa Trough. Marine and Petroleum Geology, **v. 2**, p. 222-240

Klischies, M., Petersen, S., Devey, C.W., 2019, Geological mapping of the Menez Gwen segment at 37°50'N on the Mid-Atlantic Ridge: Implications for accretion mechanisms and associated hydrothermal activity at slow-spreading mid-ocean ridges. Marine Geology, **v. 412**, p. 107-122

Kodaira, S., Sato, T., Takahashi, N., Miura, S., Tamura, Y., Tatsumi, Y., Kaneda, Y., 2007, New seismological constraints on growth of continental crust in the Izu-Bonin intra-oceanic arc: Geology, **v. 35**, p. 1031-1034

Leybourne, M. I., Schwarz-Schampera, U., de Ronde, C. E. J., Baker, E. T., Faure, K., Walker, S. L., Butterfield, D. A., Resing, J. A., Lupton, J. E., Hannington, M. D., Gibson, H. L., Massoth, G. J., Embley, R. W., Chadwick Jr., W. W., Clark, M. R., Timm, C., Graham, I. J., Wright, I. C., 2012, Submarine Magmatic-Hydrothermal Systems at the Monowai Volcanic Center, Kermadec Arc. Economic Geology, **v. 107**, p.1669-1694

Li, F., Sun, Z., Yang, H., 2018, Possible Spatial Distribution of the Mesozoic Volcanic Arc in the Present-Day South China Sea Continental Margins and Its Tectonic Implications. Journal of Geophysical Research: Solid Earth, **v. 123**, p. 6215-6235, doi:10.1029/2017JB014861

Lipman, P.W., 2000, Calderas *In:* Sigurdsson, H., Houghton, B., Rymer, H., Stix, J., McNutt, S. (*Eds.*) Encyclopedia of Volcanoes, Academic Press, p. 643-662

Lloyd, E. F., Nathan, D., Smith, I. E. M., Stewart, R. B., 1996, Volcanic history of Macauley Island, Kermadec Ridge, New Zealand. New Zealand Journal of Geology and Geophysics, **v. 39**, p.295-308

Lonsdale, P., 1986, A multibeam reconnaissance of the Tonga Trench axis and its intersection with the Louisville guyot chain. Marine Geophysical Researches, **v. 8**, p. 295–327

Lonsdale, P., 1988, Geography and history of the Louisville Hotspot Chain in the southwest Pacific. Journal of Geophysical Research, **v. 93**, p. 3078-3104

Lupton, J., Rubin, K. H., Arculus, R., Lilley, M., Butterfield, D., Resing, J., Baker, E., Embley, R., 2015, Helium isotope, C/^{3} He, and Ba-Nb-Ti signatures in the northern Lau Basin: Distinguishing arc, back-arc, and hotspot affinities: Helium and Carbon in Northern Lau Basin. Geochemistry, Geophysics, Geosystems, **v. 16**, p. 1133–1155

Martin, A., Jamieson, J. W., de Ronde, C. E. J., Humphris, S. E., Höfig, T. W., Roberts, S., Cai, Y., Nozaki, T., Zhang, X., Schlicht, L., Reyes, A. G., MacLeod, C. J., 2019, Magmatic versus seawater-dominated hydrothermal alteration: evidence from deep-sea drilling at Brothers volcano, Kermadec arc, New Zealand. American Geophysical Union, Fall Meeting 2019, abstract #V33E-0226

Martinez, F., and Taylor, B., 1996, Backarc spreading, rifting, and microplate rotation, between transform faults in the Manus Basin. Marine Geophysical Researches, **v. 18**, p. 203–224

Martinez, F., and Taylor, B., 2006, Modes of crustal accretion in back-arc basins: Inferences from the Lau Basin. *In* Christie, D. M., Fisher, C. R., Lee, S.-M., and Givens, S. (*Eds*) Geophysical Monograph Series: Washington, D. C., American Geophysical Union, p. 5–30

Mason, B. G., Pyle, D. M., Oppenheimer, C., 2004, The size and frequency of the large explosive eruptions on Earth. Bulletin of Volcanology, **v. 66**, p. 735-748

Massoth, G.J., de Ronde, C.E.J., Lupton, J.E., Feely, R.A., Baker, E.T., Lebon, G.T., Maenner, S.M., 2003, Chemically rich and diverse submarine hydrothermal plumes of the southern Kermadec volcanic arc (New Zealand). *In* Larter, R., and Leat, P. (*Eds*) Intra-oceanic subduction systems: Tectonic and magmatic processes: Geological Society London Special Publication 219, p. 119–139

Massoth, G. J., Baker, E. T., Lupton, J. E., de Ronde, C. E., Walker, S. L., Ishibashi, J., Worthington, T. J., Arculus, R. J., Resing, J. A., Greene, R. R., Lebon, G. T., Nakamura, K., Stoffers, P., 2004, A systematic reconnaissance of submarine hydrothermal venting along the south Tonga (Tofua) intra-oceanic arc. AGU Annual Meeting, EOS (Trans. Am. Geophys. Union), December V54A-08

Massoth, G.J., Arculus, R.J., Baker, E.T., Butterfield, D.A., Chadwick, W.W., Christenson, B.W., de Ronde, C.E., Embley, R.W., Evans, L.J., Faure, K., Graham, I.J., Greene, R.R., Ishibashi, J., Lebon, G.T., Lupton, J.E., Resing, J.A., Roe, K.K., Schmidt, M., Stoffers, P.,

Walker, S.L., Worthington, T.J., Wright, I.C., Yamanaka, T., 2005, Plume–vent fluid connections along the Tonga- Kermadec arc. AGU Annual Meeting, EOS (Trans. Am. Geophys. Union), December 9, V51C-1507

Massoth, G., Baker, E., Worthington, T., Lupton, J., de Ronde, C. E. J., Arculus, R., Walker, S., Nakamura, K., Ishibashi, J., Stoffers, P., Resing, J., Greene, R., Lebon, G., 2007, Multiple hydrothermal sources along the south Tonga arc and Valu Fa Ridge. Geochemistry, Geophysics, Geosystems, **v. 8**, doi:10.1029/2007GC001675

Matsumoto, T., Kobayashi, K., Yamazaki, T., Delteil, J., Ruellan, E., LAUHAVRE 97, 1997, Regional tectonics in the southern Lau Basin-Havre Trough: Preliminary results of the LAUHAVRE cruise (abstract), EOS, Transactions American Geophysical Union, Fall Meeting Supplement, F720

Maus, S., Barckhausen, U., Berkenbosch, H., Bournas, N., Brozena, J., Childers, V., Dostaler, F., Fairhead, J.D., Finn, C., von Frese, R.R.B., Gaina, C., Golynsky, S., Kucks, R., Lühr, H., Milligan, P., Mogren, S., Müller, R.D., Olesen, O., Pilkington, M., Saltus, R., Schreckenberger, B., Thébault, E., Carratori Tontini, F., 2009, EMAG2: A 2-arc min resolution Earth Magnetic Anomaly Grid compiled from satellite, airborne, and marine magnetic measurements. Geochemistry, Geophysics, Geosystems, **v. 10**, no. Q08005, p., doi:10.1029/2009GC002471

Metz, D., Watts, A. B., Grevemeyer, I., Werner, R., Huusmann, H., 2019, Updated seafloor topography and T phase seismicity at Monowai, northern Kermadec Arc. New Zealand Journal of Geology and Geophysics, 7 p., doi:10.1080/00288306.2019.1651747

Monzier, M., Robin, C., Eissen, J.-P., 1994, Kuwae (≈ 1425 A.D.): the forgotten caldera. Journal of Volcanology and Geothermal Research, **v. 59**, p. 207–218

Newhall, C. G., and Self, S., 1982, The Volcanic Explosivity Index (VEI): An Estimate of Explosive Magnitude for Historical Volcanism. Journal of Geophysical Research, **v. 87**, p. 1231-1238

Mueller, W. U., Stix, J., Corcoran, P. L., Daigneault, R., 2009, Subaqueous calderas in the Archean Abitibi greenstone belt: An overview and new ideas. Ore Geology Reviews, **v. 35**, p. 4–46

Nishizawa, A., Takahashi, N., Abe, S., 1999, Crustal structure and seismicity of the Havre Trough at 26°S. Geophysical Research Letters, **v. 26**, p. 2549–2552

Nur, A. and Ben-Avraham, Z., 1983, Volcanic gaps due to oblique consumption of aseismic ridges. Tectonophysics, **v. 99**, p. 355-362

Parson, L., Hawkins, J., Allan, J., Shipboard Scientific Party, 1992, Introduction, background, and principal results of Leg 135, Lau Basin, *In* Parson, L., Hawkins, J., Allan, J. *Eds*)

Proceedings of the Oceanic Drilling Program, Initial Reports, College Station, Texas, Ocean Drilling Program, **v. 135**, p. 5-47, doi:10.2973/odp.proc.ir.135.101.1992

Parson, L. M., and Wright, I. C., 1996, The Lau-Havre-Taupo back-arc basin: A southward-propagating, multi-stage evolution from rifting to spreading. Tectonophysics, **v. 263**, p. 1–22

Paulatto, M., Watts, A. B., Peirce, C., 2014, Potential field and bathymetric investigation of the Monowai volcanic centre, Kermadec Arc: implications for caldera formation and volcanic evolution. Geophysical Journal International, **v. 197**, p. 1484–1499

Pelletier, P. and Dupont, J., 1990, Effects of the subduction of the Louisville Ridge on the Tonga-Kermadec Arc. Oceanologica Acta, Special Issue, **v. 10**, p. 57-76

Pelletier, B., Lagabrielle, Y., Benoit, M., Cabioch, G., Calmant, S., Garel, E., 2001, Newly identified segments of the Pacific-Australia plate boundary along the North Fiji transform zone. Earth and Planetary Science Letters, **v. 193**, p. 347-358

Pearce, J. A., and Peate, D. W., 1995, Tectonic Implications of the Composition of Volcanic Arc Magmas. Annual Review of Earth and Planetary Sciences, **v. 23**, p.251-285

Pearson, V., and Daigneault, R., 2009, An Archean megacaldera complex: The Blake River Group, Abitibi greenstone belt. Precambrian Research, **v. 168**, p. 66–82

Peirce, C. and Watts, A., 2011, R/V Sonne SO215 Cruise Report; The Louisville Ridge—Tonga Trench collision: Implications for subduction zone dynamics. 76 p.

Perfit, M. R. and Davidson, J. P, 2000, Plate Tectonics and Volcanism. *In:* Sigurdsson, H., Houghton, B., Rymer, H., Stix, J., McNutt, S. (*Eds.*) Encyclopedia of Volcanoes, Academic Press, San Diego, p. 89-113

Pietruszka, A. J., Norman, M. D., Garcia, M. O., Marske, J. P., Burns, D. H., 2013, Chemical heterogeneity in the Hawaiian mantle plume from the alteration and dehydration of recycled oceanic crust. Earth and Planetary Science Letters, **v. 361**, p. 298–309

Rey, P. F., and Müller, R. D., 2010, Fragmentation of active continental plate margins owing to the buoyancy of the mantle wedge. Nature Geoscience, **v. 3**, p. 257–261

Rhys, D. A., Lewis, P. D., Rowland, J. C., 2020, Structural controls on ore localization in epithermal gold-silver deposits: A mineral systems Approach. Reviews in Economic Geology, **v. 21**, p. 83-145

Ribeiro, J. M., Stern, R. J., Kelley, K. A., Martinez, F., Manton, W. I., Ohara, Y., 2013, Nature and distribution of slab-derived fluids and mantle sources beneath the Southeast Mariana forearc rift. Geochemistry, Geophysics, Geosystems, **v. 14**, p. 4585-4607

Richard, P., 1991, Experiments on faulting in a two-layer cover sequence overlying a reactivated basement fault with oblique-slip. Journal of Structural Geology, **v. 13**, p. 459-469

Robinson, A. H., Peirce, C., Funnell, M. J., 2018, Construction and subduction of the Louisville Ridge, SW Pacific—insights from wide-angle seismic data modelling. Geophysical Journal International, **v. 215**, p. 2222-2245

Rolling Deck to Repository (R2R), 2014, Multibeam collection for TN309: Multibeam data collected aboard Thomas G. Thompson from 10-Apr-14 to 20-May-14, Auckland to Apia. NOAA National Centers for Environmental Information. [https://www.ngdc.noaa.gov/ships/thomas_g_thompson/TN309_mb.html], accessed April 16, 2021

Rowland, J., Bardsley, C., Downs, D., Sepúlveda, F., Simmons, S., Scholz, C., 2012, Tectonic Controls On Hydrothermal Fluid Flow In A Rifting And Migrating Arc, Taupo Volcanic Zone, New Zealand. New Zealand Geothermal Workshop Proceedings, 19-21 November, Auckland, New Zealand, 7 p.

Rubin, K., Soule, S. A., Chadwick, W., Fornari, D., Clague, D., Embley, R., Baker, E., Perfit, M., Caress, D., Dziak, R., 2012, Volcanic Eruptions in the Deep Sea. Oceanography, **v. 25**, p. 142–157

Ruellan, E., Delteil, J., Pelletier, A., Kobayashi, K., Matsumoto, T., Wright, I. C., Buffet, G., 1998, Back-arc opening at the transition from the Lau Basin to the Havre Trough (SW Pacific), paper presented at EGS General Assembly, Nice, France

Ruellan, E., Delteil, J., Wright, I., and Matsumoto, T., 2003, From rifting to active spreading in the Lau Basin - Havre Trough backarc system (SW Pacific): Locking/unlocking induced by seamount chain subduction: Lau Basin-Havre Trough System. Geochemistry, Geophysics, Geosystems, **v. 4**, 21 p., doi:10.1029/2001GC000261

Ruellan, E. and Lagabrielle, Y., 2005, Oceanic subductions and active spreading in the Southwest Pacific. Géomorphologie: Relief, Processus, Environment, **v. 11**, p. 121-142

Rytuba, J. J., 1994, Evolution of volcanic and tectonic features in caldera settings and their importance in localization of ore deposits. Economic Geology, **v. 89**, p. 1687–1696

Ryan, W.B.F., Carbotte, S.M., Coplan, J.O., O'Hara, S., Melkonian, A., Arko, R., Weissel, R.A., Ferrini, V., Goodwillie, A., Nitsche, F., Bonczkowski, J., Zemsky, R., 2009, Global Multi-Resolution Topography synthesis. Geochemistry, Geophysics, Geosystems, **v. 10**, Q03014, doi:10.1029/2008GC002332

Sandwell, D. T., Müller, R. D., Smith, W. H. F., Garcia, E., and Francis, R., 2014, New global marine gravity model from CryoSat-2 and Jason-1 reveals buried tectonic structure. Science, **v. 346**, p. 65–67

Schmid, F., Cremanns, M., Augustin, N., Lange, D., Petersen, F., Kopp, H., 2021, Microseismicity and Lava Flows Hint at Magmato-Tectonic Processes Near the Southern Tip of the Fonualei Rift and Spreading Center in the Lau Basin. Journal of Geophysical Research: Solid Earth, **v. 126**, doi:10.1029/2020JB021340

Schmidt, R. and Schmincke, H.-U., 1999, Seamounts, Submarine, Volcanoes, and Volcanic Islands, *In* Sigurdsson, H., Houghton, B., Rymer, H., Stix, J., McNutt, S. (*Eds.*) Encyclopedia of Volcanoes, Academic Press

Scholz, C. H., and Small, C., 1997, The effect of seamount subduction on seismic coupling. Geology, **v. 25**, p. 487-490

Schwarz-Schampera, U., Botz, R., Hannington, M., Adamson, R., Anger, V., Cormany, D., Evans, L., Gibson, H., Haase, K., Hirdes, W., Hocking, M., Juniper, K., Langley, S., Leybourne, M., Metaxas, A., Mills, R., Ostertag-Henning, Chr., Rauch, M., Rutkowski, J., Schmidt, M., Shepherd, K., Stevens, C., Tamburri, K., Tracey, D., Westernstroer, U., 2007, R/V Sonne SO192/2 Cruise Report; Marine Geoscientific Research on Input and Output in the Tonga-Kermadec Subduction Zone. 92 p.

Seebeck, H., Nicol, A., Villamor, P., Ristau, J., Pettinga, J., 2014, Structure and kinematics of the Taupo Rift, New Zealand: Taupo Rift. Tectonics, **v. 33**, p. 1178–1199

Shukuno, H., Tamura, Y., Tani, K., Chang, Q., Suzuki, T., Fiske, R. S., 2006, Origin of silicic magmas and the compositional gap at Sumisu submarine caldera, Izu-Bonin arc, Japan. Journal of Volcanology and Geothermal Research, **v. 156**, p. 187-216

Sibuet, J.-C., Letouzey, J., Barbier, F., Charvet, J., Foucher, J.-P., Hilde, T. W. C., Kimura, M., Chiao, L.-Y., Marsset, B., Muller, C., and Stéphan, J.-F., 1987, Back Arc Extension in the Okinawa Trough. Journal of Geophysical Research: Solid Earth, **v. 92**, p. 14041–14063

Sigurdsson, H., 2015, Introduction, *In* Sigurdsson, H., Houghton, B., Rymer, H., Stix, J., McNutt, S. (*Eds.*) Encyclopedia of Volcanoes, Academic Press, p. 2 - 12

Sillitoe, R. H., and Bonham, H. F., 1984, Volcanic landforms and ore deposits. Economic Geology, **v. 79**, p. 1286–1298

Sleeper, J. D., and Martinez, F., 2016, Geology and kinematics of the Niuafo'ou microplate in the northern Lau Basin. Journal of Geophysical Research: Solid Earth, **v. 121**, p. 4852–4875

Sleeper, J. D., Martinez, F., Arculus, R., 2016, The Fonualei Rift and Spreading Center: Effects of ultraslow spreading and arc proximity on back-arc crustal accretion Journal of Geophysical Research: Solid Earth, **v. 121**, p. 4814–4835

Smith, I. E. M., Stewart, R. B., Price, R. C., 2003, The petrology of a large intra-oceanic silicic eruption: the Sandy Bay Tephra, Kermadec Arc, Southwest Pacific. Journal of Volcanology and Geothermal Research, **v. 124**, p. 173-194

Smith, I. E. M., and Price, R. C., 2006, The Tonga–Kermadec arc and Havre–Lau back-arc system: Their role in the development of tectonic and magmatic models for the western Pacific. Journal of Volcanology and Geothermal Research, **v. 156**, p. 315–331

Stern, R. J., Lin, P.-N., Morris, J. D., Jackson, M. C., Fryer, P., Bloomer, S. H., Ito, E., 1990, Enriched back-arc basin basalts from the northern Mariana Trough: implications for the magmatic evolution of back-arc basins. Earth and Planetary Science Letters, **v. 100**, p. 210–225

Stern, R. J., and Bloomer, S. H., 1992, Subduction zone infancy: Examples from the Eocene Izu-Bonin-Mariana and Jurassic California arcs. Geological Society of America Bulletin, **v. 104**, p. 1621-1636

Stern, R. J., Tamura, Y., Embley, R. W., Ishizuka, O., Merle, S. G., Basu, N. K., Kawabata, H., Bloomer, S. H., 2007, Evolution of West Rota Volcano, an extinct submarine volcano in the southern Mariana Arc: Evidence from sea floor morphology, remotely operated vehicle observations and ^{40}Ar-^{39}Ar geochronological studies: West Rota Volcano, Mariana Arc. Island Arc, v. 17, p. 70–89

Stern R. J., Tamura, Y., Embley, R. W., Ishizuka, O., Merle, S. G., Basu, N. K., Kawabata, H., Bloomer, S. H., 2008, Evolution of West Rota Volcano, an extinct submarine volcano in the southern Mariana Arc: Evidence from sea floor morphology, remotely operated observations and ^{40}Ar-^{39}Ar geochronological studies. Island Arc, **v. 17**, p. 70-89

Stern, R. J., Tamura, Y., Ishizuka, O., Shukano, H., Bloomer, S. H., Embley, R. W., Leybourne, M., Kawabata, H., Nunokawa, A., Nichols, A. R. L., Kohut, E., Pujana, I., 2014, Volcanoes of the Diamante cross-chain: evidence for a mid-crustal felsic magma body beneath the Southern Izu–Bonin–Mariana arc. Geological Society, London, Special Publications, **v. 385**, p. 235–255

Stewart, M. S., Hannington, M. D., Emberly, J., Krätschell, A., Petersen, S., Brandl, P. A., Anderson, M., Baxter, A. T., Breker, K., Mercier-Langevin, P., 2020, Geological Map of the Lau Basin at 1:1,000,000 as a Digital Supplement to Geosphere (In press)

Stewart, M. S., Hannington, M. D., Emberley, J., Baxter, A. T., Krätschell, A., Petersen, S., Brandl, P. A., Anderson, M. O., Mercier-Langevin, P., Mensing, R., Breker, K., Fassbender, M. L., 2021, A new geological map of the Lau Basin reveals crustal growth processes in arc-backarc systems. Geosphere (In press)

Stoffers, P., Wright, I.C., de Ronde, C., Hannington, M., Herzig, P., and Villinger, H., 1999a, Longitudinal transect of the Kermadec-Havre arc-backarc system: Initial results of R/V Sonne Cruise SO-135: InterRidge News, v. 8, no. 1, p. 45-50

Stoffers, P., Wright, I. C., de Ronde, C., Hannington, M., Villinger, H., Herzig, P., and Shipboard Scientific Party, 1999b, Little-studied arc-backarc system in the spotlight. Eos, Transactions American Geophysical Union, **v. 80**, p. 353–359

Stoffers, P., Wright, I., and Shipboard Scientific Party (including M. Hannington), 1999c, Havre Trough-Taupo Volcanic Zone: Tectonic, magmatic and hydrothermal processes: Cruise Report SO-135, Institut fur Geowissenschaften, Christian-Albrechts Universitat, Kiel, Germany, 77 p (Appendices 164 p.)

Stoffers, P., Worthington, T., Schwarz-Schampera, U., Ackermand, D., Beaudoin, Y., Bigalke, N., Fretzdorff, S., Gibson, H., Hekinian, R., Kindermann, A., Kuhn, T., Main, W., Schreiber, K., Timm, C., Tonga'onevai, S., Türkay, M., Unverricht, D., Vailea, A., Zimmerer, M., 2002, Cruise Report SONNE 167 LOUISVILLE, Louisville Ridge: Dynamics and magmastism of a mantle plume and its influence on the Tonga-Kermadec Subduction System, Suva Fiji, Wellington New Zealand, 12 Oct. – 02 Dec. 2002, Christian-Albrechts-Universität, Kiel, Germany, 281 p., ISSN 0175-9302

Stoffers, P., Worthington, T. J., Schwarz-Schampera, U., Hannington, M. D., Massoth, G. J., Hekinian, R., Schmidt, M., Lundsten, L. J., Evans, L. J., Vaiomo'unga, R., and Kerby, T., 2006a, Submarine volcanoes and high-temperature hydrothermal venting on the Tonga arc, southwest Pacific. Geology, **v. 34**, p. 453

Stoffers, P., Worthington, T., Schwarz-Schampera, U., Evans, L., Hannington, M., Hekinian, R., Lundsten, L., Massoth, G., Schmidt, M., and Vaiomo'unga, R., 2006b, Fahrtbericht und Abschlußbericht SITKAP, Submersible Investigations of the Tonga – Kermadec Arc using PISCES, Untersuchung des Tonga – Kermadec Inselbogens mit dem Tauchboot PISCES, Auckland, New Zealand – Pago Pago, American Samoa, 06 – 29 June 2005, BMBF 03G0632A and DFG STO 110/42-1: Geologisch-Palaentologisches Institut und Museum, Christian-Albrechts-Universität, Kiel, Germany, 116 p.

Takahashi, N., Kodaira, S., Klemperer, S., Tatsumi, Y., Kaneda, Y., Suyehiro, K., 2007, Crustal structure and evolution of the Mariana intra-oceanic island arc. Geology, **v. 35**, p. 203-47

Takahashi, N., Kodaira, S., Tatsumi, Y., Kaneda, Y., Suyehiro, K., 2008, Structure and growth of the Izu-Bonin-Mariana arc crust: 1. Seismic constraint on crust and mantle structure of the Mariana arc–back-arc system. Journal of Geophysical Research, **v. 113**, B01104

Tamura, Y., Tani, K., Ishizuka, O., Chang, Q., Shukuno, H., Fiske, R. S., 2005, Are Arc Basalts Dry, Wet, or Both? Evidence from the Sumisu Caldera Volcano, Izu–Bonin Arc, Japan. Journal of Petrology, **v. 46**, p. 1769–1803

Tamura, Y., Yuhara, M., Ishii, T., Irino, N., Shukuno, H., 2003, Andesites and Dacites from Daisen Volcano, Japan: Partial-to-Total Remelting of an Andesite Magma Body. Journal of Petrology, **v. 44**, p. 2243–2260

Tappin, D. R., Bruns, T. R., Geist, E. L., 1994, Rifting of the Tonga/Lau Ridge and formation of the Lau Backarc Basin evidence from Site 840 on the Tonga Ridge *In* Hawkins, J., Parson, L., Allan, J., (*Eds*) Proceedings of the Ocean Drilling Program, Scientific Results, **v. 135**

Taylor, B., Brown, G., Fryer, P., Gill, J.B., Hochstaedter, A.G., Hotta, H., Langmuir, C.H., Leinen, M., Nishimura, A., Urabe, T., 1990, ALVIN-SeaBeam studies of the Sumisu Rift, Izu-Bonin arc. Earth and planetary Science Letters, **v. 100**, p. 127-147

Taylor, B., Klaus, A., Brown, G. R., Moore, G. F., Okamura, Y., Murakami, F., 1991, Structural development of Sumisu Rift, Izu-Bonin Arc. Journal of Geophysical Research, **v. 96**, p. 16113

Taylor, B., Zellmer, K., Martinez, F., Goodliffe, A., 1996, Sea-floor spreading in the Lau back-arc basin. Earth and planetary Letters, **v. 144**, p. 35-40

Thouret, J.-C., 1999, Volcanic geomorphology—an overview. Earth-Science Reviews, **v. 47**, p. 95–131

Till, C. B., Vazquez, J. A., Boyce, J. W., 2015, Months between rejuvenation and volcanic eruption at Yellowstone caldera, Wyoming. Geology, **v. 43**, p. 695-698

Timm, C., Graham, I. J., de Ronde, C. E. J., Leybourne, M. I., Woodhead, J., 2011, Geochemical evolution of Monowai volcanic center: New insights into the northern Kermadec arc subduction system, SW Pacific: Monowai, Northern Kermadec Arc. Geochemistry, Geophysics, Geosystems, **v. 12**, 20 p., doi:10.1029/2011GC003654

Timm, C., Bassett, D., Graham, I. J., Leybourne, M. I., de Ronde, C. E. J., Woodhead, J., Layton-Matthews, D., and Watts, A. B., 2013, Louisville seamount subduction and its implication on mantle flow beneath the central Tonga–Kermadec arc. Nature Communications, 9 p., doi:10.1038/ncomms2702

Tontini, F. C., Davy, B., de Ronde, C. E. J., Embley, R. W., Leybourne, M., Tivey, M. A., 2012, Crustal magnetization of Brothers Volcano, New Zealand, Measured by autonomous underwater vehicles: Geophysical expression of a submarine hydrothermal system. Economic Geology, **107** p. 1571-1581

Tontini, F. C., Tivey, M. A., de Ronde, C. E. J., Humphris, S. E., 2019, Heat flow and near-seafloor magnetic anomalies highlight hydrothermal circulation at Brothers Volcano caldera, southern Kermadec Arc, New Zealand. Geophysical Research Letters, **v. 46**, p. 8252-8260

Turner, S., Hawkesworth, C., Rogers, N., Worthington, T., Hergt, J., Smith, I., 1997. ^{238}U- ^{230}Th disequilibria, magma petrogenesis, and flux rates beneath the depleted Tonga-Kermadec island arc. Geochimica et Cosmochimica Acta, **v. 61**, p. 4855-4884

Turner, S. P., George, R. M. M., Evans, P. J., Hawkesworth, C. J., Zellmer, G. F., 2000, Time-scales of magma formation, ascent and storage beneath subduction-zone. Philosophical Transactions of the Royal Society of London. Series A: Mathematical, Physical and Engineering Sciences, **v. 358**, p. 1443–1464

Urabe, T., and Kusakabe, M., 1990, Barite silica chimneys from the Sumisu Rift, Izu-Bonin Arc: possible analog to hematitic chert associated with Kuroko deposits. Earth and Planetary Science Letters, **v. 100**, p. 283–290

Vallier, T. L., Stevenson, A. J., Scholl, D. W., 1985, Petrology of igneous rocks from Ata Island, Kingdom of Tonga. Circum-Pacific Council for Energy and Mineral Resources Earth Science Series, **v. 2**, Houston, Texas, Circum-Pacific Council for Energy and Mineral Resources

Wallace, L. M., Ellis, S., and Mann, P., 2009, Collisional model for rapid fore-arc block rotations, arc curvature, and episodic back-arc rifting in subduction settings: Rotation and rifting at collisional margins. Geochemistry, Geophysics, Geosystems, **v. 10**, 50 p.

Watanabe, M., Okino, K., Kodera, T., 2010, Rifting to spreading in the southern Lau Basin: Variations within the transition zone. Tectonophysics, **v. 494**, p. 226-234

Watts, A. B., Weissel, J. K., Duncan, R. A., Larson, R. L., 1988, Origin of the Louisville Ridge and its relationship to the Eltanin Fracture Zone System Journal of Geophysical Research, **v. 93**, p. 3051-3077

Watts, A. B., Sandwell, D. T., Smith, W. H. F., Wessel, P., 2006, Global gravity, bathymetry, and the distribution of submarine volcanism through space and time. Journal of Geophysical Research, **v. 111**, doi:10.1029/2005JB004083

Watts, A. B., Peirce, C., Grevemeyer, I., Paulatto, M., Stratford, W., Bassett, D., Hunter, J. A., Kalnins, L. M., de Ronde, C. E. J., 2012, Rapid rates of growth and collapse of Monowai submarine volcano in the Kermadec Arc, Nature Geoscience, **v. 5**, doi:10.1038/NGEO1473

White, J. D. L., Schipper, C. I., Kano, K., 2015, Submarine Explosive Eruptions. *In* Sigurdsson, H., Houghton, B., Rymer, H., Stix, J., McNutt, S. (*Eds.*) Encyclopedia of Volcanoes, Academic Press p. 553–569

White, L. T., Rawlinson, N., Lister, G. S., Waldhauser, F., Hejrani, B., Thompson, D. A., Tanner, D., Macpherson, C. G., Tkalčić, H., Morgan, J. P., 2019, Earth's deepest earthquake swarms track fluid ascent beneath nascent arc volcanoes. Earth and Planetary Science Letters, **v. 521**, p. 25–36

White, W. M., McBirney, A. R., Duncan, R. A., 1993, Petrology and geochemistry of the Galápagos Islands: Portrait of a pathological mantle plume. Journal of Geophysical Research: Solid Earth, **v. 98**, p. 19533–19563

Wiedicke, M. and Collier, J., 1993, Morphology of the Valu Fa Spreading Ridge in the Southern Lau Basin. Journal of Geophysical Research, **v. 98**, no. B7, p. 11,769-11,782

Worthington, T. J., Hekinian, R., Stoffers, P., Kuhn, T., Hauff, F., 2006, Osbourn Trough: Structure, geochemistry and implications of a mid-Cretaceous paleospreading ridge in the South Pacific. Earth and Planetary Science Letters, **v. 245**, p. 685-701

Wormald, S. C., Wright, I. C., Bull, J. M., Lamarche, G., Sanderson, D. J., 2012, Morphometric analysis of the submarine arc volcano Monowai (Tofua–Kermadec Arc) to decipher tectono-magmatic interactions. Journal of Volcanology and Geothermal Research, **v. 239–240**, p. 69–82

Wright, I. C., 1993, Pre-spread rifting and heterogeneous volcanism in the southern Havre Trough back-arc basin. Marine Geology, **v. 113**, p. 179–200

Wright, I. C. and Gamble, J. A., 1999, Southern Kermadec submarine caldera arc volcanoes (SW Pacific): caldera formation by effusive and pyroclastic eruption. Marine Geology, **v. 161**, p. 207-227

Wright, I. C., Carter, L., Lewis, K., 1990, GLORIA survey of the oceanic-continental transition of the Havre-Taupo, back-arc basin. Geo-Marine Letters, **v. 10 (2)**, p. 59-67

Wright, I. C., Gamble, J. A., Shane, P. A., 2003, Submarine, silicic volcanism of the Healy caldera, southern Kermadec arc (SW Pacific): I – Volcanology and eruption mechanisms. Bulletin of Volcanology, **v. 65**, p. 15-29

Wright, I. C., Worthington, T. J., and Gamble, J. A., 2006, New multibeam mapping and geochemistry of the 30°–35° S sector, and overview, of southern Kermadec arc volcanism. Journal of Volcanology and Geothermal Research, **v. 149**, p. 263–296

Wright, I. C., Chadwick, W. W., de Ronde, C. E. J., Reymond, D., Hyvernaud, O., Gennerich, H.-H., Stoffers, P., Mackay, K., Dunkin, M. A., and Bannister, S. C., 2008, Collapse and reconstruction of Monowai submarine volcano, Kermadec arc, 1998-2004: Collapse and growth of Monowai Volcano. Journal of Geophysical Research: Solid Earth, **v. 113**

Yeo, I. A., Devey, C. W., LeBas, T. P., Augustin, N., Steinführer, A., 2016, Segment-scale volcanic episodicity: evidence from the North Kolbeinsey Ridge, Atlantic. Earth and Planetary Science Letters, **v. 439**, p. 81-87, doi:10.1016/j.epsl.2016.01.029

Yu, G., Wesnousky, S. T., Ekström, G., 1993, Slip Partitioning along Major Convergent Plate Boundaries. Shallow Subduction Zones: Seismicity, Mechanics and Seismic Potential Part 1, Birkhäuser, Basel, **v. 140**, p. 183-210

Zellmer, K. E. and Taylor, B., 1999, the Niuafo'ou microplate and a 3-plate kinematic model for the Lau Basin opening. EOS, Transactions American Geophysical Union

Zellmer, K. E., and Taylor, B., 2001, A three-plate kinematic model for Lau Basin opening: Lau Basin Kinematic Model. Geochemistry, Geophysics, Geosystems, **v. 2**, ISSN: 1535-2027

Zhang, G., Smith-Duque, C., Tang, S., Li, H., Zarikian, C., D'Hondt, S., Inagaki, F., IODP Expedition 329 Scientists, 2012, Geochemistry of basalts from IODP site U1365: Implications for magmatism and mantle source signatures of the mid-Cretaceous Osbourn Trough. Lithos, **v. 144-145**, p. 73-87

Zhao, D., Maruyama, S., and Omori, S., 2007, Mantle dynamics of Western Pacific and East Asia: Insight from seismic tomography and mineral physics. Gondwana Research, **v. 11**, p. 120–131

APPENDIX A – Location Maps of Relevant Research Cruises

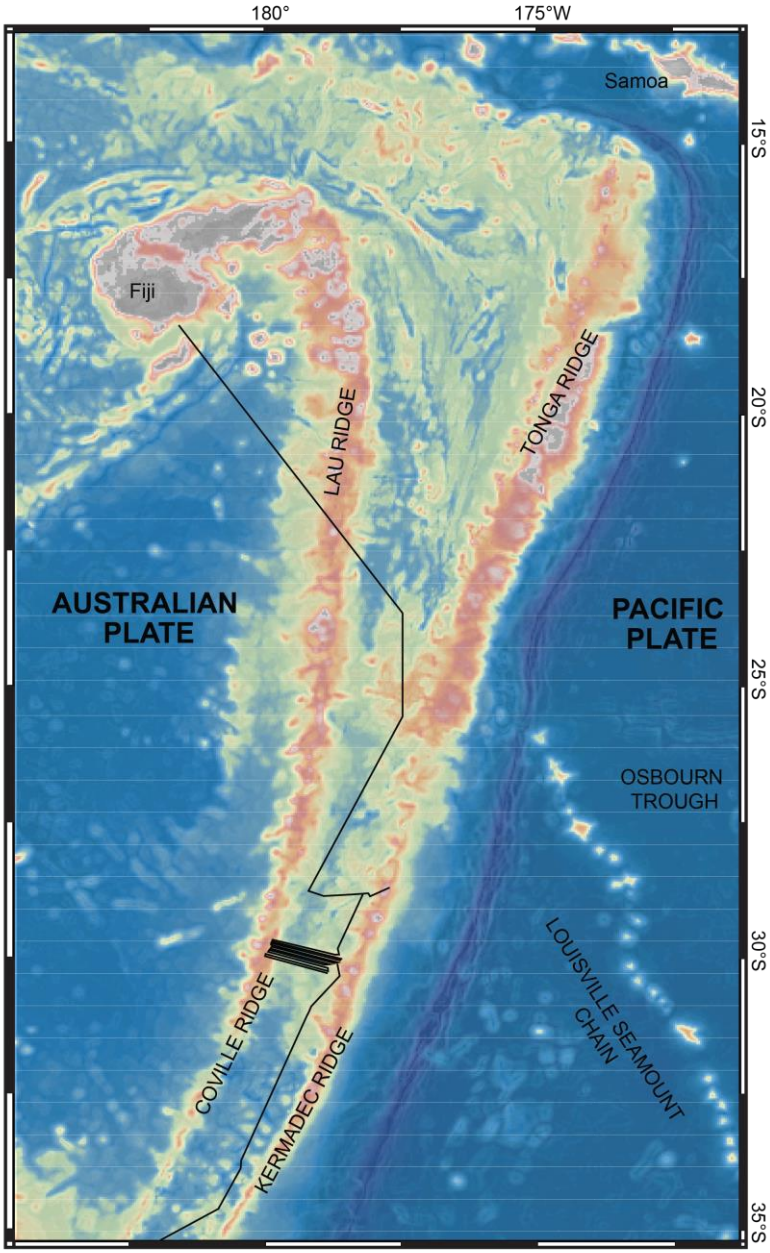

Figure A1 Summary ship track of the RV Sonne SO-135 research cruise (September 9 – October 15, 1998) (Stoffers et al., 1999a).

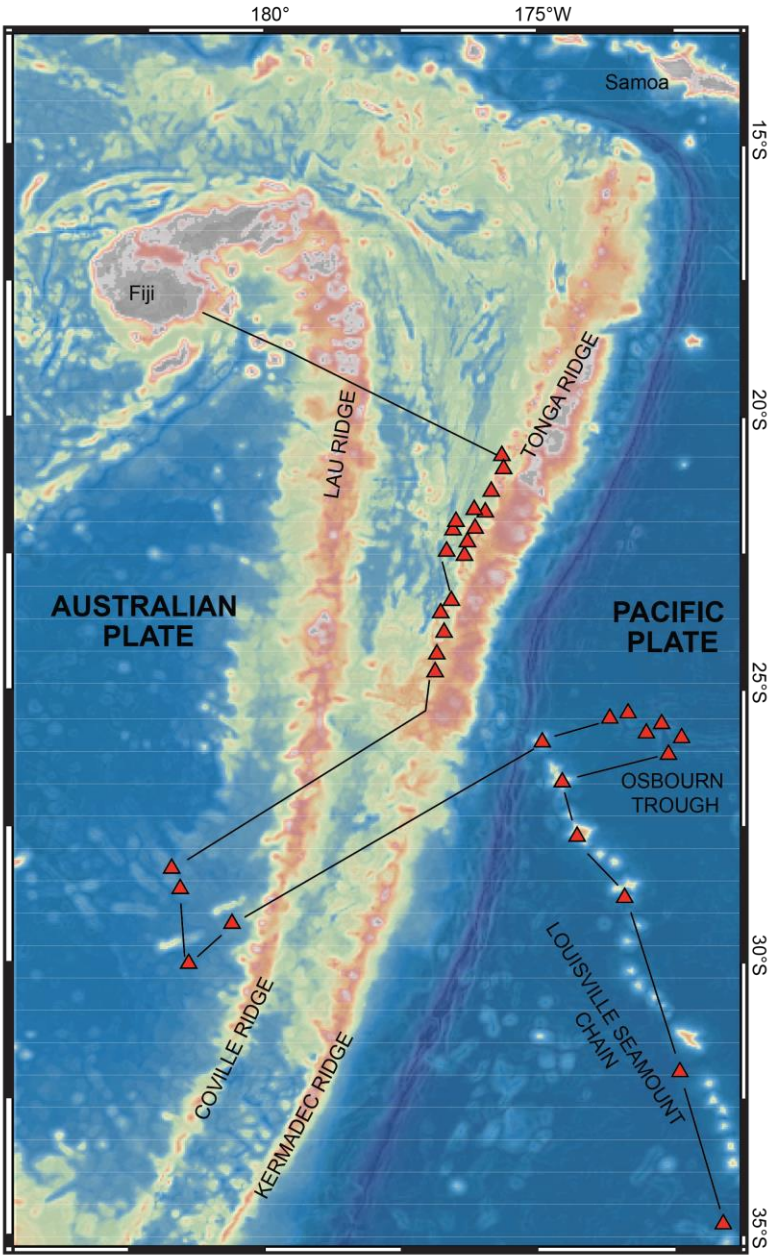

Figure A2 Summary of workstations (red triangles) and ship track of the RV Sonne SO-167 research cruise (October 12 – December 2, 2002) (Stoffers et al., 2002).

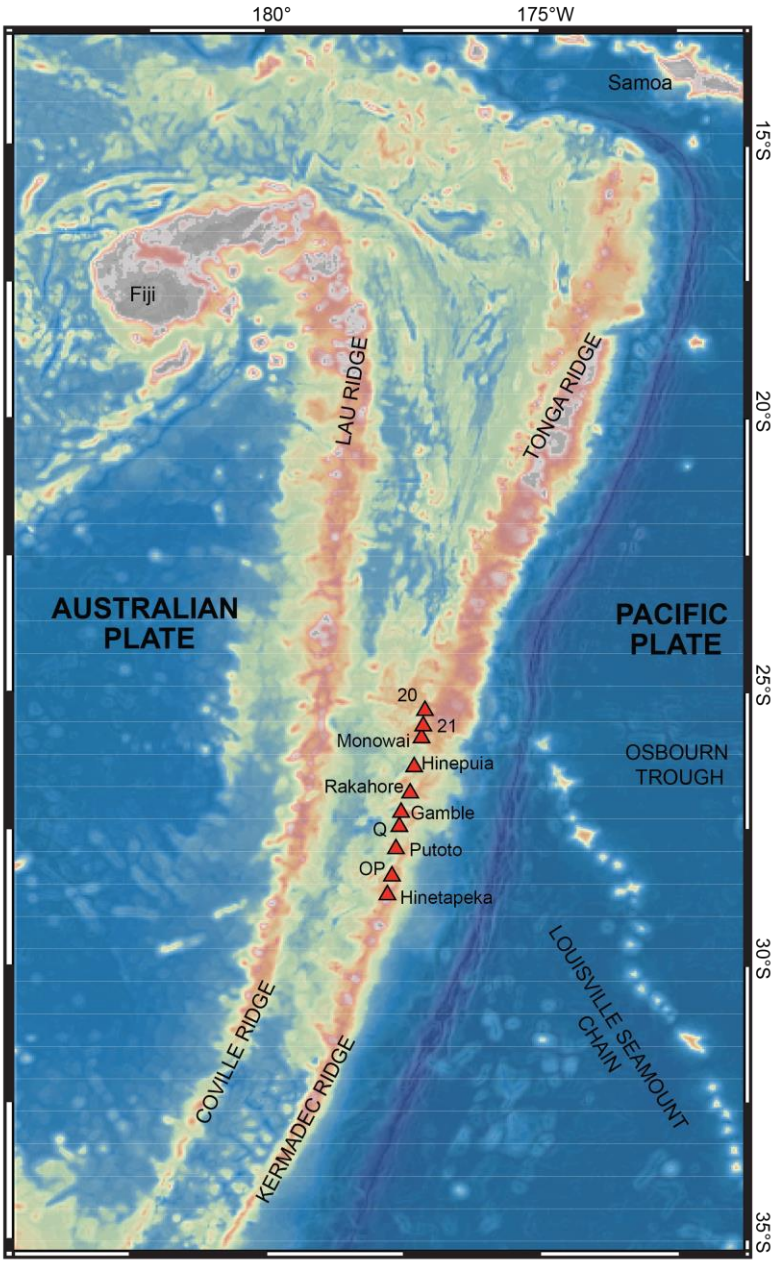

Figure A3 Summary of volcanoes visited during the MZAPLUME III research cruise (September 23 – October 17, 2004) (de Ronde et al., 2006; Graham et al., 2008).

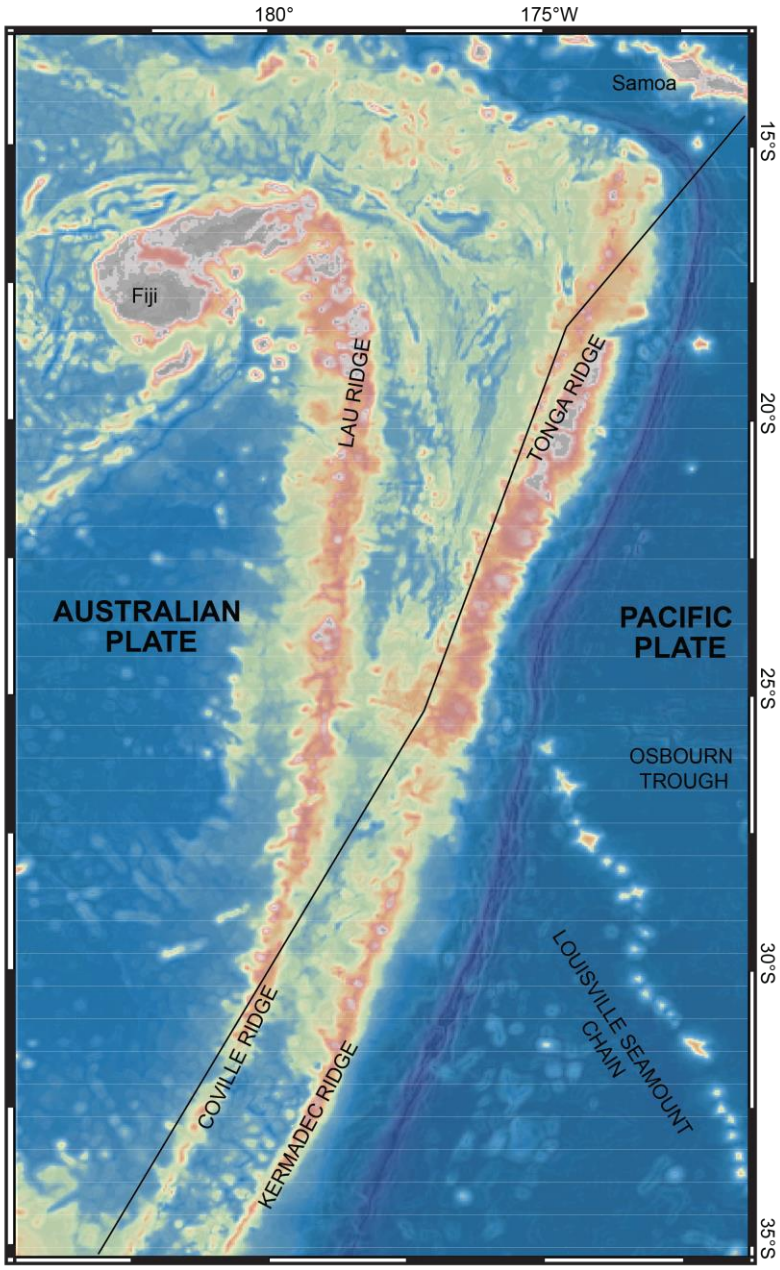

Figure A4 Summary of the ship track of the SITKAP research cruise which visited volcanoes 1, 18, and 19 (Stoffers et al., 2006b).

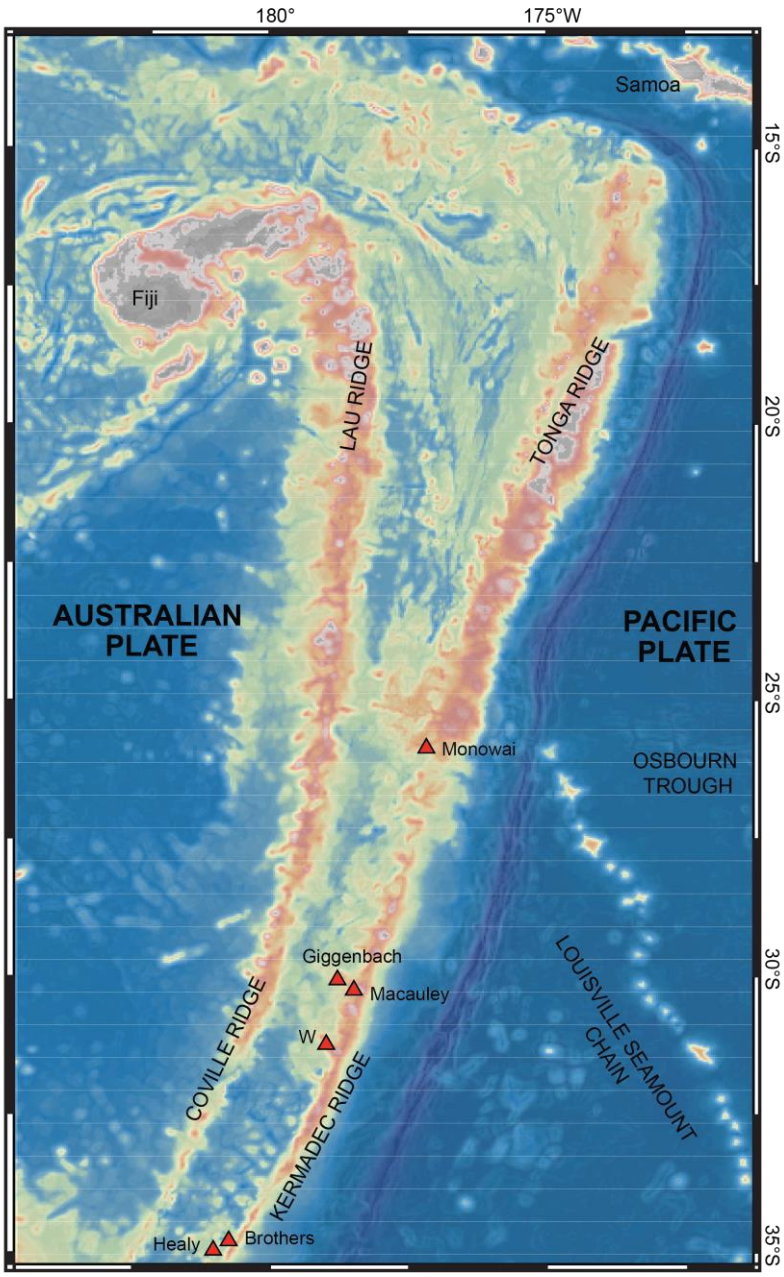

Figure A5 Summary of the volcanoes (red triangles) visited during the NZASRoF'05 expedition PISCES dives (Embley et al., 2005).

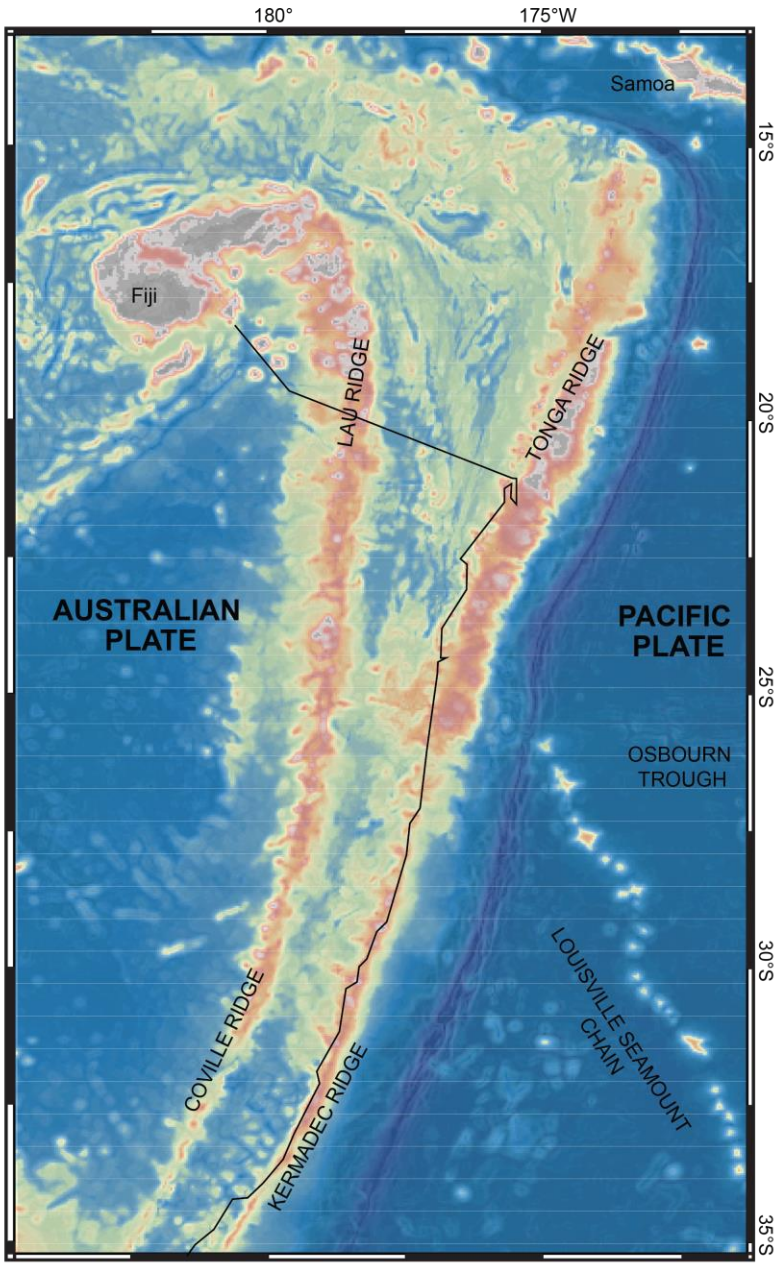

Figure A6 Summary of the ship track of the RV Sonne SO-192 research cruise (April 26 – May 17, 2007) which visited Volcano 1, Volcano 19, Volcano 21, and Monowai (Schwarz-Schampera et al., 2007).

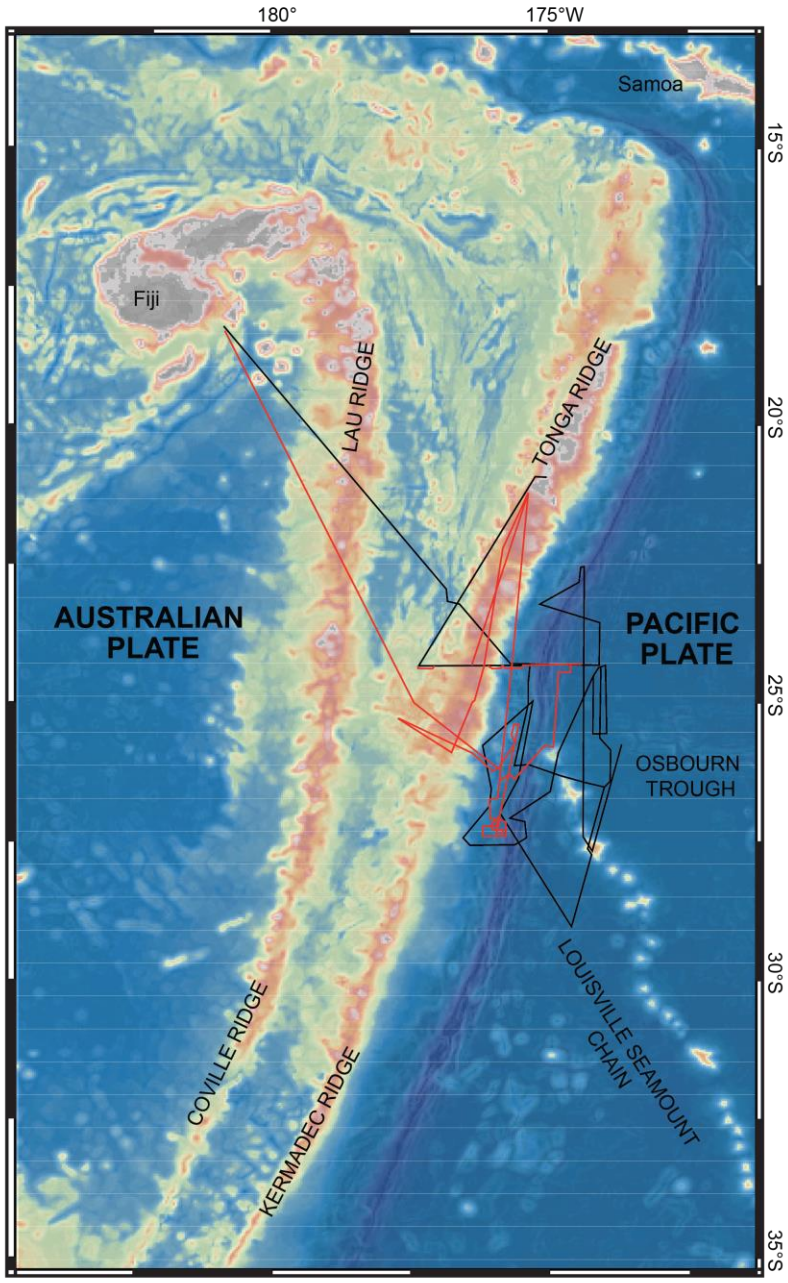

Figure A7 Summary of the ship track of the RV Sonne SO-195 research cruise (January – February 2008) (Grevemeyer and Flüh, 2008). Red lines represent the Leg 1 ship track and black lines represent the Leg 2 ship track.

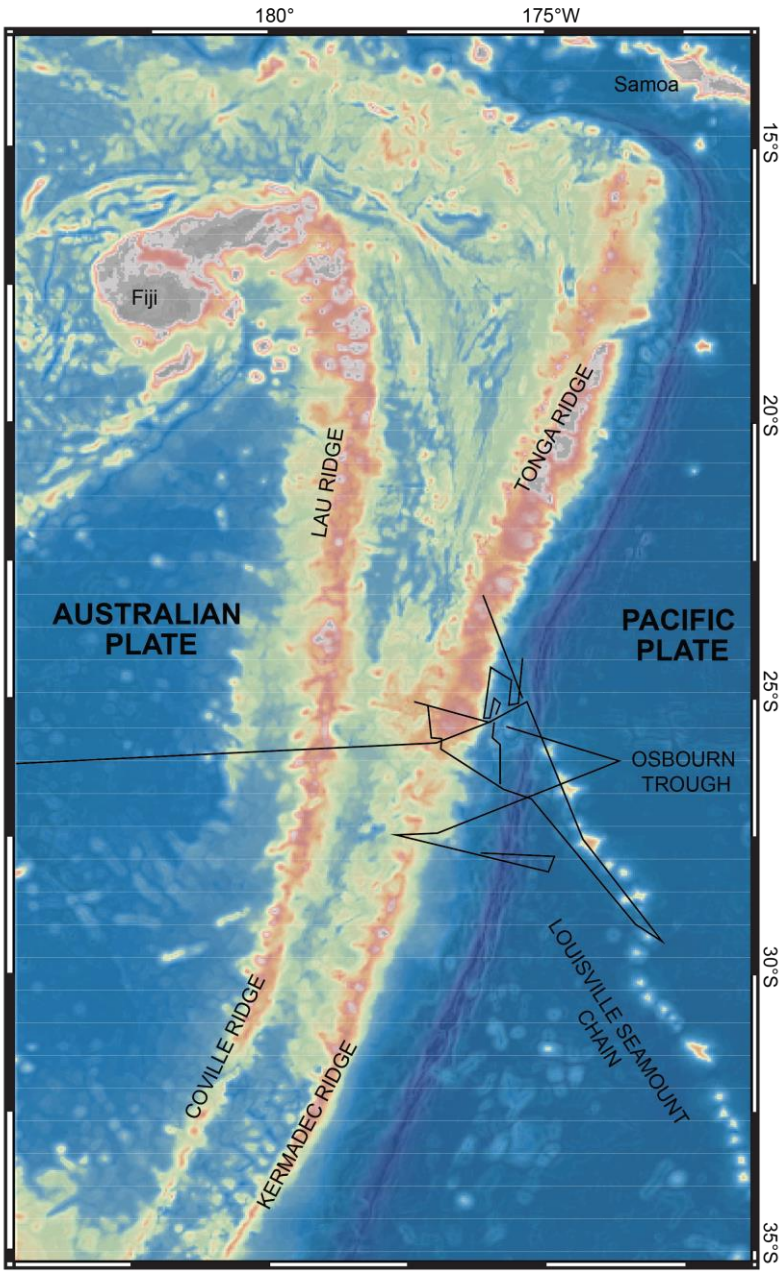

Figure A8 Summary of the ship track of the RV Sonne SO-215 research cruise (April 25 – June 11, 2011) (Peirce and Watts, 2011).

Appendix B

Geological Map of the Louisville and Monowai Arc Segments, Tonga-Kermadec Arc

2022

Scale 1 : 500,000

0 50 100 150 km

Author: Alexandra Gray

Projection: Plate Carée - WGS 1984

LABEL — Formation | Subformations — **UNIT NAME AND DESCRIPTION**

ARC-FRONT VOLCANOES

- Av1 — **Conical volcano** — Cone-shaped edifice composed of lava flows and volcaniclastic material, commonly with a summit crater and/or cut by dike complexes (>1 km diameter; width:height ≤5)
- Av2 — **Shield volcano** — Volcanic shield edifice composed of lava flows, commonly with a large central caldera (>1 km diameter; width:height >5)
- Av3 — **Dome volcano** — Dome-shaped edifice composed of lava flows, with or without a central caldera (>1 km diameter; height:width ~1) and superimposed cone
- Av4 — **Fissure volcano** — Elongate volcanic edifice composed mostly of lava flows, commonly with a central dike (>1 km length; length:width >3)
- Bavf — **Volcanic field** — A broad area of lava flows and volcaniclastic material surrounding a number of closely-spaced volcanoes

ACTIVE ARC

- *Upper* uAc — **Upper arc crust** — Undivided crust belonging to the active arc, including volcaniclastic material, flows, and dikes
  - uAc1 — **Intact upper arc crust** — Crust belonging to the active arc, mostly unaffected by underlying rifting and arc-related volcaniclastic deposits
  - uAc2 — **Intensely faulted upper arc crust** — Crust belonging to the active arc exposed in the walls of the arc rifts
  - uAc3 — **Extended upper arc crust and volcaniclastic deposits** — Foundered crust of the active arc at the floor of rift grabens

BACKARC RIFTS

- *Upper* uBar — **Axial backarc volcanic ridge** — Volcanic ridge in an active spreading center, commonly with discrete volcanic edifices (cones and domes), dike complexes, or calderas
- uBac — **Axial backarc crust** — Undivided backarc crust in the inner rift valley of an active spreading center
- *Middle* mBar — **Proximal volcanic or tectonic ridge** — Elongate volcanic edifice or coalesced ridges in the outer rift valley or on the flank, adjacent to an active spreading center or axial volcanic ridge
- mBac — **Proximal backarc crust** — Undivided backarc crust in the outer rift valley, adjacent to an active spreading center or axial volcanic ridge (may include products of off-axis volcanism)

ARC-BACKARC TRANSITION

- *Upper* uTr — **Ridge at the arc-backarc transition** — Elongate volcanic or tectonic ridge between an active or relict arc and a backarc basin (may be a product of rift volcanism or block faulting)
- *Lower* lTc — **Lower transitional arc-backarc crust** — Undivided crust at the arc-backarc transition (may include both arc and backarc crust)

RELICT ARC

- *Upper* uRac — **Upper relict-arc crust** — Arc (or forearc) crust, including relict arc volcanoes and sediments, belonging to the latest episode of arc construction prior to or during backarc basin opening
- *Lower* lRac — **Lower relict-arc crust** — Earliest exposed volcanic and intrusive rocks of former (or forearc) crust (commonly obscured by younger volcanic rocks)

SYMBOLS

- Caldera rim
- Lineament
- Caldera Ring Fault
- Caldera Collapse Scarp

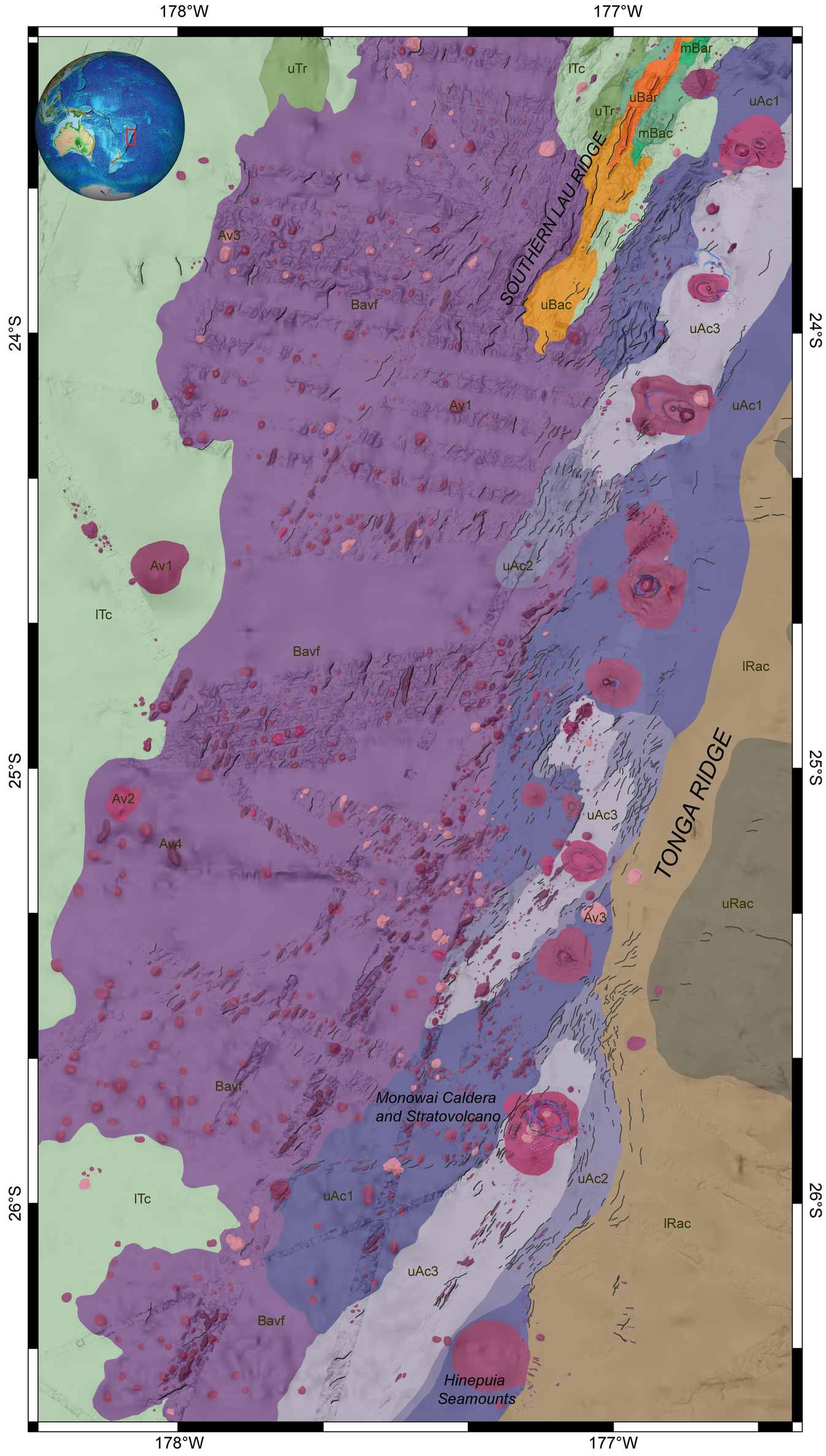

The background is the 2019 GMRT intergrated with shiptracks enhanced with slope function and multidirectional hillshade

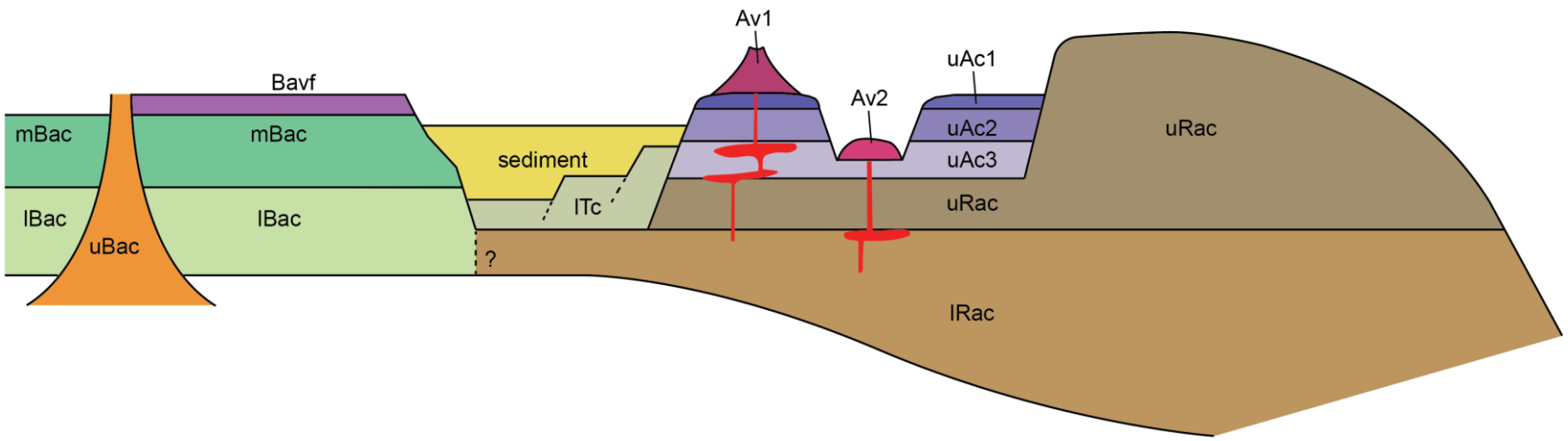

Figure B1 Schematic illustration of the relationship between the Louisville and Monowai Segment mapped units. Drilling at ODP sites on the Tonga Ridge has revealed mainly volcaniclastic and sedimentary rocks of Holocene to late Miocene age with a thickness up to 600 m thick (Parson et al., 1992). Drilling in the Tonga Forearc encountered felsic rocks of Eocene age and they may be present in the basement of the Tonga Ridge. Seismic sections across the active arc suggest that the basement is up to 20 km thick (Crawford et al., 2003; Contreras-Reyes et al., 2011).

Appendix G: Global Database of Submarine Calderas

Caldera #	Name	Latitude	Longitude	Location	Crater Shape	Crater Type	Ocean Region	Geographic Setting	Caldera Classification	Caldera Type	Rock type	Volcanoclastic (on-large ash)	Alteration	Active (y/n)	Temperature (°C)	Mineralization	Dimensions (km)	Lava (length) (km)	Lava (width) (km)	Eccentricity	Orientation (°)	Orientation error	Area (km²)	Volume (km³)	Volcanic Volume error (%)	Eruptions	Elongation	Regional Slope (Degrees)	Angle between Caldera and Regional Slope	Crater depth max (m)	Crater depth min (m)	Floor depth max (m)	Floor depth min (m)	Rim depth max (m)	Rim depth min (m)	Rim depth avg (m)	Dominance (%)	Age (Ma)	Margins/Facies?	# of margins/facies	Margins/Facies average/frame	Gross ID	Samples collected? (y/n)	Resurgence zone	Lava Height	Cone Gradient	Reference
1	Tuan-Lei Kuishou	9.85	150.00	Gakkepuro Spreading Center	~15.0	Oceanic Spreading Center	Pacificwater	Mid-Ocean Ridges	Mafic	Complex	MORB					Sulfides	4 x 2	4	2	0.87	117	20	10.00	1.000	10.00		ensialgenite	50	30	>1000	>1000											Tuan-Lei Kuishou (Wu Chaoyang), Chaoyang					Fraisse et al., 2018; Baker et al., 2018; Hagelson et al., 2008
2	Jiao Tai Tuoxin	20.00	20.00	Oceanic Spreading Center	15.0	Oceanic Spreading Center	Pacificwater	Mid-Ocean Ridges	Mafic	Complex	Basalt						15 x 12	15	12	0.40	0	10	150.00	1.000	10.00		ensialgenite	1.5	90	>200							10												Fraisse et al., 2018
3	Mariner's Basin (what graben)	22.00	20.0	Andesite Volcanic Plateau	15.00	Oceanic Spreading Center	Pacificwater	Mid-Ocean Ridges	Mafic	Arbor Graben	ENDOR			y	400		18.00 x 2.0	18.0	2.0	0.87	15	10.0	36.00	1.000	10.00		ensialgenite	1.5	90	>200		-2670	-290	-280	2170	1.00 m	0	>100	100-200		MEBA (Eric Baker)		y	700m	1.50m	Andesite et al., 2015
4	Lucky Strike (what graben)	22.00	20.0	Lucky Strike Seamount	15.00	Oceanic Spreading Center	Pacificwater	Mid-Ocean Ridges	Mafic	Complex	Basalt			y	200 and 315	Sulfide mineralogy	3 x 2	3	2	0.75	0	10	6.00	1.000	10.00		ensialgenite	1.5	90	>150	>150	-1750	-1500	-1550	-1650		0	>100			MEBA (Eric Baker), Bernadette (Eric Thomas) Pearl		y			Andesite et al., 2015; Baker et al., 2008
5	Lucky Strike	22.00	20.0	Lucky Strike Seamount	15.00	Oceanic Spreading Center	Pacificwater	Mid-Ocean Ridges	Mafic	Complex	Basalt						3 x 2	3	2	0.75	0	10	6.00	1.000	10.00		ensialgenite	1.5	90	>150	>150	-1750	-1500	-1550	-1650		0	>100			MEBA (Eric Baker)		y			Andesite et al., 2015; Baker et al., 2008
6	Nifu	27.0	15.00	Gulf Volcano Range	15.00	Oceanic Spreading Center	Pacificwater	Mid-Ocean Ridges	Mafic	Complex							1.5 x 1.0	1.5	1.0	0.65	90	15	1.50	0.500	10.00		ensialgenite	50	10	2600	-2100	2000	-2050	-2025	-2050	100					Nifu (Nifu Seamount)		n			Fraisse et al., 2018
7	Nifu	27.0	15.00	Gulf Volcano Range	15.00	Oceanic Spreading Center	Pacificwater	Mid-Ocean Ridges	Mafic	Complex							0.75 x 0.5	0.75	0.5	0.65	90	15	0.38	0.500	10.00		ensialgenite	50	10	2600	-2100	2000	-2050	-2025	-2050	100					Nifu (Nifu Seamount)		n			Fraisse et al., 2018
8	Jaser Seamount	18	150.0	Jaser de Flora	12.0	Oceanic Spreading Center	Pacificwater	Mid-Ocean Ridges	Mafic	Single	E-prOR0				328	Sulfides	3 x 2.5	3	2.5	0.83	180	50	6.00	1.000	10.00		ensialgenite	50	10	>1400											Flower (= Stanislas)		y			Fraisse et al., 2018; Sauter et al., 2010; Gillet, 1983; Hoch and Bartels, 1982
9	Jaser Seamount	18	150.0	Jaser de Flora	12.0	Oceanic Spreading Center	Pacificwater	Mid-Ocean Ridges	Mafic	Single							3 x 2.5	3	2.5	0.83	180	50	6.00	1.000	10.00		ensialgenite	50	10	>1400													y			
10	Vance Seamount, Gil Caldera	25.00	150.0	Jaser de Flora	15	Oceanic Intraplate	Pacificwater	Mid-Ocean Ridges	Mafic	Complex	MORB						3 x 2	3	2	0.75	120	50	4.50	1.000	10.00		ensialgenite	50	10	>2400											NYX Crater Jaser		y			Gaspar et al., 2005; Hoch and Bartels, 1982
11	Vance Seamount, Fuf Caldera	25.00	150.0	Jaser de Flora	15	Oceanic Intraplate	Pacificwater	Mid-Ocean Ridges	Mafic	Complex	MORB						3 x 2	3	2	0.75	120	50	4.50	1.000	10.00		ensialgenite	50	10	>2400											NYX Crater Jaser		y			Gaspar et al., 2005; Hoch and Bartels, 1982
12	Flapjack (aka Seamount 51-0) Gilnet	40.00	125.0	Gorda Ridge	15	Oceanic Intraplate	Pacificwater	Mid-Ocean Ridges	Mafic	Nested (Summit)	MORB						2.7 x 1.5	2.7	1.5	0.82	155	20	3.00	1.000	10.00		ensialgenite	50	15	>1800											NYX Crater Jaser		y	>1m		Gaspar et al., 2005; Hoch and Bartels, 1982
13	Flapjack (aka Seamount 51-0) Gilnet	40.00	125.0	Gorda Ridge	15	Oceanic Intraplate	Pacificwater	Mid-Ocean Ridges	Mafic	Complex	MORB						5.0 x 3.0	5.0	3.0	0.80	155	20	15.00	1.000	10.00		ensialgenite	50	15	>1800											NYX Crater Jaser		y			Gaspar et al., 2005; Hoch and Bartels, 1982
14	Tuesday Seamount (Tuf-Lo)	36.00	125.00	Tuesday Seamount Chain		Oceanic Intraplate	Pacificwater	Mid-Ocean Ridges	Mafic	Complex	Basalt	>50					5.0 x 3.0	5.0	3.0	0.80	45	110	15.00	1.000	10.00		ensialgenite	50-200									n				Rim Western Flyer (Kim)					Cousteau et al., 2010
15	Tuesday Seamount (Tuf-Lo)	36.00	125.00	Tuesday Seamount Chain		Oceanic Intraplate	Pacificwater	Mid-Ocean Ridges	Mafic	Complex	Basalt	>50					5.0 x 3.0	5.0	3.0	0.80	45	110	15.00	1.000	10.00		ensialgenite	50-200									n				Rim Western Flyer (Kim)					Cousteau et al., 2010
16		39.00	125.00	Tuesday Seamount Chain		Oceanic Intraplate	Pacificwater	Mid-Ocean Ridges	Mafic	Complex	Basalt	>50					5.0 x 3.0	5.0	3.0	0.80	45	110	15.00	1.000	10.00		ensialgenite	50-200									n				Rim Western Flyer (Kim)					Cousteau et al., 2010
17	Kilauea	19.42	155.28	Hawaiian Islands	>10	Oceanic Hot Spot	Pacificwater	Volcanic Oceans	Mafic	Single	Basalts						4 x 3.5	4	3.5	0.65	48	120	14.00	1.000	10.00		ensialgenite	50-200		>1000	>1000	-1000	-1000	-1000	-1000	100	>10 ka	yes	>50		NA		n			Decker and Christiansen, 1984; Gaspard et al., 1993
18	Kaikoura	42.00	180.00	Neovolcanic zone (a number)		Oceanic Hot Spot	Pacificwater	Volcanic Oceans	Mafic	Complex	Basalts, Hawaiites	>50		y	>500		10 x 8	10	8	0.60	45	20	80.00	1.000	10.00		ensialgenite	50	20	500	0	400	0	200	300	100	>10 ka	yes	>50		NA		n			Gaspar et al., 1993; Gaspard and Sigurdsson, 2000
19	Aldan	45.00	145.00	Neovolcanic zone (a number)		Oceanic Hot Spot	Pacificwater	Volcanic Oceans	Mafic	Nested	Basalts, Lesser dacites						5 x 4	5	4	0.65	125	60	63.00	10.000	10.00		ensialgenite	50-200	20	400	300	1300	-1400	-1400	-1350	10.00		>100			NA		n			Gaspar et al., 1993; Gaspard and Sigurdsson, 2000
20	Unnamed	46.00	147.00	Neovolcanic zone (a number)		Oceanic Hot Spot	Pacificwater	Volcanic Oceans	Mafic	Single	Basalt			y			3 x 2	3	2	0.65	135	60	6.00	1.000	10.00		ensialgenite	50-200	20	1000	1000	-1000	-1000	-1000	-1000	100	10				NA		n			Gaspard and Sigurdsson, 2000; Gaspard and Sigurdsson, 2000
21	Ibu	14.00	145.00	Mariana Islands	>10.0-1.0	Volcanoes in Backarc	Pacificwater	Western Basin	Mafic	Single	Basalt					Fe Oxides	10.0 x 10.0	10.0	10	0.00	110	10	100.00	10.000	10.00		ensialgenite	1000		>400	300	200	50	100	20	100					NMI Hydro 1974, SH Mariana 1981					Uwarsa and Yuan, 1988
22	Pohnpei	-13.00	155.00	Nauru Islands	>10.0-1.0	Volcanoes in Backarc	Pacificwater	Western Basin	Mafic	Single	Basalt	>50,000					10 x 5	10	5	0.80	155	30	150.00	50	10.00		ensialgenite	1000		>400	>400	-500	-500	-500	-500	1.00					Gauss 1-001, 2014 (Ed Bell of USGS); Gauss 1-004, 2014 (Ed Bell of USGS); Gauss 1-005, 2014 (Ed Bell of USGS)					Mondal et al., 1994
23	Kilinailau	-13.0	155.00	Nauru Islands	>10.0-1.0	Volcanoes in Backarc	Pacificwater	Western Basin	Mafic	Single	Basalt			y	High Temperature	Sulfides	5 x 4	5	4	0.75	120	50	15.00	1.000	10.00		ensialgenite	100	20	>2000	>1000	-2100	-2000	-2050	-2050	100					Gauss		n			Fraisse et al., 2018; Baker et al., 2018; Hickman et al., 2010
24	Wakatobi	-13.00	124.0	Banda Islands	>10.0-1.0	Volcanoes in Backarc	Pacificwater	Western Basin	Mafic	Single	Basalts					Sulfides/barite	10.0 x 10.0	10.0	10.0	0.00	110	10	100.00	50.000	10.00		ensialgenite	100	20	>500	>400	-1000	-1100	-1050	-1050	100					WAKATOB		n			Fraisse et al., 2018; Baker et al., 2018; Bachelerie et al., 2015; Pratomo et al., 2015
25	Wakatobi	-13.00	124.0	Banda Islands	>10.0-1.0	Volcanoes in Backarc	Pacificwater	Western Basin	Mafic	Single	Basalts						10.0 x 10.0	10.0	10.0	0.00	110	10	100.00	50.000	10.00		ensialgenite	100	20	>500	>400	-1000	-1100	-1050	-1050	100					Sea-level Jaser (Indonesian Seafloor Survey)		n			Fraisse et al., 2018; Baker et al., 2018; Bachelerie et al., 2015; Pratomo et al., 2015
26	Rinjani	-8.00	117.00	Flores Islands	>10.0-1.0	Volcanoes in Backarc	Pacificwater	Western Basin	Mafic	Single	Basalts/Andesite			y	340	Sulfides/barite	5 x 4	5	4	0.75	120	50	15.00	1.000	10.00		ensialgenite	100	20	>1000	>1000	-1100	-1000	-1050	-1050	100	0 - 20	500			South Rinjani (Rinjani)		n	>1m		Fraisse et al., 2018; Baker et al., 2018; Hickman et al., 2010
27	Tambora Caldera	-8.00	117.00	Sumbawa	>10.0-1.0	Volcanoes in Backarc	Pacificwater	Western Basin	Mafic	Single	Basalt						7.0 x 7.0	7.0	7.0	0.00	90	20	150.00	1.000	10.00		ensialgenite	100	20	>1100	>1100	-2000	-2000	-2000	-2000	100	0 - 20	500			Sea-level Jaser (USGS/USGS Sunbeam Survey)		n			Fraisse et al., 2018; Baker et al., 2018; Hickman et al., 2010; Lupton et al., 2012
28	Tambora Caldera	-8.00	117.00	Sumbawa	>10.0-1.0	Volcanoes in Backarc	Pacificwater	Western Basin	Mafic	Single	Basalt					Pumice	7.0 x 7.0	7.0	7.0	0.00	90	20	150.00	1.000	10.00		ensialgenite	100	20	>1100	>1100	-2000	-2000	-2000	-2000	100	0 - 20	500			Sea-level Jaser (USGS/USGS Sunbeam Survey)		n			Fraisse et al., 2018; Baker et al., 2018; Hickman et al., 2010; Lupton et al., 2012
29	Tambora Caldera	-8.00	117.00	Sumbawa	>10.0-1.0	Volcanoes in Backarc	Pacificwater	Western Basin	Mafic	Single	Basalt					Pumice	7.0 x 7.0	7.0	7.0	0.00	90	20	150.00	1.000	10.00		ensialgenite	100	20	>1100	>1100	-2000	-2000	-2000	-2000	100	0 - 20	500			Sea-level Jaser (USGS/USGS Sunbeam Survey)		n			Fraisse et al., 2018; Baker et al., 2018; Hickman et al., 2010; Lupton et al., 2012
30	Aceh (aka Jackie)	10.0	91.00	Lesser Andaman/Aceh Arc		Volcanoes in Arc	Pacificwater	Volcanoes in Arc	Mafic	Complex	MORB/Basalt	Andesite tuffs		y	200		2.0	2.0	0.0	0.00	20	120	3.00	0.500	10.00		crescent	200	5	>200						100		>1m	>50m		ADHOC					Kwiatkowski et al., 2008; Lindsay et al., 2008
31	Kerinci	-2.0	101.00	Sumatra Arc	>1.0	Volcanoes in Arc	Pacificwater	Volcanoes in Arc	Mafic	Single	Basalt			y	90	Native Sulphur	6.0 x 5.0	6.0	5.0	0.60	90	120	30.00	0.500	10.00		subduction	100	40	>400											ADHOC					Kiyosugi et al., 2015; Chaise et al., 2014; Jaser et al., 2012
32	Tofua	19.75	175.00	Tonga Islands	>10.0-1.0	Volcanoes in Arc	Pacificwater	Volcanoes in Arc	Mafic	Complex	Andesite, Basalts (Andesite	>100					6.0 x 5.0	6.0	5.0	0.65	160	60	30.00	0.500	10.00		subduction	100	10	>100											NA		n			Cauthard et al., 2011
33	Sumpan 1	21.75	175.00	Kermadec Tonga Arc	>10.0-1.0	Volcanoes in Arc	Pacificwater	Volcanoes in Arc	Mafic	Complex	Basalts (Andesite				150	Sulfide/Pyrite/barite	7 x 5.5	7	5.5	0.65	157	60	38.50	0.500	10.00		ensialgenite	100	10	>200											SHOR1 (Fraser 01, Fraser 1)		y			Fraisse et al., 2018; Wallace et al., 2009
34	Sumpan 1b-01	20.50	175.00	Kermadec Tonga Arc	>10.0-1.0	Volcanoes in Arc	Pacificwater	Volcanoes in Arc	Mafic	Complex	Andesite		Steam/sulphur species				5.0 x 5.0	5.0	5.0	0.00	100	20	19.500	1.0	10.00		ensialgenite/FeSO-sidrite	100	20	>800	>800	-800	-900	-850	-850	100					SHOR1		y	>10m	700m	Wallace et al., 2009
35	Monowai 14-01	22.50	175.00	Kermadec Tonga Arc	>10.0-1.0	Volcanoes in Arc	Pacificwater	Volcanoes in Arc	Mafic	Complex	Basalt, Andesite, Dacite		Steam/sulphur species				6.0 x 5.0	6.0	5.0	0.65	100	20	19.500	1.0	10.00		ensialgenite/FeSO-sidrite	100	20	>1000						100	100k-0ka		>100m		SHOR1		y	>10m		Wallace et al., 2009
36	Sumpan 2	20.75	175.00	Kermadec Tonga Arc	>10.0-1.0	Volcanoes in Arc	Pacificwater	Volcanoes in Arc	Mafic	Complex	Andesite, Basalts						5.0 x 5.0	5.0	5.0	0.00	100	20	19.500	1.000	10.00		subduction	100	20	>1400	>1000	-750	-900	-850	-850	100	>10ka	y	0 m		SHOR1		y	>10m		Wallace et al., 2009
37	Sumpan 3	20.75	175.00	Kermadec Tonga Arc	>10.0-1.0	Volcanoes in Arc	Pacificwater	Volcanoes in Arc	Mafic	Single	Dacite	>100m					3.0 x 3.0	3.0	3.0	0.00	100	20	9.000	1.000	10.00		ensialgenite/FeSO-sidrite	100	20	>1000						100		y	0 m		SHOR1		y	>10m	600m	Wallace et al., 2009
38	Sumpan 4b	20.75	175.00	Kermadec Tonga Arc	>10.0-1.0	Volcanoes in Arc	Pacificwater	Volcanoes in Arc	Mafic	Complex	Andesite, Basalts						5.0 x 5.0	5.0	5.0	0.00	100	20	19.500	1.000	10.00		subduction	100	20	>1000											SHOR1		y			Wallace et al., 2009
39	Sumpan 5b	21.25	175.00	Kermadec Tonga Arc	>10.0-1.0	Volcanoes in Arc	Pacificwater	Volcanoes in Arc	Mafic	Complex	Basalt/Andesite/Dacite						5.0 x 5.0	5.0	5.0	0.00	100	20	19.500	1.000	10.00		crescent	100	20	>800						100					SHOR1		y			Wallace et al., 2009
40	Monowai 17	21.50	175.00	Kermadec Tonga Arc	>10.0-1.0	Volcanoes in Arc	Pacificwater	Volcanoes in Arc	Mafic	Complex	Basalt/Andesite/Dacite	>50					7.0 x 5.0	7.0	5.0	0.70	100	20	27.500	1.000	10.00		ensialgenite/FeSO-sidrite	100	20	>1100	>1100	-1000	-1100	-1050	-1050	100					SHOR1		y			Wallace et al., 2009
41	Monowai 18	21.50	175.00	Kermadec Tonga Arc	>10.0-1.0	Volcanoes in Arc	Pacificwater	Volcanoes in Arc	Mafic	Nested	Basalt/Andesite/Dacite	>50			60	Sulfides/barite	8.0 x 5.0	8.0	5.0	0.75	100	20	40.000	1.0	10.00		ensialgenite/FeSO-sidrite	100	20	>1000	>1000	-1100	-1000	-1050	-1050	100	0 - 20	500	500m		SHOR1, SHOR2, SHOR3, SHOR4(NMI in SUBMIT 2011, 2012, 2013)		y			Wallace et al., 2009; Wallace et al., 2013
42	Monowai 19	21.50	175.00	Kermadec Tonga Arc	>10.0-1.0	Volcanoes in Arc	Pacificwater	Volcanoes in Arc	Mafic	Nested	Basalt/Andesite/Dacite	>50			60	Sulfides/barite	8.0 x 5.0	8.0	5.0	0.75	100	20	40.000	1.0	10.00		ensialgenite/FeSO-sidrite	100	20	>1000	>1000	-1100	-1000	-1050	-1050	100	0 - 20	500	500m		SHOR1, SHOR2, SHOR3, SHOR4(NMI in SUBMIT 2011, 2012, 2013)		y			Wallace et al., 2009; Wallace et al., 2013
43	Monowai-01	-28.00	177.00	Kermadec Tonga Arc	>10.0-1.0	Volcanoes in Arc	Pacificwater	Volcanoes in Arc	Mafic	Complex	Andesite/Dacite, Arrow Rhyolite			y			5.0 x 5.0	5.0	5.0	0.00	155	60	19.500	0	10.00		subduction	100	40	>500						100					NZAPLUME-01		y	200m	700m	Stewart et al., 2010; NZAPLUME Cruise Report; Graham et al., 2007
44	Monowai-04	-28.00	177.00	Kermadec Tonga Arc	>10.0-1.0	Volcanoes in Arc	Pacificwater	Volcanoes in Arc	Mafic	Complex	Andesite/Dacite, Arrow Rhyolite			y			5.0 x 5.0	5.0	5.0	0.00	155	70	19.500	0	10.00		subduction	100	10	>700						100					NZAPLUME-04		y			Graham et al. 2008; Stewart et al., 2010; NZAPLUME Cruise Report
45	Monowai-06	-28.00	177.00	Kermadec Tonga Arc	>10.0-1.0	Volcanoes in Arc	Pacificwater	Volcanoes in Arc	Mafic	Complex	Andesite/Dacite, Arrow Rhyolite			y			5.0 x 5.0	5.0	5.0	0.00	155	70	19.500	0	10.00		ensialgenite/FeS	100	10	>700						100					NZAPLUME-06		y			Graham et al. 2008; Stewart et al., 2010; NZAPLUME Cruise Report
46	Monowai-07	-28.00	177.00	Kermadec Tonga Arc	>10.0-1.0	Volcanoes in Arc	Pacificwater	Volcanoes in Arc	Mafic	Complex	Andesite/Dacite, Arrow Rhyolite			y			5.0 x 5.0	5.0	5.0	0.00	155	70	19.500	0	10.00		subduction	100	10	>700						100					NZAPLUME-07		y			Graham et al. 2008; Stewart et al., 2010; NZAPLUME Cruise Report
47	Monowai-08	-28.00	177.00	Kermadec Tonga Arc	>10.0-1.0	Volcanoes in Arc	Pacificwater	Volcanoes in Arc	Mafic	Complex	Andesite/Dacite, Arrow Rhyolite			y			5.0 x 5.0	5.0	5.0	0.00	155	70	19.500	0	10.00		ensialgenite/FeS	100	10	>700						100					NZAPLUME-08		y			Graham et al. 2008; Stewart et al., 2010; NZAPLUME Cruise Report
48	Monowai-09	-28.00	177.00	Kermadec Tonga Arc	>10.0-1.0	Volcanoes in Arc	Pacificwater	Volcanoes in Arc	Mafic	Complex	Andesite/Dacite, Arrow Rhyolite			y			5.0 x 5.0	5.0	5.0	0.00	155	70	19.500	0	10.00		subduction	100	10	>700						100					NZAPLUME-09		y			Graham et al. 2008; Stewart et al., 2010; NZAPLUME Cruise Report
49	Monowai-10	-28.00	177.00	Kermadec Tonga Arc	>10.0-1.0	Volcanoes in Arc	Pacificwater	Volcanoes in Arc	Mafic	Complex	Andesite/Dacite, Arrow Rhyolite			y			5.0 x 5.0	5.0	5.0	0.00	155	70	19.500	0	10.00		subduction	100	10	>700						100					NZAPLUME-10		y			Graham et al. 2008; Stewart et al., 2010; NZAPLUME Cruise Report
50	Monowai-11	-28.00	177.00	Kermadec Tonga Arc	>10.0-1.0	Volcanoes in Arc	Pacificwater	Volcanoes in Arc	Mafic	Complex	Andesite/Dacite, Arrow Rhyolite			y			5.0 x 5.0	5.0	5.0	0.00	155	70	19.500	0	10.00		subduction	100	10	>700						100					NZAPLUME-11		y			Graham et al. 2008; Stewart et al., 2010; NZAPLUME Cruise Report
51	LF-1	-29.00	177.00	Kermadec Tonga Arc	>10.0-1.0	Volcanoes in Arc	Pacificwater	Volcanoes in Arc	Mafic	Single	Andesite/Dacite, Arrow Rhyolite			y			3 x 2	3	2	0.65	155	70	9.000	0.5	10.00		ensialgenite/FeS	100	10	>100						100			>10		NZAPLUME-LF1		y			Graham et al. 2008; Stewart et al., 2010; NZAPLUME Cruise Report
52	Funafuti-01	-27.00	177.00	Kermadec Tonga Arc	>10.0-1.0	Volcanoes in Arc	Pacificwater	Volcanoes in Arc	Mafic	Complex	Basalt, Basalt-andesite, andesite, Dacite			y			5.0 x 2.5	5.0	2.5	0.87	155	70	12.500	0.5	10.00		ensialgenite/FeS	100	10	>150						100			>10		NZAPLUME-01		y			Graham et al. 2008; Stewart et al., 2010; NZAPLUME Cruise Report
53	Funafuti-02	-27.00	177.00	Kermadec Tonga Arc	>10.0-1.0	Volcanoes in Arc	Pacificwater	Volcanoes in Arc	Mafic	Complex	Basalt, Basalt-andesite, andesite, Dacite			y			5.0 x 2.5	5.0	2.5	0.87	155	70	12.500	0.5	10.00		ensialgenite/FeS	100	10	>150						100			>10		NZAPLUME-02		y			Graham et al. 2008; Stewart et al., 2010; NZAPLUME Cruise Report
54	Funafuti-03	-27.00	177.00	Kermadec Tonga Arc	>10.0-1.0	Volcanoes in Arc	Pacificwater	Volcanoes in Arc	Mafic	Complex	Basalt, Basalt-andesite, andesite, Dacite			y			5.0 x 2.5	5.0	2.5	0.87	155	70	12.500	0.5	10.00		ensialgenite/FeS	100	10	>150						100			>10		NZAPLUME-03		y			Graham et al. 2008; Stewart et al., 2010; NZAPLUME Cruise Report
55	Gambier 08	-27.0	177.00	Kermadec Tonga Arc	>10.0-1.0	Volcanoes in Arc	Pacificwater	Volcanoes in Arc	Mafic	Nested	Rhyolite			y			8.0 x 6.7	8.0	6.7	0.80	155	80	53.500	0.5	10.00		ensialgenite/FeS	100	10	>100						100					NZAPLUME-08		y			Graham et al. 2008; Stewart et al., 2010; NZAPLUME Cruise Report
56	Raoul-01	-29.00	177.00	Kermadec Tonga Arc	>10.0-1.0	Volcanoes in Arc	Pacificwater	Volcanoes in Arc	Mafic	Single	Rhyolite, Dacite			y			3 x 2.5	3	2.5	0.75	155	80	7.500	0.5	10.00		ensialgenite/FeS	100	10	>100						100	>5				NZAPLUME-01		y			Graham et al. 2008; Stewart et al., 2010; NZAPLUME Cruise Report
57	Raoul-02	-29.00	177.00	Kermadec Tonga Arc	>10.0-1.0	Volcanoes in Arc	Pacificwater	Volcanoes in Arc	Mafic	Single	Rhyolite, Dacite			y			3 x 2.5	3	2.5	0.75	155	80	7.500	0.5	10.00		ensialgenite/FeS	100	10	>100						100	>5				NZAPLUME-02		y			Graham et al. 2008; Stewart et al., 2010; NZAPLUME Cruise Report
58	Funafuti-04	-27.00	177.00	Kermadec Tonga Arc	>10.0-1.0	Volcanoes in Arc	Pacificwater	Volcanoes in Arc	Mafic	Complex	Basalt, Basalt-andesite, andesite, Dacite	>50					5.0 x 2.5	5.0	2.5	0.87	155	70	12.500	0.5	10.00		ensialgenite/FeS	100	10	>150						100			>10		NZAPLUME-04		y			Graham et al. 2008; Stewart et al., 2010; NZAPLUME Cruise Report
59	Funafuti-05	-27.00	177.00	Kermadec Tonga Arc	>10.0-1.0	Volcanoes in Arc	Pacificwater	Volcanoes in Arc	Mafic	Complex	Basalt, Basalt-andesite, andesite, Dacite	>50					5.0 x 2.5	5.0	2.5	0.87	155	70	12.500	0.5	10.00		ensialgenite/FeS	100	10	>150						100			>10		NZAPLUME-05		y			Graham et al. 2008; Stewart et al., 2010; NZAPLUME Cruise Report
60	Funafuti-06	-27.00	177.00	Kermadec Tonga Arc	>10.0-1.0	Volcanoes in Arc	Pacificwater	Volcanoes in Arc	Mafic	Complex	Basalt, Basalt-andesite, andesite, Dacite	>50					5.0 x 2.5	5.0	2.5	0.87	155	70	12.500	0.5	10.00		ensialgenite/FeS	100	10	>150						100			>10		NZAPLUME-06		y			Graham et al. 2008; Stewart et al., 2010; NZAPLUME Cruise Report
61	Funafuti-07	-27.00	177.00	Kermadec Tonga Arc	>10.0-1.0	Volcanoes in Arc	Pacificwater	Volcanoes in Arc	Mafic	Complex	Basalt, Basalt-andesite, andesite, Dacite	>50					5.0 x 2.5	5.0	2.5	0.87	155	70	12.500	0.5	10.00		ensialgenite/FeS	100	10	>150						100			>10		NZAPLUME-07		y			Graham et al. 2008; Stewart et al., 2010; NZAPLUME Cruise Report
62	Rekohu-01	-28.00	177.00	Kermadec Tonga Arc	>10.0-1.0	Volcanoes in Arc	Pacificwater	Volcanoes in Arc	Mafic	Nested	Rhyolite, Dacite			y			6 x 2.5	6	2.5	0.95	155	80	9.000	0.5	10.00		subduction	100	10	>200						100					NZAPLUME-01		y			Graham et al. 2008; Stewart et al., 2010; NZAPLUME Cruise Report
63	Rekohu-02	-28.00	177.00	Kermadec Tonga Arc	>10.0-1.0	Vol

Global Database of Submarine Calderas References

Acocella, V., Korme, T., Salvini, F., Funiciello, R., 2003, Elliptic calderas in the Ethiopian Rift: control of pre-existing structures. Journal of Volcanology and Geothermal Research, **v. 119**, p. 189–203

Alfaro, R., Brandsdóttir, B., Rowlands, D. P., White, R. S., Gudmundsson, M. T., 2007, Structure of the Grímsvötn central volcano under the Vatnajökull icecap, Iceland. Geophysical Journal International, **v. 168**, p. 863–876

Anderson, M. O., Hannington, M. D., Haase, K., Schwarz-Schampera, U., Augustin, N., McConachy, T. F., Allen, K., 2016, Tectonic focusing of voluminous basaltic eruptions in magma-deficient backarc rifts. Earth and Planetary Science Letters, **v. 440**, p. 43–55

Angelier, J., Lybéris, N., Le Pichon, X., Barrier, E., Huchon, P., 1982, The tectonic development of the hellenic arc and the sea of crete: A synthesis. Tectonophysics, **v. 86**, p. 159–196

Asamori, K., Umeda, K., Ogawa, Y., Oikawa, T., 2010, Electrical Resistivity Structure and Helium Isotopes around Naruko Volcano, Northeastern Japan and Its Implication for the Distribution of Crustal Magma. International Journal of Geophysics, 8 p., doi:10.1155/2010/738139

Bacon, C. R., 1983, Eruptive history of Mount Mazama and Crater Lake Caldera, Cascade Range, U.S.A. Journal of Volcanology and Geothermal Research, **v. 18**, p. 57–115

Bailey, R. A., Dalrymple, G. B., Lanphere, M. A., 1976, Volcanism, structure, and geochronology of Long Valley Caldera, Mono County, California: Journal of Geophysical Research, **v. 81**, p. 725–744

Baker, E. T., Embley, R. W., Walker, S. L., Resing, J. A., Lupton, J. E., Nakamura, K., de Ronde, C. E. J., Massoth, G. J., 2008, Hydrothermal activity and volcano distribution along the Mariana arc. Journal of Geophysical Research: Solid Earth, **v. 113**, 16 p.

Bartel, B. A., Hamburger, M. W., Meertens, C. M., Lowry, A. R., Corpuz, E., 2003, Dynamics of active magmatic and hydrothermal systems at Taal Volcano, Philippines, from continuous GPS measurements. Journal of Geophysical Research, **v. 108**, 15 p.

Bassett, D., Kopp, H., Sutherland, R., Henrys, S., Watts, A. B., Timm, C., Scherwath, M., Grevemeyer, I., de Ronde, C. E. J., 2016, Crustal structure of the Kermadec arc from MANGO seismic refraction profiles. Journal of Geophysical Research: Solid Earth, **v. 121**, p. 7514–7546

Berkenbosch, H. A., de Ronde, C. E. J., Paul, B. T., Gemmell, J. B., 2015, Characteristics of Cu isotopes from chalcopyrite-rich black smoker chimneys at Brothers volcano, Kermadec arc, and Niuatahi volcano, Lau basin. Mineralium Deposita, **v. 50**, p. 811–824

Björnsson, A., Saemundsson, K., Einarsson, P., Tryggvason, E., Grönvold, K., 1977, Current rifting episode in north Iceland. Nature, **v. 266**, p. 318–323

Björnsson, H., and Guðmundsson, M. T., 1993, Variations in the thermal output of the subglacial Grímsvötn Caldera, Iceland. Geophysical Research Letters, **v. 20**, p. 2127–2130

Boccaletti, M., Nicolich, R., Tortorici, L., 1990, New data and hypothesis on the development of the Tyrrhenian basin. Palaeogeography, Palaeoclimatology, Palaeoecology, **v. 77**, p. 15–40

Brounce, M., Kelley, K. A., Stern, R., Martinez, F., Cottrell, E., 2016, The Fina Nagu volcanic complex: Unusual submarine arc volcanism in the rapidly deforming southern Mariana margin. Geochemistry, Geophysics, Geosystems, **v. 17**, p. 4078–4091

Brown, G. C., Everett, S. P., Rymer, H., McGarvie, D. W., Foster, I., 1991, New light on caldera evolution—Askja, Iceland. Geology, **v. 19**, p. 352-355

Calderone, G. M., Grönvold, K., Oskarsson, N., 1990, The welded air-fall tuff layer at Krafla, northern Iceland: A composite eruption triggered by injection of basaltic magma. Journal of Volcanology and Geothermal Research, **v. 44**, p. 303–314

Canadian American Seamount Expedition, 1985, Hydrothermal vents on an axis seamount of the Juan de Fuca ridge. Nature, **v. 313**, p. 212–214

Cardigos, F., Colaço, A., Dando, P. R., Ávila, S. P., Sarradin, P.-M., Tempera, F., Conceição, P., Pascoal, A., Serrão Santos, R., 2005, Shallow water hydrothermal vent field fluids and communities of the D. João de Castro Seamount (Azores). Chemical Geology, **v. 224**, p. 153–168

Carey, S., Nomikou, P., Bell, K. C., Lilley, M., Lupton, J., Roman, C., Stathopoulou, E., Bejelou, K., Ballard, R., 2013, CO_2 degassing from hydrothermal vents at Kolumbo submarine volcano, Greece, and the accumulation of acidic crater water. Geology, **v. 41**, p. 1035–1038

Caulfield, J. T., Cronin, S. J., Turner, S. P., Cooper, L. B., 2011, Mafic Plinian volcanism and ignimbrite emplacement at Tofua volcano, Tonga. Bulletin of Volcanology, **v. 73**, p. 1259-1277

Chesner, C. A., 2012, The Toba Caldera Complex. Quaternary International, **v. 258**, p. 5–18

Chesner, C. A., and Rose, W. I., 1991, Stratigraphy of the Toba Tuffs and the evolution of the Toba Caldera Complex, Sumatra, Indonesia. Bulletin of Volcanology, **v. 53**, p. 343–356

Chiarabba, C., Amato, A., Delaney, P. T., 1997, Crustal structure, evolution, and volcanic unrest of the Alban Hills, Central Italy. Bulletin of Volcanology, **v. 59**, p. 161–170

Clague, D. A., Reynolds, J. R., Davis, A. S., 2000, Near-ridge seamount chains in the northeastern Pacific Ocean. Journal of Geophysical Research: Solid Earth, **v. 105**, p. 16541–16561

Cole, J. W., Brown, S. J. A., Burt, R. M., Beresford, S. W., Wilson, C. J. N., 1998, Lithic types in ignimbrites as a guide to the evolution of a caldera complex, Taupo volcanic centre, New Zealand. Journal of Volcanology and Geothermal Research, **v. 80**, p. 217-237

Coumans, J. P., Stix, J., Clague, D. A., Minarik, W. G., 2015, The Magmatic Architecture of Taney Seamount-A, NE Pacific Ocean. Journal of Petrology, **v. 56**, p. 1037–1067

Crawford, W. C., Rai, A., Singh, S. C., Cannat, M., Escartin, J., Wang, H., Daniel, R., Combier, V., 2013, Hydrothermal seismicity beneath the summit of Lucky Strike volcano, Mid-Atlantic Ridge. Earth and Planetary Science Letters, **v. 373**, p. 118–128

Curray, J. R., 1989, The Sunda Arc: A model for oblique plate convergence. Netherlands Journal of Sea Research, **v. 24**, p. 131–140

Davy, B. W., and Caldwell, T. G., 1998, Gravity, magnetic and seismic surveys of the caldera complex, Lake Taupo, North Island, New Zealand. Journal of Volcanology and Geothermal Research, **v. 81**, p. 69-89

Dawson, P. B., Chouet, B. A., Okubo, P. G., Villaseñor, A., Benz, H. M., 1999, Three-dimensional velocity structure of the Kilauea Caldera, Hawaii. Geophysical Research Letters, **v. 26**, p. 2805–2808

Decker, R. W., and Christiansen, R. L., 1984, Explosive Eruptions of Kilauea Volcano, Hawaii *In* national Research Council (*Eds*) Explosive Volcanism: Inception, Evolution, and Hazards. National Academy Press, Washington, p. 122-132

Deino, A. L., Orsi, G., de Vita, S., Piochi, M., 2004, The age of the Neapolitan Yellow Tuff caldera-forming eruption (Campi Flegrei caldera – Italy) assessed by 40Ar/39Ar dating method. Journal of Volcanology and Geothermal Research, **v. 133**, p. 157–170

Deplus, C., Bonvalot, S., Dahrin, D., Diament, M., Harjono, H., Dubois, J., 1995, Inner structure of the Krakatau volcanic complex (Indonesia) from gravity and bathymetry data. Journal of Volcanology and Geothermal Research, **v. 64**, p. 23–52

de Ronde, C. E. J., Daughney, C., Wright, I., Embley, B., Arculus, R., Faure, K., Baker, E., Graham, I., Christenson, B., Law, C., Massoth, G., Garlick, R., Safi, K., George, S., Wilson, C., Gerring, P., Britten, K., Greene, R., Dunkin, M., Stanley, R., Walker, S., McDonall, S., Baier, A., Vailea, ‘A., Houia, S., Graaf, J., 2006, NZAPLUME III New Zealand American PLUme Mapping Expedition, 23 September – 17 October, 2004

Di Vito, M. A., Isaia, R., Orsi, G., Southon, J., de Vita, D., D’Anonio, M., Pappalardo, L., Piochi, M., 1999, Volcanism and deformation since 12,000 years at the Campi Flegrei caldera (Italy). Journal of Volcanology and Geothermal Research, **v. 91**, p. 221-246

Embley, R. W., de Ronde, C. E. J., Merle, S. G., Davy, B., Tontini, F. C., 2012, Detailed Morphology and Structure of an Active Submarine Arc Caldera: Brothers Volcano, Kermadec Arc. Economic Geology, **v. 107**, p. 1557–1570

Finn, C. A., and Morgan, L. A., 2002, High-resolution aeromagnetic mapping of volcanic terrain, Yellowstone National Park. Journal of Volcanology and Geothermal Research, **v. 115**, p. 207–231

Fiske, R. S., Naka, J., Iizasa, K., Yuasa, M., Klaus, A., 2001, Submarine silicic caldera at the front of the Izu-Bonin arc, Japan: Voluminous seafloor eruptions of rhyolite pumice. Geological Society of America Bulletin, **v.** 113, p. 813-824

Fouquet, Y., Pelleter, E., Konn, C., Chazot, G., Dupré, S., Alix, A. S., Chéron, S., Donval, J. P., Guyader, V., Etoubleau, J., Charlou, J. L., Labanieh, S., Scalabrin, C., 2018, Volcanic and hydrothermal processes in submarine calderas: The Kulo Lasi example (SW Pacific). Ore Geology Reviews, **v. 99**, p. 314–343

Francis, P. W., Hammill, M., Kretzschmar, G., Thorpe, R. S., 1978, The Cerro Galan Caldera, North-west Argentina and its tectonic setting. Nature, **v. 274**, p. 749–751

Fujiwara, S., Murakami, M., Nishimura, T., Tobita, M., Yarai, H., Kobayashi, T., 2017, Volcanic deformation of Atosanupuri volcanic complex in the Kussharo caldera, Japan, from 1993 to 2016 revealed by JERS-1, ALOS, and ALOS-2 radar interferometry. Earth, Planets and Space, **v. 69**, 14 p.

Gamo, T., Masuda, H., Yamanaka, T., Okamura, K., Ishibashi, J., Nakayama, E., Obata, H., Shitashima, K., Nishio, Y., Hasumoto, H., Watanabe, M., Mitsuzawa, K., Seama, N., Tsunogai, Kouzuma, F., Sano, Y., 2004, Discovery of a new hydrothermal venting site in the southernmost Mariana Arc: Al-rich hydrothermal plumes and white smoker activity associated with biogenic methane. Geochemical Journal, **v. 38**, p. 527–534

Gena, K., Mizuta, T., Ishiyama, D., Urabe, T., 2001, Acid-sulphate Type Alteration and Mineralization in the Desmos Caldera, Manus Back-arc Basin, Papua New Guinea. Resource Geology, **v. 51**, p. 31–44

Geshi, N., Shimano, T., Chiba, T., Nakada, S., 2002, Caldera collapse during the 2000 eruption of Miyakejima Volcano, Japan. Bulletin of Volcanology, **v. 64**, p. 55–68

Geyer, A., and Martí, J., 2008, The new worldwide collapse caldera database (CCDB): A tool for studying and understanding caldera processes. Journal of Volcanology and Geothermal Research, **v. 175**, p. 334–354

Glasby, G. P., Iizasa, K., Yuasa, M., Usui, A., 2000, Submarine Hydrothermal Mineralization on the Izu–Bonin Arc, South of Japan: An Overview. Marine Georesources and Geotechnology, **v. 18**, p. 141–176

Graham, I. J., Reyes, A. G., Wright, I. C., Peckett, K. M., Smith, I. E. M., Arculus, R. J., 2008a, Structure and petrology of newly discovered volcanic centers in the northern Kermadec-southern Tofua arc, South Pacific Ocean. Journal of Geophysical Research: Solid Earth, **v. 113**, 24 p.

Greene, H. G., and Exon, N. F., 1988, Acoustic stratigraphy and hydrothermal activity within Epi Submarine Caldera, Vanuatu, New Hebrides Arc. Geo-Marine Letters, **v. 8**, p. 121–129

Gudmundsson, M. T., and Högnadóttir, T., 2007, Volcanic systems and calderas in the Vatnajökull region, central Iceland: Constraints on crustal structure from gravity data Journal of Geodynamics, **v. 43**, p. 153–169

Heming, R. F., 1974, Geology and Petrology of Rabaul Caldera, Papua New Guinea. Geological Society of America Bulletin, **v. 85**, p. 1253-1264

Hill, D. P., Bailey, R. A., Ryall, A. S., 1985, Active tectonic and magmatic processes beneath Long Valley Caldera, eastern California: An overview. Journal of Geophysical Research, v. 90, p. 11111-11120

Holk, G. J., Taylor, B. E., Galley, A. G., 2008, Oxygen isotope mapping of the Archean Sturgeon Lake caldera complex and VMS-related hydrothermal system, Northwestern Ontario, Canada. Mineralium Deposita, **v. 43**, p. 623–640

Honsho, C., Ura, T., Kim, K., 2013, Deep-sea magnetic vector anomalies over the Hakurei hydrothermal field and the Bayonnaise knoll caldera, Izu-Ogasawara arc, Japan: Journal of Geophysical Research: Solid Earth, **v. 118**, p. 5147–5164

Honsho, C., Ura, T., Asada, A., Kim, K., Nagahashi, K., 2015, High-resolution acoustic mapping to understand the ore deposit in the Bayonnaise knoll caldera, Izu-Ogasawara arc. Journal of Geophysical Research: Solid Earth, **v. 120**, p. 2070–2092

Hooft, E. E. E., and Detrick, R. S., 1995, Relationship between axial morphology, crustal thickness, and mantle temperature along the Juan de Fuca and Gorda Ridges. Journal of Geophysical Research: Solid Earth, **v. 100**, p. 22499–22508

Iizasa, K., Yuasa, M., Yokota, S., 1992, Mineralogy and geochemistry of volcanogenic sulfides from the Myojinsho submarine caldera, the Shichito-Iwojima Ridge, Izu-Ogasawara Arc, northwestern Pacific. Marine Geology, **v. 108**, p. 39–58

Iizasa, K., Fiske, R. S., Ishizuka, O., Yuasa, M., Hashimoto, J., Ishibashi, J., Naka, J., Horii, Y., Fujiwara, Y., Imai, A., Koyama, S., 1999, A Kuroko-Type Polymetallic Sulfide Deposit in a Submarine Silicic Caldera. Science, **v. 283**, p. 975–977

Janiszewski, H. A., Abers, G. A., Shillington, D. J., and Calkins, J. A., 2013, Crustal structure along the Aleutian island arc: New insights from receiver functions constrained by active-source data. Geochemistry, Geophysics, Geosystems, **v. 14**, p. 2977–2992

Kalacheva, E., Taran, Y., Voloshina, E., Inguaggiato, S., 2017, Hydrothermal system and acid lakes of Golovin caldera, Kunashir, Kuril Islands: Geochemistry, solute fluxes and heat output. Journal of Volcanology and Geothermal Research, **v. 346**, p. 10-20

Kandlbauer, J., and Sparks, R. S. J., 2014, New estimates of the 1815 Tambora eruption volume. Journal of Volcanology and Geothermal Research, **v. 286**, p. 93–100

Katase, F., Iizasa, K., Mizuno, K., Asada, A., Matsuda, T., Saito, Y., 2016, Seafloor Hydrothermal Deposits Exploration by Bathymetry and Backscattering Data Using Multibeam Echo-Sounder in the Higashi-Aogashima Caldera. The Journal of the Marine Acoustics Society of Japan, **v. 43**, p. 208–218

Katsui, Y., Ando, S., Inaba, K. Formation and Magmatic Evolution of Mashu Volcano, East Hokkaido, Japan. Journal of the Faculty of Science, Hokkaido University, Series IV, **v. 16**, p. 533-552

Klischies, M., Petersen, S., Devey, C. W., 2019, Geological mapping of the Menez Gwen segment at 37°50′N on the Mid-Atlantic Ridge: Implications for accretion mechanisms and associated hydrothermal activity at slow-spreading mid-ocean ridges. Marine Geology, **v. 412**, p. 107–122

Koschinsky, A., Seifert, R., Knappe, A., Schmidt, K., Halbach, P., 2007, Hydrothermal fluid emanations from the submarine Kick'em Jenny volcano, Lesser Antilles Island arc. Marine Geology, **v. 244**, p. 129–141

Kudo, T., Sasaki, M., Uchiyama, Y., Nozawa, A., Sasaki, H., Tokizawa, T., Takarada, S., 2007, Petrological variation of large-volume felsic magmas from Hakkoda-Towada caldera cluster:

Implications for the origin of high-K felsic magmas in the Northeast Japan Arc. Island Arc, **v. 16**, p. 133-155

Kwoun, O.-I., Lu, Z., Neal, C., Wicks, C., 2006, Quiescent deformation of the Aniakchak Caldera, Alaska, mapped by InSAR. Geology, **v. 34**, p. 5-8

Lagmay, A. M. F., Rodolfo, K. S., Siringan, F. P., Uy, H., Remotigue, C., Zamora, P., Lapus, M., Rodolfo, R., Ong, J., 2007, Geology and hazard implications of the Maraunot notch in the Pinatubo Caldera, Philippines. Bulletin of Volcanology, **v. 69**, p. 797–809

Larter, R. D., Vanneste, L. E., Morris, P., Smythe, D. K., 2003, Structure and tectonic evolution of the South Sandwich arc. Geological Society, London, Special Publications, **v. 219**, p. 255–284

Ligi, M., Cocchi, L., Bortoluzzi, G., D'Oriano, F., Muccini, F., Caratori Tontini, F., de Ronde, C. E. J., Carmisciano, C., 2014, Mapping of Seafloor Hydrothermally Altered Rocks Using Geophysical Methods: Marsili and Palinuro Seamounts, Southern Tyrrhenian Sea. Economic Geology, **v. 109**, p. 2103–2117

Lindsay, J. M., Shepherd, J. B., and Wilson, D., 2005, Volcanic and Scientific Activity at Kick 'em Jenny Submarine Volcano 2001-2002: Implications for Volcanic Hazard in the Southern Grenadines, Lesser Antilles. Natural Hazards, **v. 34**, p. 1–24

Linse, K., Copley, J. T., Connelly, D. P., Larter, R. D., Pearce, D. A., Polunin, N. V. C., Rogers, A. D., Chen, C., Clarke, A., Glover, A. G., Graham, A. G. C., Huvenne, V. A. I., Marsh, L., Reid, W. D. K., Roterman, C. N., Sweeting, C. J., Zwirglmaier, K., Tyler, P. A., 2019, Fauna of the Kemp Caldera and its upper bathyal hydrothermal vents (South Sandwich Arc, Antarctica). Royal Society Open Science, **v. 6**, 26 p.

Lupton, J., Lilley, M., Butterfield, D., Evans, L., Embley, R., Massoth, G., Christenson, B., Nakamura, K., Schmidt, M., 2008, Venting of a separate CO_2 -rich gas phase from submarine arc volcanoes: Examples from the Mariana and Tonga-Kermadec arcs. Journal of Geophysical Research: Solid Earth, **v. 113**, 21 p.

Machida, H., Blong, R. J., Specht, J., Moriwaki, H., Torrence, R., Hayakawa, Y., Talai, B., Lolok, D., Pain, C. F., 1996, Holocene explosive eruptions of Witori and Dakataua caldera volcanoes in West New Britain, Papua New Guinea Quaternary International, **v. 34–36**, p. 65–78

Maeno, F., and Taniguchi, H., 2006, Silicic lava dome growth in the 1934–1935 Showa Iwo-jima eruption, Kikai caldera, south of Kyushu, Japan. Bulletin of Volcanology, **v. 68**, p. 673–688

Maeno, F., and Taniguchi, H., 2007, Spatiotemporal evolution of a marine caldera-forming eruption, generating a low-aspect ratio pyroclastic flow, 7.3 ka, Kikai caldera, Japan: Implication from near-vent eruptive deposits Journal of Volcanology and Geothermal Research, **v. 167**, p. 212–238

Marra, F., Freda, C., Karner, D. B., Renne, P. R., Gaeta, M., Palladino, D. M., Trigila, R., Cavarretta, G. Post-caldera activity in the Alban Hills volcanic district (Italy). Bulletin of Volcanology, **v. 65**, p. 227-247

Martí, J., Mitjavila, J., Araña, V., 1994, Stratigraphy, structure and geochronology of the Las Cañadas caldera (Tenerife, Canary Islands). Geological Magazine, **v. 131**, p. 715–727

Martí, J., Vila, J., Rey, J., 1996, Deception Island (Bransfield Strait, Antarctica): an example of a volcanic caldera developed by extensional tectonics. Geological Society, London, Special Publications, **v. 110**, p. 253–265

Martí, J., Geyer, A., Aguirre-Diaz, G., 2013, Origin and evolution of the Deception Island caldera (South Shetland Islands, Antarctica) Bulletin of Volcanology, **v. 75**, 18 p.

McKee, C. O., 2015, Tavui Volcano: neighbour of Rabaul and likely source of the Middle Holocene penultimate major eruption in the Rabaul area. Bulletin of Volcanology, **v. 77**, 21 p.

Monzier, M., Robin, C., Eissen, J.-P., 1994, Kuwae (≈ 1425 A.D.): the forgotten caldera. Journal of Volcanology and Geothermal Research, **v. 59**, p. 207–218

Nairn, I. A., Wood, C. P., Bailey, R. A. The Reporoa Caldera, Taupo Volcanic Zone: source of the Kaingaroa Ignimbrites. Bulletin of Volcanology, **v. 56**, p. 529-537

Nakagawa, T., Takai, K., Suzuki, Y., Hirayama, H., Konno, U., Tsunogai, U., Horikoshi, K., 2006, Geomicrobiological exploration and characterization of a novel deep-sea hydrothermal system at the TOTO caldera in the Mariana Volcanic Arc. Environmental Microbiology, **v. 8**, p. 37–49

Nakahigashi, K., Shinohara, M., Suzuki, S., Hino, R., Shiobara, H., Takenaka, H., Nishino, M., Sato, T., Yoneshima, S., Kanazawa, T., 2004, Seismic structure of the crust and uppermost mantle in the incipient stage of back arc rifting - northernmost Okinawa Trough. Geophysical Research Letters, **v. 31**, 4 p.

Nelson, C. H., Bacon, C. R., Robinson, S. W., Adam, D. P., 1994, The volcanic, sedimentologie, and paleolimnologic history of the Crater Lake caldera floor, Oregon: Evidence for small caldera evolution. Geological Society of America Bulletin, **v.106**, p. 684-704

Noguchi, T., Shinjo, R., Ito, M., Takada, J., Oomori, T., 2011, Barite geochemistry from hydrothermal chimneys of the Okinawa Trough: insight into chimney formation and fluid/sediment interaction. Journal of Mineralogical and Petrological Sciences, **v. 106**, p. 26–35

Nomikou, P., Carey, S., Papanikolaou, D., Croff Bell, K., Sakellariou, D., Alexandri, M., Bejelou, K., 2012, Submarine volcanoes of the Kolumbo volcanic zone NE of Santorini Caldera, Greece. Global and Planetary Change, **v. 90–91**, p. 135–151

Ogawa, Y., Ichiki, M., Kanda, W., Mishina, M., Asamori, K., 2014, Three-dimensional magnetotelluric imaging of crustal fluids and seismicity around Naruko volcano, NE Japan. Earth, Planets and Space, **v. 66**, 13 p.

Ondréas, H., Cannat, M., Fouquet, Y., Normand, A., Sarradin, P. M., Sarrazin, J., 2009, Recent volcanic events and the distribution of hydrothermal venting at the Lucky Strike hydrothermal field, Mid-Atlantic Ridge. Geochemistry, Geophysics, Geosystems, **v. 10**, 18 p.

Park, J.-W., Campbell, I. H., Kim, J., Moon, J.-W., 2015, The Role of Late Sulfide Saturation in the Formation of a Cu- and Au-rich Magma: Insights from the Platinum Group Element Geochemistry of Niuatahi-Motutahi Lavas, Tonga Rear Arc. Journal of Petrology, **v. 56**, p. 59–81

Passaro, S., Milano, G., D'Isanto, C., Ruggieri, S., Tonielli, R., Bruno, P. P., Sprovieri, M., Marsella, E., 2010, DTM-based morphometry of the Palinuro seamount (Eastern Tyrrhenian Sea): Geomorphological and volcanological implications. Geomorphology, **v. 115**, p. 129–140

Passaro, S., Milano, G., Sprovieri, M., Ruggieri, S., Marsella, E., 2011, Quaternary still-stand landforms and relations with flank instability events of the Palinuro Bank (southeastern Tyrrhenian Sea). Quaternary International, **v. 232**, p. 228–237

Ponomareva, V. V., Kyle, P. R., Melekestsev, I. V., Rinkleff, P. G., Dirksen, O. V., Sulerzhitsky, L. D., Zaretskaia, N. E., Rourke, R., 2004, The 7600 (14C) year BP Kurile Lake caldera-forming eruption, Kamchatka, Russia: stratigraphy and field relationships. Journal of Volcanology and Geothermal Research, **v. 136**, p. 199-222

Ramos, E. G., 2002, Origin and geologic features of Taal Lake, Philippines. Aquatic Ecosystem Health and Management, **v. 5**, p. 155-162

Self, S., Rampino, M. R., Newton, M, S., Wolff, J. A., 1984, Volcanological study of the great Tambora eruption of 1815. Geology, **v. 12**, p. 659-663

Searle, R. C., 1971, A Gravity Survey of Ngorongoro Caldera, Tanzania. Bulletin Volcanologique, **v. 35**, p. 350-357

Skilling, I. P., 1993, Incremental caldera collapse of Suswa volcano, Gregory Rift Valley, Kenya. Journal of the Geological Society, **v. 150**, p. 885–896

Sparks, R. S. J., Francis, P. W., Hamer, R. D., Pankhurst, R. J., O'Callaghan, L. O., Thorpe, R. S., Page, R., 1985, Ignimbrites of the Cerro Galan caldera, NW Argentina. Journal of Volcanology and Geothermal Research, **v. 24**, p. 205–248

Spinks, K. D., Acocella, V., Cole, J. W., Bassett, K. N., 2005, Structural control of volcanism and caldera development in the transtensional Taupo Volcanic Zone, New Zealand. Journal of Volcanology and Geothermal Research, **v. 144**, p. 7-22

Steck, L. K., Thurber, C. H., Fehler, M. C., Lutter, W. J., Roberts, P. M., Baldridge, W. S., Stafford, D. G., Sessions, R., 1998, Crust and upper mantle *P* wave velocity structure beneath Valles Caldera, New Mexico: Results from the Jemez teleseismic tomography experiment. Journal of Geophysical Research: Solid Earth, **v. 103**, p. 24301–24320

Stern, R. J., Tamura, Y., Embley, R. W., Ishizuka, O., Merle, S. G., Basu, N. K., Kawabata, H., Bloomer, S. H., 2007, Evolution of West Rota Volcano, an extinct submarine volcano in the southern Mariana Arc: Evidence from sea floor morphology, remotely operated vehicle observations and ^{40}Ar-39Ar geochronological studies: West Rota Volcano, Mariana Arc. Island Arc, **v. 17**, p. 70–89

Stern, R. J., Tamura, Y., Ishizuka, O., Shukano, H., Bloomer, S. H., Embley, R. W., Leybourne, M., Kawabata, H., Nunokawa, A., Nichols, A. R. L., Kohut, E., Pujana, I., 2014, Volcanoes of the Diamante cross-chain: evidence for a mid-crustal felsic magma body beneath the Southern Izu–Bonin–Mariana arc. Geological Society, London, Special Publications, **v. 385**, p. 235–255

Stoffers, P., Worthington, T., Schwarz-Schampera, U., Ackermand, D., Beaudoin, Y., Bigalke, N., Fretzdorff, S., Gibson, H., Hekinian, R., Kindermann, A., Kuhn, T., Main, W., Schreiber, K., Timm, C., Tonga'onevai, S., Türkay, M., Unverricht, D., Vailea, A., Zimmerer, M., 2002, Cruise

Report SONNE 167 LOUISVILLE, Louisville Ridge: Dynamics and magmastism of a mantle plume and its influence on the Tonga-Kermadec Subduction System, Suva Fiji, Wellington New Zealand, 12 Oct. – 02 Dec. 2002, Christian-Albrechts-Universität, Kiel, Germany, 281 p., ISSN 0175-9302

Stoffers, P., Worthington, T. J., Schwarz-Schampera, U., Hannington, M. D., Massoth, G. J., Hekinian, R., Schmidt, M., Lundsten, L. J., Evans, L. J., Vaiomo'unga, R., Kerby, T., 2006, Submarine volcanoes and high-temperature hydrothermal venting on the Tonga arc, southwest Pacific. Geology, **v. 34**, p. 453-456

Stüben, D., Bloomer, S. H., Taïbi, N. E., Neumann, Th., Bendel, V., Püschel, U., Barone, A., Lange, A., Shiying, W., Cuizhong, L., Deyu, Z., 1992a, First results of study of sulphur-rich hydrothermal activity from an island-arc environment: Esmeralda Bank in the Mariana Arc. Marine Geology, **v. 103**, p. 521–528

Stüben, D., Bloomer, S. H., Taïbi, N. E., Neumann, Th., Bendel, V., Püschel, U., Barone, A., Lange, A., Shiying, W., Cuizhong, L., Deyu, Z., 1992b, First results of study of sulphur-rich hydrothermal activity from an island-arc environment: Esmeralda Bank in the Mariana Arc. Marine Geology, **v. 103**, p. 521–528

Sturkell, E. and Sigmundsson, F., 2000, Continuous deflation of the Askja caldera, Iceland, during the 1983-1998 noneruptive period. Journal of Geophysical Research, **v. 105**, p. 25671-25684

Suñe-Puchol, I., Aguirre-Díaz, G. J., Dávila-Harris, P., Miggins, D. P., Pedrazzi, D., Costa, A., Ortega-Obregón, C., Lacan, P., Hernández, W., Gutiérrez, E., 2019, The Ilopango caldera complex, El Salvador: Origin and early ignimbrite-forming eruptions of a graben/pull-apart caldera structure. Journal of Volcanology and Geothermal Research, **v. 371**, p. 1–19

Takahashi, N., Suyehiro, K., Shinohara, M., 1998, Implications from the seismic crustal structure of the northern Izu-Bonin arc. The Island Arc, **v. 7**, p. 383–394

Tamura, Y., Tani, K., Ishizuka, O., Chang, Q., Shukuno, H., Fiske, R. S., 2005, Are Arc Basalts Dry, Wet, or Both? Evidence from the Sumisu Caldera Volcano, Izu–Bonin Arc, Japan. Journal of Petrology, v. 46, p. 1769–1803

Tatsumi, Y., Suzuki-Kamata, K., Matsuno, T., Ichihara, H., Seama, N., Kiyosugi, K., Nakaoka, R., Nakahigashi, K., Takizawa, H., Hayashi, K., Chiba, T., Shimizu, S., Sano, M., Iwamaru, H., Morozumi, H., Sugioka, H., Yamamoto, Y., 2018, Giant rhyolite lava dome formation after 7.3 ka supereruption at Kikai caldera, SW Japan. Scientific Reports, **v. 8**, 9 p.

Torres, R. C., Self, S., Punongbayan, R. S., 1995, Attention focuses on Taal: Decade volcano of the Philippines. Eos, Transactions American Geophysical Union, **v. 76**, p. 241–241

Tsunogai, U., Ishibashi, J., Wakita, H., Gamo, T., Watanabe, K., Kajimura, T., Kanayama, S., Sakai, H., 1994, Peculiar features of Suiyo Seamount hydrothermal fluids, Izu-Bonin Arc: Differences from subaerial volcanism. Earth and Planetary Science Letters, **v. 126**, p. 289–301

Usui, A., and Nishimura, A., 1992, Submersible observations of hydrothermal manganese deposits on the Kaikata Seamount, Izu-Ogasawara (Bonin) Arc. Marine Geology, **v. 106**, p. 203–216

Walker, J. A., Williams, S. N., Kalamarides, R. I., Feigenson, M. D., 1993, Shallow open-system evolution of basaltic magma beneath a subduction zone volcano: The Masaya Caldera Complex, Nicaragua. Journal of Volcanology and Geothermal Research, **v. 56**, p. 379–400

Wilson, C. J. N., Rogan, A. M., Smith, I. E. M., Northey, D. J., Nairn, I. A., Houghton, B. F. Caldera volcanoes of the Taupo Volcanic Zone, New Zealand. Journal of Geophysical Research, **v. 89**, p. 8463-8484

Wormald, S. C., Wright, I. C., Bull, J. M., Lamarche, G., Sanderson, D. J., 2012, Morphometric analysis of the submarine arc volcano Monowai (Tofua–Kermadec Arc) to decipher tectono-magmatic interactions. Journal of Volcanology and Geothermal Research, **v. 239–240**, p. 69–82

Worthington, T. J., Gregory, M. R., Bondarenko, V., 1999, The Denham Caldera on Raoul Volcano: dacitic volcanism in the Tonga–Kermadec arc. Journal of Volcanology and Geothermal Research, **v. 90**, p. 29–48

Wright, I. C., and Gamble, J. A., 1999, Southern Kermadec submarine caldera arc volcanoes (SW Pacific): caldera formation by effusive and pyroclastic eruption. Marine Geology, **v. 161**, p. 207-227

Wright, I. C., Gamble, J. A., Shane, P. A., 2003, Submarine silicic volcanism of the Healy caldera, southern Kermadec arc (SW Pacific): I – volcanology and eruption mechanisms. Bulletin of Volcanology, **v. 65**, p. 15–29

Wright, I. C., Worthington, T. J., Gamble, J. A., 2006, New multibeam mapping and geochemistry of the 30°–35° S sector, and overview, of southern Kermadec arc volcanism. Journal of Volcanology and Geothermal Research, **v. 149**, p. 263–296

Zharkov, R. V., 2019, Thermal springs of the Ushishir volcano (Russia). IOP Conference Series: Earth and Environmental Science, **v. 324**, 7 p.